Ultra-High Frequency Nanoelectromechanical Systems with Low-Noise Technologies for Single-Molecule Mass Sensing

Thesis by

Philip Xiao-Li Feng

In Partial Fulfillment of the Requirements

for the Degree of

Doctor of Philosophy

California Institute of Technology
Pasadena, California

2006

(Defended August 14, 2006)

© 2006

Philip Xiao-Li Feng

All Rights Reserved

to my wife, and our parents

Acknowledgements

First and foremost I would like to express my deep gratitude to my advisor, Professor Michael Roukes, for his consistent support throughout the past four years. I highly appreciate the abundant resources he has invested in me and my work, and the precious freedom and opportunities he has lent to me. Imprinted by his dedication to research programs in sustaining strong support for the whole group, I am especially grateful to him for his inspiration, encouragement, patience and trust that helps keep my confidence undiminished in science and technology. Amongst many things, Michael as a physicist deserves my respect for his courage and passion in pushing forward with his broad vision, for his firm attitude on doing only the most high-profile research with in-depth understandings, publishing only the very best results in an era of pervasive and increasing overpublication, and for his persistent pursuit of preciseness and perfection in our work. All these will continue to inspire and motivate me.

Sincere appreciation is extended to my thesis committee, Professors Marc Bockrath, Ali Hajimiri, Changhuei Yang from Caltech, and Professor Ron Lifshitz from Tel Aviv University, for taking their previous time in reading and commenting my thesis. My thanks go to Professors Scott Fraser, Ali Hajimiri, Axel Scherer, Yu-Chong Tai, and Changhuei Yang for being on my candidacy committee and offering insightful comments and helpful suggestions.

I have been very fortunate to collaborate with some of the world's best scientists and engineers in some major projects of my thesis work. My close and happy collaboration with Dr. Chris White from Professor Ali Hajimiri's group has been exciting, stimulating and productive. I highly appreciate Ali's technical comments and suggestions, as well as his support and encouragement. My collaboration with Rongrui He from Professor Peidong Yang's group at Berkeley has been another experience of success and happiness. I am also grateful to Professor Chris Zorman and Professor Mehran Mehregany for high-quality SiC material supply and their careful comments on my drafts, and for the beneficial discussions with both Mehran and Chris.

I am very much indebted to Dr. Xue-Ming Henry Huang for training me systematically and working together for many midnights in the cleanroom and labs, for his having a big heart to share with me his own experience and lessons and to offer me valuable advices. I am grateful to Dr. Jack Ya-Tang Yang and Dr. Carlo Callegari for helping me in the instrumentation lab and for the months the three of us spent there together with long runs of heavy experiments almost 7 days every week, as well as those memorable sessions at the Red Door café. I thank Dr. Hong X. Tang for his help with my early-days cleanroom obligations in maintaining and modifying the CAIBE system. I have had the privilege to collaborate with Henry, Jack, Carlo, Meher Prakash, Hong, Dr. Henk Postma, Rassul Karabalin, Dr. Wayne Hiebert, and Selim Hanay, on various topics.

My special thanks go to Dr. Kamil Ekinci who has been generous in offering help even though he had gone on with his new career before I joined the group. I have enjoyed many discussions with Meher, Inna Kozinsky, Rassul Karabalin, Henk, Dr. Warren Fon, Igor Bargatin, Sotiris Masmanidis, Mo Li, Hong, Dr. Dirk Orgassa, Dr. Sequoyah Aldridge, Dr. Matt LaHaye, Dr. Edward Myers, Ben Gudlewski, Dr. Radovan Urban, Wayne, Selim, Wonhee Lee, Junho Suh, Dr. Jessica Arlett, Renaud Richard, James Maloney, Blake Axelrod, and many other members and alumni of the group. I thank Steve Stryker for his great suggestions and nice work with many components design, machining and repairing for our systems. My thanks are extended to Nils Asplund and Dr. Guy DeRose for their help with instruments in the cleanrooms and labs.

I sincerely thank Ms. Exie-Marie Leagons, Ms. Linda Dosza, and Ms. Loly Ekmekjian, for their countless times of nice help and support.

I thank all my friends here for helping each other and having lots of good time together that have made our lives around Caltech much happier. Particularly I thank my basketball friends for playing every week, which has helped keep me strong and sharp.

Finally, I am deeply in debt to my family and I find myself unable to completely express in words my gratitude and gratefulness. During the years my wife and I have been studying abroad, our parents have been always tolerant and ready to help despite the formidably long distances from our homeland. My now 2-year old daughter has really been an incredible treasure for me: a lot of breakthroughs in the projects of my thesis have been made when we were expecting her; her sweet smile, laughter and talking are my best reward that keep me optimistic and energetic. Any single piece of my work would not have been done without my wife's understanding, support, patience, and love, all through the vicissitudes of this journey.

Acronyms

AC	Alternating Current
AFM	Atomic Force Microscope
APCVD	Atmospheric Pressure Chemical Vapor Deposition
BAR	Bulk Acoustic Resonator
BioNEMS	Biofunctionalized Nanoelectromechanical Systems
BPF	Band-Pass Filter
CAIBE	Chemical Assisted Ion Beam Etch
CFDRC	A commercial simulation software, developed by the CFD Research Corporation (www.cfdrc.com), with CFD standing for Computational Fluid Dynamics
CMOS	Complementary Metal-Oxide-Semiconductor
CNT	Carbon Nanotube
CSAC	Chip-Scale Atomic Clock
CVD	Chemical Vapor Deposition
DC	Direct Current
DR	Dynamic Range
DSHO	Damped Simple Harmonic Oscillator

DUT	Device Under Test
ECR	Electron Cyclotron Resonance
EMF	Electromotive Force
ESI	Electro-Spray Ionization
FDT	Fluctuation Dissipation Theorem
FEMLAB	A commercial simulation software, developed by the COMSOL Inc. (www.comsol.com), with FEM standing for Finite Element Method
FET	Field-Effect Transistor
FFT	Fast Fourier Transform
FM	Frequency Modulation
FWHM	Full Width Half Maximum
GPS	Global Position System
GSM	Global System for Mobile Communications
HF	High Frequency (3MHz – 30MHz)
HV	High Vacuum (≤ or ~10^{-6}Torr)
IC	Integrated Circuits
IF	Intermediate Frequency
LC	Inductive-Capacitive
LIA	Lock-In Amplifier
LNA	Low-Noise Amplifier
LO	Local Oscillator
LPF	Low-Pass Filter

MEMS	Microelectromechanical Systems
MRFM	Magnetic Resonance Force Microscope
MS	Mass Spectrometry
MWCNT	Multi-Walled Carbon Nanotube
NEMS	Nanoelectromechanical Systems
NW	Nanowire
PLL	Phase-Locked Loop
PMMA	Polymethyl-methacrylate
PPB (ppb)	Part Per Billion
PPM (ppm)	Part Per Million
PSD	Phase Sensitive Detector
Q	Quality Factor
QCM	Quartz Crystal Microbalance
QEM	Quantum Electro-Mechanics
RC	Resistive-Capacitive
RF	Radio Frequency
RSBR	Resonance Signal-to-Background Ratio
SAW	Surface Acoustic Wave
SEM	Scanning Electron Microscope
SET	Single-Electron Transistor
SHO	Simple Harmonic Oscillator
SWCNT	Single-Walled Carbon Nanotube

TCXO	Temperature Compensated Crystal Oscillator
TCVCXO	Temperature Compensated Voltage Controlled Crystal Oscillator
UHF	Ultra-High Frequency (300MHz – 3GHz)
UHV	Ultra-High Vacuum (≤ or ~10^{-10} Torr)
VCO	Voltage Controlled Oscillator
VCTCXO	*same as* TCVCXO (above)
VHF	Very-High Frequency (30MHz – 300MHz)
XO	(Quartz) Crystal Oscillator

Abstract

Advancing today's very rudimentary nanodevices toward functional nanosystems with considerable complexity and advanced performance imposes enormous challenges. This thesis presents the research on ultra-high frequency (UHF) nanoelectromechanical systems (NEMS) in combination with low-noise technologies that enable single-molecule mass sensing and offer promises for NEMS-based mass spectrometry (MS) with single-Dalton sensitivity. The generic protocol for NEMS resonant mass sensing is based on real-time locking and tracking of the resonance frequency as it is shifted by the mass-loading effect. This has been implemented in two modes: (i) creating an active self-sustaining oscillator based on the NEMS resonator, and (ii) a higher-precision external oscillator phase-locking to and tracking the NEMS resonance.

The first UHF low-noise self-sustaining NEMS oscillator has been demonstrated by using a 428MHz vibrating NEMS resonator as the frequency reference. This stable UHF NEMS oscillator exhibits ~0.3ppm frequency stability and ~50zg (1zg=10^{-21}g) mass resolution with its excellent wideband-operation (~0.2MHz) capability. Given its promising phase noise performance, the active NEMS oscillator technology also offers important potentials for realizing NEMS-based radio-frequency (RF) local oscillators, voltage-controlled oscillators (VCOs), and synchronized oscillators and arrays that could lead to nanomechanical signal processing and communication. The demonstrated NEMS oscillator operates at much higher frequency than conventional crystal oscillators

and their overtones do, which opens new possibilities for the ultimate miniaturization of advanced crystal oscillators.

Low-noise phase-locked loop (PLL) techniques have been developed and engineered to integrate with the resonance detection circuitry for the passive UHF NEMS resonators. Implementations of the NEMS-PLL mode with generations of low-loss UHF NEMS resonators demonstrate improving performance, namely, reduced noise and enhanced dynamic range. Very compelling frequency stability of ~0.02ppm and unprecedented mass sensitivity approaching 1zg has been achieved with a typical 500MHz device in the narrow-band NEMS-PLL operation.

Retaining high quality factors (Q's) while scaling up frequency has become crucial for UHF NEMS resonators. Extensive measurements, together with theoretical modeling, have been performed to investigate various energy loss mechanisms and their effects on UHF devices. This leads to important insights and guidelines for device Q-engineering.

The first VHF/UHF silicon nanowire (NW) resonators have been demonstrated based on single-crystal Si NWs made by bottom-up chemical synthesis nanofabrication. Pristine Si NWs have well-faceted surfaces and exhibit high Q's ($Q\approx 13100$ at 80MHz and $Q\approx 5750$ at 215MHz). Given their ultra-small active mass and very high mass responsivity, these Si NWs also offer excellent mass sensitivity in the ~10−50zg range.

These UHF NEMS and electronic control technologies have demonstrated promising mass sensitivity for kilo-Dalton-range single-biomolecule mass sensing. The achieved performance roadmap, and that extended by next generations of devices, clearly indicates realistic and viable paths toward the single-Dalton mass sensitivity. With further elaborate engineering, prototype NEMS-MS is optimistically within reach.

Preface

The preface presents a brief account of the history of the author's research as a graduate student at Caltech. While the major projects are described in much greater technical detail in the thesis chapters and related publications, the author hopes that this preface will sketch the whole context of the thesis and provide the logic sequences with which the topics had originally been chosen and approached. Importantly, the thesis work has benefited from a lot of collaborations and they are also reviewed here accordingly.

(i) Starting and Warming-Up Projects

I joined Professor Michael Roukes' group[1] in late Summer 2002, with great enthusiasm for NEMS, and also a lot of curiosities for a number of other attractive research topics in the Roukes group[2]. Within the NEMS subgroup (at that time we had roughly 5 subgroups, namely NEMS, BioNEMS, Spintronics, MRFM, and Phonon/Calorimetry, and about 30 people in total), major thrusts then included mass sensing and noise processes in NEMS resonators, GHz resonators and quantum measurements, nanotube

---

[1] A very interesting picture of the "*Chez Nano*" *Café* appeared on the website <nano.caltech.edu> then.

[2] In hindsight, I was very fortunate to have obtained a free trial copy of the September 2001 issue of *Scientific American*—a special issue on Nanotech, with a collection of fine and enlightening articles written by some leading researchers in this field. I was very much fascinated and I read this handy issue many times. Later, this guided me to approach Dr. Roukes, author of a featured article "*Plenty of Room, Indeed*" that strongly intrigued me and stimulated me with my new research adventures at Caltech.

resonators, NEMS resonators with single-electron transistors (SETs), and so on. My track has been mainly on engineering NEMS devices and measurements systems, particularly at very-high and ultra-high frequencies, for the mass sensing and phase noise experiments.

Before I came, former postdoctoral scholar Dr. Kamil Ekinci had built an ultra-high vacuum (UHV) system and conducted NEMS mass detection experiments with Henry Huang (former graduate student) and they achieved attogram-scale (1ag=10^{-18}g) sensitivity in detecting evaporated gold (Au) atoms with a 32MHz NEMS resonator [1]. After Kamil left for his faculty position at Boston University, the UHV system was modified by former graduate student Jack Yang and postdoctoral scholar Dr. Carlo Callegari to prepare for new experiments on mass sensing and the surface behavior of gas species on NEMS resonators. Meanwhile, Henry had been off the UHV system and primarily pushing for GHz resonators by making even smaller devices, and by the time I joined, he had just found the 1.014GHz and 1.029GHz resonances [2], and was planning to do some other projects [3].

I started by designing circuit boards, making and testing subassemblies (including surface-mount components based limiter, oscillator, mixer, phase-shifter, filters, etc., and some control circuits) for potential use in the mass sensing experiments, while learning from Jack and Carlo the principles and operations of the UHV system and the large cryogenic apparatus (liquid He dewar, superconducting magnet, etc.), and some major measurement instruments involved. Earlier they had spent a few months putting things together to measure gas adsorption-desorption on a 125MHz device but were not happy with its not so impressive quality factor (Q~1300) [4]. While the whole large sophisticated system exhaustingly drew Jack and Carlo's resources and efforts, I found fun in wearing a gown and harboring myself in the cleanroom, where I got trained by

Henry who had ample and fresh experience in making many devices from 10MHz to beyond 1GHz.

I then tested my first batches of resonant NEMS devices (mostly in 150−200MHz range) in the UHV system with Jack's help. It was in this effort, after iterations of continuous fabrication and searching for resonances, that I learned hands-on lessons and developed some intuition for the many subtleties on how to get decent and very good Q's for these VHF devices.

Having made major progress in the gas control and measurement systems, Carlo left to take his faculty position at Graz University of Technology in Austria in January 2003. I took over and worked with Jack day in and day out on the UHV system. Late in March 2003, Jack and I were lucky enough to take the zeptogram sensitivity data (~7zg noise floor) with a 133MHz device cooled down to ~4K with He exchange-gas [4,5]. But then after several more runs of exchange-gas the device was killed. In early May 2003 I made a 190MHz device (with $Q\approx5200$ at ~25K) and we set off to seriously study the effects of surface behavior of absorbed gas on the device. After many runs of tests and discussions we thought we found some interesting regime of operation and we communicated with Carlo. We invited Carlo to come back and he did in mid July 2003 and stayed for 3 weeks. We managed to have repeatable access to the right regime and good conditions, which enabled us to measure the phase noise caused by surface adsorbates fluctuation (could be adsorption-desorption and/or adsorbates surface diffusion, after analyzing data and comparing to theories, and many discussions and debates. It seemed by Spring 2006 the picture was getting much clearer and leading to a strong end of the story) [4,6]. After a lot more measurements of phase noise on this device at various temperatures with gas and without gas during Fall 2003, Jack asked me to keep this amazing 190MHz device sitting in the UHV system for potential data-taking while he began his thesis writing. Later, in February 2004, Jack and I re-scrutinized the

system, reinstalled the nozzle, carefully calibrated gas flux and device performance, and finally we managed to take the real-time frequency shift step data versus pulsed mass loading of gas flux from the gated nozzle, with a real-time noise floor of 20zg [5]. Besides the representative 100zg steps data shown in [5], we also had 50zg steps and 30zg steps data with shorter gas flux pulse times. Jack went to work with Applied Materials in San Jose right after defending his thesis that summer.

Back in Summer 2003, I collaborated with Henry and made the first suspended nanostructures from the bulk 6H-SiC material [7]. We demonstrated 170−175MHz 6H-SiC NEMS resonators (with decent *Q*'s~3000). We also extensively discussed the issues of *Q*'s in many such experiments and thought about interesting topics along this direction. Later that summer Henry and I collaborated with postdoctoral scholar Dr. Henk Postma in making carbon nanotube (CNT) resonators. Henk focused on demonstrating flexural CNT resonators and also planned to couple the device to a single-electron transistor (SET) in measurement. Henry designed a paddle structure in the middle of a CNT and proposed to make torsional resonators to achieve higher *Q* and potential application for zepto-Newton force sensing [3]. I focused on device fabrication. To suspend nanotubes, especially the single-walled carbon nanotubes (SWCNTs) with paddles, the yield was very low. Finally I managed to suspend a paddle-on-SWCNT device but we were not successful in measuring resonance signals out of it [8].

Since the beginning of Fall 2003, I started to take leading roles in several projects and to prepare for the infrastructure for my thesis work. With Jack and Henry's advice and help, I successively refurbished and modified two small cryostat systems and prepared handy accessories and electronics to speed up my experiments. In December I fabricated devices and performed experiments to explore the possibility of on-chip magnetomotive transduction of HF (~10MHz) NEMS resonators [9], with Henry's help

before he defended his thesis and went to Columbia University for a postdoctoral position. A few months later, based on the suggestions from Michael and Dr. Hong X. Tang, I conducted experiments with the second generation of devices [9]. In Fall 2003, I also designed and made free-free beam resonators with torsional supporting beams (instead of lateral supporting beams), and tested them with Jack's help. Not very surprisingly, some of these explorations were not successful on their first shots due to practical limitations. As technologies are being advanced, these ideas are worth revisiting with new generations of designs and devices.

(ii) Concentrating on UHF NEMS and Low-Noise Technologies: Thesis Projects

After several discussions with Michael also back in Summer 2003, I calculated the ultimate phase noise of some ~400MHz devices, and we were thinking of experiments in this direction. I decided to embark on this. It was then that I had a blueprint perspective of my thesis work—it should be focused on pushing for the limits of NEMS mass sensing and phase noise, by developing technologies with UHF (≥300MHz) devices. Also after that summer I began to take a major responsibility in meeting the milestones of our DARPA program, with the outcomes from my research projects.

Around the end of Fall 2003, I started to make generations of UHF devices, and to improve their signal electronic detection techniques. For each device I managed to integrate its tuned resonance detection system into an UHF low-noise phase-locked loop. I systematically did their phase noise and frequency stability measurements and built a roadmap of UHF NEMS performance [10]. Having repeatedly observed that Q decreases as frequency increases and this becomes more acute for UHF devices [11], I performed a series of experiments and analyses to study the Q factors and dissipation issues in UHF devices [12]. These experiments continued till the end of Fall 2004.

In parallel, late in 2003, we initiated an collaborative effort with Professor Ali Hajimiri's group to develop NEMS resonator-based oscillators, on which I closely collaborated with former graduate student Chris White from the Hajimiri group. At the beginning when we could understand the issues and examine our available technologies from both sides, it seemed impossible and impractical to accomplish our goal. Luckily we were persistent and didn't stop our meetings and discussions, gradually we found our paths. When my UHF roadmap approached the 500MHz NEMS node, the time seemed to be ripe for us to experiment with our thoughts about NEMS oscillators. After tedious tests, calibrations, and simulations, in November 2004 we were able to read out very large resonance signals from >400MHz devices. We continued to be very lucky to successfully realize the continuous stable oscillations in mid December. I then focused on fine tunings and the oscillator system became very stable and easy to run. So I stuck with the system and kept it running every day throughout the Christmas and New Year recess, till January 2005, to finish making all the important measurements I could think of [13]. Several weeks later, I revisited the system to make some other measurements to explore the nonlinear behavior of the NEMS oscillator.

Up to this point, virtually all our high-performance VHF/UHF resonators for NEMS mass sensing were based on top-down nanofabricated SiC devices. Meanwhile there had been a surge in studying bottom-up low-dimensional nanostructures, and of particularly interest were CNTs and nanowires (NWs). CNTs and NWs have also been expected for NEMS, but just as with our earlier trials with CNT resonators, the yield of making free-standing CNT and NW mechanical structures is very low; the assembly and integration difficulties further compromise their promises for high-performance NEMS. Although we had this conservative view for bottom-up devices and believed that top-down NEMS would dominate (especially for engineering applications), we were open-minded and kept an eye on the latest advances in bottom-up techniques.

So, in Spring 2005, Michael connected me with Professor Peidong Yang's group at Berkeley, and encouraged me to explore the possibilities of engineering their new Si nanowire structures into high frequency resonators. I communicated with graduate student Rongrui He from Peidong's group and we discussed the possible issues of Si NW devices and the design of sample handling system and procedures. Early in Summer 2005, Rongrui flew down to Pasadena with bunch of samples and stayed for a week. After taking care of both DC and RF electrical connections issues of these Si NWs and couple of unsuccessful runs due to their very high DC resistance and impedance mismatch, we metallized some NWs and were lucky to quickly demonstrate as high as 200MHz resonators (with quite good *Q*'s), which are still the highest record for bottom-up nanowire structures. This was encouraging and convinced us that even these grown NWs could be very robust resonators. After Rongrui headed back to Berkeley I went on to revisit and re-examine the initially intractable pristine (non-metallized), high-impedance Si NWs. I overcame the issues and further explored their piezoresistive effect in detection. I then performed extensive measurements of frequency stability and phase noise for all these Si NW resonators [14]. These bottom-up devices also have quite good frequency stability that translates into very impressive zeptogram-scale mass resolution.

Table 1 Mass sensing performance of HF/VHF SiC NEMS, as of 2002.

Resonance Frequency (MHz)	Device Dimensions $L(\mu m)\times w(nm)\times t(nm)$	Quality Factor Q	Active Device Mass M_{eff} (pg)	Dynamic Range (dB)	Frequency Stability σ_A (1sec)	Mass Sensitivity δM (ag)
13†	17.4×600×70	3000	13	60	1×10^{-7}	2.6
33†	14.2×670×260	3000	8	60	2×10^{-7}	2.5
125‡	1.6×800×70	1300	1	80	4×10^{-7}	0.75

(†These two HF/VHF devices were made by Henry and tested by Kamil and Henry [1]. ‡This VHF device was made by Jack and tested by Jack, Carlo and myself while I was getting trained [4].)

With these projects, I have obtained substantive experimental data for the bulk of my thesis work. Toward the overall goals around NEMS mass sensing, all the technologies

developed in the above projects have shown unprecedented mass resolutions deep in the zeptogram regime (the best is ~3zg with typical ~500MHz devices). To summarize, Table 1 and Table 2 highlight the major milestones of NEMS mass sensitivity before and after the work of this thesis.

Table 2 Mass sensing performance of VHF/UHF SiC NEMS, as of 2006.

Resonance Frequency (MHz)	Device Dimensions L(μm)×w(nm)×t(nm)	Quality Factor Q	Active Device Mass M_{eff} (fg)	Dynamic Range (dB)	Frequency Stability σ_A (1sec)	Mass Sensitivity δM (zg)
133*	2.3×150×70	5000	73	80	7×10^{-8}	7 (@4K)
190*	2.3×150×100	5000	96	80	7.4×10^{-8}	20
295	2.66×170×80	3000	118	80	4.7×10^{-8}	15
420	1.8× 150×100	1200	82	90	3.1×10^{-7}	67
411	1.7×120×80	2600	53	85	6.6×10^{-8}	10
428	1.65×120×80	2500	55	90	2.5×10^{-8}	4
482	1.6×120×80	2000	52	98	2.1×10^{-8}	3

(*These two VHF devices were tested in collaboration with Jack and Carlo, and completed by Feb. 2004 [4-6], not the major results from this thesis.)

(iii) Additional Projects and Extended Collaborations

Besides the above thesis projects, one late piece of collaborative work worth mentioning is on the VHF NEMS parametric resonator and amplifier [15]. Graduate student Rassul Karabalin, who joined us in Summer 2004, took a lead in this effort. Michael had the original idea of doing purely mechanical parametric amplification in NEMS devices for many years and former graduate student Darrell Harrington had first demonstrated a 27MHz parametric resonator several years ago [16]. It was highly desired to realize mechanical parametric amplification with VHF/UHF NEMS in order for better performance. So naturally, Rassul was directed to me to start experiments on the VHF parametric resonators after he spent couple of months doing theories and simulations. In November 2004, I designed a new process for nanofabrication of VHF parametric resonators that involved two layers of electron-beam writing but only one step to release

device plus avoiding wet etch. This process is more convenient and suitable for VHF devices than the old process used for making similar but much larger structures [16]. First shooting for ≥100MHz, we went through the new process and Rassul finished the fabrication training with me rather quickly. We were delighted and pushed forward to measurements. With two generations of devices we developed several schemes to see the parametric amplification effects in 110MHz and 140MHz devices from Spring to Summer 2005. We also observed that the effect of joule heating scaled up more strongly in these much smaller devices, thus shadowing the parametric amplification effects we wanted to exploit. Later Rassul continued to do more theoretical modeling of the thermal effect and scaling [15] when I was pulled to the NEMS mass spectrometry (NEMS-MS) project. Meanwhile, I also collaborated with Rassul in exploring transduction schemes for VHF/UHF resonators based on electrostatic coupling through nanometer gaps [17].

Briefly, the NEMS-MS project aimed to develop NEMS-based MS [18]. It was envisioned by Michael probably at least as early as when he asked Kamil to build up the UHV system for doing NEMS mass sensing. Now with the great mass sensitivity we have demonstrated, it is time to push toward the Holy Grail—single-molecule mass sensing. Ultimately, NEMS capability for single-molecule sensing with single-Dalton sensitivity will lead to weighing single molecules only by their masses and this provides a sheer new paradigm for MS. To this grand goal, our first task is to do single-biomolecule sensing/counting with our demonstrated zeptogram sensitivity. Since Fall 2004, postdoctoral scholar Dr. Wayne Hiebert had been designing new parts for the UHV system. In Fall 2005, the system was refurbished, with an electro-spray ionization (ESI) unit installed on top to generate the ionized biomolecule flux, which would be guided by a hexapole assembly all the way to the NEMS device. In late Fall 2005, the vacuum system began to work and we did tests and calibrations of the system. In Winter 2005, I ran a 300MHz device with a sufficiently low noise floor for catching

molecules, but we suffered from very low molecule flux and caption rate. Since Wayne left for his new career at the National Institute of Nanotechnology in Canada early 2006, graduate student Selim Hanay has taken over and been working on the ion guiding to improve the molecule flux delivered to the NEMS detector. Looking forward to new efforts on this, my major thrust is to integrate even better UHF NEMS into this system and to ensure the molecule-counting capability is really attained in the system. Currently this project is still in progress.

Bibliography

[1] K.L. Ekinci, X.M.H. Huang, M.L. Roukes, "Ultrasensitive nanoelectromechanical mass detection", *Appl. Phys. Lett.* **84**, 4469-4471 (2004).

[2] X.M.H. Huang, C.A. Zorman, M. Mehregany, M.L. Roukes, "Nanodevice motion at microwave frequencies", *Nature* **421**, 496 (2003).

[3] X.M.H. Huang, *Ultrahigh and Microwave Frequency Nanomechanical Systems* (Ph.D. Thesis, Advisor: M.L. Roukes), California Institute of Technology (2004).

[4] Y.T. Yang, *Phase Noise in Nanoelectromechanical Systems* (Ph.D. Thesis, Advisor: M.L. Roukes), California Institute of Technology (2004).

[5] Y.T. Yang, C. Callegari, X.L. Feng, K.L. Ekinci, M.L. Roukes, "Zeptogram-scale nanomechanical mass sensing", *Nano Lett.* **6**, 583-586 (2006).

[6] Y.T. Yang, C. Callegari, X.L. Feng, M.L. Roukes, "Surface adsorbates fluctuation and phase noise in VHF NEMS", *to be published* (2006).

[7] X.M.H. Huang, X.L. Feng, M.L. Roukes, *et al.*, "Fabrication of suspended nanomechanical structures from bulk 6H-SiC substrates", *Mat. Sci. Forum* **457-460**, 1531-1534 (2004). Earlier as *ibid*, presented at *Int. Conf. on SiC & Related Materials (ICSCRM 2003)*, Lyon, France, Oct. 5-10 (2003).

[8] X.M.H. Huang, X.L. Feng, H.W.Ch. Postma, M.L. Roukes, "Torsional nanotube-paddle structure and resonator", *unpublished data* (2003).

[9] X.L. Feng, X.M.H. Huang, H.X. Tang, M.L. Roukes, "On-chip magnetomotive transduction of HF/VHF NEMS resonators", *unpublished data* (2004).

[10] X.L. Feng, M.L. Roukes, "Frequency stability and phase noise in ultra-high frequency NEMS resonators", *to be published* (2006).

[11] X.M.H. Huang, X.L. Feng, C.A. Zorman, M. Mehregany, M.L. Roukes, "VHF, UHF and microwave frequency nanomechanical resonators" (invited article), *New J. Phys.* **7**, 247 (2005).

[12] X.L. Feng, C.A. Zorman, M. Mehregany, M.L. Roukes, "Dissipation in single-crystal SiC UHF nanomechanical resonators", *Tech. Digest of the 2006 Solid-State Sensors, Actuators & Microsystems Workshop (Hilton Head 2006)*, 86-89, Hilton Head Island, SC, June 4-8 (2006). [Extended full-length article to be submitted to *JMEMS*.]

[13] X.L. Feng, C.J. White, A. Hajimiri, M.L. Roukes, "Ultra-high frequency low-noise self-sustaining oscillator with vibrating nanomechanical resonator", *to be published* (2006).

[14] X.L. Feng, R.R. He, P.D. Yang, M.L. Roukes, "High-performance silicon nanowire VHF/UHF nanomechanical resonators", *to be published* (2006).

[15] R. Karabalin, X.L. Feng, M.L. Roukes, "Very-high frequency nanomechanical parametric resonator and amplifier", *to be published* (2006).

[16] D.A. Harrington, *Physics and Applications of Nanoelectromechanical Systems* (Ph.D. Thesis, Advisor: M.L. Roukes), California Institute of Technology (2003).

[17] X.L. Feng, R. Karabalin, M.L. Roukes, "Integrated transduction of VHF NEMS resonators with nanometer-scale gaps", *unpublished data* (2005).

[18] W.K. Hiebert, X.L. Feng, S. Hanay, M.L. Roukes, "Toward single-molecule nanomechanical mass spectrometry", Presented at *Annual Meeting of American Physics Society*, Los Angeles, CA, March 21-25 (2005).

Contents

Acknowledgements······v
Acronyms······vii
Abstract······xi
Preface······xiii

Contents······xxv
List of Figures······xxix
List of Tables······xxxiii

Chapter 1 Introduction and Overview······1
1.1 Background and Motivations······2
1.2 Nanoelectromechanical Systems······3
1.3 Ultimate Miniaturization of Resonant Mass Sensors······4
1.4 *Engineering* NEMS for Single-Molecule Mass Sensing······6
1.5 Thesis Organization and Chapter Overview······7
Bibliography······10

Chapter 2 Foundations of VHF, UHF and Microwave NEMS Resonators······13
2.1 Theoretical Foundation······14
2.1.1 Beam Resonators and Their Basic Characteristics······14
2.1.2 Noise Processes······20
2.1.3 Nonlinearity and Dynamic Range······29
2.1.4 Basics and Metrics of NEMS Mass Sensing······31
2.2 Experimental Foundation······34
2.2.1 Silicon Carbide (SiC) Material for RF NEMS······34
2.2.2 Nanofabrication of NEMS Resonators······37
2.2.3 Transduction of VHF/UHF/Microwave NEMS Resonance······39
2.2.4 Resonance Detection and Electronic Readout······41
Bibliography······44

Chapter 3 Ultra-High Frequency Low-Noise Self-Sustaining Oscillator Based upon *Vibrating* Nanomechanical Resonator······47
3.1 Introduction to Self-Sustaining Oscillator······48
3.2 Crystal Oscillators: from Quartz to *Vibrating* NEMS······49
3.3 Large-Signal UHF Resonance Readout for NEMS Oscillator······52
3.3.1 Resonance Signal-to-Background Ratio *(RSBR)* ······52
3.3.2 High-Resolution Bridge-Balancing and Background-Nulling······60
3.4 Self-Sustaining Oscillator with UHF NEMS Resonator······64
3.4.1 Oscillation Conditions and Calibrations······64
3.4.2 NEMS Oscillator Basic Characteristics······65
3.5 Phase Adjustment and Oscillator Frequency Detuning······70
3.6 NEMS Oscillator Frequency Pulling and Nonlinear Behavior······72
3.7 Phase Noise of UHF NEMS Oscillator······75
3.8 Frequency Stability and Mass Sensitivity······78
3.9 Advanced NEMS Oscillators and NEMS Oscillator Arrays······80
3.10 Chapter Summary······83
Bibliography······85

Chapter 4 UHF NEMS Resonators with Low-Noise Phase-Locked Loops······89
4.1 Nanomechanical Mass Sensing Protocols······90
4.2 Embedding NEMS Resonator into Phase-Locked Loop (PLL) ······92
4.3 Frequency Stability of UHF NEMS Resonators in PLL······100
4.4 Phase Noise of UHF NEMS Resonators in PLL······102
4.5 Roadmaps of UHF NEMS Resonators: Specs and Performances······104
4.6 From UHF NEMS to Local Oscillators for CSAC······110
4.7 NEMS Resonator Arrays with Phase-Locked Loops······112
4.8 Chapter Summary······113
Bibliography······114

Chapter 5 Dissipation in UHF Single-Crystal SiC Nanomechanical Resonators······117
5.1 Energy Dissipation in Mechanical Resonators······118
5.2 The Issue of Dissipation in UHF NEMS······120
5.3 Experimental Details······122
5.4 Dissipation Mechanisms and Contributions······128
5.4.1 Magnetomotive Damping Effect······128
5.4.2 Thermoelastic Damping······129
5.4.3 Clamping Losses······131
5.4.4 Dissipation due to the Metallization Layers······133
5.4.5 Surface Loss······133
5.5 Resonance Frequency Temperature Coefficient······135
5.6 Chapter Summary······136

Bibliography······139

Chapter 6 High-Performance Silicon Nanowire VHF Nanoelectromechanical Resonators······143
6.1 Si NWs: Nanoelectronic and Nanomechanical Building Blocks······145
6.2 Suspended Si NWs in Microtrenches······147
6.3 Metallized Si NW VHF Resonators······149
6.4 Pristine (Non-Metallized) Si NW VHF Resonators······152
6.5 Piezoresistive Detection of Si NW Resonators······156
6.6 Si NW Mechanical Properties Measured in Resonant Mode······160
6.7 Frequency Stability and Mass Sensitivity of Si NW Resonators······162
6.8 Quality Factor and Energy Losses of Si NW Resonators······164
6.9 Comparison with Other Nanowire Resonators······166
6.10 Chapter Summary······167
Bibliography······169

Chapter 7 Conclusions and Perspectives······173
7.1 Concluding Remarks······173
7.2 Perspectives and Future Topics······175

Appendix A List of Major Instruments and Apparatus······A-1
A.1 Vacuum Systems······A-1
A.2 Cryogenic Apparatus······A-1
A.3 Instruments for Electronic Measurements······A-2
A.4 Nanofabrication and Characterization Instruments······A-3

Appendix B NEMS Resonator with the Damped Harmonic Oscillator Model······B-1
Bibliography······B-6

Appendix C A Note on the Quality Factor (*Q*)······C-1
C.1 The Lorentzian Function······C-1
C.2 Resonance, *Q*, and Their Connections to Lorentzian······C-2
C.3 The Specific Case of Magnetomotive NEMS Resonator······C-3
C.4 The Mysterious $\sqrt{3}$······C-6

Appendix D A Note on NEMS Oscillator Phase Noise, and Phase Noise Comparison······D-1
D.1 NEMS Oscillator Phase Noise Data······D-1
D.2 Method 1 (“Normalizing Offset Frequency to Carrier”)······D-3
D.3 Method 2 (“Carrier Frequency Dividing”)······D-4
D.4 Comparison between Method 1 and Method 2······D-5
D.5 Extended Discussion on FOM······D-7

D.6 Selected Comparisons D-9
Bibliography D-12

Appendix E A Note on the Measures of Frequency Stability E-1
Bibliography E-6

List of Figures

Chapter 2 Foundations of VHF, UHF and Microwave NEMS Resonators

Fig. 2.1 Schematics of beam resonator and dynamic vibration············14
Fig. 2.2 Beam resonator in the damped simple harmonic oscillator (DSHO) model············18
Fig. 2.3 Definition of phase noise per unit bandwidth············24
Fig. 2.4 Illustration of power-laws of the spectra of **(a)** frequency noise and **(b)** phase noise, and **(c)** dependency of Allan deviation on the averaging time············27
Fig. 2.5 Examples of FEMLAB simulation and design of UHF NEMS resonators based on SiC beams············34
Fig. 2.6 Examples of CFDRC simulations············35
Fig. 2.7 Measured surface roughness of the SiC wafer used in this work············36
Fig. 2.8 Surface nanomachining process flow for nanofabrication of SiC NEMS············37
Fig. 2.9 SEM images of typical suspended 3C-SiC NEMS beam resonators············38
Fig. 2.10 Schematic of magnetomotive transduction of NEMS beam resonator············39
Fig. 2.11 Equivalent circuit model of the magnetomotively-transduced NEMS resonator····40
Fig. 2.12 Scaling of resonance frequency and circuit model parameters of NEMS············41
Fig. 2.13 Electronic readout schemes and measurements diagrams············42

Chapter 3 Ultra-High Frequency Low-Noise Self-Sustaining Oscillator Based upon *Vibrating* Nanomechanical Resonator

Fig. 3.1 Illustration of a self-sustaining oscillator system············48
Fig. 3.2 Phasor representation of the *RSBR* and the relation of resonance signal and the background at $\omega=\omega_0$············54
Fig. 3.3 Effect of phase difference upon *RSBR*············55
Fig. 3.4 Effect of magnitude of the background response upon *RSBR*············56
Fig. 3.5 Dependency of *RSBR* upon phase difference between resonance and background··57
Fig. 3.6 Effect of non-constant but linear background upon the resonance shape and *RSBR*············58
Fig. 3.7 Network analysis measurement and open-loop calibration scheme of the UHF resonance detection with the high-resolution balanced-bridge circuit············61
Fig. 3.8 Background suppression by high-resolution bridge-balancing and nulling techniques············62

Fig. 3.9 Significant enhancement of *RSBR* with the use of high-resolution bridge-balancing and background-nulling techniques······63
Fig. 3.10 Realizing self-oscillation with NEMS······65
Fig. 3.11 Measurement setup for realizing the self-sustaining oscillation with UHF NEMS resonators······66
Fig. 3.12 Demonstration of the UHF NEMS Oscillator······67
Fig. 3.13 NEMS oscillator frequency detuning with varied loop phase change······71
Fig. 3.14 Duffing behavior of the NEMS resonator calibrated in measurements······73
Fig. 3.15 Measured NEMS oscillator output frequency pulling with calibrated sustaining amplification gain change······74
Fig. 3.16 Phase noise performance of the NEMS oscillator······76
Fig. 3.17 Phase noise measured at different drive levels······78
Fig. 3.18 NEMS oscillator frequency stability······79
Fig. 3.19 Schematic and design of advanced NEMS oscillators······81
Fig. 3.20 Schematic and design of active NEMS oscillators with arrays of NEMS resonators······82

Chapter 4 UHF NEMS Resonators with Low-Noise Phase-Locked Loops

Fig. 4.1 Block diagram of NEMS resonance phase detection scheme······93
Fig. 4.2 UHF NEMS detection embedded into low-noise phase-locked loop for real-time precise locking and tracking of NEMS resonance frequency······95
Fig. 4.3 Schematic of the electromechanical resonances readout scheme······96
Fig. 4.4 Detected electromechanical resonances of pairs of UHF NEMS resonators from the bridge scheme······97
Fig. 4.5 Demonstration of temperature-programmed resonance frequency shifting and real-time frequency locking and tracking for UHF NEMS······98
Fig. 4.6 Scheme and setup for measuring the NEMS resonator frequency stability with the NEMS-PLL system······100
Fig. 4.7 Measured Allan deviation as a function of averaging time for a family of UHF NEMS resonators······101
Fig. 4.8 Scheme and setup of measuring the phase noise of UHF NEMS resonators in the NEMS-PLL system······102
Fig. 4.9 Phase noise performance of generations of UHF NEMS resonators······102
Fig. 4.10 Ideally intrinsic dynamic range and practically achievable dynamic range specifications of the UHF NEMS resonators······105
Fig. 4.11 Measured frequency stability of UHF NEMS resonators vis-à-vis LO requirements for Rb^{87} 6.8GHz CSAC······110
Fig. 4.12 Measured phase noise of UHF NEMS resonators and oscillator vis-à-vis LO requirements for Rb^{87} 6.8GHz CSAC······111
Fig. 4.13 Schematic and design of NEMS-PLL······112

Chapter 5 Dissipation in UHF Single-Crystal SiC Nanomechanical Resonators

Fig. 5.1 Quality factor versus resonance frequency for devices made of various materials·120
Fig. 5.2 Quality factor versus resonance frequency for VHF/UHF SiC NEMS··················121
Fig. 5.3 SEM of a typical single-crystal 3C-SiC UHF NEMS resonator····························123
Fig. 5.4 Resonance signal of a 428MHz NEMS resonator··124
Fig. 5.5 Measured dissipation as a function of temperature··126
Fig. 5.6 Experimental results of dissipation in several generations of UHF NEMS···········132
Fig. 5.7 Measured resonance frequency as a function of temperature································135

Chapter 6 High-Performance Silicon Nanowire VHF Nanoelectromechanical Resonators

Fig. 6.1 Si NWs nanomechanical resonators prepared by VLS epitaxial growth process····148
Fig. 6.2 Metallized Si NWs as VHF NEMS resonators··151
Fig. 6.3 VHF NEMS resonators based on high-impedance pristine Si NWs······················153
Fig. 6.4 Piezoresistive frequency down-conversion detection scheme with bridge circuit for pairs of Si NWs resonators···157
Fig. 6.5 VHF NEMS resonance transduction by the combination of magnetomotive excitation and piezoresistive detection···159
Fig. 6.6 Si NW resonator frequency stability characteristics···163
Fig. 6.7 Measured frequency stability performance···164
Fig. 6.8 Measured dissipation Q^{-1} as a function of temperature for two metalized Si NW resonators··165

List of Tables

Chapter 2 Foundations of VHF, UHF and Microwave NEMS Resonators

Table 2-1 Selected material properties of SiC, in comparison with Si, GaAs, and Diamond··35

Chapter 3 Ultra-High Frequency Low-Noise Self-Sustaining Oscillator Based upon *Vibrating* Nanomechanical Resonator

Table 3-1 Basic specifications of the UHF NEMS oscillator and its NEMS resonator··········68

Chapter 4 UHF NEMS Resonators with Low-Noise Phase-Locked Loops

Table 4-1 UHF NEMS resonator devices specs and performances··································107

Table 4-2 Dynamic range specs of UHF NEMS resonators··107

Table 4-3 Power handling specs of 3C-SiC VHF/UHF NEMS resonators························108

Chapter 5 Dissipation in UHF Single-Crystal SiC Nanomechanical Resonators

Table 5-1 Temperature dependency of Q^{-1} in various micro- & nanomechanical resonators···127

Table 5-2 Properties of 3C-SiC for thermoelastic damping calculations···························130

Table 5-3 Effect of aspect ratio on the Q^{-1}···132

Table 5-4 Parameters for calculating the dissipation due to metallization layers·············133

Chapter 6 High-Performance Silicon Nanowire VHF Nanoelectromechanical Resonators

Table 6-1 Specifications and performance of some measured VHF Si NW resonators········156

Table 6-2 Young's modulus measured by dynamic method with the resonances of the Si NW resonators···132

Chapter 7 Conclusions and Perspectives

Table 7-1 *Realistic* roadmap and path toward single-Dalton mass sensitivity with NEMS··174

Chapter 1

Introduction and Overview

The work of this thesis is on the research of ultra-high frequency (UHF) nanoelectromechanical resonators and their technologies for ultra-sensitive mass sensing, towards single-molecule mass detection and mass spectrometry. This chapter starts with a historical sketch of the big picture background and general motivations, and then zooms in to briefly introduce the field of nanoelectromechanical systems (NEMS) and some important concepts. The chapter then discusses the pertinent context and focuses on our research goals, strategies, technical approaches and uniqueness. The author emphasizes the roles of engineering, and advocates for engineering of NEMS resonators, especially those working at high frequencies, to fulfil their promising application potentials and to advance technologies. In many aspects, this chapter provides the author's hindsight and renewed views based on retrospect after several years working in this field. The chapter ends with illustrating the organization of the thesis and providing an overview of the topics of the following chapters.

1.1 Background and Motivations

The last decade has witnessed a great many scientific research achievements and progress at very small length scales. Nanoscience and nanotechnology has attracted increasing research attention and this trend has been greatly accelerated worldwide, by the government endorsement of the national nanotechnology initiative (NNI) in the US and similar national programs in other major countries [1]. To the author's understanding, nanoscience and nanotechnology have been both stimulated by the great visions and ideas of scientists, and driven by advances in technology and engineering. Late Nobel laureate and eminent physicist Richard Feynman first systematically presented his far-reaching vision of *miniaturization*—science and engineering at very small size scales—in his famous talk, *There is Plenty of Room at the Bottom*, at Caltech in 1959, where he envisioned many interesting things such as shrinking the size of the computers, rearranging atoms, making micromachines, making precise small things with imprecise large tools, and so on [2]. In 1983 Feynman revisited his original talk and updated some of the ideas [3]. On the technology side and in practice, with the revolution of microelectronics and the semiconductor integrated circuit (IC) industry, great advances have been attained in micromachining techniques. Miniaturization then quickly propagated to more fields and microelectromechanical systems (MEMS) have emerged since the 1980's. Technology innovations are ceaseless and now people can routinely make various nanoscale devices with advanced nanofabrication techniques.

Although the recent "nano-boom" and many forecasts about futuristic nanotechnology may sound encouraging (mostly in their superficial ways, though), they should not lead to unrealistic optimism and fanaticism. As addressed in an insightful article, *Plenty of Room, Indeed*, by Michael Roukes in 2001 [4], what we can do now is still very rudimentary and we are still quite far from realizing Feynman's grand vision; many fundamental physics and engineering challenges need to be overcome before we can

mass-produce nanodevices and systems. This is still true now in 2006. Although much progress has been achieved in nanoscience and nanotechnology, there is still vast room for more and more concrete advances and contributions to be made by many teams of scientists and engineers, before the vague details in the big picture become clearer. Within the grand vision, in exploring the physics and engineering of suspended nanostructures [4], the exciting and intriguing field of nanoelectromechanical systems, has emerged.

1.2 Nanoelectromechanical Systems

Nanoelectromechanical Systems (NEMS), if broadly defined, should include all structures and devices that satisfy (i) having both *electro-* (conducting) and *mechanical-* (movable) parts *and* having the *electromechanical transduction* function, and (ii) having one characteristic dimension in the ~1−100nm size scale (according to NNI convention [1]). For example, a simple beam-structured nanoelectromechanical resonator possesses both *electro-* (resistance) and *mechanical-* (suspended movable beam) parts, and the beam's mechanical motion can be converted into an electrical signal and be read out with certain transduction schemes, thus it is viewed as a NEMS device.

Today most NEMS are rudimentary and are based on nanostructures made by either *top-down* lithographical nanofabrication such as those in [4], or *bottom-up* chemical synthesis such as nanotubes (NTs) [5] and nanowires (NWs) [6]. They are actually nanoelectromechanical *structures* instead of *systems*, because they are usually individual nanoscale objects that people manage to characterize by using external discrete components and instruments, and are thus still far from real *integrated systems*, which are most desirable in realizing nanotechnology. Nonetheless, people simply call these structures and devices NEMS.

NEMS as an attractive field is worth thinking of from multiple viewpoints, and this would have interesting implications in turning NEMS into enabling technologies. (i) From the physics viewpoint, the emergence of NEMS was originated from some mesoscopic physics studies back in the late 1980's [4,7,8]. Even at that time, sub-100nm and sub-10nm structures (mesoscopic *systems*) were made by advanced nanofabrication for electronic transport measurements. It was just natural to take further steps to suspend these mesoscopic systems and to excite them into motion for exploration of new physics and engineering. This has turned out to be a significant and successful evolution. (ii) From the engineering point of view, NEMS can be viewed as MEMS shrunk down to the nanoscale. This view is helpful in NEMS engineering as one can always first learn from the many techniques developed for MEMS (especially in fabrication processes). However, it is always critical to work out the scaling laws, and in some cases size really matters and what is suitable for MEMS will not work well for NEMS. (iii) The microelectronics viewpoints are also helpful for engineering the desirable integrated NEMS. Scaling and large scale integration of NEMS needs to learn many lessons from those of microelectronics governed by the Moore's law [9,10]. An interesting example is that as sizes are reduced, the practical limits for both NEMS and microelectronics are set by parasitics [10] and their solutions should be expected to be analogous too. Several helpful review introductions to NEMS with mingled physics and engineering viewpoints and focuses can be found in [11-14].

1.3 Ultimate Miniaturization of Resonant Mass Sensors

Amongst the various types of NEMS, probably the most attractive are those working in their resonant modes, a.k.a., nanomechanical resonators or NEMS resonators, because they are inherently endowed with many excellent characteristics such as surprisingly high operating frequency (frequency scales up as sizes shrink), ultra-small mass, ultra-low power consumption, etc. [12-14]. In principle these characteristics imply ultra-fast

(ultra-wide band), ultra-sensitive, ultra-low power devices and their large-scale integrations; hence they are expected to hold promise for applications ranging from sensing, signal processing and communication, to computation [12-14]. Here we confine our discussion in the context of mass sensing, while later in Chapter 3 the mechanical signal processing and communication context will be more relevant and will be addressed there.

Mechanical resonant mass sensors have existed for about half a century and the miniaturization of mechanical resonators was started in mid 1960's, marked by the demonstration of resonant gate transistors [15-17]. Initially these were aimed at introducing high-*Q* but IC-compatible components for frequency selectivity with IC, but this actually kicked off the miniaturization of *vibrating* resonant mass sensors by using IC processes. Some early micromachined resonant structures and arrays in SiO_2 were reported by Kurt Petersen in 1978 [18]. In 1986 Roger Howe and Richard Muller reported a micromachined poly-Si beam resonator for mass (vapor pressure) sensing [19]. In the following two decades, with the advances in MEMS technologies, many more researchers have developed various MEMS resonant mass sensors for different applications.

The topic has become more intriguing as nanofabrication techniques allow us to make much smaller mechanical resonators in deep sub-micron and even molecular scales. Such ultrasmall resonators can be so responsive that they can readily resolve tiny little or infinitesimal amounts of loaded masses which have been invisible to much larger MEMS and macroscopic sensors. In principle, NEMS resonators can lead the resonant mass sensing to enter the sensitivity regimes from the femtogram (10^{-15}g) to yoctogram (10^{-24}g), as compared to MEMS resonators' mass sensitivity in the picogram (10^{-12}g) to femtogram (10^{-15}g) range, and quartz crystal microbalance's nanogram (10^{-9}g) sensitivity. Hence NEMS are the most promising for mass sensing at the single-molecule level and

for key applications in *quantitative* biological science and engineering such as proteomics and mass spectrometry (MS). In fact, there have been great expectations for any new technologies that can offer alternatives to reform and eventually replace the conventional expensive and complicated MS. Therefore our strategies and technical routes consist of: (i) pushing for the ultimate limits of NEMS sensitivity (the ultimate sensitivity required for MS is 1Dalton=1.66yoctogram), (ii) *real-time* single-molecule (mass) counting, and (iii) weighing molecules and distinguishing them with single-Dalton resolution.

1.4 *Engineering* NEMS for Single-Molecule Mass Sensing

Engineering viewpoints and *new engineering solutions* are crucial to meeting the great challenges posed by the above strategic goals. Actually, after more than a decade fundamental research on the governing physics and basic properties and behavior of NEMS resonators, it is now time to aggressively make strides in engineering NEMS for realistic and practical applications.

Here the author seriously emphasizes this and advocates for NEMS engineering, as there is a great need and also a capacious arena for it. Generalized to the whole blueprint of nanoscience and nanotechnology, from today's existing diverse nanodevices to their applications, most of the bottlenecks and unsolved problems are of engineering. For future NEMS of large scale integration on the chip level, more engineering challenges include yield, assembly, interconnection, integration, packaging and reliability, etc. Some of these may be directly learned from today's IC and MEMS industry, some of them may only be solved by creating *new engineering paradigms*.

Particularly for engineering NEMS toward mass sensing at the single-molecule level, we stress the significance of a *generic protocol* in which the sensing events are monitored in real time, rather than simply performing separate measurements with unloaded and loaded devices. There are two approaches to implementing this: (i) build an active

self-sustaining oscillator system with the NEMS resonator; and (ii) integrate the NEMS resonance into a phase-locked loop (PLL) to track the resonance. To approach the mass sensitivity limits with each approach, there are a number of engineering issues to be addressed, such as optimal device design, high-efficiency transduction, parasitic effects, noise, scaling laws, and so on.

It is the theme of this thesis to develop ultra-high frequency (UHF) resonant NEMS technologies incorporated with feedback control and low-noise electronics, to realize their system-level operation, to evaluate their performance, and to explore their potentials in approaching the above strategic goals. The main results and progress are overviewed in the following section.

1.5 Thesis Organization and Chapter Overview

Following the introduction and overview in this chapter, in **Chapter 2** we lay the foundations of VHF, UHF and Microwave nanomechanical resonators. Both basic theoretical principles and experimental techniques are included, with an emphasis on transforming general fundamentals to the specific nanomechanical resonators operating in these high frequency[①] ranges.

Chapter 3 is on the development of a low-noise, stable, self-sustaining oscillator with a low-loss UHF vibrating NEMS resonator as its frequency-determining element. The self-sustaining oscillator is important because it demonstrates the feasibility of building *active* oscillators with *passive* nanomechanical vibrating resonators, and thus converting

[①]Throughout the text, "high frequency" is used in its *literal* meaning which can be taken as an inclusive but less formal designation of a loosely-defined wide range possibly covering several frequency bands in the radio frequency spectrum; while the *high frequency* band (3-30MHz) itself is referred as its *technical* term acronym, HF.

direct current (DC) power into radio-frequency (RF)[②] power utilizing NEMS resonators. The NEMS oscillator operates in the UHF band, which is much higher than attained by the state-of-the art MEMS oscillators based on vibrating MEMS resonators. This technology readily demonstrates mass sensitivity in the zeptogram-scale, as well as its unique advantages.

In parallel to the self-sustaining oscillator operation, we present the development of the technologies of embedding UHF NEMS resonators into low-noise phase-locked loop (PLL) systems in **Chapter 4**. In this approach, a more stable frequency source is often used to work as a voltage-controlled oscillator (VCO) to drive a NEMS resonator and to lock to and track the resonance. This NEMS-PLL system-level operation represents another generic approach of real-time NEMS resonance locking and tracking. This technology has shown NEMS mass sensitivity that is sufficient for single-biomolecule sensing.

An important issue that has arisen in engineering NEMS is the trade-off between scaling devices (both sizes and operating frequency) and attaining high quality factors (low loss or dissipation). The dissipation issues have become especially keen for UHF NEMS resonators. **Chapter 5** is dedicated to carefully exploring the dissipation mechanisms and limiting factors on the device quality factor. Important and dominant energy loss mechanisms have been identified and guidelines and possible solutions for quality factor engineering are discussed.

[②]Radio-frequency (RF) is the interesting portion of the electromagnetic spectrum in which electromagnetic waves can be generated by alternating current (AC) signals fed to an antenna. Broadly-defined RF usually covers from kHz to GHz ranges. The term RF used in the thesis complies with this convention but also has an emphasis on the ranges from HF band to 1GHz (beyond 1GHz we often use the term *microwave*), and implications on communications.

Besides pursuing the ultimate performance of the best *top-down* UHF NEMS resonators, we have been keeping an open eye to the possibilities of devices made by *bottom-up* chemical synthesis techniques. **Chapter 6** presents our latest efforts with high-performance resonators based on Si nanowires (NWs). We demonstrate that these Si NWs are robust resonators that can operate in the VHF/UHF ranges. The Si NW resonators have been realized with both metallized and pristine (non-metallized) high-impedance NWs. Their wonderful piezoresistive effect offers very promising piezoresistive detection. With comprehensive characterizations of the basic specifications, frequency stability and dissipation issues, we show that the Si NWs have excellent performance comparable to that of the state-of-the-art *top-down* devices.

Finally in **Chapter 7**, the research effort toward the engineering of UHF NEMS resonators for ultimate sensitivity and low-noise applications is summarized, with major conclusions drawn and future interesting short-term and long-term research topics suggested and envisioned.

Bibliography

[1] National Research Council, “Small wonders, endless frontiers—A review of the national nanotechnology initiative”, Washington, D.C.: National Academy Press (2002). [More at the NNI website www.nano.gov].

[2] R.P. Feynman, “There is plenty of room at the bottom”, *J. Microelectromech. Systems* **1**, 60-66 (1992). [Reprinted, originally a talk by Feynman on Dec. 29, 1959, at the Annual Meeting of the APS, at Caltech, Pasadena, CA, first published as a chapter in H.D. Gilbert, Ed., *Miniaturization*, New York: Reinhold Publishing Corp. (1961)].

[3] R.P. Feynman, “Infinitesimal Machinery”, *J. Microelectromech. Systems* **2**, 4-14 (1993). [Based on Feynman’s talk, *ibid*, on Feb. 23, 1983, at the Jet Propulsion Laboratory, Pasadena, CA].

[4] M.L. Roukes, “Plenty of room, indeed”, *Scientific American* **285**, Issue 3 (Sept.) 48-57 (2001).

[5] H.J. Dai, “Controlling nanotube growth”, *Physics World* **13**, No. 6 (June) 43-47 (2000).

[6] Y.N. Xia, P.D. Yang, *et al.* “One-dimensional nanostructures: synthesis, characterization and applications”, *Adv. Mater.* **15**, 353-389 (2003).

[7] M.L. Roukes, A. Scherer, S.J. Allen Jr., H.G. Craighead, R.M. Ruthen, E.D. Beebe, J.P. Harbison, “Quenching of the Hall effect in a one-dimensional wire”, *Phys. Rev. Lett.* **59**, 3011-3014 (1987).

[8] B.P. Van der Gaag, A. Scherer, “Microfabrication below 10nm”, *Appl. Phys. Lett.* **56**, 481-483 (1990).

[9] G.E. Moore, “Cramming more components onto integrated circuits”, *Electronics* **39**, No. 8 (Apr.) 114-117 (1965). [Reprinted as *ibid*, *Proc. IEEE* **86**, 82-85 (1988).]

[10] S.E. Thompson, S. Parthasarathy, “Moore’s law: the future of Si microelectronics”, *Materials Today* **9**, No. 6 (June) 20-25 (2006).

[11] M.L. Roukes, “Nanoelectromechanical systems face the future”, *Physics World* **14**, No. 2 (Feb.) 25-31 (2001).

[12] M.L. Roukes, “Nanoelectromechanical systems”, *Tech. Digest of the 2000 Solid-State Sensor and Actuator Workshop (Hilton Head 2000)* 1-10, Hilton Head Island, SC, June 4-8, (2000).

[13] M.L. Roukes, "Mechanical Computation: Redux?" *Tech. Digest of 2004 IEEE IEDM*, 539-542, San Francisco, CA, Dec. 13-15 (2004).

[14] K.L. Ekinci, M.L. Roukes, "Nanoelectromechanical systems", *Rev. Sci. Instr.* **76**, 061101 (2005).

[15] H.C. Nathanson, R.A. Wickstrom, "A resonant-gate silicon surface transistor with high-*Q* band-pass properties", *Appl. Phys. Lett.* **7**, 84-86 (1965).

[16] H.C. Nathanson, W.E. Newell, R.A. Wickstrom, "'Tuning forks' sound a hopeful note", *Microelectronics* September 20, 84-87 (1965).

[17] H.C. Nathanson, W.E. Newell, R.A. Wickstrom, J.R. Davis Jr., "The resonant gate transistor", *IEEE Trans. Electron Dev.* **ED-14**, 117-133 (1967).

[18] K.E. Petersen, "Dynamic micromechanics on silicon: techniques and devices", *IEEE Trans. Electron Dev.* **ED-25**, 1241-1250 (1978).

[19] R.T. Howe, R.S. Muller, "Resonant-microbridge vapor sensor", *IEEE Trans. Electron Dev.* **ED-33**, 499-506 (1986).

Chapter 2

Foundations of VHF, UHF and Microwave NEMS Resonators

This chapter presents the pertinent knowledge base for NEMS resonators and lays both theoretical and experimental foundations for the projects presented in the upcoming chapters. Throughout the discussions of fundamentals that may still hold in wider ranges, we emphasize our particular interest in their applicability for beam-structured VHF, UHF and microwave NEMS resonators. After introducing some key concepts and basic characteristics of NEMS resonators, we discuss a lumped-parameter model, the damped simple harmonic model for a beam-structured resonator. With this model we analyze the fundamental noise process of the resonators and gain an insight into some fundamental performance limits for real experiments. We then focus on the basic methods and techniques in experiments of NEMS resonators. Single-crystal silicon carbide (SiC) is introduced as the material of choice for our NEMS VHF/UHF/microwave resonators, followed by descriptions of SiC epilayer preparation and SiC NEMS nanofabrication. We introduce transduction, i.e., excitation and detection schemes of NEMS resonators. We discuss several available electrical detection and readout schemes for the SiC NEMS resonators.

2.1 Theoretical Foundation

2.1.1 Beam Resonators and Their Basic Characteristics

2.1.1.1 Beam Resonator Vibration and Dynamic Response

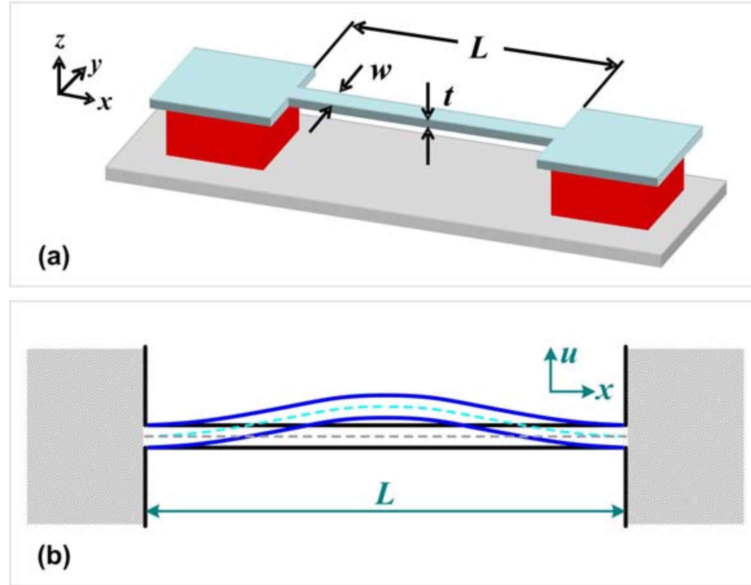

Fig. 2.1 Schematics of beam resonator and dynamic vibration. **(a)** Schematic of a suspended beam resonator structure with characteristic dimensions. **(b)** Schematic of flexural mode beam vibration.

One of the most interesting NEMS resonators is based on a beam structure as simple as shown in Fig. 2.1(a), with beam length L, width w, and thickness t. The beam can be driven to *in-plane* (displacement in y direction) and *out-of-plane* (displacement in z direction) flexural vibrations. Fig. 2.1(b) displays the flexural beam displacement ($u=y$ for in-plane and $u=z$ for out-of-plane). The flexural beam dynamics is readily described by the Euler-Bernoulli theory [1],

$$\rho A \frac{\partial^2 u(x,t)}{\partial t^2} + \frac{\partial^2}{\partial x^2}\left(EI \frac{\partial^2 u(x,t)}{\partial x^2} \right) = 0, \tag{2-1}$$

where $A=wt$ is the beam cross area, EI is the *flexural rigidity* with E the Young's (elastic) modulus and I the moment of inertia ($I_y=w^3t/12$ for in-plane vibration, and $I_z=wt^3/12$ for out-of-plane vibration). The general solution of eq. (2-1) (by separation of variables) is given by

$$u_n(x,t) = \left[a_n(\cos\lambda_n x - \cosh\lambda_n x) + b_n(\sin\lambda_n x - \sinh\lambda_n x)\right]\cdot e^{j\omega_n t}, \quad (2\text{-}2)$$

where λ_n are eigenvalues of flexural mode shapes and ω_n are eigenfrequencies of vibrations. The mode shape eigenvalues λ_n are determined by the beam boundary conditions, among which the most representative and of our interest are:

$$\text{(i) Doubly-Clamped: } \begin{cases} u(x=0,t) = u(x=L,t) = 0 \\ \left.\dfrac{\partial u(x,t)}{\partial x}\right|_{x=0} = \left.\dfrac{\partial u(x,t)}{\partial x}\right|_{x=L} = 0 \end{cases}, \quad (2\text{-}3a)$$

$$\text{(ii) Free-Free: } \begin{cases} \left.\dfrac{\partial^2 u(x,t)}{\partial x^2}\right|_{x=0} = \left.\dfrac{\partial u^2(x,t)}{\partial x^2}\right|_{x=L} = 0 \\ \left.\dfrac{\partial^3 u(x,t)}{\partial x^3}\right|_{x=0} = \left.\dfrac{\partial u^3(x,t)}{\partial x^3}\right|_{x=L} = 0 \end{cases}, \quad (2\text{-}3b)$$

$$\text{(iii) Cantilever: } \begin{cases} u(x=0,t) = \left.\dfrac{\partial u(x,t)}{\partial x}\right|_{x=0} = 0 \\ \left.\dfrac{\partial u^2(x,t)}{\partial x^2}\right|_{x=L} = \left.\dfrac{\partial u^3(x,t)}{\partial x^3}\right|_{x=L} = 0 \end{cases}, \quad (2\text{-}3c)$$

where 'clamped' means both displacement and deflection angle (slope of the deflection curvature) are zero; 'free' means no bending moment and no shear force. Both (i) doubly-clamped beam and (ii) free-free beam cases yield the same fundamental mode eigenvalue with $\lambda_n L$=4.730 and thus same eigenfrequency:

$$\omega_0 = \frac{(4.730)^2}{L^2}\sqrt{\frac{EI}{\rho A}} = \frac{22.4}{L^2}\sqrt{\frac{EI}{\rho A}}\,, \tag{2-4}$$

and hence we have

$$f_0 = \frac{\omega_0}{2\pi} = 1.03\frac{w}{L^2}\sqrt{\frac{E}{\rho}} \quad \text{(in-plane)}, \tag{2-5a}$$

$$f_0 = \frac{\omega_0}{2\pi} = 1.03\frac{t}{L^2}\sqrt{\frac{E}{\rho}} \quad \text{(out-of-plane)}. \tag{2-5b}$$

The (iii) cantilever beam case yields the fundamental mode eigenvalue with $\lambda_n L$=1.857, and its corresponding frequency is

$$\omega_0 = \frac{(1.875)^2}{L^2}\sqrt{\frac{EI}{\rho A}} = \frac{3.52}{L^2}\sqrt{\frac{EI}{\rho A}}\,, \tag{2-6}$$

and therefore

$$f_0 = \frac{\omega_0}{2\pi} = 0.161\frac{w}{L^2}\sqrt{\frac{E}{\rho}} \quad \text{(in-plane)}, \tag{2-7a}$$

$$f_0 = \frac{\omega_0}{2\pi} = 0.161\frac{t}{L^2}\sqrt{\frac{E}{\rho}} \quad \text{(out-of-plane)}. \tag{2-7b}$$

The above results clearly show that for beam-structured NEMS resonators to pursue high frequency applications, doubly-clamped and free-free beams are preferred. More detailed analyses and solutions for higher-order harmonic modes can be found in [1-3].

2.1.1.2 Energy Dissipation and Quality Factor

The quality factor (Q) of a resonant system is defined as the energy stored in the system divided by the energy dissipated,

$$Q \equiv 2\pi \frac{E}{\Delta E}, \tag{2-8}$$

where E is the total stored energy and ΔE is the energy loss per cycle (*i.e.*, $\Delta E/(2\pi)$ the energy loss per radian). If driving power $P=\omega\cdot\Delta E/(2\pi)$ is put into the resonance to compensate the energy loss per cycle and to sustain constantly steady-state oscillation, then we have

$$Q \equiv 2\pi \frac{E}{\Delta E} = \omega \frac{E}{P}. \tag{2-9}$$

Note here the power pumped into the resonator,

$$P = \omega \frac{\Delta E}{2\pi} = \frac{\omega E}{Q}, \tag{2-10}$$

is exactly the resonator's power dissipation or consumption.

In experiments, the resonator Q can be measured in two ways. In frequency-domain measurement, Q can be determined by identifying the full-width at half maximum (FWHM) of the Lorentzian-shaped power signal (note not the amplitude signal) of the resonance,

$$Q = \frac{f_0}{FWHM}. \tag{2-11}$$

In practice, this is usually performed by fitting the power signal resonance curve to the Lorentzian (or equivalently by fitting the amplitude signal to the square-root of the Lorentzian). In time-domain, the measurement is usually implemented within a "ring-down" process. When the excitation is turned off, the resonator vibration amplitude should follow an exponential decay,

$$A(t) = A_0 \exp\left(-\frac{t}{\tau}\right), \tag{2-12}$$

where $A(t)$ is the amplitude at a function of time, and τ is the ring-down time constant—the time required to the amplitude to decrease by a factor of e. The quality factor Q is related to the ring-down time constant τ by

$$Q = \frac{\omega_0 \tau}{2} = \pi f_0 \tau \, . \tag{2-13}$$

2.1.1.3 Beam Resonator in the Damped Simple Harmonic Oscillator Model

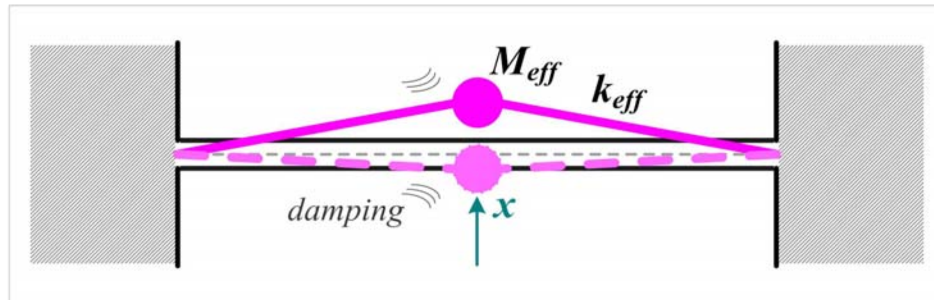

Fig. 2.2 Beam resonator in the damped simple harmonic oscillator (DSHO) model. The distributed deflection along the beam length is ignored and the beam vibration is represented by 1D oscillation of a mass-string system.

From the point of view of systems with *lumped parameters*, we can describe the beam resonator vibration by a damped simple harmonic oscillator[①] (DSHO) model. As delineated in Fig. 2.2, the model damped system consists of a *massless string* with a *dynamic stiffness* (or simply taken as *spring constant*) k_{eff}, and an *effective active mass* M_{eff}. This way the distributed transverse deflection of the beam is conveniently *lumped* into the one-dimensional motion of the effective mass M_{eff}, with its displacement overlapping with that of the beam's midpoint in the fundamental flexural mode. Mathematically, this model actually predigests the partial differential equation (*e.g.*, eq.

[①]For convenience, the term "oscillator" here simply complies with the conventional use in physics and mechanics textbooks—in the mechanical domain, usually the device (or system) is called an oscillator as long as it oscillates, such as "simple harmonic oscillator", "Duffing oscillator", without distinguishing the device being passive or active. Sometimes clarification is needed, especially in the electrical domain. We make the distinction: a *resonator* is *passive*, and an *oscillator* is *self-sustaining* and *active*. Hence more strictly here both the device and model are to be termed with *resonator*.

(2-1)) of the Euler-Bernoulli theory into an ordinary differential equation and thus greatly simplifies a lot of important analyses that follow. The governing equation of this DSHO model is

$$M_{eff}\frac{d^2x}{dt^2}+\gamma_{eff}\frac{dx}{dt}+k_{eff}x=F(t), \tag{2-14}$$

where the damping coefficient is $\gamma_{eff}=M_{eff}\omega_0/Q$ (so long as $Q\geq 10$), and $F(t)$ is the driving force. If the driving is harmonic it is more interesting to examine the dynamic response in the frequency domain. In the vicinity of the fundamental resonance, the driven DSHO model describes the flexural motion of a beam resonator with accuracy $\leq 1\%$ for $Q\geq 10$. The frequency-dependent amplitude response $\boldsymbol{a}(\omega)$ upon applying the driving force $\boldsymbol{F}(\omega)$ is

$$\boldsymbol{a}(\omega)=\frac{\boldsymbol{F}(\omega)}{\left(k_{eff}-M_{eff}\omega^2\right)+jM_{eff}\omega_0\omega/Q}, \tag{2-15}$$

in which we note that both $\boldsymbol{F}(\omega)$ and $\boldsymbol{a}(\omega)$ contain not only magnitude but also phase information. They are *phasors*, *i.e.*, *complex* variables as functions of frequencies. At each specific frequency ω, the time-domain instantaneous displacement is $x(t)=|\boldsymbol{a}(\omega)|\cos(\omega t+\varphi)$ for harmonic driving force $F(t)=|\boldsymbol{F}(\omega)|\cos(\omega t)$, with φ the phase difference between the drive and response. We can then define the dynamic transfer function, or the dynamic *responsivity* $\Re_a(\omega)$ of the "force→displacement" transduction for the resonator beam,

$$\Re_a(\omega)\equiv\frac{\boldsymbol{a}(\omega)}{\boldsymbol{F}(\omega)}=\frac{1}{\left(k_{eff}-M_{eff}\omega^2\right)+jM_{eff}\omega_0\omega/Q}. \tag{2-16}$$

Clearly the *responsivity* $\Re_a(\omega)$ is also a phasor; and it is very meaningful that the $\Re_a(\omega)$ is the *dynamic compliance* of the resonator, and the response described by eq. (2-16) can

be viewed as an extension of the well-known Hooke's law $F=kx$ from statics to resonance mode.

Now we turn to map the beam resonator within the context of the DSHO model. Let the amplitude of the lumped point mass M_{eff} simulate that of the beam resonator's midpoint. For uniform load upon the beam (applied force per unit length is constant and has uniform distribution over beam length), we first solve for the midpoint amplitude versus force based on beam deflection theory by following Timoshenko [1]; in the meantime, in the DSHO model let the same total force apply upon the effective mass and yield the same amplitude; also note that $k_{\mathrm{eff}}=M_{\mathrm{eff}}\omega_0^2$ with ω_0 determined by Euler-Bernoulli theory as in eqs. (2-4) and (2-6); hence we arrive at the following relations for a doubly-clamped beam resonator (out-of-plane):

$$\begin{cases} k_{eff} = 32E\left(\dfrac{t}{L}\right)^3 w \\ M_{eff} = 0.765\rho Lwt = 0.765M \end{cases} . \tag{2-17}$$

Likewise, we have the following for a cantilever beam resonator (out-of-plane):

$$\begin{cases} k_{eff} = \dfrac{3}{4}E\left(\dfrac{t}{L}\right)^3 w \\ M_{eff} = 0.645\rho Lwt = 0.645M \end{cases} . \tag{2-18}$$

Note that M is the real physical mass of the beam; and w and t should be exchanged in the k_{eff} equations in both cases if switching from out-of-plane to in-plane vibration.

2.1.2 Noise Processes

Noise is becoming increasingly important for systems with shrinking dimensions. For beam-resonator-based NEMS, it is plausible to suppose that the noise issue may be more severe because intuitively smaller systems are more susceptible to noise. Ultimately

noise processes set the lower-end limits for the sensitivity, stability, and reliability of NEMS resonators in their various applications. There can be many sources imposing noise upon a NEMS resonator in a practical scenario, but from a system viewpoint virtually all the noise sources can be categorized into either (i) *intrinsic noise* directly from the resonator device itself, or (ii) *extrinsic* noise introduced by measurement electronics. In fact, what we call *intrinsic noise* from the device itself, more accurately and strictly, refers to the noise arising from the interactions between the device and its environment. Some of the interactions are spontaneous and occur when the device is in equilibrium with its pristine environment (*e.g.*, thermal bath). Some other device-environment interactions are associated with non-equilibrium physical or chemical processes (*e.g.,* adsorption-desorption, mass loading), which are often made possible within deliberately designed or controlled environments. What we call *extrinsic electronic noise* only but always shows up in our observations as long as the device is under test within a system involving realistic instruments.

Due to their random and statistical nature, and to various physics origins, it is always difficult to quantitatively model noise processes, especially for a realistic system involving both intrinsic and extrinsic noise. For beam resonators, the above lumped-parameter, damped SHO model greatly facilitates the otherwise more intractable noise analyses. Nonetheless, here we primarily focus on the most important intrinsic noise that is inevitable for every NEMS resonator and thus affects the ultimately achievable performance of the device.

2.1.2.1 Thermomechanical Noise

At finite temperature, a resonator device is at least inevitably engaged in interactions with its surroundings, such as a thermal bath, which is in thermodynamic equilibrium with the resonator. Even in thermodynamic equilibrium at constant temperature, stochastic force from random agitation in the thermal bath is driving the resonator into mechanical motion

and at the same time the motion is damped by the same stochastic force[②]. We call this the *thermomechanical motion* (or thermomechanical fluctuation) of the resonator device. Sharing the same underlying physics with the well-known Brownian motion [4,5], this motion can be mathematically described by the Langevin equation [5]. Equivalently, and more generally, the phenomenon is dictated by the fluctuation-dissipation theorem (FDT) which is accounted in more detail in [5]. The thermomechanical motion of a NEMS resonator and its resulting noise impose fundamental limits upon the device response transduction, and ultimately upon achievable performance in applications.

For a NEMS beam resonator in its damped 1D SHO representation, equipartition theorem [5] demands that

$$\frac{1}{2}k_B T = \frac{1}{2}k_{eff}\left\langle x_{th}^{2}\right\rangle = \frac{1}{2}M_{eff}\omega_0^{2}\left\langle x_{th}^{2}\right\rangle, \qquad (2\text{-}19)$$

where k_B is the Boltzmann constant (k_B=1.38065×10^{-23}J/K) and T is absolute temperature of the resonator and thermal bath in equilibrium. Note that x_{th} is the thermomechanical displacement of the effective mass, $\langle x_{th}^2\rangle$ is the mean-square displacement with $\langle\ \rangle$ denoting ensemble average (as it is usually used in statistical physics), and thus the root-mean-square quantity is $\langle x_{th}^2\rangle^{1/2}$.

In frequency-domain description, the stochastic force has a white spectrum. In other words, the thermomechanical force spectral density is white,

$$S_F(\omega) = \frac{4k_B T M_{eff}\omega_0}{Q}, \quad \text{in [N}^2\text{/Hz]}; \qquad (2\text{-}20)$$

[②]On the nature of the stochastic force: in brief it is the effect of a continuous series of stochastic atomic/molecular collisions and interactions with the thermal bath, which can be through solid materials and structures (such as mechanical resonator devices and their supports, etc.) and not necessarily in fluids as was in the case of the original Brownian motion observations.

and thus the RMS force density is

$$S_F^{\frac{1}{2}}(\omega)=\sqrt{\frac{4k_BTM_{eff}\omega_0}{Q}}, \quad \text{in [N/}\sqrt{\text{Hz}}\text{]}. \tag{2-21}$$

With the responsivity given in eq. (2-16), the spectral density of the resonator's thermomechanical motion displacement is

$$S_x(\omega)=\left|\Re_a(\omega)\right|^2 S_F(\omega)=\frac{4k_BT\omega_0}{M_{eff}Q}\cdot\frac{1}{\left(\omega^2-\omega_0^{\,2}\right)^2+\omega^2\omega_0^{\,2}/Q^2}, \quad \text{in [m}^2\text{/Hz]}. \tag{2-22}$$

Here note in general the spectral density is measured in the scale of power per Hertz or modulus square per Hertz, which determines its unit for each specific quantity.

As eq. (2-22) displays, the device has its *thermomechanical resonance* driven by the thermomechanical noise force. At the peak of the thermomechanical resonance the RMS displacement is

$$S_x^{\frac{1}{2}}=\sqrt{\frac{4k_BTQ}{M_{eff}\omega_0^{\,3}}}, \quad \text{in [m/}\sqrt{\text{Hz}}\text{]}. \tag{2-23}$$

Eqs. (2-21) and (2-23) represent the resonator's intrinsic force noise floor and displacement noise floor, respectively, set by the resonator's thermomechanical fluctuations. Forces and displacements below these levels cannot be resolved if the resonator is employed as a force sensor and/or a displacement detector.

2.1.2.2 Phase Noise and Frequency Noise

Besides the displacement and force noise in resonators, frequency and phase noise are of the most importance, and are particularly crucial for resonant sensors and resonance-based signal generation and processing. A comprehensive introduction to the key concepts and methods of frequency and phase noise in signal sources is given by

Robins in [6]. Here our treatment continues to aim at the intrinsic fundamental limits of frequency and phase noise in NEMS resonators, still following the SHO model context.

(i) Phase Noise

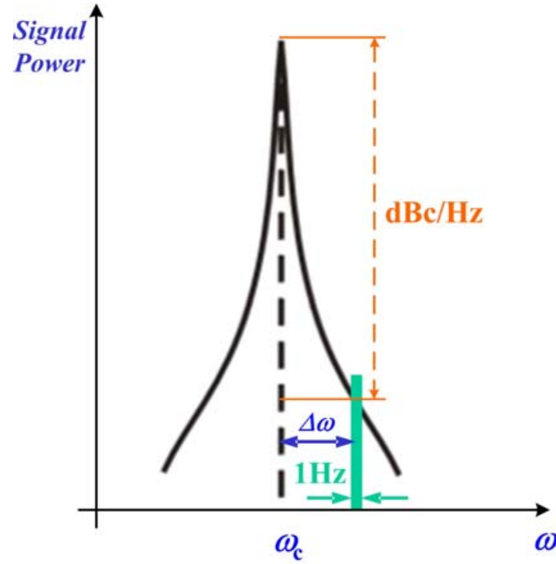

Fig. 2.3 Definition of phase noise per unit bandwidth.

In the frequency domain spectrum signal from a resonator as illustrated in Fig. 2.3, phase noise is a measure of spectral purity and it is defined as the power of noise sideband per unit bandwidth in the units of decibels below the carrier (dBc/Hz),

$$S_{\phi}(\Delta\omega) = 10\log\left[\frac{P_{sideband}(\omega_c + \Delta\omega,\ 1Hz)}{P_{carrier}}\right] \quad \text{in [dBc/Hz]}, \tag{2-24}$$

in which $P_{\text{sideband}}(\omega_c+\Delta\omega,\ 1\text{Hz})$ is the single-side noise power at an offset frequency $\Delta\omega$ from the carrier, in a measurement bandwidth of 1Hz, and P_{carrier} is the total power under the power spectrum. For a NEMS beam resonator operating at fundamental mode, carrier frequency is simply the resonance frequency, $\omega_c=\omega_0$. The phase noise induced by the thermomechanical fluctuation is

$$S_\phi(\Delta\omega) = 10\log\left[\frac{S_x(\omega_0+\Delta\omega)}{\langle x_C{}^2\rangle}\right] \quad \text{in [dBc/Hz]}, \tag{2-25}$$

where $S_x(\omega_0+\Delta\omega)$ [m^2/Hz] is the mean-square displacement per Hertz at $\Delta\omega$ offset frequency and $\langle x_C{}^2\rangle$ is the mean-square displacement at the maximum allowable drive level. For harmonic vibration, $\langle x_C{}^2\rangle = a_C{}^2/2$ with a_C being the maximum possible amplitude in linear regime. Let $E_C = M_{eff}\omega_0{}^2 a_C{}^2/2$; this defines the maximum energy level of the resonator, and hence applying eq. (2-22) we have

$$S_\phi(\Delta\omega) \approx 10\log\left[\frac{k_B T\omega_0}{E_C Q(\Delta\omega)^2}\right] = 10\log\left[\frac{k_B T}{P_C Q^2}\left(\frac{\omega_0}{\Delta\omega}\right)^2\right] \quad \text{in [dBc/Hz]}, \tag{2-26}$$

where the approximation holds for $\omega_0/Q \ll \Delta\omega \ll \omega_0$, and $P_C = \omega_0 E_C/Q$ is the maximum drive power level. This clearly shows that thermomechanical-fluctuation-caused phase noise has $1/f^2$ dependency in the phase noise spectrum. Here we use f as the offset frequency for convenience in the *power-law* description of the noise spectrum, or in fact we have $(\omega_0/\Delta\omega)^2 = (f_0/f)^2$ in eq. (2-26).

(ii) Frequency Noise

The phase noise can also be viewed and measured as frequency noise, because phase is the time-integral of frequency (a.k.a., the famous '$\phi = \omega t$'). Besides the carrier phase term $\phi_c(t) = \omega_c t$, let the instantaneous excess phase term be $\phi(t) = \phi_0 \sin(\Delta\omega t)$ assuming a sinusoidal modulation at offset frequency $\Delta\omega$; thus instantaneous frequency varies as $\delta\omega(t) = d\phi/dt = \Delta\omega\phi_0\cos(\Delta\omega t)$. Hence if we define the *fractional frequency variation* $y = \delta\omega(t)/\omega_0$ [7,8], we have

$$\Re_y \equiv \frac{\partial y}{\partial\phi} = \frac{1}{\omega_0}\frac{\partial(\delta\omega)}{\partial\phi} = \frac{1}{\omega_0}\frac{\partial(\delta\omega)/\partial t}{\partial\phi/\partial t} = \frac{\Delta\omega}{\omega_0}. \tag{2-27}$$

Therefore the noise spectrum of the fractional frequency variation is

$$S_y(\Delta\omega) = \left|\Re_y\right|^2 S_\phi(\Delta\omega) = \left(\frac{\Delta\omega}{\omega_0}\right)^2 S_\phi(\Delta\omega) = \frac{k_B T}{P_C Q^2}, \quad \text{in [1/Hz]}. \tag{2-28}$$

Note here that in calculating the $S_y(\Delta\omega)$ we use the absolute unit for $S_\phi(\Delta\omega)$ [1/Hz] instead of the decibel unit [dBc/Hz]. This result indicates that the thermomechanical-fluctuation-induced fractional frequency variation noise $S_y(\Delta\omega)$ is white. The spectrum of the absolute frequency noise is also flat and we have

$$S_{\Delta\omega}(\Delta\omega) = \omega_0^{\ 2} S_y(\Delta\omega) = \frac{\omega_0^{\ 2} k_B T}{P_C Q^2}, \quad \text{in [Hz}^2\text{/Hz]}. \tag{2-29}$$

Beyond the consideration of thermomechanical limited phase noise, some of the above analyses hold for more general cases. At least we can arrive at the following relations:

$$S_\phi(\Delta\omega) = \frac{\omega_0^{\ 2}}{(\Delta\omega)^2} S_y(\Delta\omega) = \frac{1}{(\Delta\omega)^2} S_{\Delta\omega}(\Delta\omega). \tag{2-30}$$

Here to avoid confusion we note: (i) $\omega=\omega(t)$ is the time-dependent instantaneous frequency of the resonator; (ii) ω_0 is the resonance frequency and also the carrier frequency ($\omega_c=\omega_0$); (iii) $\Delta\omega$ is the offset frequency from the carrier, *i.e.*, it is the time-independent Fourier frequency that appears in any spectral density (sometimes for convenience in speaking of the power laws of the spectral density we use f as $\Delta\omega$).

The relations in eq. (2-30) clarify that the power law of the phase noise spectrum is 2 orders lower than that of the frequency noise. We illustrate this in Fig. 2.4. For instance, flat (white) and $1/f$ frequency noise spectra translate into phase noise spectra with $1/f^2$ and $1/f^3$ power laws, respectively.

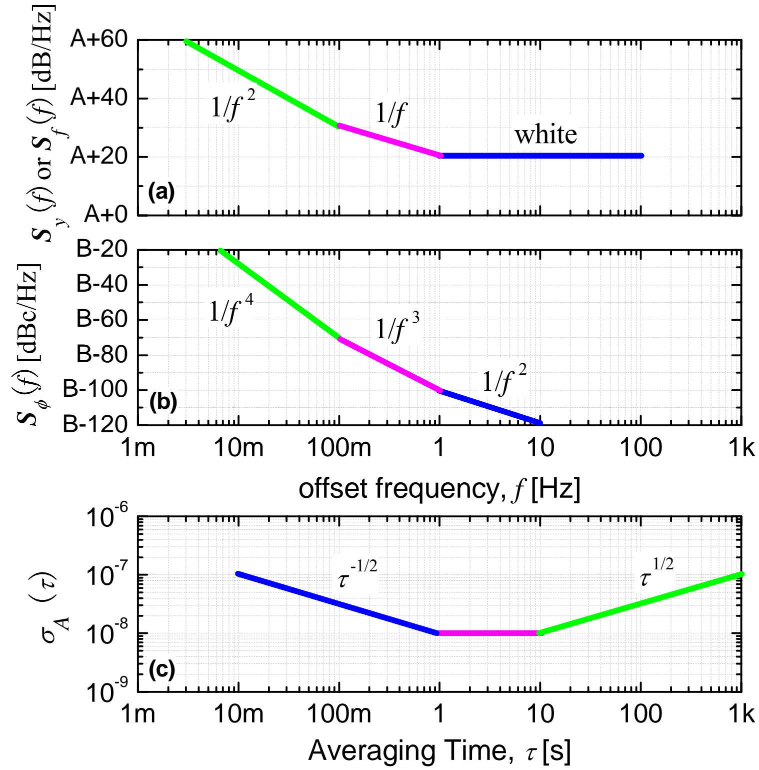

Fig. 2.4 Illustration of power-laws of the spectra of **(a)** frequency noise and **(b)** phase noise, and **(c)** dependency of Allan deviation on the averaging time. (Here A and B are offset constants; and for the axes labels, only the decades and differences are meaningful.)

(iii) Time-Domain Characterization of Phase Noise: Frequency Stability

In the time domain, phase noise is more suitably described as frequency stability (or equivalently, frequency instability). There is a very important quantity for this measure—the Allan deviation [7-9]—which is widely used in the resonator, frequency control, communication and timekeeping instruments, and other communities. Sometimes the square of Allan deviation—Allan variance, is also used. Allan deviation is the deviation of variations between every two adjacent measured average fractional frequencies, as a function of the averaging time interval. This definition can be readily used to characterize the frequency stability of the NEMS beam resonator with nominal resonance frequency $\omega_0=2\pi f_0$:

$$\sigma_A(\tau) = \sqrt{\frac{1}{2(N-1)}\sum_{i=1}^{N}\left(\frac{\overline{\omega}_{i+1}-\overline{\omega}_i}{\omega_0}\right)^2} = \sqrt{\frac{1}{2(N-1)}\sum_{i=1}^{N}\left(\frac{\bar{f}_{i+1}-\bar{f}_i}{f_0}\right)^2} \,. \qquad (2\text{-}31)$$

Here $\bar{f}_i$ is the measured average frequency in the *i*th time interval. By examining the Allan deviation with various averaging time intervals, it is possible to attain comprehensive understanding of the frequency stability performance within the ranges of interest.

The conversion relation between the phase noise spectral density and Allan deviation is

$$\sigma_A(\tau) = \frac{2\sqrt{2}}{(\omega_0\tau)}\sqrt{\int_0^\infty S_\phi(\Delta\omega)\sin^4\left(\frac{\Delta\omega\tau}{2}\right)d(\Delta\omega)} \,. \qquad (2\text{-}32)$$

Now consider the frequency stability limit set by thermomechanical fluctuations, with eqs. (2-26) and (2-32) we determine the Allan deviation to have a $\sigma_A(\tau) \sim \tau^{-1/2}$ dependency:

$$\sigma_A(\tau) = \frac{1}{Q}\sqrt{\frac{\pi k_B T}{P_C\tau}} = \sqrt{\frac{\pi k_B T}{E_C\omega_0 Q\tau}} \,. \qquad (2\text{-}33)$$

Likewise, we obtain $\sigma_A(\tau) \sim \tau^{1/2}$ for $1/f^2$ drifting frequency noise spectrum (which has phase noise following $1/f^4$), and $\sigma_A(\tau)$ independent of τ ($\sim \tau^0$) for $1/f$ frequency noise (with its phase noise spectrum following $1/f^3$). We have illustrated this in Fig. 2.4 together with the noise spectral density power laws.

Often both the frequency-domain and time-domain measures of phase noise (or frequency noise) are used. For practical reasons, phase noise spectra are usually used to characterize short-term (very small τ and very large $\Delta\omega$) frequency instability, and Allan deviation is more often employed when it becomes more and more difficult to directly measure the very-close-to-carrier (very smaller $\Delta\omega$) phase noise.

2.1.2.3 Extended Discussion on Noise Processes

We should point out that noise from various origins is not new and unique for NEMS resonators but is ubiquitous for all mechanical resonator devices. It is only the fact that its effects are more frequently 'rediscovered' and problems revisited when new technologies are being developed. There exist studies on noise processes in mechanical resonators and sensors based on both conventional quartz crystals and recent MEMS resonators [10-14]. An introductory study on the noise processes in NEMS resonators can be found in [15]. Investigations focused on specific noise processes such as adsorption-desorption noise have been performed for both MEMS devices [12-14] and NEMS resonators [15,16]. Although the physical origins of the noise processes remain the same despite the resonators' size-scaling, the most important for studying noise in NEMS resonators is to gain *quantitative* understanding and to determine the *ultimate limits* and dominant noise sources. Despite these efforts, today our understanding of various noise processes in NEMS is still far from enough, especially at the system level—for in most cases we can only deal with the simplest models, which can be too unrealistic for practical systems (*e.g.*, systems involving multiple devices, and those undergoing complicated physical/chemical processes). Albeit it may sound eternal, engineering noise will remain a key, and a lot more needs to be done to understand and then control or take advantage of noise processes, before we can embrace the best capabilities the devices intrinsically allow for.

2.1.3 Nonlinearity and Dynamic Range

The *signal ceiling* or *onset of nonlinearity* of a NEMS resonator is also of great importance, in parallel to the aforementioned noise floor analyses. Smaller devices unavoidably lead to lower energy storage and power handling. Thus this creates a challenge in achieving excellent phase noise performance, as manifested in eqs. (2-26) and (2-33). For a vibrating NEMS beam resonator, an intrinsic limit is set by the

maximum usable vibration amplitude beyond which a bifurcation point can be reached, where bistable states exist and the device response undergoes hysteresis [17]. In physics and mechanics, the onset of nonlinearity is often taken ideally right at the bifurcation point. In engineering practice it is usually defined as the 1dB compression point (to be in consistency with the general definition of the signal ceiling for electronic components in measurement systems), which often yields more conservative estimations than by bifurcation. We extend the DSHO model by adding nonlinear terms into eq. (2-14),

$$M_{eff}\frac{d^2x}{dt^2}+\gamma_{eff}\frac{dx}{dt}+\left(1+k_1x+k_2x^2+\cdots\right)k_{eff}x=F(t), \tag{2-34}$$

where $k(x)\equiv k_{eff}\left(1+k_1x+k_2x^2+\cdots\right)$ is the nonlinear stiffness. For convenience we keep the conventions such as linear stiffness $k_{\mathrm{eff}}=M_{\mathrm{eff}}\omega_0^2$ and definitions of Q in the weak nonlinear regime.

For a doubly-clamped beam resonator, the nonlinear effect is primarily from longitudinal tension in the beam when the beam is driven to large amplitudes. In this case, the nonlinear stiffness is $k(x)=k_{eff}\left(1+k_2x^2\right)$ and we obtain the Duffing equation with damping:

$$M_{eff}\frac{d^2x}{dt^2}+\gamma_{eff}\frac{dx}{dt}+k_{eff}x+k_3x^3=F(t), \tag{2-35}$$

with the cubic nonlinear coefficient $k_3=k_{\mathrm{eff}}k_2$. The bifurcation point (critical amplitude) can then be solved [17,18],

$$a_C=\omega_0\frac{L^2}{\pi^2}\sqrt{\frac{\sqrt{3}\rho}{EQ}}\ . \tag{2-36}$$

In the analysis by Postma *et al.* in [18], it is found that the *maximum usable* amplitude is $0.745a_C$, according to the 1dB compression point convention. Combining this amplitude signal ceiling and the displacement noise floor set by thermomechanical fluctuation as in eq. (2-23), we have the intrinsic device dynamic range,

$$DR\ [\mathrm{dB}] = 20\log\left[\frac{0.745a_C}{\sqrt{2S_x\Delta f}}\right], \tag{2-37}$$

with Δf being the measurement bandwidth. This is the maximum possible dynamic range and the practically achievable dynamic range is often smaller than this, due to noise floor mismatch and operation lower than the maximum usable amplitude.

For cantilever beams, however, there are various mechanisms of nonlinear effects and it is not clear which is dominant [19]. For a given cantilever resonator, modeling all nonlinear effects and predicting the onset of nonlinearity still appear very difficult. For most NEMS cantilevers, we expect that geometric and material nonlinearities, and effects due to boundary conditions, may have important contributions.

2.1.4 Basics and Metrics of NEMS Mass Sensing

The above treatment of the basic properties and noise and dynamic range of NEMS resonators has significant implications for the emerging applications of NEMS mass sensing. As mentioned in Chapter 1, although resonant mass sensors have existed for over 50 years and their miniaturization has been one major thrust in the MEMS community during the past two decades, new insights into this 'old' paradigm have been gained in revisiting it with the new NEMS technologies, based on several key concepts and metrics. In NEMS mass sensing, mass is detected as the frequency shift due to the mass-loading effect upon a resonator. We care about the lower limit—the *smallest mass* δM the device can detect—which we define as the *mass sensitivity* (or *mass resolution*). Mass resolution is determined by the smallest resonance frequency shift we can resolve,

i.e., the *frequency resolution* $\delta\omega_0$ (as $\delta M \ll M_{\text{eff}}$ always holds when considering the lower limit),

$$\delta M = \frac{\partial M_{eff}}{\partial \omega_0}\delta\omega_0 = \frac{\delta\omega_0}{\Re}. \tag{2-38}$$

Here we call $\Re$ the *mass responsivity* (in [Hz/g]). It is the responsivity of the 'mass change→frequency shift' transduction in the mass-loading effect,

$$\Re \equiv \frac{\partial\omega_0}{\partial M_{eff}} = -\frac{\omega_0}{2M_{eff}}. \tag{2-39}$$

Following our above analyses in the DSHO model, by integrating the thermomechanical- fluctuation-induced frequency noise in the available measurement bandwidth, we can determine the thermomechanical noise limited frequency resolution (method is detailed in [20] by Ekinci *et al.*),

$$\delta\omega_0 \approx \sqrt{\frac{k_B T}{E_C}\frac{\omega_0 \Delta f}{Q}}. \tag{2-40}$$

This indicates that both noise floor and signal ceiling come into play, thus leading to the mass resolution depending on available dynamic range,

$$\delta M \approx 2M_{eff}\sqrt{\frac{\Delta f}{Q\omega_0}}\cdot 10^{(-DR/20)}. \tag{2-41}$$

This result provides very important insights into guidelines for device engineering. Beyond the essence presented here, extended analyses of mass sensing limits set by other noise processes can be found in [20]. These limits superpose and the thermomechanical noise is the most important intrinsic mechanism in many cases of interest.

We have seen that the smallest mass a NEMS resonator can sense is a combination of how responsive the device is (how large $\Re$ is) and how small a frequency fluctuation can be measured. In pushing the fundamental limits of resonant mass sensing to single-Dalton resolution, the NEMS resonators are the most promising candidates, because they combine these two attributes the best—retaining the highest mass responsivity while improving frequency noise performance by scaling up the resonator frequency.

In practical measurements, especially when the extrinsic noise dominates, from eqs. (2-38) and (2-39) we have

$$\delta M = -2M_{eff}\left(\delta\omega_0/\omega_0\right), \tag{2-42}$$

where the practical noise floor of ($\delta\omega_0/\omega_0$) is not intrinsically limited by thermomechanical noise and thus yielding mass resolution not as good as predicted by eq. (2-41). The practical mass resolution achieved in a measurement would be

$$\delta M\left(\tau\right) = 2M_{eff}\left\langle\delta\omega_0/\omega_0\right\rangle_\tau = 2\sqrt{2}M_{eff}\sigma_A\left(\tau\right). \tag{2-43}$$

Here $\langle\delta\omega_0/\omega_0\rangle_\tau$ denotes the achieved *fractional frequency resolution*—the RMS fractional frequency fluctuation as a function of averaging time in the measurement—which is directly related to the measured Allan deviation. Therefore eq. (2-43) dictates that the realistic lower limit of mass resolution should be approached by engineering smaller devices with higher frequency stability.

2.2 Experimental Foundation

2.2.1 Silicon Carbide (SiC) Material for RF NEMS

We use SiC as the structural material for our NEMS resonators. In fact, SiC has been an excellent microelectronic and MEMS material for high-profile (expensive) applications in stringent conditions and environments [21,22]. SiC has many polytypes [21,22] and single-crystal 3C-SiC is used in this thesis work. Table 2-1 collects some important SiC material properties, in comparison with those of Si, GaAs, and diamond. Conventional Si is still the dominant MEMS material and GaAs has also been used in MEMS for its piezoelectricity, but SiC is more attractive for RF NEMS thanks to its high *elastic modulus-to-density ratio* (E/ρ). This was also experimentally verified in [23], where given the same resonator dimensions, SiC could yield much higher resonance frequency than Si and GaAs could. Compared to diamond, SiC has the advantages of easy single crystal growth and relatively more mature SiC electronics. The first GHz doubly-clamped beam resonator and many more in UHF ranges have been made with SiC [24,25], confirming that SiC is perfectly suitable for VHF/UHF/microwave NEMS.

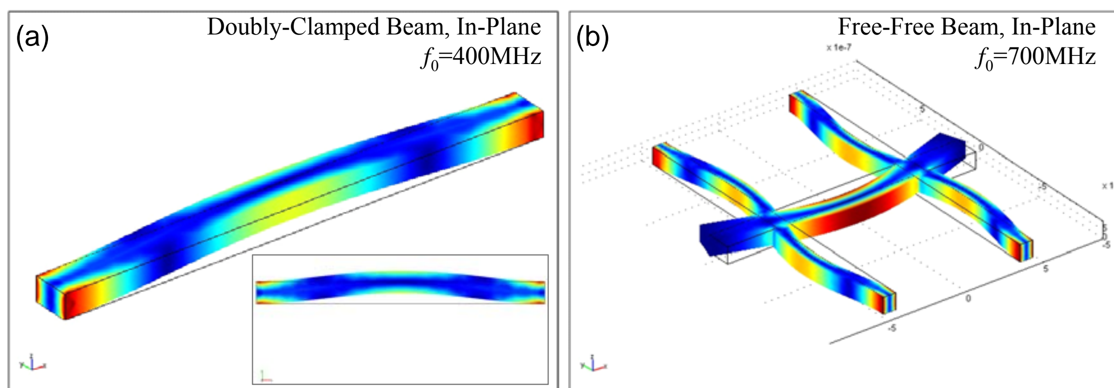

Fig. 2.5 Examples of FEMLAB simulation and design of UHF NEMS resonators based on SiC beams. Eigenfrequency analysis, and simulations of the mode shape and deflection, in color maps, of **(a)** the fundamental in-plane flexural mode of a 400MHz doubly-clamped beam; and **(b)** an in-plane free-free beam with its fundamental mode resonance frequency at 700MHz.

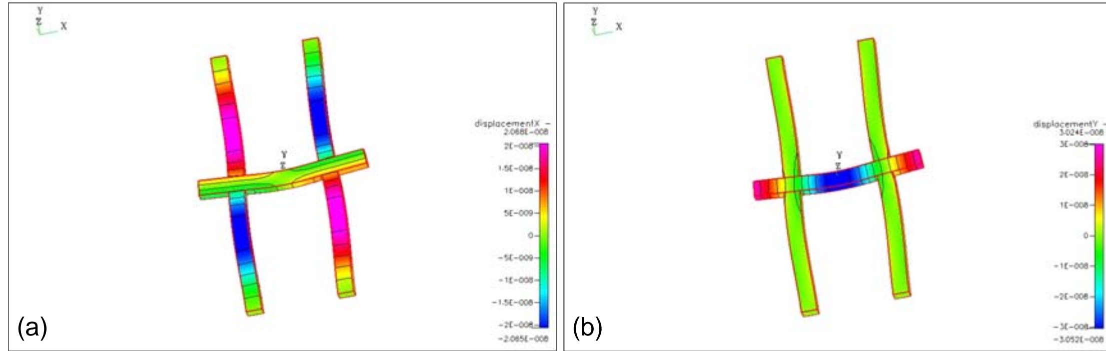

Fig. 2.6 Examples of CFDRC simulations. A 500MHz in-plane free-free beam with snapshots of its time-domain displacement, also in color maps. **(a)** X-displacement and **(b)** Y-displacement.

For the design of UHF devices, we use doubly-clamped and free-free beams rather than cantilevers. Before and in iterations with device fabrication processes, we employ finite element simulation tools including FEMLAB and CFDRC in the design. With given dimensions and reliable parameters such as material properties, we usually use FEMLAB to perform eigenfrequency analyses to predict the resonance frequencies of the NEMS devices with reasonably good accuracy. Such examples are illustrated in Fig. 2.5. We also use CFDRC to compute the transient response and time-domain vibrations of NEMS devices, as illustrated in Fig. 2.6. with examples.

Table 2-1 Selected material properties of SiC, in comparison with Si, GaAs, and Diamond.

Material / Property	3C-SiC	6H-SiC	Diamond	Si	GaAs
Mass Density [kg/m^3]	2850	2850	3520	2330	5320
Young's Modulus [GPa]	430	430	1035	180	460
Thermal Conductivity [W/(cm·K)]	5.0	4.9	20	1.5	0.5
Thermal Expansion Coeff. [$\times 10^{-6}$/K]	3.8	4.2	1.1	2.6	6.9
Max. Operating Temp. [^{o}C]	873	1240	460	300	1100
Melting Point [^{o}C]	Sublimes at 1825	Sublimes at 1825	1238	1415	Phase Change at 1400
Band Gap [eV]	2.2	2.9	5.45	1.12	1.42
Dielectric Constant	9.7	9.7	5.7	11.9	13.2
Physical Stability	Excellent	Excellent	Fair	Good	Fair
Doping	Hard	Moderate	Hard	Easy	Easy

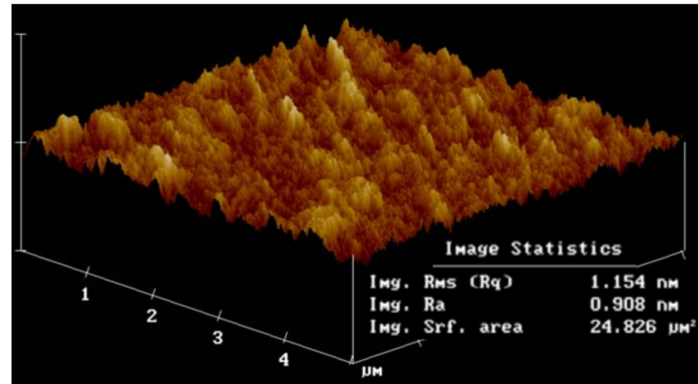

Fig. 2.7 Measured surface roughness of the SiC wafer used in this work.

Briefly, the 3C-SiC films used in this work are heteroepitaxially grown on 100mm (4in.) diameter (100) Si wafers in an RF-induction-heated, atmospheric pressure chemical vapor deposition reactor [26,27]. SiH_4 and C_3H_8 are used as precursors, and H_2 is used as a carrier gas. The epitaxial process is a two-step, high-temperature (1280°C) procedure, involving the carbonization of the Si surface in a C_3H_8/H_2 ambient followed by epitaxial growth using SiH_4, C_3H_8 and H_2. Originally the epitaxial growth recipe was optimized for micron-thick films. Recent efforts have also made it suitable for producing ~50−250nm thick films with sufficient surface quality for e-beam lithography and subsequent nanomachining. The defects density in these thinner films has also been minimized.

Previous study [25] shows the SiC wafer surface roughness can greatly affect the performance of devices. Recently progress has been made in controlling the surface roughness in 3C-SiC growth [27]. Fig. 2.7 shows measured surface roughness from one of such wafers we have been using in this work. The measured RMS roughness is only ~1.15nm over a 5μm×5μm region and multiple measurements throughout the same wafer surface yield RMS roughness values all in the range of 1−2nm.

2.2.2 Nanofabrication of NEMS Resonators

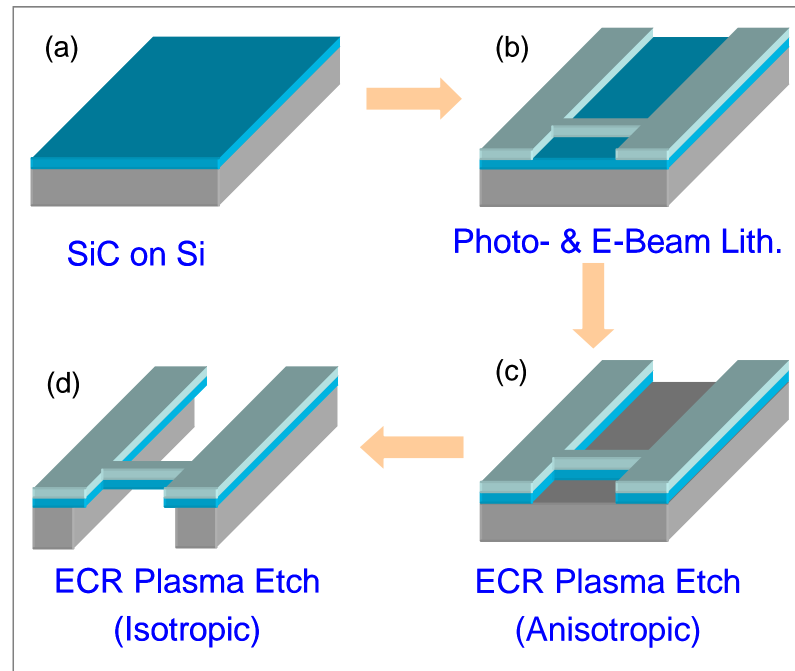

Fig. 2.8 Surface nanomachining process flow for nanofabrication of SiC NEMS resonators.

For the SiC epi-layer on Si substrate wafers, we use a surface nanomachining process to make NEMS resonators. A simplified process flow is shown in Fig. 2.8. The complete fabrication involves a combination of optical and electron-beam lithography techniques. The process begins by using standard photoresist and optical lithography to define the large-area contact pads comprising a 2−4nm thick Cr adhesion layer and an 80nm thick Au film. The substrates are then coated with a bi-layer polymethyl-methacrylate (PMMA) thin film, which is then patterned by electron-beam lithography into a metallic lift-off mold to define the sub-micron mechanical structures of the SiC devices. The pattern on the metal mask (typically ~30nm Al, followed by ~5nm Ti) is transferred to the 3C-SiC structural layer by using a NF_3/Ar anisotropic etch with an electron cyclotron resonance (ECR) plasma etching system. The newly patterned 3C-SiC beams are then suspended by simply etching the underlying Si substrate using an

isotropic NF_3/Ar ECR etch (same gas but at lower bias voltage). The metallic etch mask remains on the SiC beams to be used as the active conducting layer for subsequent DC electrical or RF electromechanical measurements. The low-mass density of Al metallization helps in reducing mass loading, thus resulting in a higher frequency for the same device geometry as compared with a denser metal (such as commonly used Au). The thin Ti top layer can help prevent oxidation of Al. We have carefully experimented with the metallization layers and our tailoring now routinely yields devices with DC resistance in the range of ~70−150Ω (for different device lengths). This is very important for RF measurements because the device's impedance becomes well-matched to 50Ω when it is at low temperatures.

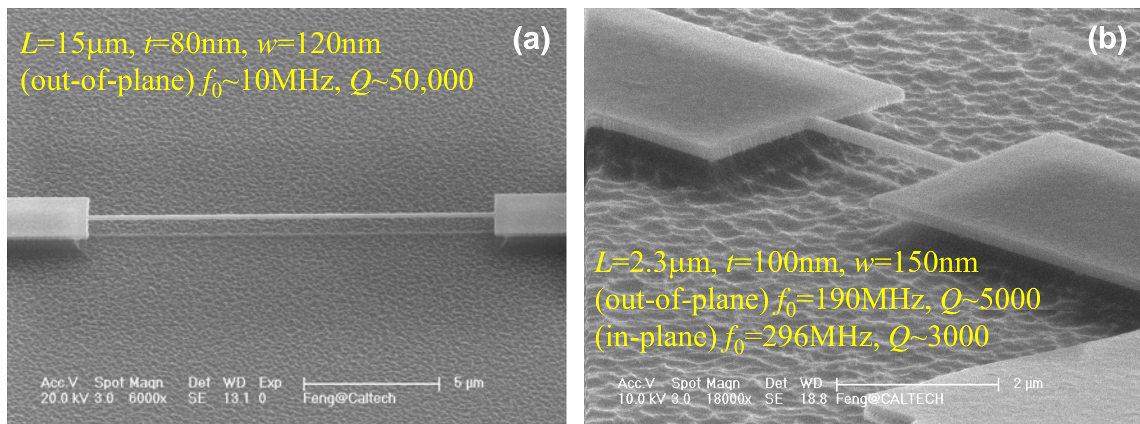

Fig. 2.9 SEM images of typical suspended 3C-SiC NEMS beam resonators. **(a)** A large aspect-ratio beam with 10MHz fundamental frequency. **(b)** A much shorter beam that can operate in VHF/UHF ranges.

Fig. 2.9(a) shows a typical long-beam device having a large aspect ratio (~125), with its fundamental frequency at about 10MHz. Fig. 2.9(b) shows a much shorter beam that can operate in the VHF & UHF ranges with either out-of-plane or in-plane flexural modes. In the development of generations of such devices with operating frequencies scaling from HF to UHF ranges, we have also engineered the device release (dry etch) process that eventually defines the 3D structure of the device. We carefully control the undercut in the dry etch so that its effects on the clamping losses are minimized.

2.2.3 Transduction of VHF/UHF/Microwave NEMS Resonance

Although several resonance transduction (both excitation and detection) schemes have been demonstrated or proposed for NEMS resonators, thus far they only work up to HF or at most VHF range. For MEMS resonators, electrostatic transduction has been the most successful and it prevails from kHz all the way up to GHz. However, it suffers from large motional resistance and parasitic coupling when it is scaled down to NEMS resonators and the scaling solutions are not clear yet. As a result, the magnetomotive transduction [28,29] with which the first NEMS resonators were demonstrated in MHz and GHz ranges, still remains the most efficient for VHF/UHF/microwave resonators [23-25].

As sketched in Fig. 2.10, the metallization layers on top of the surface of the resonator body are employed to drive the resonator and to detect its resonant motion. The driving RF current $\boldsymbol{i}$ passes through the device within a properly arranged magnetic field (*e.g.*, as shown in Fig. 2.10), and generates an RF Lorentz force $\boldsymbol{F}$, which actuates the resonator, and excites the mechanical resonance when the driving frequency hits the resonance frequency. The mechanical resonance in turn generates an electromotive voltage $\boldsymbol{v}$, which is electronically detected and thus the resonant mechanical motion is measured accordingly.

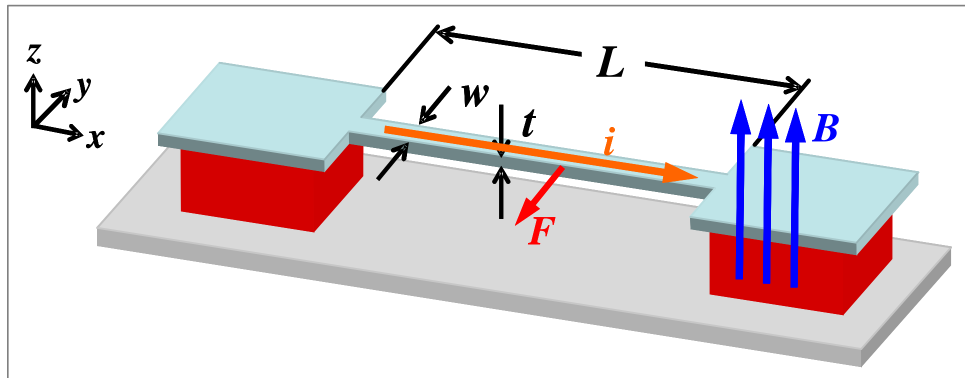

Fig. 2.10 Schematic of magnetomotive transduction of NEMS beam resonator.

In magnetomotive transduction, the equivalent circuit model of the electromechanical resonance is a parallel LRC tank given by

$$\begin{cases} R_m = \dfrac{\eta Q B^2 L^2}{M\omega_0} \\ C_m = \dfrac{M}{\eta B^2 L^2} \\ L_m = \dfrac{\eta B^2 L^2}{M\omega_0^{\ 2}} \end{cases} . \tag{2-44}$$

Here B is the magnetic field and η is the mode shape constant. The derivation of this model is detailed in [28].

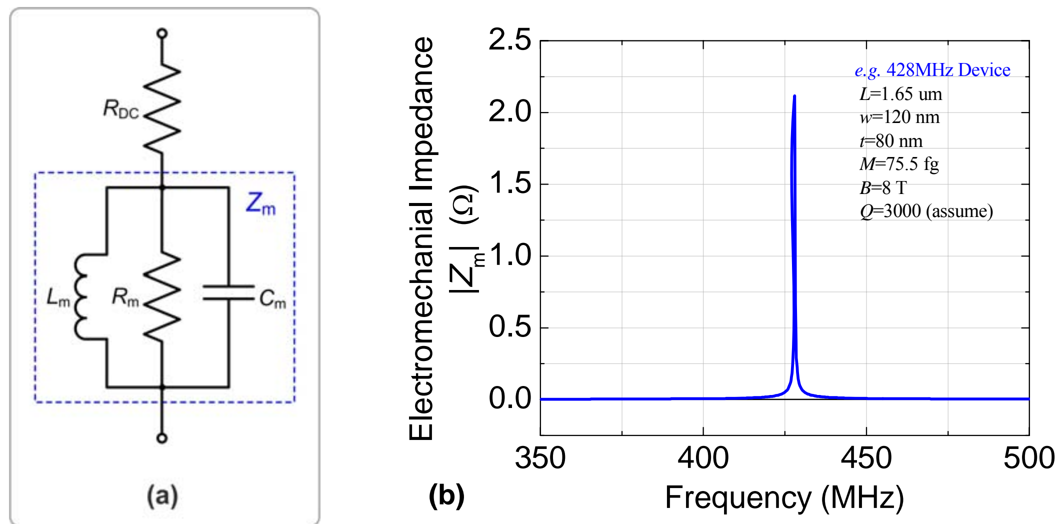

Fig. 2.11 Equivalent circuit model of the magnetomotively-transduced NEMS resonator. **(a)** Circuit model consisting of series DC resistance and parallel LRC tank. **(b)** An example of the electromechanical resonance predicted by the circuit model.

Consider the DC resistance of the device, the complete equivalent circuit model is shown in Fig. 2.11(a). As an example, Fig. 2.11(b) shows the electromechanical impedance of a typical UHF NEMS resonator as dictated by the circuit model.

With the typical NEMS fabrication technology we have (*e.g.*, *t*=100nm, *w*=150nm), using the above circuit model, we have estimated the circuit model parameters versus the

designed resonance frequency, in the frequency range we are interested in. The results are presented in Fig. 2.12. Clearly seen is that the electromechanical impedance decreases very much as the device size is reduced and the frequency is scaled up.

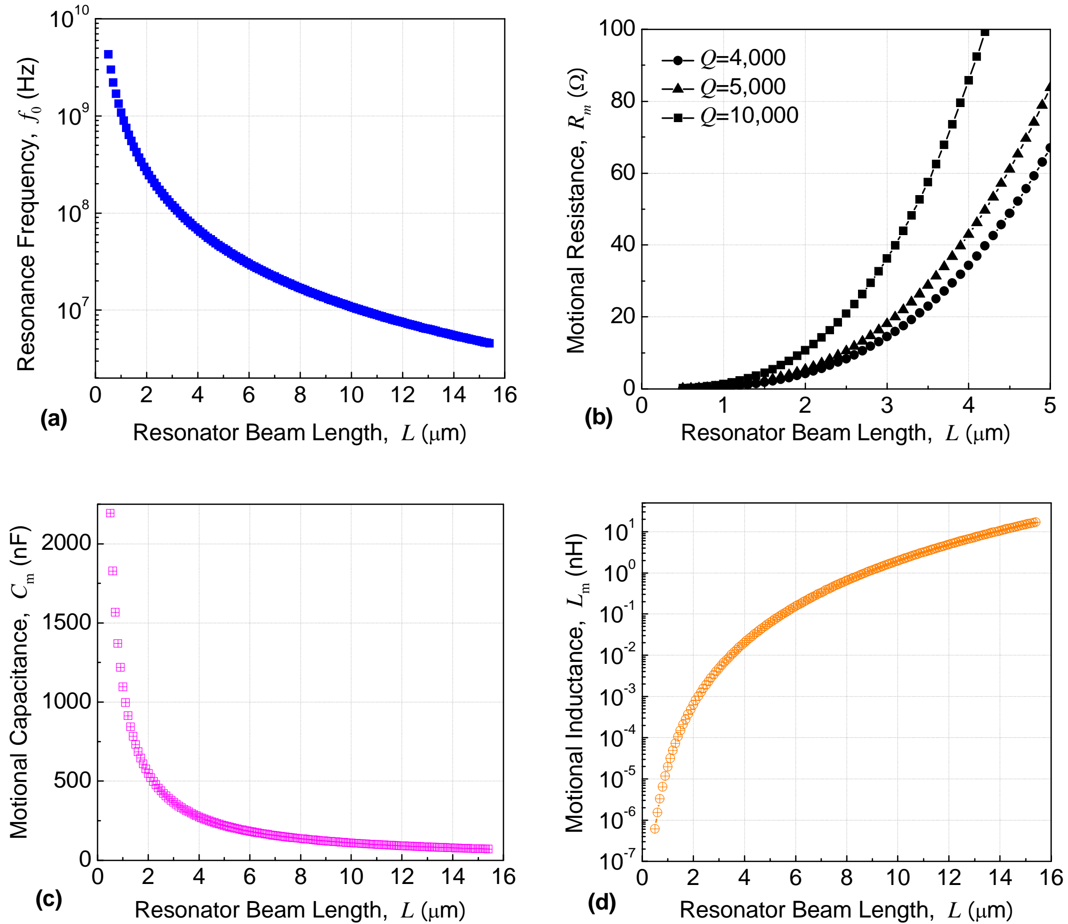

Fig. 2.12 Scaling of resonance frequency and circuit model parameters of the NEMS resonators.

2.2.4 Resonance Detection and Electronic Readout

Two-port network analysis is probably the most canonical and also convenient approach to perform RF detection and measurements of a NEMS resonance. Fig. 2.13 demonstrates the most important three schemes of two-port network analyses for NEMS resonators. All these schemes have hitherto been implemented in real measurements.

The efficiency of each is limited by interplay between the resonance's electromechanical impedance and the response due to the impedance mismatch and parasitic effects.

The *transmission* scheme in Fig. 2.13(a) has been directly used for HF and up to ~200MHz resonators with close to 50Ω impedance, and used with shunt 50Ω resistance to decrease the impedance mismatch for devices having large DC resistances (from >100Ω to well in the kΩ range) such as nanowires [30]. The *reflection* scheme shown in Fig. 2.13(b) has been more often applied to HF/VHF resonators [23,28,29], mostly by employing a directional coupler in lieu of the circulator shown.

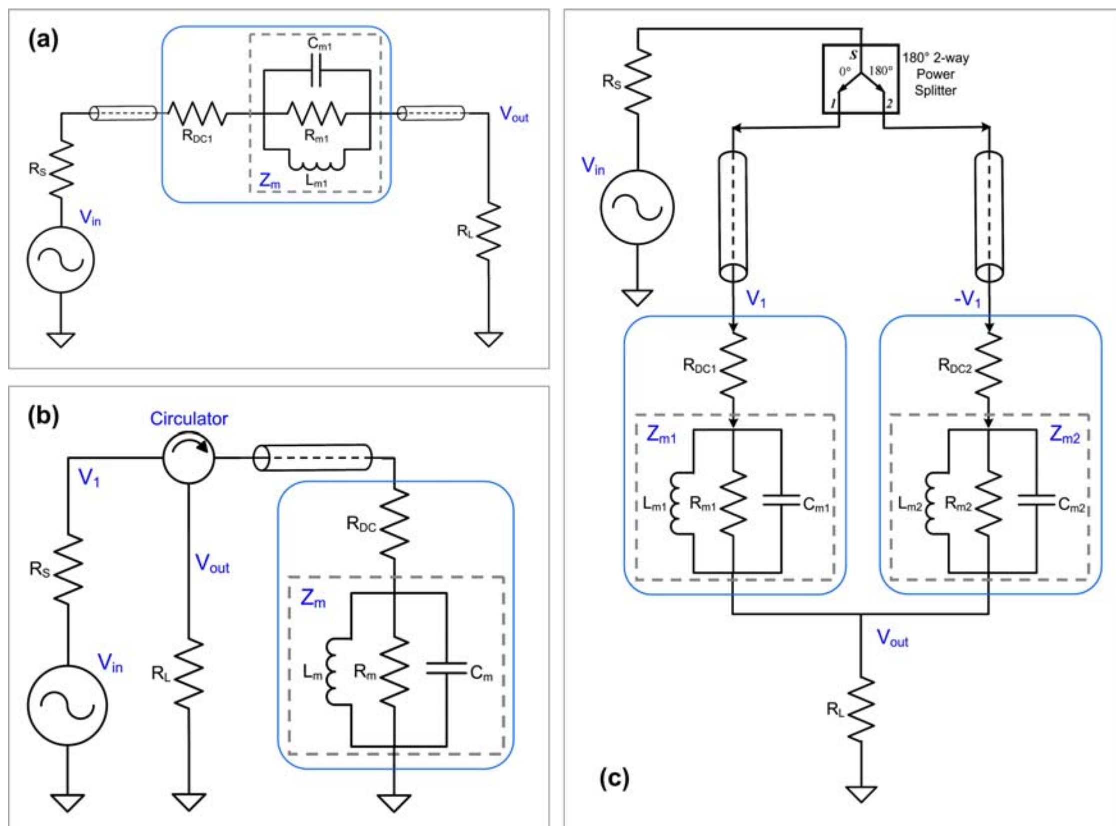

Fig. 2.13 Electronic readout schemes and measurements diagrams. **(a)** Two-port transmission measurement scheme with single device. **(b)** Two-port reflection measurement with single device. **(c)** Two-port balanced-bridge measurement with a pair of devices.

Both the transmission and reflection schemes quickly lose their efficiency when the device frequency approaches the UHF range and the device electromechanical impedance

becomes even smaller, as compared to the effect of any commonly existing parasitics. As shown in Fig. 2.13(c), a prototype of the balanced-bridge scheme [31] was developed to evade this issue to some extent. This scheme involves a pair of devices with very close DC resistances, and has been proven to have better efficiency than both the transmission and reflection schemes in detecting UHF NEMS resonances. However, this scheme and its underlying theory only take care of the effects of the DC resistance mismatch and its better efficiency has only been manifested with VHF devices. It still suffers from only obtaining very small resonance signals when implemented in the UHF range. Later we made improvements, or the second generation of the bridge scheme [25], but this progress was unsubstantial and did not completely solve the problem. Our latest but significant improvements for large signal readout from a typical UHF NEMS resonance was catalyzed and squeezed out in our desperate development of the NEMS oscillator technology. The analyses and implementation of this third generation bridge scheme is presented in Chapter 3.

Bibliography

[1] S. Timoshenko, D.H. Young, W. Weaver Jr, *Vibration Problems in Engineering*, New York: Wiley (1974).

[2] D.A. Harrington, M.L. Roukes, "Electrical tuning of the frequency, nonlinearity, and dissipation factor of NEMS resonators", *Caltech Technical Report CMP-106*, Rev. 12 (1994).

[3] A.N. Cleland, *Foundations of Nanomechanics: From Solid-State Theory to Device Applications*, Berlin: Springer (2002).

[4] G.E. Uhlenbeck, L.S. Omstein, "On the theory of the Brownian motion", *Phys. Rev.* **36**, 823-841 (1930).

[5] F. Reif, *Fundamentals of Statistical and Thermal Physics*, New York: McGraw-Hill (1965).

[6] W.P. Robins, *Phase Noise in Signal Sources*, London: Peter Peregrinus Ltd. & IEE (1984).

[7] J.A. Barnes, A.R. Chi, L.S. Cutler, *et al.*, "Characterization of frequency stability", *IEEE Trans. Instru. & Meas.* **IM-20**, 105-120 (1971).

[8] J. Rutman, F.L. Walls, "Characterization of frequency stability in precision frequency sources", *Proc. IEEE* **79**, 952-960 (1991).

[9] D.W. Allan, "Time and frequency (time-domain) characterization, estimation, and prediction of precision clocks and oscillators", *IEEE Trans. Ultrason. Ferr. & Freq. Contr.* **UFFC-34**, 647-654 (1987).

[10] J.R. Vig, F.L. Walls, "Fundamental limits on the frequency instabilities of quartz crystal oscillators", *Proc. IEEE 48th Int. Freq. Contr. Symp.* 506-523 (1994); *or*, F.L. Walls, J.R. Vig, *ibid*, *IEEE Trans. Ultrason. Ferr. & Freq. Contr.* **42**, 576-589 (1995).

[11] T.B. Gabrielson, "Mechanical-thermal noise in micromachined acoustic and vibration sensors", *IEEE Trans. Electron Devices* **40**, 903-909 (1993).

[12] Y.K. Yong, J.R. Vig, "Resonator surface contamination—a cause of frequency fluctuations", *IEEE Trans. Ultrason. Ferr. & Freq. Contr.* **36**, 452-458 (1989).

[13] Y.K. Yong, J.R. Vig, "Modeling resonator frequency fluctuations induced by adsorbing and desorbing surface molecules", *IEEE Trans. Ultrason. Ferr. & Freq. Contr.* **37**, 543-550 (1990).

[14] J.R. Vig, Y. Kim, "Noise in microelectromechanical system resonators", *IEEE Trans. Ultrason. Ferr. & Freq. Contr.* **46**, 1558-1565 (1999).

[15] A.N. Cleand, M.L. Roukes, "Noise processes in nanomechanical resonators", *J. Appl. Phys.* **92**, 2758-2769 (2002).

[16] Y.T. Yang, *Phase Noise in Nanoelectromechanical Systems* (Ph.D. Thesis, Advisor: M.L. Roukes), California Institute of Technology (2004).

[17] A.H. Nayfeh, D.T. Mook, *Nonlinear Oscillations*, New York: John Wiley & Sons (1979).

[18] H.W.Ch. Postma, I. Kozinsky, A. Husain, M.L. Roukes, "Dynamic range of nanotube- and nanowire-based electromechanical systems", *Appl. Phys. Lett.* **86**, 223105 (2005).

[19] P. Malatkar, *Nonlinear Vibrations of Cantilever Beams and Plates* (Ph.D. Thesis, Advisor: A.H. Nayfeh), Virginia Polytechnic Institute and State University (2003).

[20] K.L. Ekinci, Y.T. Yang, M.L. Roukes, "Ultimate limits to inertial mass sensing based upon nanoelectromechanical systems", *J. Appl. Phys.* **95**, 2682-2689 (2004).

[21] M. Mehregany, C.A. Zorman, N. Rajan, C.H. Wu, "Silicon carbide MEMS for harsh environments", *Proc. IEEE* **86**, 1594-1610 (1998).

[22] M. Mehregany, C.A. Zorman, S. Roy, A.J. Fleischman, C.H. Wu, N. Rajan, "Silicon carbide for microelectromechanical systems", *Int. Mat. Rev.* **45**, 85-108 (2000).

[23] Y.T. Yang, K.L. Ekinci, X.M.H. Huang, L.M. Schiavone, M.L. Roukes, C.A. Zorman, M. Mehregany, "Monocrystalline silicon carbide nanoelectromechanical systems", *Appl. Phys. Lett.* **78**, 162-164 (2001).

[24] X.M.H. Huang, C.A. Zorman, M. Mehregany, M.L. Roukes, "Nanodevice motion at microwave frequencies", *Nature* **421**, 496 (2003).

[25] X.M.H. Huang, X.L. Feng, C.A. Zorman, M. Mehregany, M.L. Roukes, "VHF, UHF and microwave frequency nanomechanical resonators" (invited article), *New J. Phys.* **7**, 247 (2005).

[26] C.A. Zorman, A.J. Fleischman, A.S. Dewa, M. Mehregan, C. Jacob, S. Nishino, P. Pirouz, "Epitaxial growth of 3C-SiC films on 4 in. diam (100) silicon wafers by atmospheric pressure chemical vapor deposition", *J. Appl. Phys.* **78**, 5136-5138 (1995).

[27] X.A. Fu, C.A. Zorman, M. Mehregany, "Surface roughness control of 3C-SiC films during the epitaxial growth process", *J. Electrochem. Soc.* **151**, G910-G914 (2004).

[28] A.N. Cleland, M.L. Roukes, "Fabrication of high frequency nanometer scale mechanical resonators from bulk Si crystals", *Appl. Phys. Lett.* **69**, 2653-2655 (1996).

[29] A.N. Cleland, M.L. Roukes, "External control of dissipation in a nanometer-scale radio frequency mechanical resonator", *Sensors & Actuators A* **72**, 256-261 (1999).

[30] A. Husain, J. Hone, H.W.Ch. Postma, X.M.H. Huang, T. Drake, M. Barbic, A. Scherer, M.L. Roukes, "Nanowire-based very-high-frequency electromechanical resonator", *Appl. Phys. Lett.* **83**, 1240-1242 (2003).

[31] K.L. Ekinci, Y.T. Yang, X.M.H. Huang, M.L. Roukes, "Balanced electronic detection of displacement in nanoelectromechanical systems", *Appl. Phys. Lett.* **81**, 2253-2255 (2002).

Chapter 3

Ultra-High Frequency Low-Noise Self-Sustaining Oscillator Based upon *Vibrating* Nanomechanical Resonator

This chapter describes the demonstration of a stable, low-noise, self-sustaining active oscillator operating at ultra-high frequency (UHF), based upon a 428MHz vibrating nanomechanical device. The low-loss nanomechanical resonator fabricated from high-quality single-crystal silicon carbide is excited into flexural vibrating modes and the resonance is detected in parasitics-immunized large signal utilizing high-resolution readout circuitry engineered for UHF NEMS resonators. Stable self-sustaining oscillation is realized using the UHF nanomechanical resonator as the frequency-selective element embedded in a low-noise feedback control loop. This nanomechanical-resonator-based active oscillator exhibits excellent frequency stability and mass sensitivity for mass sensing applications. This initial, unoptimized NEMS oscillator already exhibits fairly good phase noise performance for RF applications. The active self-oscillating mode of vibrating nanodevices also provides a generic self-sensing and detecting technology for measurement methodologies and instrumentations in fundamental physics and biology.

3.1 Introduction to Self-Sustaining Oscillators

Self-sustaining oscillators possess the unique property of spontaneously generating periodically occurring events and sustaining these oscillations by extracting energy from non-periodic sources. They exist in nature in many areas ranging from biological circadian rhythms [1] to fluids flows [2] and dynamic systems [3]. They also find important applications in human-enabled (*engineered*) systems such as navigation and communication [4], sensors and transducers [5], and clocks and timekeeping [6], where the technological progress has mainly been driven to attain ultra-fast (wide bandwidth) operation, high-precision, low-power and ultra-high integration densities.

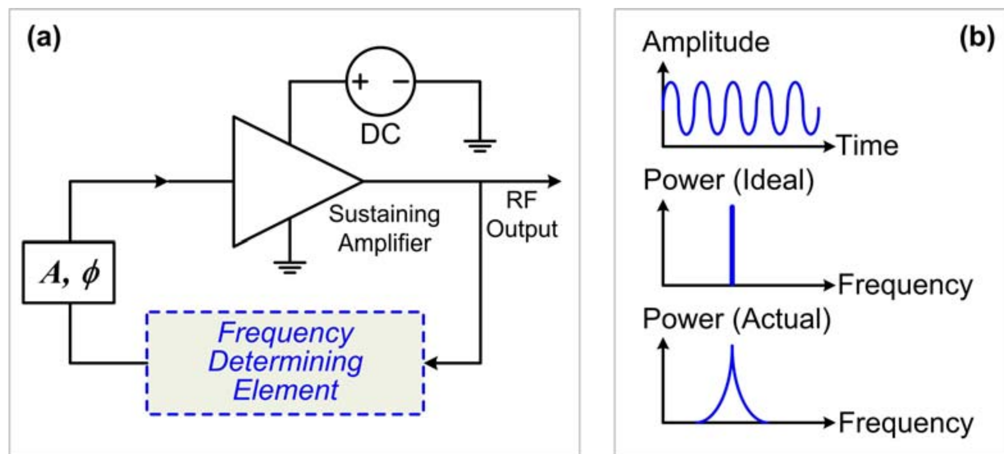

Fig. 3.1 Illustration of a self-sustaining oscillator system. **(a)** Schematic of a typical RF self-sustaining oscillator which consists of a frequency-determining element and a sustaining amplifier as its key components. **(b)** Illustration of the RF output (both time-domain waveform and frequency-domain spectrum) of a self-sustaining oscillator.

Stable and low-noise RF *electrical* oscillators are probably the most important self-oscillatory units for these applications, especially for modern communications and instrumentations with their increasing requirements on performance. Fig. 3.1(a) shows the conceptual construction of such an RF oscillator, which consists of a frequency-determining (selecting) element, a sustaining amplifier, and amplitude and phase control in the feedback path. The oscillator converts DC power into RF power,

with its RF output illustrated in Fig. 3.1(b). An excellent oscillator should continuously output coherent waveforms and ideally the frequency-domain power spectrum should only have a singular frequency component, while in reality it always has noise sidebands.

3.2 Crystal Oscillators: from Quartz to *Vibrating* NEMS

In most conventional electrical oscillators, the frequency selectivity is determined by tank circuits of passive components, such as the classical Wien-bridge (RC) oscillator which launched Hewlett-Packard in 1940 [7], and modern LC oscillators [8]. Quartz crystals were used in oscillators as stable RF sources for radio broadcasting, by radio amateurs, in the 1920's. For its desirable properties (*e.g.*, very-high-Q's of 10^4–10^5 or even 10^6, and highly stable resonance frequencies), quartz technology grew rapidly during the World War II and has since played major roles working as frequency sources and time bases in the aforementioned applications [9,10]. However, these off-chip quartz units have continued to resist shrinkage in the relentless miniaturization of microelectronics, thus prohibiting the development of microchip-based integrated systems such as wireless on-chip transceivers. Moreover, miniaturized IC-compatible devices can work in remarkably higher frequency ranges beyond those of conventional quartz oscillators (up to ~20-30MHz with fundamental modes and ~200MHz with higher overtones).

Early ideas of integrating micromachined mechanical resonators for tuned circuits were discussed and demonstrated in mid 1960's [11]. Later, effort towards *micromechanical signal processing* with MEMS resonators was pioneered by Clark T.C. Nguyen in the early 1990's [12]. Nguyen first made a monolithic CMOS oscillator with a 16.5kHz poly-Si comb-driven MEMS resonator [13], initiated and dedicated to the development of vibrating MEMS resonator based oscillators and filters for RF communication applications [14]. MEMS reference oscillators have been demonstrated with flexural mode doubly-clamped beams resonators at about 10MHz [15,16]. Recently better performance has been achieved by a MEMS oscillator based on a 60MHz

wine-glass mode disk resonator [17] which is a representative of the state-of-the-art MEMS reference oscillators. The improved phase noise performance is quite promising for some applications, although still inferior to that of quartz. At higher frequencies, although several kinds of VHF/UHF/GHz MEMS resonators have been realized lately [18], the scaling of motional resistances in the series-tank circuit models of these capacitively-transduced resonators is presently hindering them from being readily turned into low-noise reference oscillators.

We take proactive steps further down to nanoscale, and consider *nanomechanical signal processing*. Operating at higher frequencies than their MEMS counterparts in VHF/UHF/GHz ranges, the recently-highlighted NEMS devices made of both lithographically-patterned nanobeam structures [19,20] and chemically-synthesized nanowires [21,22] and nanotubes [23], however, are all *passive* resonators. It is also desirable to implement *active* oscillators with these devices but this remains an open challenge.

Major technical difficulties common for making oscillators with both MEMS and NEMS resonators arise from the fact that their electromechanical characteristics (described by equivalent circuit models) become increasingly incongruous with available electronics and circuit design techniques. But there are specificities for each case. While capacitively-transduced MEMS resonators suffer from very larger motional resistances, a typical magnetomotively-transduced UHF NEMS resonator is compromised by its very small electromechanical impedance albeit their total impedance can still be fairly closely matched to RF electronics.

In parallel to its central status in frequency control, quartz technology has also played a chief role in resonant mass sensing [5] since the advent of quartz crystal microbalance (QCM), marked by the publication of the Sauerbrey equation in 1959 [24]. The self-sustaining crystal oscillators lead to a generic method for doing fast mass detection

in real time. Not surprisingly, attaining excellent performance in MEMS/NEMS oscillators for both frequency control and resonant sensing demands and shares some of the same merits as the quartz crystal oscillators. Therefore, the development of NEMS-resonators-based oscillators is a thrust toward the miniaturization limits of crystal oscillators within both contexts of mechanical signal processing and resonant mass sensing.

This Chapter deals with the experimental demonstration of a NEMS oscillator and the characterization of its system-level performance. Our NEMS oscillator is the highest-frequency oscillator reported among all with flexural-mode vibrating MEMS and NEMS devices. Compared to many other rudimentary nanodevcies prototypes, this is among the first nanodevice-embedded *systems* with practical complexity and functionality; and it demonstrates considerable potentials for sensing and RF applications.

As depicted in Fig. 3.1, the self-sustaining oscillator outputs coherent RF signals while it only needs a DC power supply. Here we attempt to replace the frequency determining elements, conventionally piezoelectric crystals [9,10,25] and lately MEMS resonators [12-18], with a high-Q SiC UHF NEMS resonator. A doubly-clamped beam resonator has been patterned and fabricated from high-quality SiC epilayer with an optimized UHF SiC NEMS process [20]. The device's mechanical resonance is excited and transduced magnetomotively [20]. The specific device has dimensions of 1.65μm (L) × 120nm (w) × 80nm (t) (excluding the ~50nm metallization layers on top), having its in-plane fundamental mode resonance at 428MHz with $Q \approx 2500$.

3.3 Large-Signal UHF Resonance Readout for NEMS Oscillator

3.3.1 Resonance Signal-to-Background Ratio (*RSBR*)

Although the NEMS resonators operate in higher frequency bands (VHF, UHF and microwave) than their MEMS counterparts of the same kinds, self-sustaining oscillators have not yet been possible by utilizing MEMS or NEMS resonators operating well in these bands. The major obstacle for realizing self-oscillation with our UHF NEMS resonators is that thus far the resonance signals read out from the UHF NEMS resonators are very small, while the embedding background response is usually overwhelming and dominates over the useful resonance signals. To clearly address this issue, here we define the *resonance signal-to-background ratio* (*RSBR*) as the figure of merit, to characterize a resonance signal and its magnitude in the context of the embedding parasitic background response[①],

$$RSBR(\omega)[\mathrm{dB}] \equiv 20\log\left(\frac{\left|\vec{V}_r(\omega)+\vec{V}_b(\omega)\right|}{\left|\vec{V}_b(\omega)\right|}\right), \tag{3-1}$$

where $\vec{V}_r(\omega)$ is the resonance signal and $\vec{V}_b(\omega)$ is the background signal; both are frequency-dependent complex variables (*i.e.*, vectors functions of frequency) and need to be carefully analyzed as phasors in a phase plane at any given frequency. A great convenience of this figure of merit is that the *RSBR* can be directly read from the resonance measurement instruments such as a network analyzer. The *RSBR* goes to 0dB off-resonance, as off-resonance the resonance signal vanishes. Given the complex

---

[①]We note that this may also be called *on-to-off-resonance ratio*, or *ratio of on-resonance to off-resonance*, as sometimes used in characterizing various resonances, in some other communities.

nature and frequency dependency, we make the *RSBR* more transparent in the following form,

$$RSBR(\omega)[\mathrm{dB}] = 10\log\left(\frac{V_r^2(\omega)+V_b^2(\omega)+2V_r(\omega)V_b(\omega)\cos[\Delta\phi(\omega)]}{V_b^2(\omega)}\right), \tag{3-2}$$

in which $V_r(\omega)$ and $V_b(\omega)$ are norms of $\vec{V}_r(\omega)$ and $\vec{V}_b(\omega)$, respectively (*i.e.*, amplitudes of both signals and both phase-independent, $V_r(\omega)=\left|\vec{V}_r(\omega)\right|$ and $V_b(\omega)=\left|\vec{V}_b(\omega)\right|$); and $\Delta\phi(\omega)\equiv\phi_r(\omega)-\phi_b(\omega)$ is the phase difference of the resonance signal with respect to the background response.

As an ideal case, if both the resonance signal and the background signal are *in phase* throughout the frequency range that the resonance covers, *i.e.*, $\Delta\phi(\omega)=0$ for $\omega_0-\Delta\omega\leq\omega\leq\omega_0+\Delta\omega$, with ω_0 the resonance frequency and $\Delta\omega$ the resonance width, then we have,

$$RSBR_{in-phase}(\omega)[\mathrm{dB}] = 20\log\left(1+\frac{V_r(\omega)}{V_b(\omega)}\right). \tag{3-3}$$

Still more ideally, it is also favorable that in the vicinity of resonance, the background response is constant, non-frequency-dependent, or at least a simple (*e.g.*, linear) function of frequency that can be easily nulled out or subtracted. The maximum *RSBR* value is usually achieved at the frequency of resonance peak, and $RSBR(\omega=\omega_0)$ is used for characterization. In practical measurements of NEMS resonators, however, both *in-phase* and *frequency-independent* background responses are rare, especially for UHF NEMS.

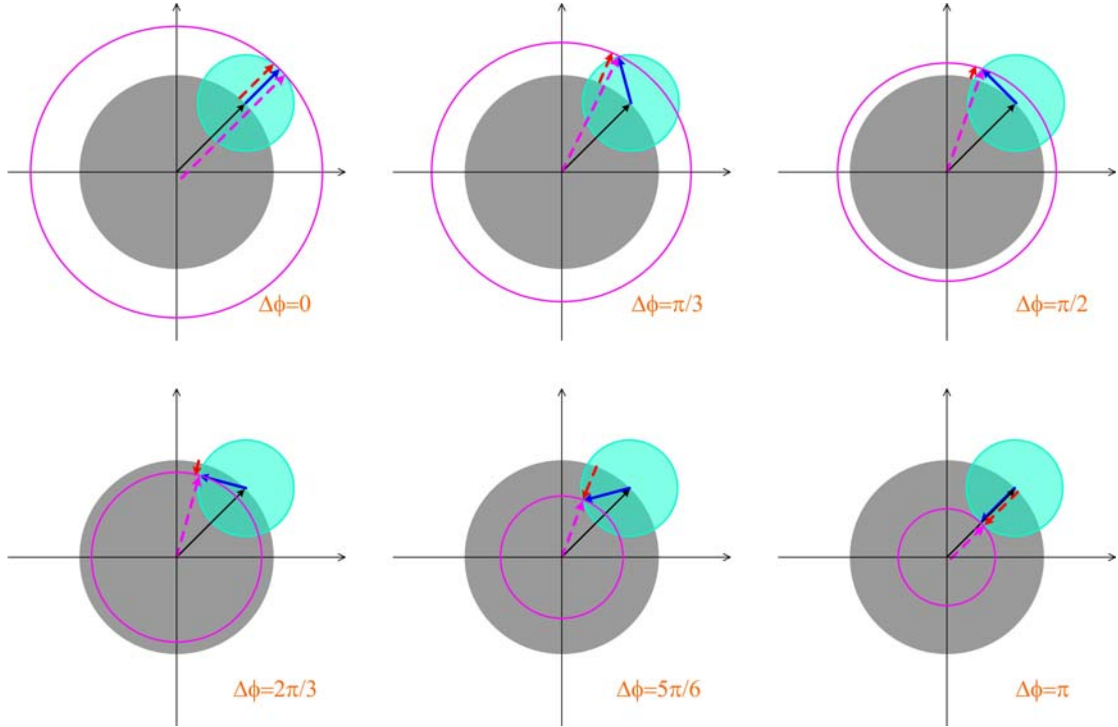

Fig. 3.2 Phasor representation of the *RSBR* and the relation of resonance signal and the background at $\omega=\omega_0$ (*i.e.*, only the 'slice' at the resonance peak along the frequency axis) with the phase difference between resonance signal and background varied from 0 to π. The phasor representations: $\vec{V}_b(\omega_0)$ is *black*, $\vec{V}_r(\omega_0)$ is *blue*, $\vec{V}_b(\omega_0)+\vec{V}_r(\omega_0)$ is *magenta*, and *red* is $\left(\left|\vec{V}_b(\omega_0)+\vec{V}_r(\omega_0)\right|-\left|\vec{V}_b(\omega_0)\right|\right)\cdot\hat{r}$ where $\hat{r}$ is the *radial* vector with *unit* module $\left|\hat{r}\right|=1$. A positive *red* vector (pointing radially out from the origin) indicates the resonance peak is above the background (*RSBR*>0dB); and a negative *red* vector (pointing toward the origin) represents that the resonance is below background (*RSBR*<0dB).

To illustrate the effect of the background response visually, we shall use the phasor representation. Shown in Fig. 3.2 are the phasor representations of both the resonance signal and the background at the resonance frequency ($\omega=\omega_0$), with the phase difference $\Delta\phi(\omega_0)$ varied from 0 to π. We assume the amplitudes of both resonance and background are phase-independent. For convenience, we use $V_b=2V_r$ in the drawings while in reality usually $V_b>>V_r$ and their sizes in the drawings would be much more widely discrepant.

Fig. 3.2 explicitly shows that when the background response is larger than or dominates over the interested resonance signal (V_b~V_r *to* $V_b>>V_r$), even only the phase difference can play a key role in determining the resulting *RSBR* that we measure (*RSBR*

decreases from positive to negative as $\Delta\phi(\omega_0)$ is increased from 0 to π). Note that ideally, the phase effect would become negligible if $V_b << V_r$, which is almost always not the case for NEMS resonance detection. Still, the scenario in Fig. 3.2 is highly simplified as it only takes care of the effect at one point, $\omega=\omega_0$.

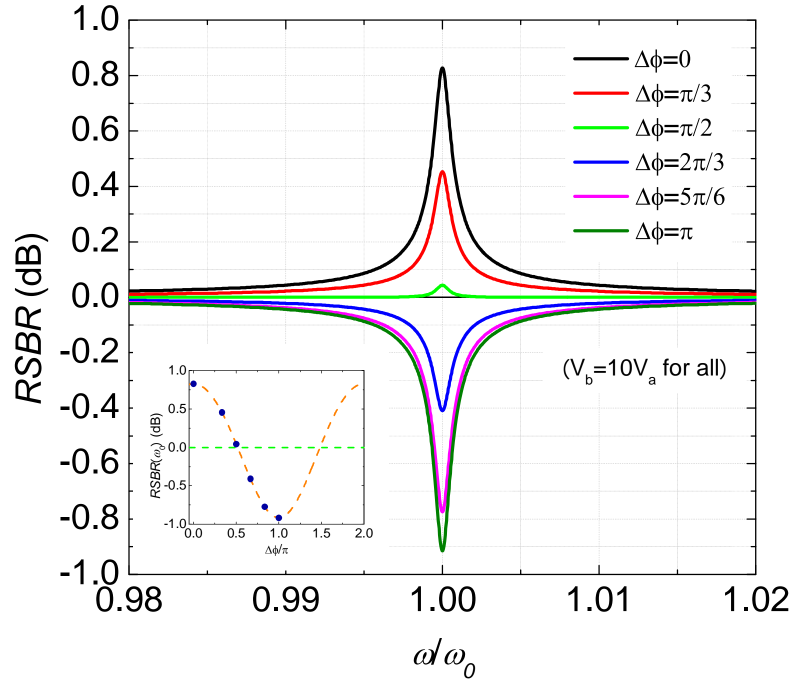

Fig. 3.3 Effect of phase difference upon *RSBR* for $V_r(\omega)=V_a\cdot H_a(\omega)$ and $V_b=10V_a$. Inset: *RSBR* at the resonance peak, $RSBR(\omega_0)$ as a function of $\Delta\phi$.

To examine the effect over the frequency range of the resonance peak, and to clearly demonstrate the significant impact of the frequency-dependent background response and phase difference upon the *RSBR* in typical detections, we consider a resonance signal with its peak amplitude of $V_r(\omega_0)=V_a$=1nVolt (1nVolt=1×10^{-9}Volt),

$$V_r(\omega)=V_a\cdot H_a(\omega)=V_a\cdot\frac{1/Q}{\sqrt{\left[1-(\omega/\omega_0)^2\right]^2+(\omega/(\omega_0 Q))^2}}, \quad (3\text{-}4)$$

where $H_a(\omega)$ is the normalized resonance response of a driven resonator with a quality factor Q. Again, first consider a very simplified case of frequency-independent,

constant background $V_b(\omega)=10V_a=10$nVolt, and further assume that the phase difference between the resonance and background is constant $\Delta\phi(\omega)=\Delta\phi$, over the frequency range of interest. As depicted in Fig. 3. 3, for a constant background of 10 times the resonance peak amplitude, the resonance peak *RSBR*, $RSBR(\omega_0)$, is always smaller than 1dB and it varies from 0.83dB to -0.92dB as $\Delta\phi$ changes from 0 to π. The $RSBR(\omega_0)$ dependency on $\Delta\phi$ is essentially the same as illustrated in Fig. 3.2, with the only difference that in Fig. 3.3, the ratio of resonance peak amplitude to background is 1/10 and in Fig. 3.2 it is 1/2.

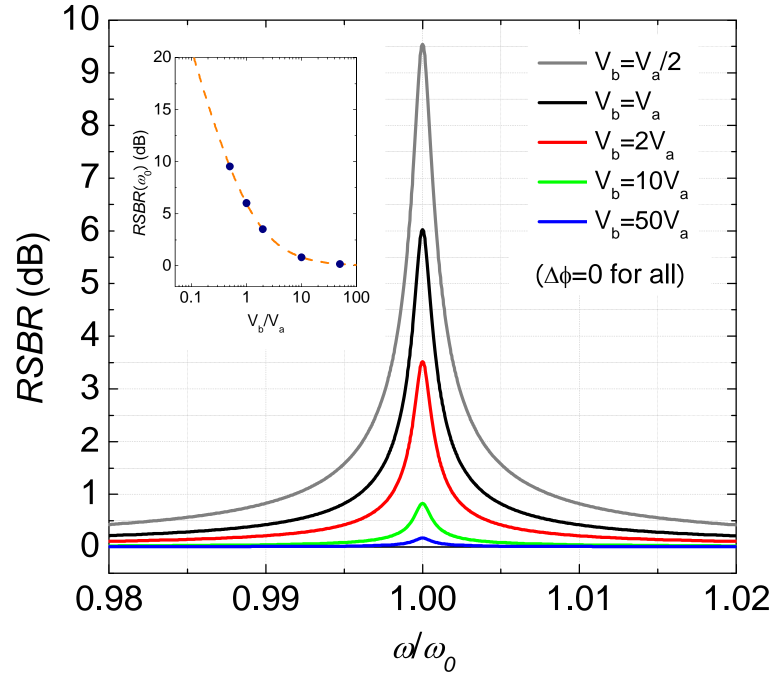

Fig. 3.4 Effect of magnitude of the background response upon *RSBR*, for $V_b=\alpha V_a$ (α=1/2, 1, 2, 10, 50) with $V_r(\omega)=V_a{\cdot}H_a(\omega)$ and $\Delta\phi=0$. Inset: *RSBR* at the resonance peak, $RSBR(\omega_0)$ as a function of α.

In another case we assume the resonance is simply always *in phase* with the background ($\Delta\phi(\omega)=\Delta\phi=0$), and we examine the effect of the magnitude of the background. As shown in Fig. 3.4 and its inset, background magnitude $V_b(\omega)=\alpha V_a$ is changed by varying α; and the $RSBR(\omega_0)$ changes from 9.5dB to 0.17dB as α is varied from 1/2 to 50. Abandon the *in-phase* assumption and allow $\Delta\phi$ to change; each curve

with a specific α in Fig. 3.4 can be extended into a family of curves each corresponding to a specific phase difference. Shown in Fig. 3.5 are such a family of curves for $V_b=V_a$ (α=1 case in Fig. 3.4). If compared to Fig. 3.3, although qualitatively the effect of varying phase difference is similar, quantitatively in Fig. 3.5 $RSBR(\omega_0)$ changes more dramatically, from 6dB to -∞dB (theoretically) as $\Delta\phi$ is varied from 0 to π. This illustrates that $RSBR(\omega_0)$ is more sensitive to phase difference in the case of $V_b=V_a$ than in cases of $V_b>>V_a$ and $V_b>V_a$, as shown in Fig. 3.3 and illustrated in Fig. 3.2.

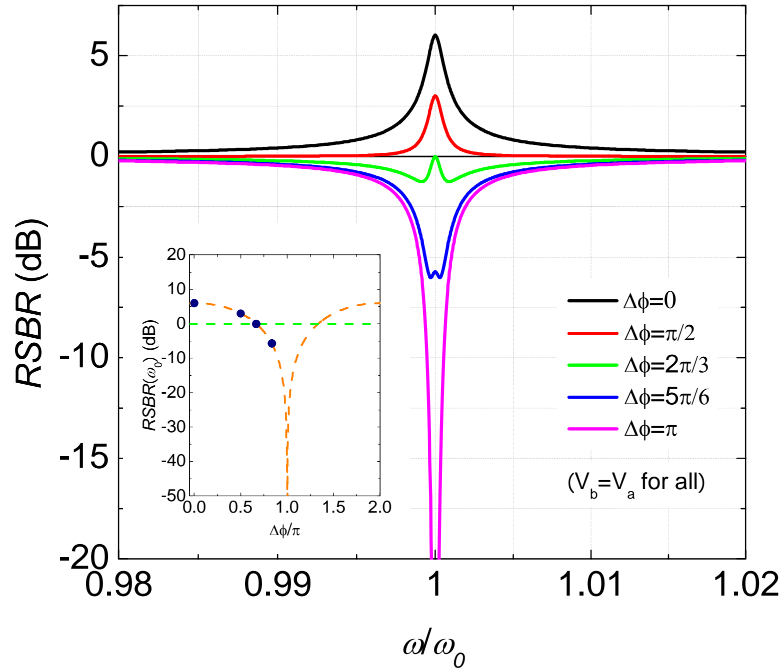

Fig. 3.5 Dependency of *RSBR* upon the phase difference between resonance and background, for $V_b=V_a$. Inset: *RSBR* at the resonance peak, $RSBR(\omega_0)$ as a function of $\Delta\phi$.

In reality, the situations are always more complicated because the background is hardly constant or flat over the frequency range. Still, we consider simplified special cases where the background is linearly frequency dependent, for example, $V_b=V_{b0}+b_\pm(\omega-\omega_0)$ where b_+ and b_- are positive and negative slopes, respectively. Shown in Fig. 3.6 are the effects on the *RSBR* with the background as a linear function of frequency. For easy comparison, we use $V_{b0}=10V_a$ (same as in Fig. 3.3) and also plot the constant background

case. It is shown that as the phase difference is varied, even the resonance peak shape is changed. This is dramatically different than the cases where the background is constant, as shown in the previous several figures. In practice, in a frequency range that embraces the resonance signal, although sometimes the background can be close to a polynomial or even linear function of frequency, often it can be nonlinear and far from constant or some typical friendly fitting functions, thus making the detected resonance peaks have quite funky shapes (see some examples in Fig. 3.6) as compared to a normal resonance signal given by eq. (3-4) whose power spectrum is very well approximated by a Lorentzian, as addressed in Chapter 2.

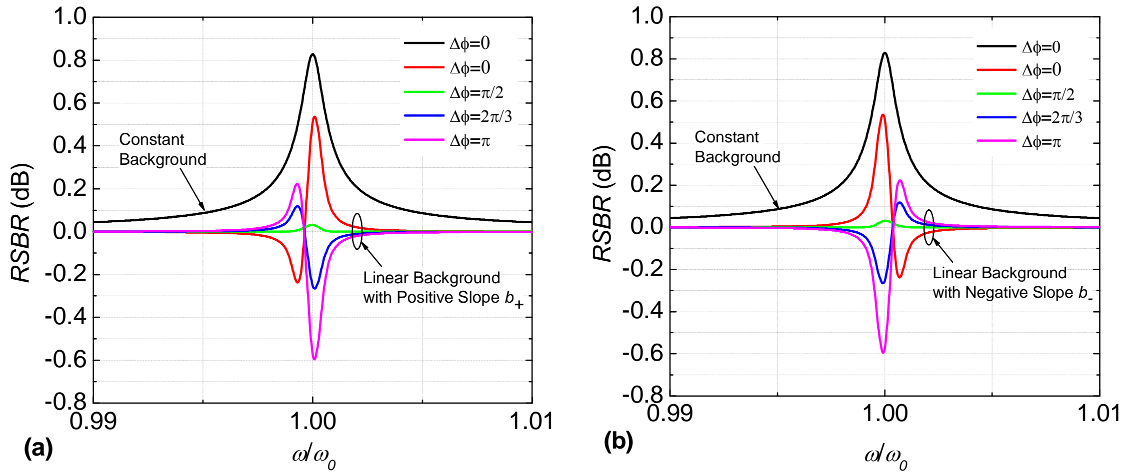

Fig. 3.6 Effect of non-constant but linear background upon the resonance shape and *RSBR*. **(a)** for linear background as function of frequency with a positive slope $V_b=V_{b0}+b_+(\omega-\omega_0)$ ($b_+>0$). **(b)** for linear background with a negative slope $V_b=V_{b0}+b_-(\omega-\omega_0)$ ($b_+<0$). As a reference, the case with in phase ($\Delta\phi=0$) constant background V_{b0} is plotted in both **(a)** and **(b)**.

The above analyses with introducing and discussing *RSBR* are very useful and important. First, a much clearer understanding of the behavior of the detected resonance signal can be gained from the analyses and modeling. Moreover, techniques can be sought and developed for better detection of resonance signals. In real experimental measurements, particularly with VHF and UHF NEMS resonators, we have observed many detected resonance signals like those shown in Fig. 3.3 and Fig. 3.6, since in most cases the background response is large and non-constant. As the frequency is scaled up

with ever-shrinking device sizes, these $RSBR(\omega_0)$<1dB and even smaller signals and their abnormal shapes constitute big issues and challenges.

One method of retrieving and extracting NEMS resonance signals from the measured response involving the embedding background is to use the carefully recorded magnitude and phase data (or equivalently, both components in the X and Y quadratures). This kind of data includes the frequency dependence of both the background and resonance, in the interested range. The background and phase difference, both as functions of frequency, can be decomposed manually or by using software programs, and then subtracted, leaving only the useful resonance signal, which should essentially be consistent with eq. (3-4). This sort of 'postprocessing' background subtraction technique has been widely used in the studies of NEMS resonators where the resonance curves are pretty much the final data, and it is valid and convenient for characterizing the basic properties and performance of the resonators based on the resonance data. Besides, this background subtraction process does not enhance *RSBR*.

However, if further operation and processing of the resonance signal is needed, it is desirable to have resonance signal with as large an *RSBR* as possible for the subsequent signal processing after the resonance readout. In this case, the postprocessing background subtraction technique would not help. One must devise some *real-time and analog* schemes (other than digital or software-based data postprocessing) that can effectively suppress the background, take care of the effect of phase difference and enhance *RSBR*, so that the resonance signal is friendly enough for direct manipulations in the next stages. The aforementioned analyses on *RSBR* provide some intuition upon this issue: For a specific NEMS device with its resonance signal strength given by eq. (3-4), the *RSBR* can be enhanced by generating an in-phase, constant background with as small as possible magnitude.

In generations of experiments with VHF/UHF doubly-clamped beam resonators, we have found that direct reflection or transmission measurements of single device are valid to find and read out resonance signals up to ~200MHz. For smaller and >200MHz devices, the recently proposed balanced-bridge detection scheme [26] has proven to be better, and for >100MHz devices it has demonstrated a visible advantage.

However, engineering NEMS into systems with attractive functionalities and promising performances requires much more beyond just finding resonance signals. There is still an intractable bottleneck—bridge scheme does help in finding UHF resonances which could be otherwise invisible, but the signals found are still too small—somehow having similar or lower efficiency as reflection (or transmission) scheme having in the HF/VHF ranges. This is rooted from the fact that the prototype bridge scheme (and its analysis) was based on a DC bridge and it did not concern the frequency-dependent nature of both magnitude and phase of the background.

3.3.2 High-Resolution Bridge-Balancing and Background-Nulling

We have developed high-resolution balancing and background-nulling techniques based on the foregoing analysis of *RSBR* and the limitations of the prototype bridge circuit. The high-resolution techniques take care of both the frequency-dependent magnitude and phase of the background, and non-idealities such as reflection, attenuation, excess phase lag introduced by not only the device, but also every component, including every cable and microstripe, used in each branch of the bridge circuit. We perform computer simulations of the frequency response of the whole bridge circuit, and calibration of frequency response of every component to gain enough pre-knowledge of the unbalanced magnitude and its sources (limiting factors). Then we apply calibrated, high-precision, tunable amplitude and phase controls to each branch. To best null the background response arising from *mismatch*, *reflection*, *dispersion*, etc., we have applied techniques

and controls including *impedance matching*, *isolation*, *phase shifting, attenuation,* etc., to perfectly match the two branches and null the background.

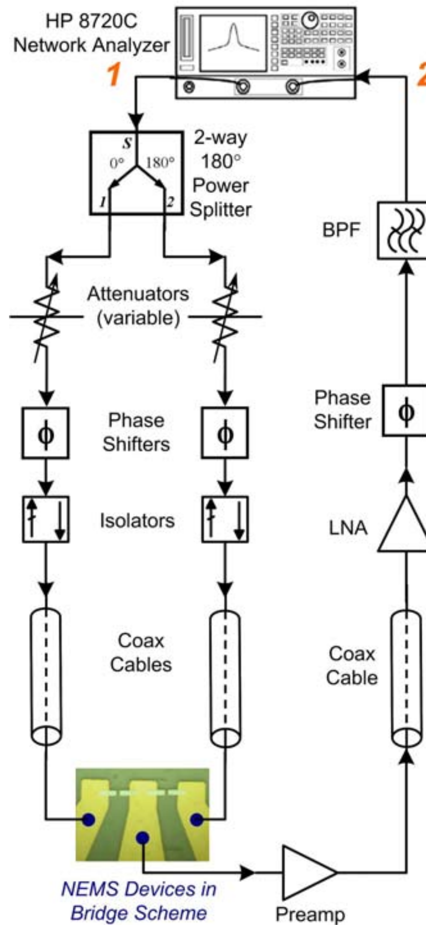

Fig. 3.7 Network analysis measurement and open-loop calibration scheme of the UHF resonance detection with the high-resolution balanced-bridge circuit. The band-pass filter (BPF) is optional in the resonance detection.

As shown in Fig. 3.7, the UHF NEMS resonance detection is implemented and optimized in the mode of open loop network analysis by connecting a microwave network analyzer (HP 8720C) between nodes 1 and 2 for two-port measurement. Fig. 3.8 shows the significant effect of background nulling with the above high-resolution balanced-bridge circuit. For the same pair of devices, compared to the results from the prototype of the balanced-bridge circuit (black) [26] and the improved version (green) [20], the high-resolution balancing has further achieved ~30–40dB background

suppression (blue) in a very wide band of interest. In fact, we have identified that the new techniques now really allow us to approach the practical limits of the balanced-bridge circuit, with the bridge point really approaching 'ground'.

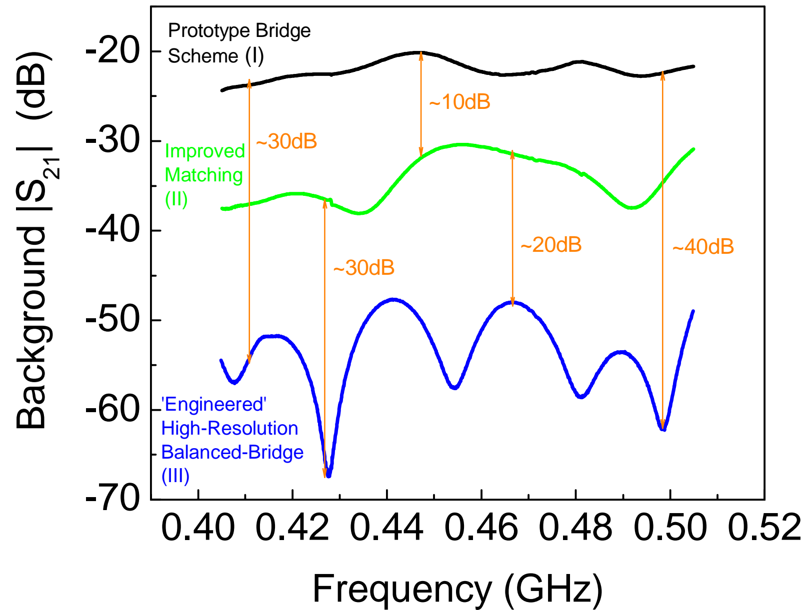

Fig. 3.8 Background suppression by high-resolution bridge-balancing and nulling techniques. Over 100MHz frequency span, ~30–40dB background suppression has been achieved.

The only practical limitations are from the amplitude and phase tuning resolutions of the matching and balancing components we use here. With this practically ultimately low background, we are now able to read out UHF NEMS resonance signals with a typical signal-to-background ratio of ~5–10dB in a wide band, which is comparable to signal levels from much larger and stiffer MEMS resonators [17,27]. This indicates a profound improvement in the UHF NEMS signal detection. For example, as shown in Fig. 3.9, is the great enhancement in detected *RSBR*, from ~0.5dB to ~10dB, for the same 428MHz resonance.

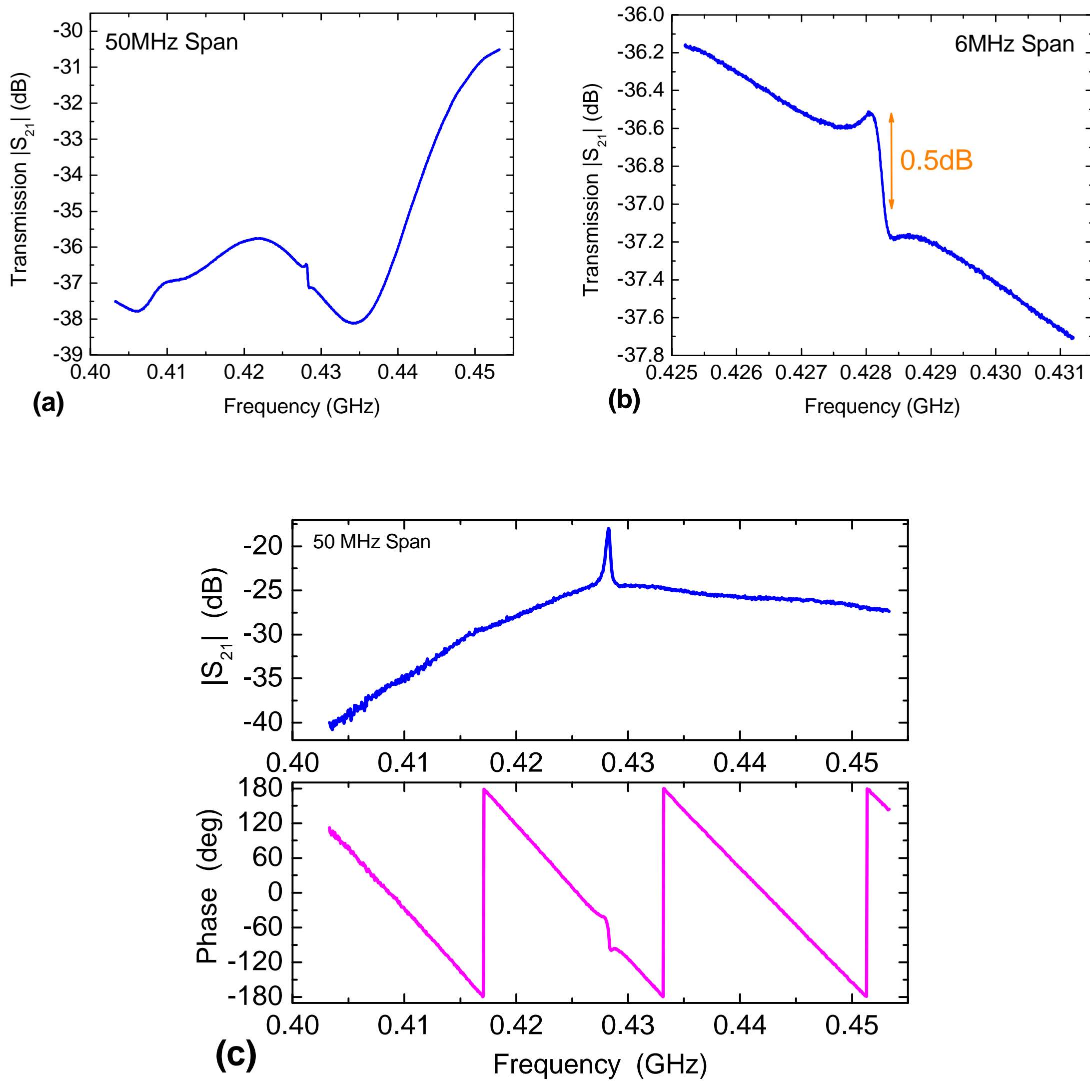

Fig. 3.9 Significant enhancement of *RSBR* with the use of high-resolution bridge-balancing and background-nulling techniques. **(a)** & **(b)** The 428MHz resonance signal read out by using an earlier version of bridge scheme [20], with *RSBR* of the order ~0.1–0.5dB, and with signals upon with self-oscillation is impossible to be realized. **(c)** The 428MHz resonance signal from the high-resolution balanced-bridge scheme, with typical ~8–10dB *RSBR*, and over very wide band, thus allowing for the resonator's frequency-selection capability for achieving self-sustaining oscillation.

3.4 Self-Sustaining Oscillation with UHF NEMS Resonator

3.4.1 Oscillation Conditions and Calibrations

Retrieving a resonance signal with a large *RSBR* over a wide band makes it possible to use nanoresonators for frequency reference and selection. To attain self-oscillation in a closed loop, at the selected frequency, the overall loop response should satisfy the Barkhausen criteria [4], *i.e.*, loop gain:

$$|H(\omega)| \geq 1 \text{ (0dB)}, \tag{3-5a}$$

and loop phase change:

$$\phi\,[H(\omega)] = 2n\pi, \tag{3-5b}$$

where n is an integer and $H(\omega)$ is the frequency-dependent loop transfer function. We first perform open loop calibrations in the network analysis mode, to precisely tune the open loop gain and phase change to meet the Barkhausen criteria. When the loop is closed, due to the inevitable reflection and phase change, the *real* (closed-loop) values of loop gain and loop phase change can be slightly different but the oscillation conditions can be restored by minor adjustments that make up the slight changes due to the closing loop action.

As Fig. 3.10 (a) illustrates, when the loop gain is tuned to allow loop gain $|H(\omega)| \geq 1$ in the frequency range of $(\omega_1 = \omega_0 - \delta_1, \omega_2 = \omega_0 + \delta_2)$ (δ_1, $\delta_2 << \omega_0/Q$), the loop phase change can be tuned such that at some certain frequency $\omega \in (\omega_0 - \delta_1, \omega_0 + \delta_2)$, the Barkhausen criteria are met and self-oscillation is attained. The practical scenario of this implementation in real experiments is demonstrated by Fig. 3.10 (b) and (c), with the measured open loop gain and open phase change, respectively.

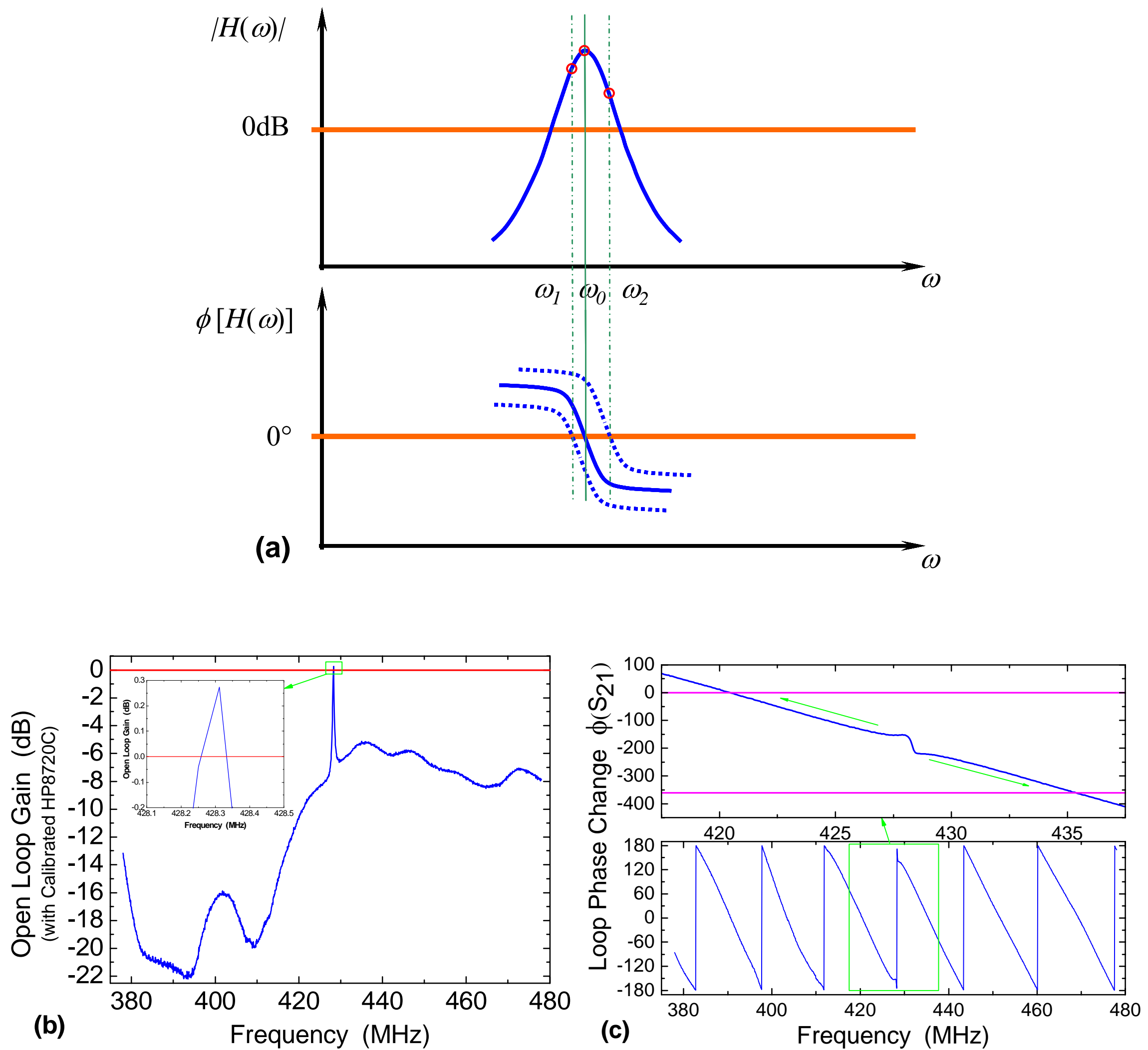

Fig. 3.10 Realizing self-oscillation with NEMS. **(a)** Schematic of satisfying the Barkhausen criteria for self-oscillation and optimizing the NEMS output by tuning loop phase shift. **(b)** Loop gain measurement (in open loop scenario) for setting the oscillation condition at the vicinity of peak of the resonance signal. **(c)** Measured loop phase change (in open loop scenario): arrows show the loop phase change can be tuned to 0 or 2π to satisfy the self-oscillation condition.

3.4.2 NEMS Oscillator Basic Characteristics

After open loop calibration, as illustrated in Fig. 3.11, the network analyzer is removed and the loop is closed by feeding output back to input (connecting points 1 and 2) and the oscillation with the NEMS resonator is realized. In stable oscillation, the only input to the system is the DC power supply for the sustaining amplifiers, and the output

radio-frequency signal can be straightforwardly characterized. One compelling characteristic of the NEMS oscillator is, in its closed-loop mode, once the Barkhausen criteria is satisfied at the resonance peak, the stable oscillation is easily switched on/off by simply turning on/off the DC power supply for the sustaining amplifiers.

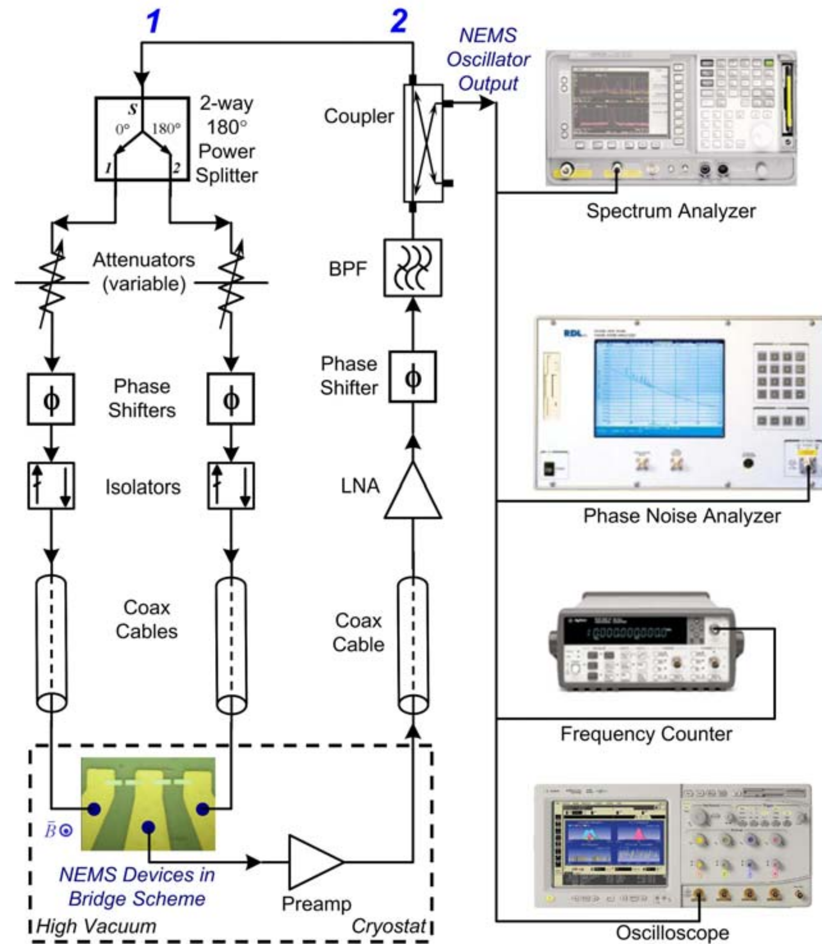

Fig. 3.11 Measurement setup for realizing the self-sustaining oscillation with UHF NEMS resonators. The sample chip consists of a pair of doubly-clamped vibrating NEMS resonator devices made by a nanofabrication process for high-frequency SiC NEMS (bright color showing Al metallization of the devices and close-in pads), and conducting pads defined by photolithography (yellow color, Au metallization) for wire-bonding. On-stage temperature sensor and heater for controlling the sample temperature are mounted on the backside of the sample stage. The sample is secured in a high-vacuum chamber ($<10^{-7}$ Torr). In the magnetomotive transduction setup, the chamber is housed in a cryostat where the superconducting magnet runs and provides an up to 8 Tesla strong magnetic field for magnetomotive excitation. The pair of NEMS devices are connected to room-temperature electronic system outside of the cryostat via three coaxial cables (each 6 feet long) to a balanced-bridge circuit scheme. The feedback loop of the NEMS oscillator consists of low-noise amplifier, phase shifter, filters for setting the oscillation conditions and a directional coupler to facilitate the oscillator output to be characterized straightforwardly.

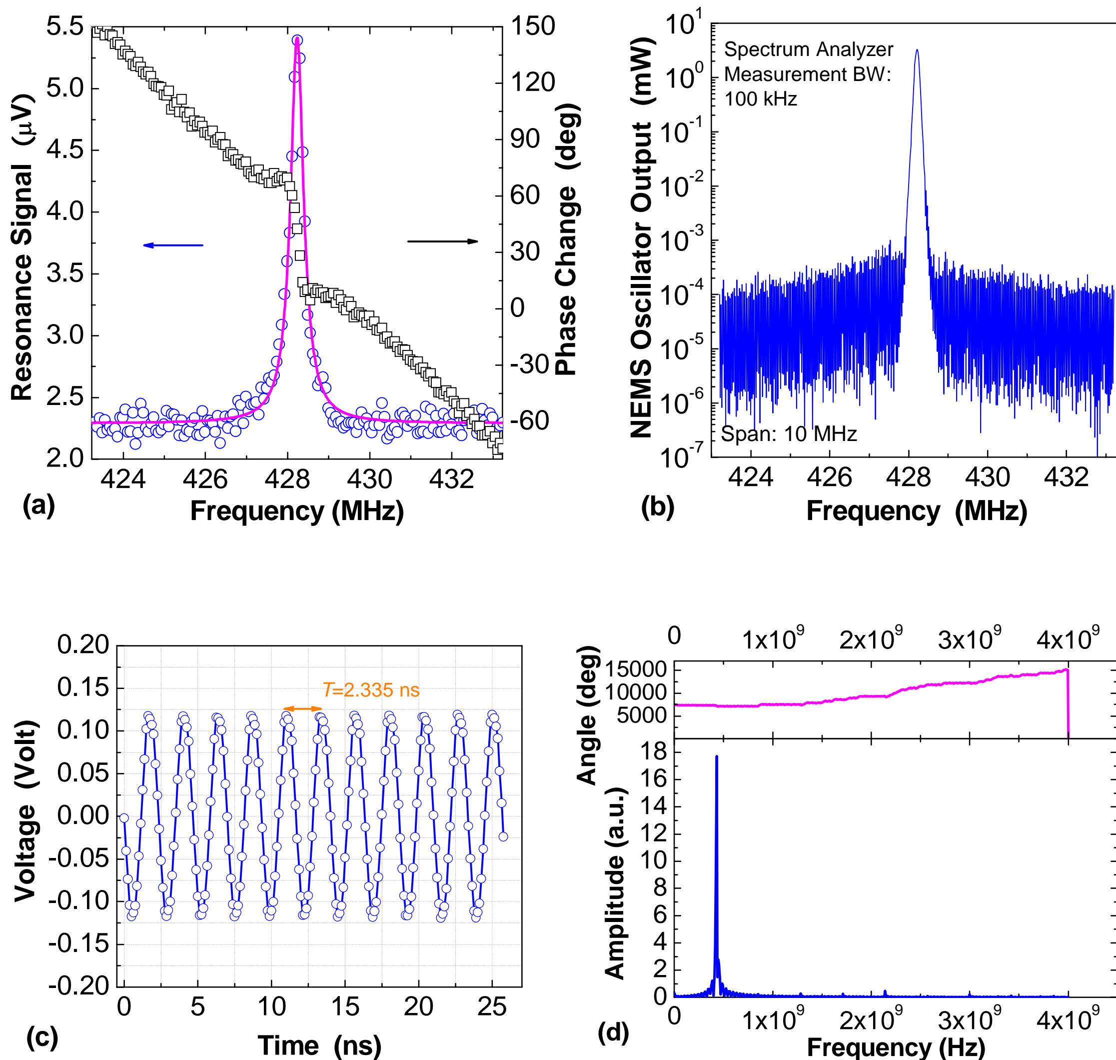

Fig. 3.12 Demonstration of the UHF NEMS Oscillator. **(a)** Resonance signal (open loop response) from the 428MHz NEMS resonator, which serves as the frequency-determining element of the oscillator. The resonance signal is accurately measured with a calibrated microwave network analyzer. Resonance-to-background ratio of 8dB is achieved. The solid line is from the Lorentzian fit to the resonance. **(b)** Power spectrum of stable self-oscillation of the NEMS oscillator with peak output power 5dBm, measured by a spectrum analyzer. **(c)** Time-domain output waveform of the NEMS oscillator, measured by a high-speed oscilloscope. **(d)** FFT spectrum of the measured time-domain output waveform, which verifies the direct power spectrum measurement.

In its self-oscillating mode, the NEMS oscillator is readily characterized. Fig. 3.12 summarizes the basic characteristics of this first UHF NEMS oscillator, with the larger *RSBR* resonance signal (calibrated, and referred to the preamplifier) highlighted in Fig. 3.12 (a). Fig. 3.12 (b) shows a representative measured power spectrum at the output of

the NEMS oscillator. The output peak power is 5dBm (*i.e.*, 3.2mWatt RF power, or equivalently, 0.405Volt for 50Ω standard). Fig. 3.12 (c) shows the time-domain stable oscillation waveforms measured by a fast oscilloscope, and Fig. 3.12 (d) is the FFT spectrum of the measured time-domain waveform data.

Table 3-1 Basic specifications of the UHF NEMS oscillator and its NEMS resonator

Specification	Value
Device Length	1.65 μm
Device Thickness (structural layer)	80 nm
Device Width	120 nm
Resonance f_0	428.2 MHz
Structural Material	3C-SiC (single-crystal)
Metallization	10 nm Ti atop 40 nm Al
Device Active Mass	57.8 fg
Device DC Resistance R_{DC} (T≈300K)	92.9 Ω
Device DC Resistance R_{DC} (T≈22K)	51.7 Ω
$S_{x,\mathrm{th}}^{1/2}$ (device)	1.75×10^{-15} m/√Hz
$S_{V,\mathrm{th}}^{1/2}$ (device)	3.25×10^{-11} volt/√Hz
$S_{F,\mathrm{th}}^{1/2}$ (device)	2.93×10^{-16} N/√Hz
DR (device) (intrinsic, 1Hz ENBW)	114 dB
$S_{V,\mathrm{real}}^{1/2}$ (system, refer to in put of preamp)	2.47×10^{-10} volt/√Hz
$S_{x,\mathrm{eff}}^{1/2}$ (effective displacement sensitivity)	1.33×10^{-14} m/√Hz
DR (device, available, 1Hz)	96 dB
Resonance Signal-to-Background Ratio (*RSBR*)	8 dB
Output Power	3.2 mWatt (5 dBm)

We have carefully examined the specifications of the oscillator system and its frequency-determining element, the UHF NEMS resonator, as some characteristics summarized in Table 3-1. In the mechanical domain, the doubly-clamped resonator can be modeled as a Duffing mechanical oscillator (see Chapter 2) (the 'oscillator' here is just a conventional nomenclature, different from the stable electrical oscillator, which is self-sustaining). The ultimate noise floor of the NEMS resonator's displacement is set by the thermomechanical noise—when the device is driven to resonance by the stochastic

process, *i.e.*, Brownian motion (random thermal fluctuation), the displacement spectral density is

$$S_x^{1/2} = \sqrt{\frac{4k_B TQ}{M_{eff}\omega_0^3}}, \tag{3-6}$$

where T is temperature, Q is the resonator's quality factor, m the mass and ω_0 the resonance frequency. Set by equation of Duffing oscillator, the critical amplitude is

$$a_C = \frac{\omega_0 L^2}{\pi^2}\sqrt{\frac{\sqrt{3}\rho}{EQ}}, \tag{3-7}$$

where L is the beam length, ρ the mass density and E the modulus of elasticity of the resonator material. As the useful onset of nonlinearity is defined by the 1dB compression point, where the displacement is $0.745a_C$, the intrinsic dynamic range (DR) of the NEMS device itself is then determined by the ratio of the onset of nonlinearity to the thermomechanical noise floor [28],

$$DR\,[\text{dB}] = 20\log\left(\frac{0.745a_C}{\sqrt{2S_x\Delta f}}\right), \tag{3-8}$$

in which Δf is the measurement bandwidth. In magnetomotive transduction, the noise floor of the electromagnetomotive voltage, generated by the thermomechanical motion of the resonator, is

$$S_V^{1/2} = BL\sqrt{\frac{4k_B TQ}{M_{eff}\omega_0}}, \tag{3-9}$$

where B is the magnetic field in the magnetomotive transduction. With the parameters of the device and experimental settings, ideally we have critical displacement amplitude of $a_C \approx 1.6$nm, displacement noise floor of $S_{x,\text{th}}^{1/2} = 1.75\text{fm}/\sqrt{\text{Hz}}$, and thus a dynamic range

of DR=114dB, and a voltage noise floor of $S_{V,\mathrm{th}}^{1/2}$=0.0325nVolt/√Hz, ultimately determined by the NEMS device itself. If employed for force detection, the device's thermomechanical-noise-limited force sensitivity is $S_{F,\mathrm{th}}^{1/2}$=0.29fN/√Hz.

In the electrical domain, however, the real dynamic range that can be achieved is determined by both the onset of nonlinearity and the noise floor of the detection system, referred to the input of the low-noise preamplifier which has a noise temperature T_{n}=9K at the frequencies of interest, and an input impedance of 50Ω.

In the electronic detection of the device resonance, at a device temperature of T=22K, the voltage noise floor is $S_{V,\mathrm{real}}^{1/2}$=0.247nVolt/√Hz, refer to the input of the preamplifier, as limited by the Johnson noise from the equivalent resistance of the devices and the noise from the preamplifier. This corresponds to a displacement sensitivity of $S_{x,\mathrm{eff}}^{1/2}$=13.3fm/√Hz, achieved in the detection. This then leads to an available dynamic range of $DR_{\mathrm{available}}$=96dB. The less-than-ideal dynamic range is because of the fact that the actual noise floor referred to the input of the preamplifier dominates over the intrinsic noise floor of the NEMS resonator device.

3.5 Phase Adjustment and Oscillator Frequency Detuning

In establishing self-oscillation, we have found that in the vicinity of loop gain larger than 1, the self-oscillation peak frequency can be detuned by finely tuning the loop phase change. As sketched in Fig. 3.10 (a), and shown in Fig. 3.13 with measured data, when the loop phase change is tuned, the oscillation frequency can be swept within the range of $(\omega_0 - \delta_1, \omega_0 + \delta_2)$, from one side to the other side of the resonance peak frequency ω_0; and the oscillator output power is also observed to go across the maximum. The frequency detuning due to loop phase change variation is about 300ppm/90deg, as shown in Fig. 3.13 (a). For better stability and phase noise performance, it is desirable to tune

the system to set the oscillation at the frequency of the resonance peak. We make sure this has been attained for every important measurement and calibration.

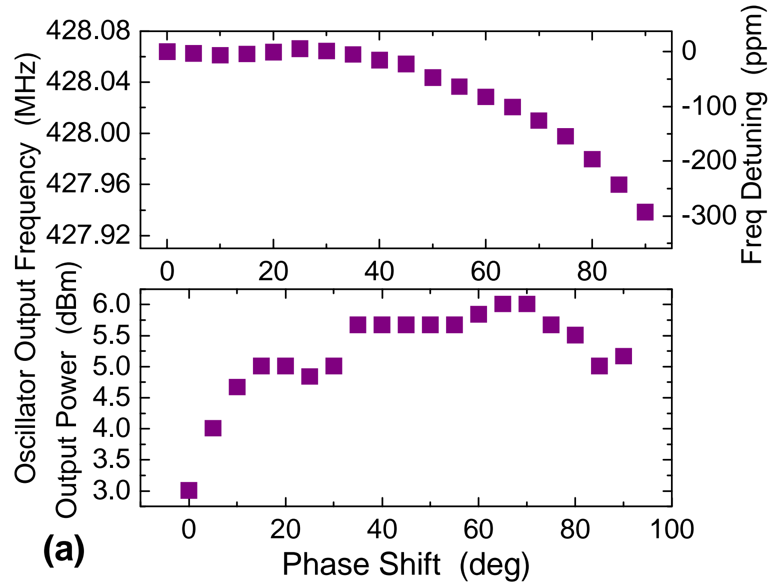

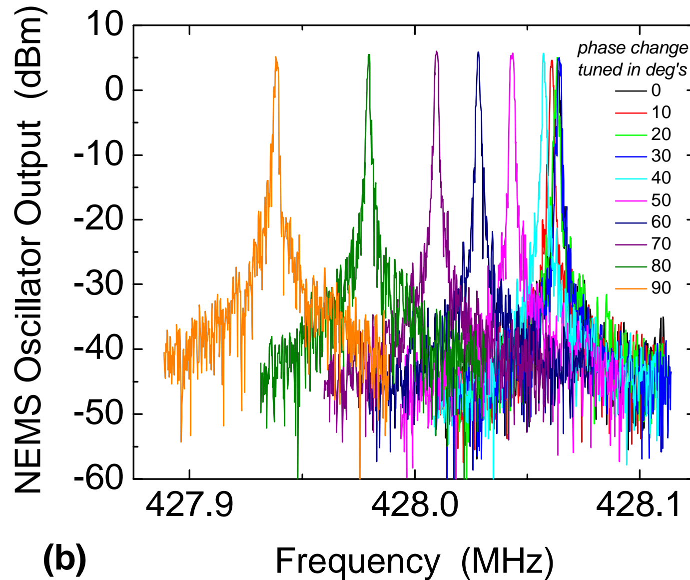

Fig. 3.13 NEMS oscillator frequency detuning with varied loop phase change. **(a)** Oscillator frequency and output power variations as the phase is shifted to satisfying the oscillation from one side to the other side of the resonance peak (as also illustrated in **Fig. 3.10 (a)**). **(b)** Raw data of the oscillator output power spectrum as the loop phase-change is tuned (all data taken while NEMS resonator is operating at stabilized temperature, and at fixed sustaining amplifiers gains, simply tuning only the loop phase change).

3.6 NEMS Oscillator Frequency Pulling and Nonlinear Behavior

We have also demonstrated that the NEMS oscillator frequency can be pulled by the loop gain tuning and the magnetic field change. The NEMS oscillator frequency pulling mechanisms are based on the fact that both the loop gain and magnetic field change induce change of the driving force upon the doubly-clamped resonator, which is readily described by the *forced Duffing equation* (see Chapter 2 for general discussion),

$$\frac{d^2 y}{dt^2} + 2\mu \frac{dy}{dt} + \omega_0^2 y + \alpha y^3 = \Gamma \cos(\Omega t), \tag{3-10}$$

where y is the beam displacement (in-plane), $2\mu \equiv \omega_0/Q$ with μ the damping coefficient, $\Gamma \equiv F/m$ with m the device mass; F the driving force, and Ω the driving frequency. The cubic nonlinearity coefficient is $\alpha = (2\pi/L)^4 E/(18\rho)$, determined by the geometry and elastic properties of the beam. This coefficient α can also be related to the critical displacement a_C (defined at the onset of nonlinearity), $\alpha = \left(8\sqrt{3}\omega_0^2\right)/\left(9Qa_C^2\right)$. Based on the Duffing equation description of the doubly-clamped beam resonator, both the *amplitude* and the *resonance peak frequency* are dependent on the driving force. The relationship between the NEMS resonator beam amplitude a and the frequency pulling σ ($\sigma \equiv \omega_{\mathrm{peak}} - \omega_0$, with ω_{peak} the resonance peak frequency) is readily described by the *frequency-response equation*,

$$\left[\mu^2 + \left(\sigma - \frac{3\alpha}{8\omega_0} a^2\right)\right]^2 = \frac{\Gamma}{4\omega_0^2}, \tag{3-11}$$

in which $\left(d\sigma/da\right)\big|_{a_C} = \infty$ sets the onset of nonlinearity and the critical amplitude a_C. As the drive strength Γ is increased, the relationship between the resonance peak frequency ω_{peak} and the amplitude at this peak frequency, i.e., the *backbone* curve, is

$$\sigma_{peak} \equiv \omega_{peak} - \omega_0 = \frac{\omega_0}{\sqrt{3}Q}\left(\frac{a_{peak}}{a_C}\right)^2, \tag{3-12}$$

where $a_{peak} = \Gamma Q / \omega_0^2$, and $a_C = \left(\sqrt{3}/2\right) a_{peak,C} = \left(\sqrt{3}/2\right)\Gamma_C Q / \omega_0^2$, with $a_{\mathrm{peak,C}}$ the peak amplitude at the critical driving Γ_C. With these relations, eq. (3-12) can be rewritten as

$$\sigma_{peak} \equiv \omega_{peak} - \omega_0 = \frac{4\omega_0}{3\sqrt{3}Q}\left(\frac{\Gamma}{\Gamma_C}\right)^2, \tag{3-13}$$

where the drive force Γ is readily determined by the transduction scheme and RF driving power sent to the device in a real measurement, and thus the backbone behavior in eqs. (3-12) and (3-13) can be calibrated by sweeping the driving force in measurements. Therefore, both the backbone curve and the frequency-response curves can be experimentally determined.

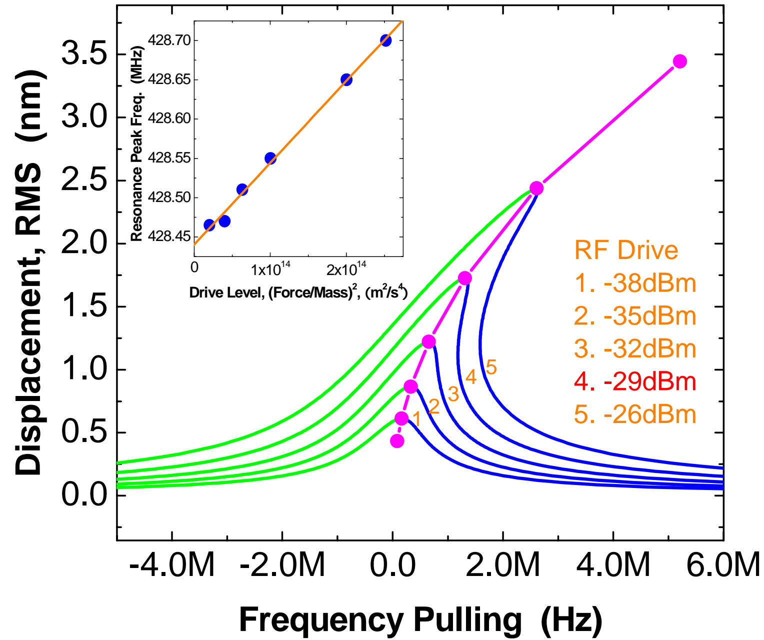

Fig. 3.14 Duffing behavior of the NEMS resonator calibrated in measurements: the frequency-response curves and the backbone curve (resonator peak amplitude versus resonance peak frequency). The family of frequency-response curves shows the NEMS beam resonator displacement in nanometers versus frequency (as described in eq. (3-11)). **Inset**: the linear fit of measured frequency pulling versus driving force squared ($\Gamma^2 = (F/m)^2$), according to eq. (3-13).

As shown in the inset of Fig. 3.14, the measured frequency pulling versus *squared* driving force is fit linearly according to eq. (3-13), and then the behavior described in eqs. (3-11), (3-12) and (3-13) can be quantitatively determined. By combining the extracted data from measurements and the theory of Duffing nonlinearity, the frequency-response curves are reproduced and plotted in Fig. 3.14, which show the onset of nonlinearity is attained when the RF power sent to the NEMS device is about -29dBm, exactly the same as observed in network analysis measurements. This verifies the validity of the above analyses, and also demonstrates reliable prediction of device absolute displacement (in nanometers) as the driving force is increased. It is noted that because the cubic nonlinearity coefficient $\alpha>0$, the frequency pulling is a spring stiffening effect.

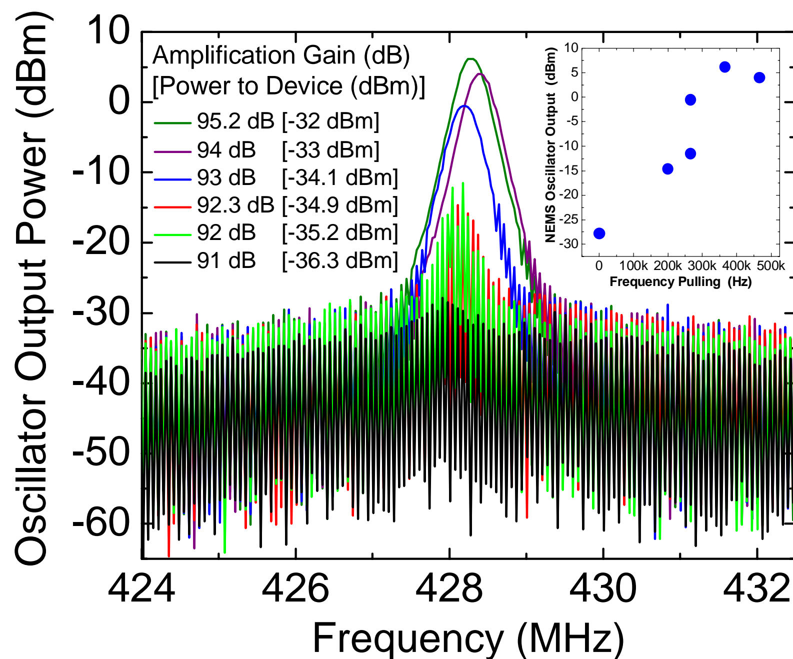

Fig. 3.15 Measured NEMS oscillator output frequency pulling with calibrated sustaining amplification gain change (*i.e.*, the change of RF power sent to the NEMS device). **Inset**: NEMS oscillator output power versus frequency pulling. Note when the sustaining amplification gain is smaller than some certain value (here ~90dB) there is no measurable oscillation.

The above analyzed and calibrated effect of NEMS resonator directly determines the behavior and performance of the NEMS oscillator. As shown in Fig. 3.15, when the

feedback amplification gain is changed and thus the RF power driving the device is changed accordingly, the NEMS oscillator output spectrum changes both its peak power and peak frequency (in each case, the loop phase change is tuned to optimize the oscillation to happen at the resonance peak frequency, as addressed in the previous section). The oscillation frequency is pulled upward, as a result of the resonator's frequency stiffening effect, when the loop gain is increased. Shown in the inset of Fig. 3.15 is the relation of oscillator output versus oscillation frequency, which follows the tendency as depicted by the backbone curve of the NEMS resonator in Fig. 3.14.

The nature of the frequency pulling effect of the NEMS oscillator is based on the transition from linear to nonlinear regime of a doubly-clamped beam Duffing-type resonator, as the driving force is increased. Spontaneously, it becomes very intriguing to drive the NEMS resonator into the nonlinear regime, and to realize and then characterize the nonlinear oscillation with NEMS. Moreover, once self-oscillation is realized with a nonlinear NEMS resonator, the noise-induced switching of self-oscillations between the bistable states of the same frequency-determining resonator could be very interesting and important for both fundamental research and technological applications [29].

3.7 Phase Noise of the UHF NEMS Oscillator

As illustrated in the oscillator system setup in Fig. 3.11, the oscillator mode greatly facilitates the characterization of the oscillator. Measurements ranging from spectrum analysis to phase noise and frequency stability can all be performed by directly measuring the output of the NEMS oscillator. In this regard, the NEMS oscillator technology has a major advantage for characterizing the noise, stability and sensitivity of the NEMS-resonator-embedded system, as compared to the other technology of using an external oscillator to drive the passive resonator and to detect and track its resonance in a phase-locked loop (PLL).

We have conducted systematic studies on the NEMS oscillator's phase noise and frequency stability performance, since noise and sensitivity are crucial for both communications and sensors applications, and the trade-off is that the smaller and more sensitive the device, the more susceptible it is to noise. Of practical importance, low phase noise is desirable for UHF signal processing and communications [4,12-18,30], and sensitivity is most essential for transducer applications such as mass sensors [31,32].

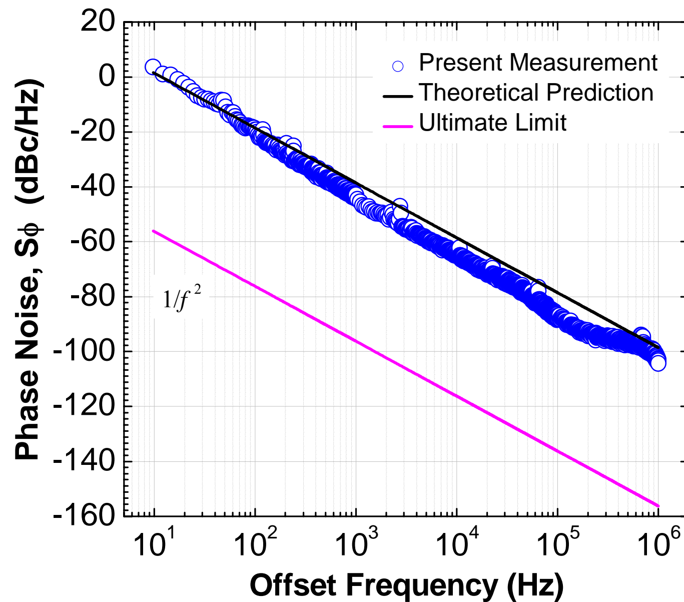

Fig. 3.16 Phase noise performance of the NEMS oscillator for offset frequency from 10Hz to 1MHz, measured by a specialized phase noise analyzer (RDL NTS-1000B Phase Noise Analyzer). Shown are the measured data, the theoretical prediction based on oscillator phase noise theory [33] and the calculated ultimate phase noise performance limited only by the NEMS resonator device itself.

Measured phase noise performance of the oscillator system is shown in Fig. 3.16. The measured data suggests the present system performance is thermal noise limited (*i.e.*, following the $1/f^2$ power law on the phase noise plot). Given the detection noise floor analysis in Section 3.4.2, the electronic thermal noise (Johnson) plus the amplifier noise overwhelms the thermomechanical noise of the NEMS device. Hence the thermal noise induced phase noise limits the oscillator performance, leaving the device's thermomechanical noise induced phase noise still a fundamental limit to be approached.

The measured phase noise is readily modeled based on the intuitive understanding of phase noise in terms of *phase diffusion* [33]. As the extrinsic electronic noise at the input of the preamplifier dominates, the measured phase noise can then be predicted by

$$S_{\phi}(\omega) = \frac{2D}{\omega^2 + D^2}, \tag{3-14}$$

where D is the phase diffusion constant and ω the offset frequency. Phase diffusion constant can be determined by electrical domain measurement according to

$$D \approx \frac{k_B T}{P_s} \cdot \frac{\omega_0^2}{Q^2}, \tag{3-15}$$

where P_S is the power dissipated in the equivalent resistive element that contributes the same amount of electronic noise. As shown in Fig. 3.16, the theory predicts $1/f^2$ behavior and matches pretty well with the measured data. The ultimate phase noise performance set by the NEMS device's intrinsic thermomechanical noise is also shown in Fig. 3.16 (theoretical discussions and equations are addressed in Chapter 2). This limit could be achieved if the transduction and feedback electronics are ideally noise-matched to the NEMS device. The comparison of measured data and calculations suggests important guidelines for further optimization and engineering of the NEMS oscillators with improved phase noise performance. By approaching the thermomechanical noise floor of the NEMS resonators, it will become possible for NEMS oscillators to compete with or even win over the phase noise performance of conventional bulky crystal oscillators.

Fig. 3.17 shows the measured phase noise when the UHF NEMS device is driven at different levels to assume different vibrating amplitudes in the self-oscillating mode. Note in this set of measurements, we still keep the device operating well in the linear regime, which we assure by our careful calibrations as discussed in the previous sections.

The measured data demonstrates decreased phase noise as the NEMS resonator is driven to larger amplitudes within its mechanical dynamic range. Here a small increment is used in increasing the drive in order to make sure reliable phase noise measurement can be performed by the analyzer at all the levels in this range. Our observed phase noise dependence on resonator amplitude is more reasonable compared to that in another study reported in [34], because better phase noise performance should be expected with increasing power handled by the resonator.

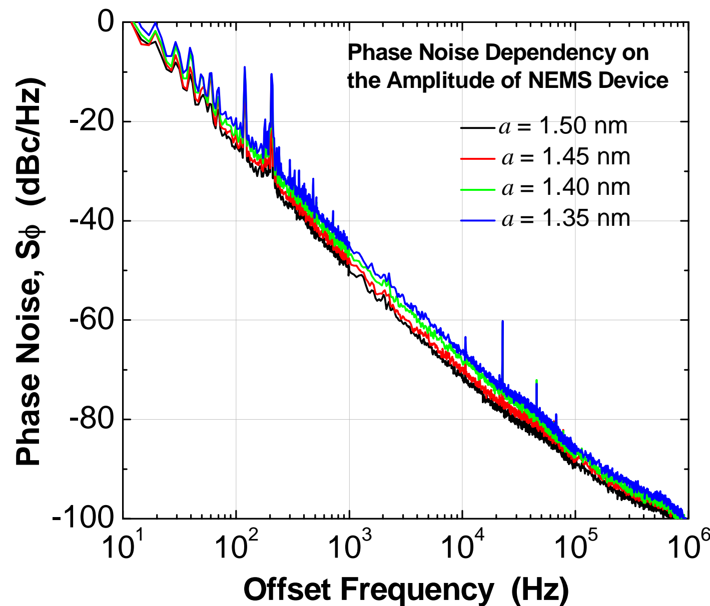

Fig. 3.17 Phase noise measured at different drive levels, showing that within the dynamic range of the NEMS device, the higher the drive, the lower the phase noise.

3.8 Frequency Stability and Mass Sensitivity

Time-domain frequency stability is another crucial specification and measured data are shown in Fig. 3.18. The NEMS oscillator's instantaneous output oscillating frequency is recorded with a high-precision counter in real time, with the raw data shown in Fig. 3.18 (a). The measurements have been performed at stabilized temperature, but under non-vibration-proof condition in a non-electrical-screening room. Fig. 3.18 (b)

demonstrates the Allan deviation as a function of averaging time [35] (see also Chapter 2 for discussions and equations about Allan deviation).

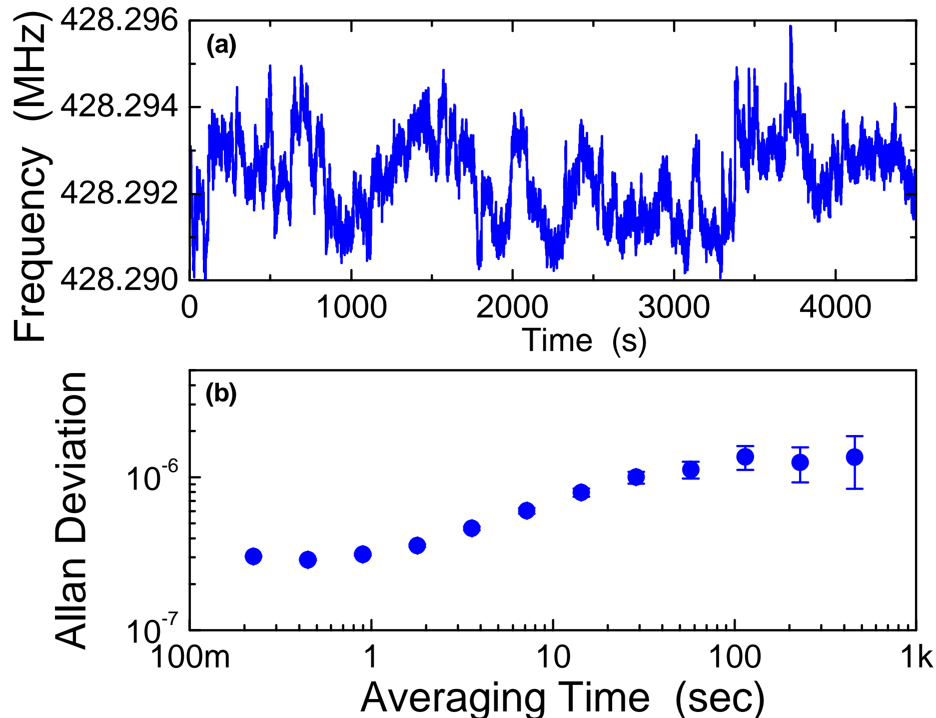

Fig. 3.18 NEMS oscillator frequency stability. **(a)** Instantaneous oscillating frequency of the NEMS oscillator output, measured by a precise counter in real time, for a time interval of longer than one hour. **(b)** Allan deviation of the NEMS oscillator, showing a typical behavior of a crystal oscillator, with a minimum of 3×10^{-7} for averaging time in the range of about 0.2−1sec. For 200msec to 1sec interval, the NEMS oscillator's fractional frequency fluctuation is ~0.3ppm. The data also show that the maximum observed frequency instability is just about 1ppm, even for intervals as long as 10 minutes to ~1 hour.

The measured Allan deviation versus averaging time shows similar characterizations with those of crystal oscillators and other time standards [25,36], with the optimized value of 3×10^{-7} (3ppm) at ~0.2−1sec averaging time. This level of frequency stability directly translates into a real-time mass sensitivity of ~50zg, given the UHF NEMS device's ultra-small mass (57.8fg) and ultra-high mass responsivity (3.7Hz/zg) [31,32]. Compared to the alternative scheme for real-time mass sensing by incorporating VHF/UHF NEMS resonators into low-noise PLLs [32,37], the NEMS oscillator provides

much wider band operations (~0.2MHz) and does not need an external more stable active oscillator to drive the passive NEMS resonator device, while completely allowing self-oscillating and self-sensing. This uniqueness is even more remarkable for arrays of NEMS sensors, where arrays of engineered NEMS oscillators work as independent sensors and their self-sensing signals, each from an individual oscillator's RF output, can be retrieved, recorded and processed in parallel at the same time. This indicates a great advantage over the cantilever static deflection measurements with optical techniques [38,39] for arrays of sensors where the real-time dynamic response from sensors could not be detected concurrently.

3.9 Advanced NEMS Oscillators and NEMS Oscillator Arrays

The above realization and characterization of the first self-sustaining NEMS oscillator at UHF immediately makes it possible for future exploration and engineering of more advanced NEMS oscillators such as coupled oscillators, and voltage-controlled oscillators (VCOs). It also stimulates the designs of novel oscillators based on arrays of coupled NEMS resonators and active NEMS oscillator arrays that may be interesting for multiplexing sensing and multi-channel information/signal processing.

Fig. 3.19 (a) demonstrates the designs of two self-sustaining NEMS oscillators with their frequency determining NEMS resonators coupled by certain mechanisms. The coupling between two similar oscillators here is *non-mechanical*; but can be electrostatic, or magnetic (spin-coupled). The coupling can then introduce interesting frequency tuning and pulling effects and that the synchronization between the two active oscillators can be tuned and realized, which is very important and interesting for signal generation, processing and pattern forming applications.

Moreover, by introducing frequency tuning via DC voltage coupling to either of the NEMS resonators as shown in Fig. 3.19 (b), voltage-controlled oscillator can be realized.

Meantime, the NEMS VCO functionality can be further enhanced by synchronization with another NEMS oscillator or NEMS VCO through coupling between the NEMS resonators.

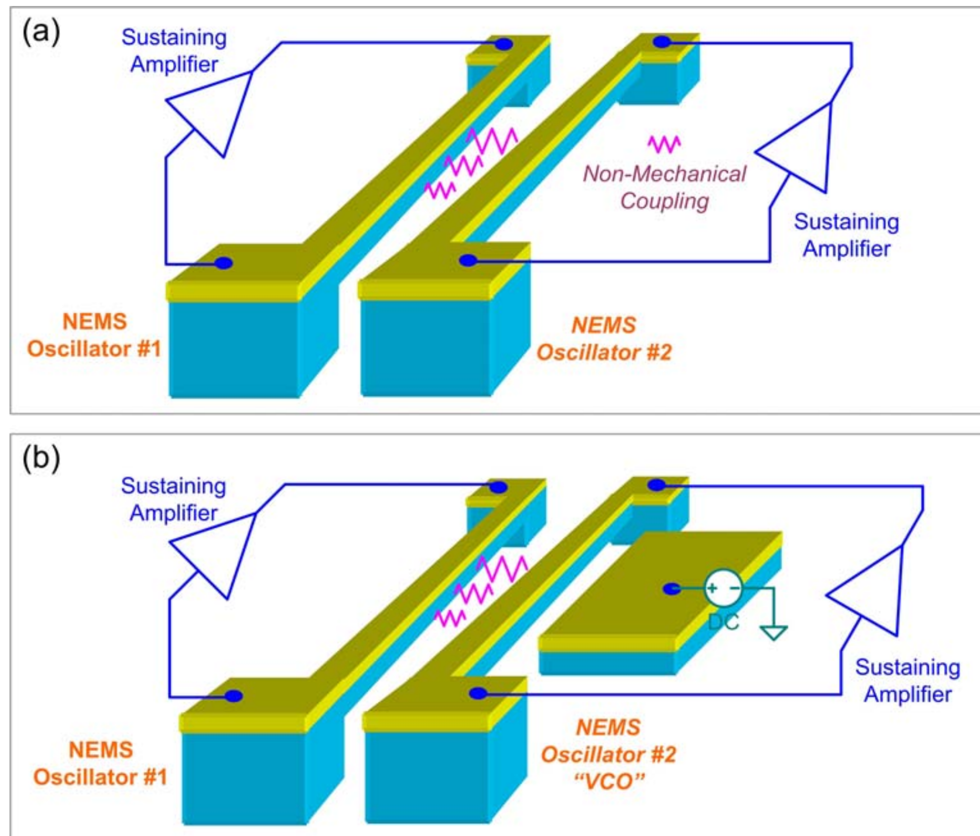

Fig. 3.19 Schematic and design of advanced NEMS oscillators. **(a)** Coupled oscillators with non-mechanical coupling, and **(b)** voltage-controlled oscillators (VCOs) based on NEMS resonators and coupled NEMS resonators.

Fig. 3.20 (a) shows the design of self-sustaining oscillator based on an array of *mechanically*-coupled NEMS resonators. Mechanically-coupled arrays possess much larger signal strength and power handling capability, as compared to single resonator device. The better power handling and lower phase noise performance of such NEMS oscillators with arrayed resonators are interesting for future nanomechanical signal processing and communication applications.

The schematic shown in Fig. 3.20 (b) demonstrates a new paradigm of multiplexing signal/information processing based on an array of self-sustaining NEMS oscillators. Each of the NEMS oscillators in the array is based on a NEMS resonator integrated with its tuned feedback circuit. As arrays of vibrating NEMS resonator devices are being batch-fabricated with growing yield, this technology would be of critical importance for *real-time*, multi-channel sensing and parallel signal detection technologies based on large arrays of NEMS devices.

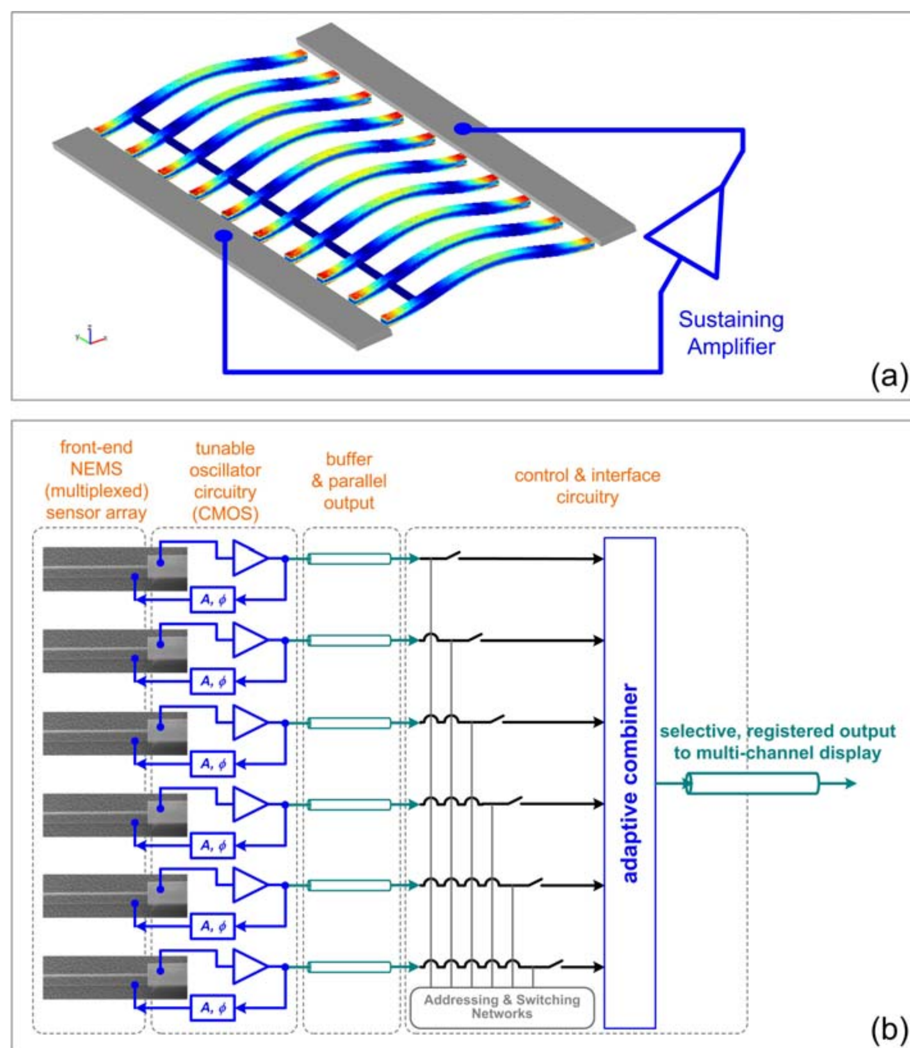

Fig. 3.20 Schematic and design of active NEMS oscillators with arrays of NEMS resonators. **(a)** NEMS oscillator based on arrays of coupled NEMS resonators. **(b)** NEMS oscillator arrays for multiplexing signal/information processing based on arrays of NEMS resonators and their sustaining feedback back loops, and the multiplexing control and interface circuits.

3.10 Chapter Summary

The work presented in this chapter is the first demonstration of a self-sustaining oscillator with low-noise performance and high frequency stability by using a vibrating UHF nanomechanical device as the frequency-determining element. The operating frequency (well in the UHF range) is much higher than both ordinary quartz crystal units (including those with overtones) and recently reported oscillators based on vibrating MEMS resonators. This has been possible because of not only the low-loss resonator device, but also the unprecedented large signal readout from UHF NEMS resonators by greatly enhancing the *RSBR*. We believe this is an important milestone for engineering rudimentary nanoscale devices into functional systems with considerable complexities and performance. Apparently, this is a further step on the way to the unceasing miniaturization of crystal oscillators; and immediately this technology provides a promising protocol for real-time high-precision nanomechanical resonant mass sensing, with both individual and arrays of nanodevices.

The self-oscillating NEMS systems would also be useful tools for the development of new measurement paradigms for detecting nanomechanical resonators coupled to single-quanta effects [40,41], to register single-molecule, single-spin and single-photon coupling events. The NEMS oscillator technology also makes it possible to realize self-oscillating systems based on ultrahigh-Q nanophotonic resonators, considering radiation-pressure driven mechanical resonators [42] and other possible optical-mechanical coupling effects. The UHF NEMS resonator operates at RF power in the picowatt to nanowatt range, suggesting possibilities for ultra-high-density integration of arrayed sensory and signal processing systems, with modern integrated circuit technologies [43].

Demonstration of the NEMS oscillator clearly shows that UHF nanomechanical resonators can be embedded into feedback control circuitry to realize complex

system-level functions and performance that are critical for future practical applications of nanodevices. The NEMS oscillator specifications and performance make it very attractive for ultra-sensitive transducers in a self-oscillating and self-sensing mode, with particular advantage for arrays of sensors, and also for novel measurement schemes for probing fundamental physical and biological phenomena.

For further exploration and engineering, advanced NEMS oscillators such as coupled and synchronized NEMS oscillators, voltage-controlled NEMS oscillators have been proposed and considered to be interesting. NEMS oscillators based on coupled arrays of NEMS resonators may be expected to have better power handling and phase noise performance. Active NEMS oscillator arrays where each oscillator has its own feedback control would be an important technology for real-time multiplexing NEMS sensing.

Bibliography

[1] *e.g.* S.M. Reppert, D.R. Weaver, "Coordination of circadian timing in mammals" (Review Article), *Nature* **418**, 935-941 (2002).

[2] *e.g.* E. Celik, D. Rockwell, "Shear layer oscillation along a perforated surface: a self-excited large scale instability", *Phys. Fluids* **14**, 4444-4447 (2002).

[3] *e.g.* M.A. Andronow, "Poincaré limit cycles and the theory of self-sustaining oscillations", *Comptes rendus de l'Académie des Sciences* **189**, 559-561 (1929).

[4] A. Hajimiri, T.H. Lee, *The Design of Low Noise Oscillators*, Boston: Kluwer (1999).

[5] M.D. Ward, D.A. Buttry, "In situ interfacial mass detection with piezoelectric transducers", *Science* **249**, 1000-1007 (1990).

[6] S. Knappe, V. Shah, P.D.D. Schwindt, L. Hollberg, J. Kitching, L.A. Liew, J. Moreland, "A microfabricated atomic clock", *Appl. Phys. Lett.* **85**, 1460-1462 (2004).

[7] W.R. Hewlett, "Variable frequency oscillation generator", US Patent 2,268,872 (1942). [Patent Application July 11, 1939]

[8] D. Ham, A. Hajimiri, "Concepts and methods in optimization of integrated LC VCOs", *IEEE J. Solid-State Circuits* **36**, 896-909 (2001).

[9] R.J. Thompson, Jr., "The development of the quartz crystal oscillator industry of world war II", *IEEE Trans. Ultrason. Ferroelect. & Freq. Cont.* **52**, 694-697 (2005).

[10] E.A. Gerber, R.A. Sykes, "State of the art—quartz crystal units and oscillators", *Proc. IEEE* **54**, 103-116 (1966).

[11] W.E. Newell, "Miniaturization of tuning forks", *Science* **161**, 1320-1326 (1968).

[12] C.T.C Nguyen, *Micromechanical Signal Processors*, Ph.D. Thesis (Advisor: Roger T. Howe), University of California, Berkeley (1994).

[13] C.T.C. Nguyen, R.T. Howe, "An integrated CMOS micromechanical resonator high-*Q* oscillator", *IEEE J. Solid-State Circuits* **34**, 440-455 (1999); *and* ——, "CMOS micromechanical resonator oscillator", *Tech. Digest of 1993 IEEE IEDM*, 199-202, Washington DC, Dec. 5-8 (1993).

[14] C.T.C. Nguyen, "Frequency selective MEMS for miniaturized low-power communication devices", *IEEE Trans. Microwave Theory & Techniques* **47**, 1486-1503 (1999).

[15] S. Lee, M.U. Demirci, C.T.C. Nguyen, "A 10-MHz micromechanical resonator Pierce reference oscillator for communications", *Tech. Digest of the 11th Int. Conf. on Solid-State Sensors & Actuators (Transducers'01)*, 1094-1097, Munich, Germany, June 10-14 (2001).

[16] T. Mattila, O. Jaakkola, J. Kiihamäki, J. Karttunen, T. Lamminmäki, P. Rantakari, A. Oja, H. Seppä, H. Kattelus, I. Tittonen, "14MHz micromechanical oscillator", *Sensors and Actuators A* **97-98**, 497-502 (2002).

[17] Y.W. Lin, S. Lee, S.S. Li, Y. Xie, Z.Y. Ren, C.T.C. Nguyen, "Series-resonant VHF micromechanical resonator reference oscillators" *IEEE J. Solid-State Circuits* **39**, 2477-2491 (2004); *and* ——, "60-MHz wine-glass micromechanical-disk reference oscillator", *Tech. Digest of 2004 IEEE Int. Solid-State Circuit Conf.*, 322-323, San Francisco, CA, Feb. 14-19 (2004); *and* Y.W. Lin, S. Lee, Z. Ren, C.T.C. Nguyen, "Series-resonant micromechanical resonator oscillator", *Tech. Digest of 2003 IEEE IEDM*, 961-964, Washington DC, Dec. 8-10 (2003).

[18] C.T.C. Nguyen, "Vibrating RF MEMS technology: fuel for an integrated micromechanical circuit revolution? (invited)", *Tech. Digest of the 13th Int. Conf. on Solid-State Sensors & Actuators (Transducers'05)*, 243-246, Seoul, Korea, June 5-9 (2005).

[19] X.M.H. Huang, C.A. Zorman, M. Mehregany, M.L. Roukes, "Nanodevice motion at microwave frequencies", *Nature* **421**, 496 (2003).

[20] X.M.H. Huang, X.L. Feng, C.A. Zorman, M. Mehregany, M.L. Roukes, "VHF, UHF and microwave frequency nanomechanical resonators" (invited article), *New J. Phys.* **7**, 247 (2005).

[21] A. Husain, J. Hone, H.W.Ch. Postma, X.M.H. Huang, T. Drake, M. Barbic, A. Scherer, M.L. Roukes, "Nanowire-based very-high-frequency electromechanical resonator", *Appl. Phys. Lett.* **83**, 1240-1242 (2003).

[22] X.L. Feng, R.R. He, P.D. Yang, M.L. Roukes, "High-performance silicon nanowire VHF/UHF nanomechanical resonators", *to be published* (2006).

[23] V. Sazonova, Y. Yaish, H. Ustunel, D. Roundy, T.A. Arias, P.L. McEuen, "A tunable carbon nanotube electromechanical oscillator", *Nature* **431**, 284-287 (2004).

[24] See *Sauerbrey equation* at www.en.wikipedia.org. [Original (in German): G. Sauerbrey, "Verwendung von schwingquarzen zur wägung dűnner schichten und zur mikrowägung" (translation: Use of vibrating quartz for thin film weighing and microweighing), Z. Physik A **155**, 206-222 (1959).]

[25] L.L. Lewis, "An introduction to frequency standards", *Proc. IEEE* **79**, 927-935 (1991).

[26] K.L. Ekinci, Y.T. Yang, X.M.H. Huang, M.L. Roukes, "Balanced electronic detection of displacement in nanoelectromechanical systems", *Appl. Phys. Lett.* **81**, 2253-2255 (2002).

[27] J. Wang, Z. Ren, C.T.C. Nguyen, "1.156-GHz self-aligned vibrating micromechanical disk resonator", *IEEE Trans. Ultrason. Ferroelect. & Freq. Cont.* **51**, 1607-1628 (2005).

[28] H.W.Ch. Postma, I. Kozinsky, A. Husain, M.L. Roukes, "Dynamic range of nanotube- and nanowire-based electromechanical systems", *Appl. Phys. Lett.* **86**, 223105 (2005).

[29] J.S. Aldridge, A.N. Cleland, "Noise-enabled precision measurements of a Duffing nanomechanical resonator", *Phys. Rev. Lett.* **94**, 156403 (2005).

[30] J.R. Vig, Y. Kim, "Noise in microelectromechanical system resonators", *IEEE Trans. Ultrason. Ferr. & Freq. Contr.* **46**, 1558-1565 (1999).

[31] K.L. Ekinci, Y.T. Yang, M.L. Roukes, "Ultimate limits to inertial mass sensing based upon nanoelectromechanical systems", *J. Appl. Phys.* **95**, 2682-2689 (2004).

[32] Y.T. Yang, C. Callegari, X.L. Feng, K.L. Ekinci, M.L. Roukes, "Zeptogram-scale nanomechanical mass sensing", *Nano Lett.* **6**, 583-586 (2006).

[33] D. Ham, A. Hajimiri, "Virtual damping and Einstein relation in oscillators", *IEEE J. Solid-State Circuits* **38**, 407-418 (2003).

[34] S. Lee, C.T.C. Nguyen, "Phase noise amplitude dependence in self-limiting wine-glass disk oscillators", *Tech. Digest of the 2004 Solid-State Sensors, Actuators & Microsystems Workshop (Hilton Head 2004)*, 33-36, Hilton Head Island, SC, June 6-10 (2004).

[35] D.W. Allan, "Time and frequency (time-domain) characterization, estimation, and prediction of precision clocks and oscillators", *IEEE Trans. Ultrason. Ferr. & Freq. Contr.* **UFFC-34**, 647-654 (1987).

[36] S.R. Stein, J.R. Vig, in *The Froelich-Kent Encyclopedia of Telecommunications*, Vol. **3** (Froehlich, F. E. and Kent, A. eds.), Marcel Dekker, inc., New York, pp. 445-500 (1992). *Or*, "*Frequency Standards for Communications*," as U.S. Army Laboratory Command Technical Report SLCET-TR-91-2 (Rev. 1), NTIS Accession No. AD-A243211 (October 1991).

[37] X.L. Feng, M.L. Roukes, *et al.*, "Frequency stability and phase noise in UHF NEMS resonators", *to be published* (2006).

[38] G.H. Wu, R.H. Datar, K.M. Hansen, T. Thundat, R.J. Cote, A. Majumdar, "Bioassay of prostate-specific antigen (PSA) using microcantilevers", *Nat. Biotech* **19**, 856-860 (2001).

[39] R. Mckendry, J.Y. Zhang, Y. Arntz, T. Strunz, M. Hegner, H.P. Lang, M.K. Baller, U. Certa, E. Meyer, H.J. Güntherodt, C. Gerber, "Multiple label-free biodetection and quantitative DNA-binding assays on a nanomechanical cantilever array", *Proc. Nat. Acad. Sci.* **99**, 9783-9788 (2002); *and* N. Backmann, C. Zahnd, F. Huber, A. Bietsch, A. Plückthun, H.P. Lang, H.J. Güntherodt, M. Hegner, C. Gerber, "A label-free immunosensor array using single-chain antibody fragments", *Proc. Nat. Acad. Sci.* **102**, 14587-14592 (2005).

[40] M.D. LaHaye, O. Buu, B. Camarota, K.C. Schwab, "Approaching the quantum limit of a nanomechanical resonator", *Science* **304**, 74-77 (2004).

[41] K.C. Schwab, M.L. Roukes, "Putting mechanics into quantum mechanics", *Physics Today* No. 7 (July), 36-42 (2005).

[42] H. Rokhsari, T.J. Kippenberg, T. Carmon, K.J. Vahala, "Radiation-pressure-driven micro-mechanical oscillator", *Opt. Exp.* **13**, 5293-5301 (2005).

[43] A. Hajimiri, H. Hashemi, A. Natarajan, X. Guan, A. Komijani, "Integrated phased array systems in silicon", *Proc IEEE* **93**, 1637-1655 (2005).

Chapter 4

Ultra-High Frequency NEMS Resonators with Low-Noise Phase-Locked Loops

Phase-locking and resonance frequency tracking technologies offer a generic solution for real-time sensing applications based on resonant mechanical devices. This Chapter presents the development of systems with UHF vibrating NEMS resonators embedded in low-noise phase-locked loops (PLLs), and the frequency stability and phase noise performance characterized by using this UHF NEMS-PLL technology. The study is carried out for generations of UHF NEMS resonators in the 200~500MHz range and thus creates roadmaps of characteristics and performances of UHF NEMS resonators. It is demonstrated that these UHF NEMS devices have excellent frequency stabilities that, if directly employed for resonant mass sensing, translate into unprecedented mass sensitivities well in the zeptogram (zg) range, approaching 1zg level with ~500MHz devices. Besides the NEMS resonant mass sensing paradigm, the NEMS-PLL technology is also a canonical method to measure the phase noise of NEMS resonators. The demonstrated excellent characteristics of these devices are approaching the projected specifications of the local oscillator (LO) required for the development of microfabricated chip-scale atomic clocks (CSAC).

4.1 Nanomechanical Mass Sensing Protocols

The mass sensing technologies employing resonant mechanical devices have had a moderately long history featuring the wide applications of quartz crystal microbalance (QCM) since the late 1950's [1,2]. Resonant mass sensing is based on the simple principle of a resonator's *mass loading effect*—due to the mass attached to the resonator body, the resonance frequency is shifted (as analyzed in Chapter 2); the frequency shift can be measured with high precision, which is a feat well established in physics, and thus the loaded mass is measured. MEMS and NEMS resonant sensors, working with the same principle, have become especially attractive because their smaller and smaller masses—enabled by the continuously shrunk devices—lead to more and more responsive devices and thus generally promise higher sensitivities. Naturally nanoscale resonators are interesting candidates to take resonant mass sensing into the regime where single-molecule events can possibly be probed. Ultimately, it is expected to achieve real-time single-molecule counting with single-Dalton resolution. This chapter describes some of our latest efforts and progress toward these goals. It is mainly on the technology of NEMS resonators with low-noise PLLs, which is a powerful alternative in parallel to the self-sustaining oscillator technology discussed in Chapter 3.

Recently, researchers have been racing for the records of pushing the practical limits of mass sensing with MEMS and NEMS devices. It has been reported that micron-scale MEMS cantilevers can achieve femtogram-scale ($1fg=10^{-15}g$) and attogram-scale ($1ag=10^{-18}g$) sensitivity [3-8], and resonance frequency changes induced by single cell and virus attached onto these devices have been measured [5-8]. However, these studies have usually been done in separate experiments in which a device's resonance frequency is first measured, and the device is then taken out of the measurement system (chamber) for a process involving the attachment of containments, and at last the device is reloaded and measured again to search for a difference in resonance frequency. It may be

possible that the measured minute frequency shift is due to the loading mass of the containments and thus demonstrating the device's mass sensitivity, but this paradigm is somehow awkward and cannot be directly implemented or easily implanted for sensing or detection in practice.

A valid *sensing* or *detection* protocol necessarily implies that when the events are occurring, the sensor or detector is working (sensing or detecting). So we have been making efforts to develop a generic protocol for *real-time* and *in situ nanomechanical mass sensing*—a protocol that would allow us to not only read out the resonance signals of the devices, but also to apply feedback and control over the signals so that we can monitor, lock, and track the resonance signals in real time while the mass loading events are taking place *in situ*. We believe this is crucial and probably the indispensable route towards future functional NEMS-based sensors and detectors for real applications. Further, according on the theoretical foundations in Chapter 2, we aim to push for the fundamental limits of mass sensing technologies within this protocol by utilizing high-performance NEMS.

There are two primary approaches for feedback control and real-time NEMS resonance locking and tracking. One is to apply positive feedback upon the NEMS resonance signal to realize a self-sustaining oscillator system (see Chapter 3); the other is to apply negative feedback and involves the use of phase-locking techniques. The phase-locking protocol requires a voltage-controlled oscillator (VCO), which should be much more stable and less noisy than the device under test (DUT)—the NEMS resonators in the present studies. It is more convenient and flexible to test, implement and engineer the phase-locking technology for passive resonator devices within a laboratory setting.

With the above goals and strategies, recently analyses have been done to address the influencing factors for the responsivities and frequency fluctuation resolutions of NEMS devices in real-time sensing measurements, and to discuss the ultimate limits of mass

sensitivity [9]. Experimentally, phase-locked loop schemes have been specifically devised for HF and VHF NEMS resonators, and real-time sensing experiments have been carried out with demonstrated attogram- to zeptogram-scale sensitivities [10,11]. These advances are exciting and encouraging us to continue pushing the limits of nanomechanical mass sensing. In this effort, we have designed and fabricated generations of NEMS resonators operating in the UHF regime, and performed extensive experiments with the engineered PLL systems incorporating the UHF devices.

4.2 Embedding NEMS Resonator into PLL

Phase-locking techniques, or specifically, phase-locked loop (PLL) systems have evolved to be very mature technologies since the early research dating back to the 1930's. They have been extremely useful in radios, communications, computers, instruments and many other electronic applications. There are many textbooks and monographs on PLL systems and their applications in various fields. References [12-15] provide excellent introductions to PLL systems and cover some of the most important modern topics and applications.

Despite the maturity of PLL techniques, it has been non-trivial to incorporate a NEMS resonance signal into a low-noise PLL to have the PLL lock onto and track the NEMS resonance in real time. This is primarily due to the specificities of the NEMS resonance signals, rather than the PLL principles and techniques. For HF NEMS resonators, a PLL based on the conventional simple *homodyne* detection scheme has been used [10]. For VHF devices, however, this scheme has become less effective due to the reduction in NEMS signal strength. We have then explored two routes to conquer this for the VHF resonators. One is using a mechanically-coupled two-port device to separate the drive and sensing elements so that the direct electrical feedthrough or cross-talk coupling from the drive port to the sensing port can be suppressed. In this case, the PLL is still based on the homodyne detection scheme and it works but it has been difficult to achieve

high-Q's and scale up the frequencies for the mechanically-coupled two-port devices with the available technologies. The other is introducing a frequency modulation phase-locked loop (FM-PLL) scheme but still using a one-port single doubly-clamped beam resonator. It has turned out that the FM-PLL scheme is working very well [11, 16]. In each of these demonstrations of HF and VHF NEMS devices with PLL, the NEMS resonance signal have been read out by the reflection measurement scheme with a single device.

For UHF NEMS devices, the resonance signals are better read out by using a bridge circuit (as discussed in Chapter 2 and Chapter 3), and the bridge detection circuit is incorporated in the whole PLL system [15]. This actually also provides an advantage that two resonances detected from the bridge circuit can both be embedded into the PLL, respectively, if needed, thus allowing us to characterize more devices.

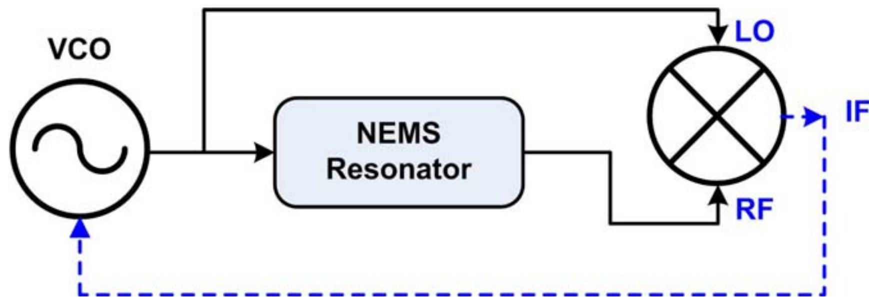

Fig. 4.1 Block diagram of NEMS resonance phase detection scheme—the core for implementing a PLL with NEMS resonator. Dashed line indicates feedback for closed-loop operation.

Fig. 4.1 shows the essential ingredients of the NEMS resonance phase detection scheme upon which the PLL is built. The signal from a stable VCO is split, "processed" by the NEMS and mixed with itself. In other words, the VCO drives the NEMS resonator, and the NEMS response signal is mixed against the initial VCO driving signal. Note in this schematic the NEMS resonance block includes the balanced-bridge resonance detection circuit. As the VCO driving frequency is swept through the resonance, the NEMS induces a large phase shift (ideally 90°) with respect to the original

driving signal. The mixing of the RF and LO signals yields a quasi-DC signal at the IF port. In the open-loop operation mode, the resulting IF signal can be monitored directly and its magnitude measures the difference between the VCO frequency and the NEMS resonance frequency. Naturally, since the IF has the correct form for an error signal, it can be fed back to the VCO (dashed line) to lock the VCO frequency to the NEMS resonance frequency—this is the closed-loop mode.

In practical operations, the open-loop mode is used mainly for testing and for the absolute stability of the NEMS in conditions of no thermal drift and no mass accretion. The closed-loop mode is particularly amenable to track thermal- and mass-induced frequency changes. In case there is no mass accretion but the NEMS is subject to thermal fluctuations and other random noise processes, the closed-loop mode can then be employed to measure the frequency fluctuation noise floor due to these mechanisms. It is very convenient to use a precise counter to record the frequency output of the VCO. This lays the foundation for its applications in real-time phase locking and resonance frequency tracking.

As shown in Fig. 4.1, if the phase detector is operated far from saturation (*i.e.*, as a mixer) we have the following signals at the mixer ports,

$$\begin{aligned} &\mathrm{LO}: A_{\mathrm{VCO}} \sin(\omega t) \\ &\mathrm{RF}: A_{\mathrm{NEMS}} \sin(\omega t + \varphi) \\ &\mathrm{IF}: -\frac{A_{\mathrm{VCO}} A_{\mathrm{NEMS}}}{2} \left[\cos\varphi - \cos(2\omega t + \varphi)\right] \end{aligned} \quad , \qquad (4\text{-}1)$$

where A demotes the amplitude of a signal as it arrives at the mixer, and ω is the frequency.

If a phase detector (mixer optimized to operate at saturated inputs) is used instead, the IF signal still has a DC component varying as $\cos\varphi$, but now it is independent of A_{NEMS} and A_{VCO}. In either case the DC component of the IF signal can be used as an error

signal to lock to the frequency at which φ =90°. When the PLL is locked to the resonance frequency, the average VCO output frequency equals the NEMS resonance frequency.

The simple analysis and explanation above based on Fig. 4.1 is just the first-order key concept of the NEMS resonance phase detection and resonance frequency tracking. A practical UHF NEMS-PLL system would appear like shown in Fig. 4.2 or involving even more components. As shown, after the mixer, the IF signal is usually amplified by a low-noise amplifier (LNA) and the also processed by a low-pass filter (LPF) or band-pass filter (BPF) before it is fed back to the VCO as the control-voltage 'error' signal. Particularly, in the FM-PLL scheme, the 'error' signal is 'carried' by the FM signal and thus a BPF with an appropriate frequency window is required.

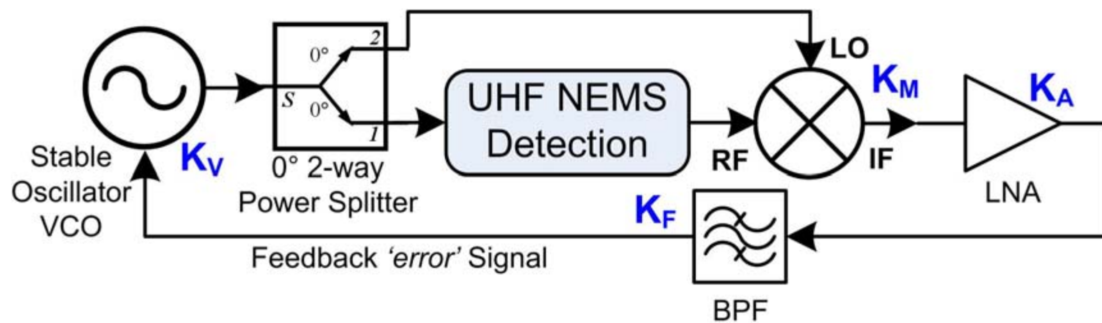

Fig. 4.2 UHF NEMS detection embedded into low-noise phase-locked loop for real-time precise locking and tracking of NEMS resonance frequency.

Shown in Fig. 4.3 is the balanced-bridge detection circuit used in this study. It corresponds to the 'UHF NEMS Detection' block in Fig. 4.2. This is an early improved version of the prototype bridge circuit [18], similar to the one used in [19] but with enhanced phase shift tuning and compensation, whereas still with lower resolution if compared to the best engineered bridge circuit for self-oscillation of UHF NEMS in Chapter 3. Nevertheless, the application of the FM-PLL scheme compensates this to some extent and the phase detection from the FM-PLL scheme has already attained fairly good signals from the UHF resonances read out by using the circuit shown in Fig. 4.3.

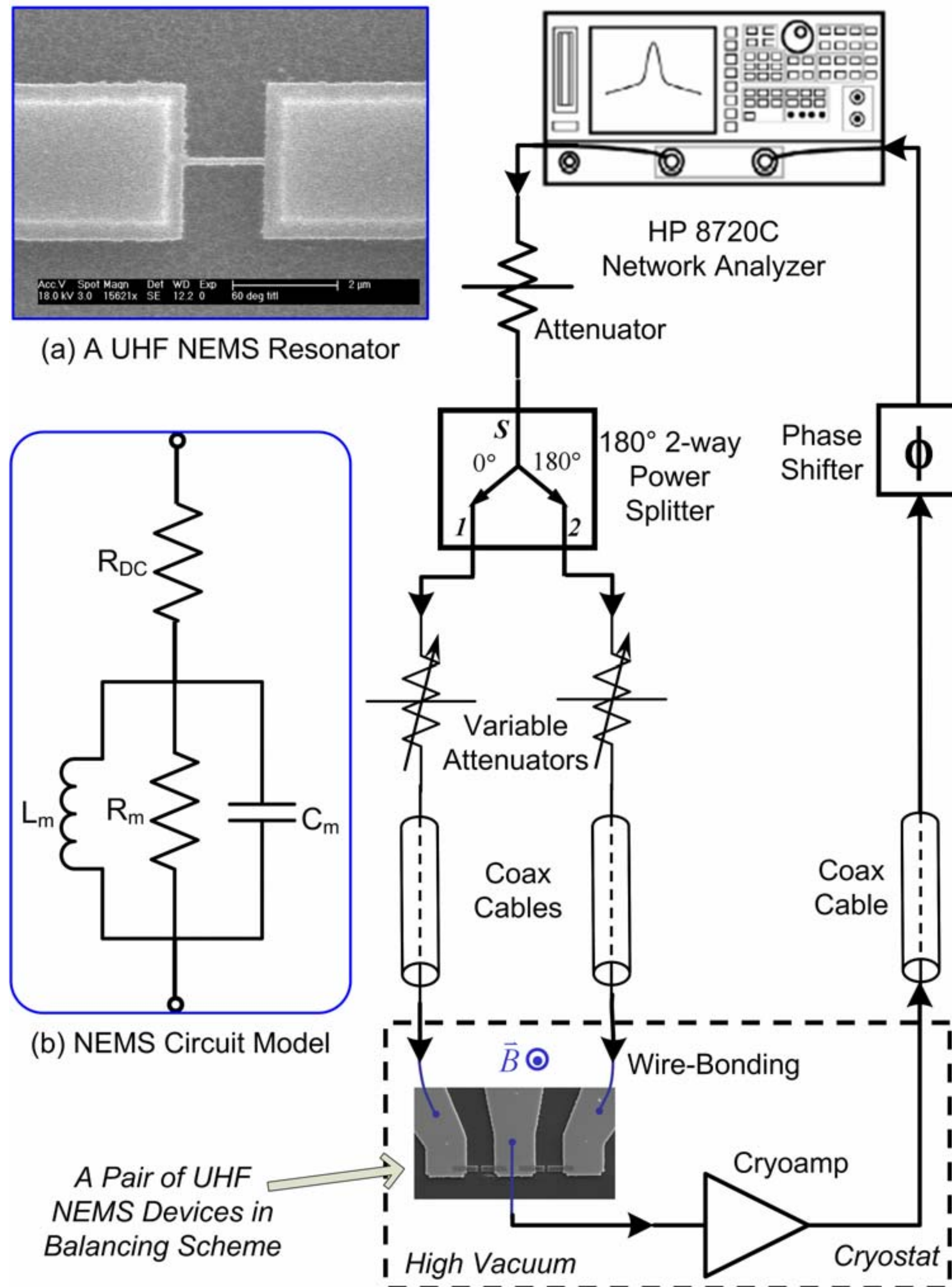

Fig. 4.3 Schematic of the electromechanical resonances readout scheme, with a balanced electronic detection circuit specifically modified and optimized for UHF NEMS. Inset **(a)**: SEM image of a typical UHF SiC NEMS (top view, the etched undercut indicating that device is freely suspended). Inset **(b)**: the parallel LRC tank circuit model for a magnetomotively-transduced NEMS. The total impedance of the device includes the DC impedance R_{DC} and the electromechanical impedance $Z_m(=R_m//(1/j\omega C_m)//j\omega L_m)$.

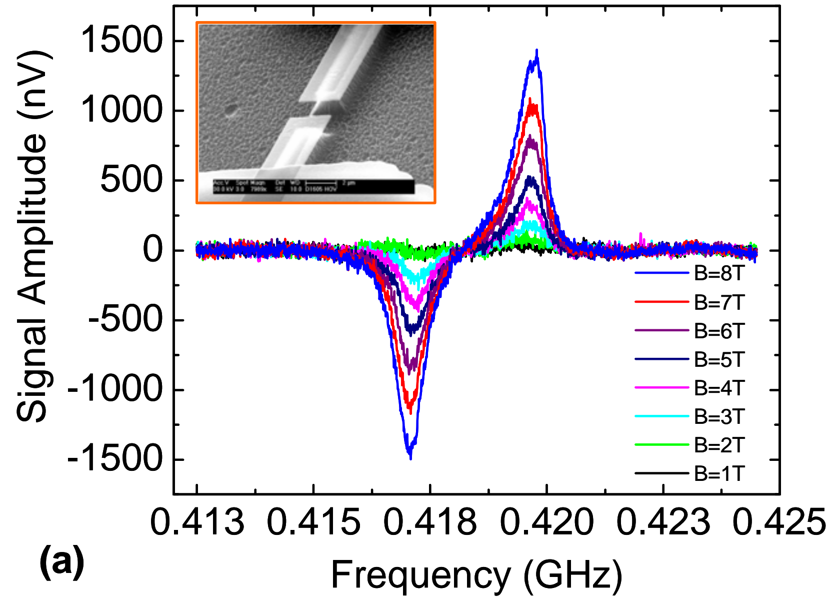

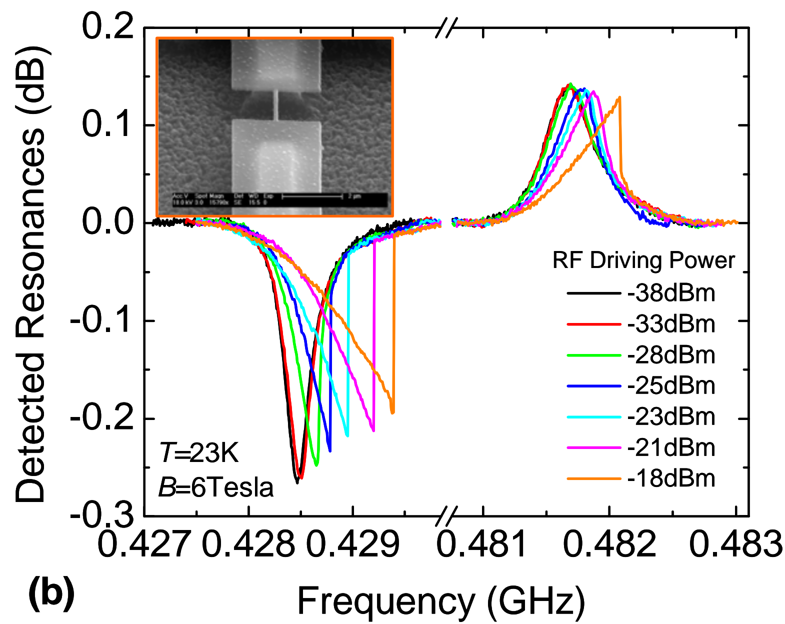

Fig. 4.4 Detected electromechanical resonances of pairs of UHF NEMS resonators from the bridge scheme. **(a)** Resonances at 417.2MHz and 419.9MHz, respectively, both having $Q\approx1200$. The plotted signal is referred to the input of the preamplifier. **Inset**: An SEM image of this ~420MHz NEMS resonator, with measured dimensions of $L\approx1.8\mu m$, $w\approx150nm$ and $t\approx100nm$. **(b)** Resonances at 428MHz ($Q\approx2500$) and 482MHz ($Q\approx2000$), respectively. Shown are the resonance curves as the driving RF power is increased. **Inset**: SEM image showing a typical suspended UHF NEMS resonator device.

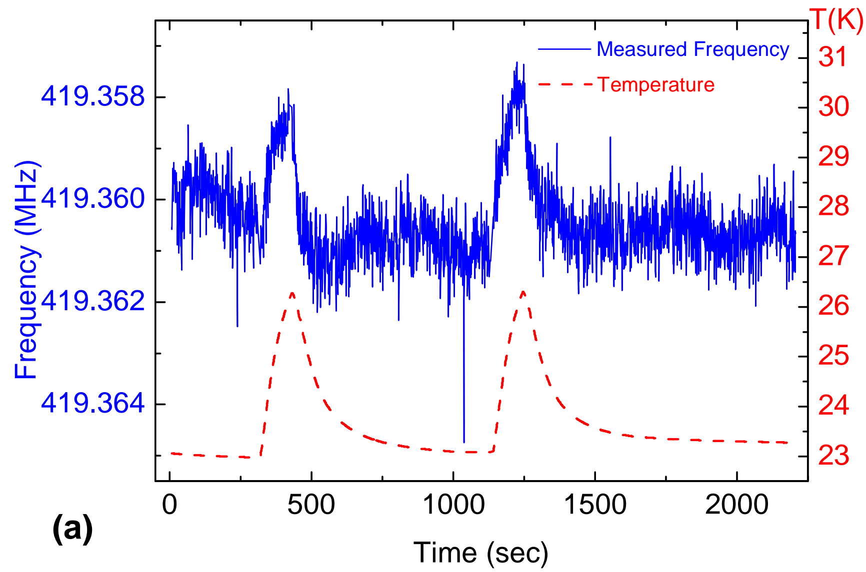

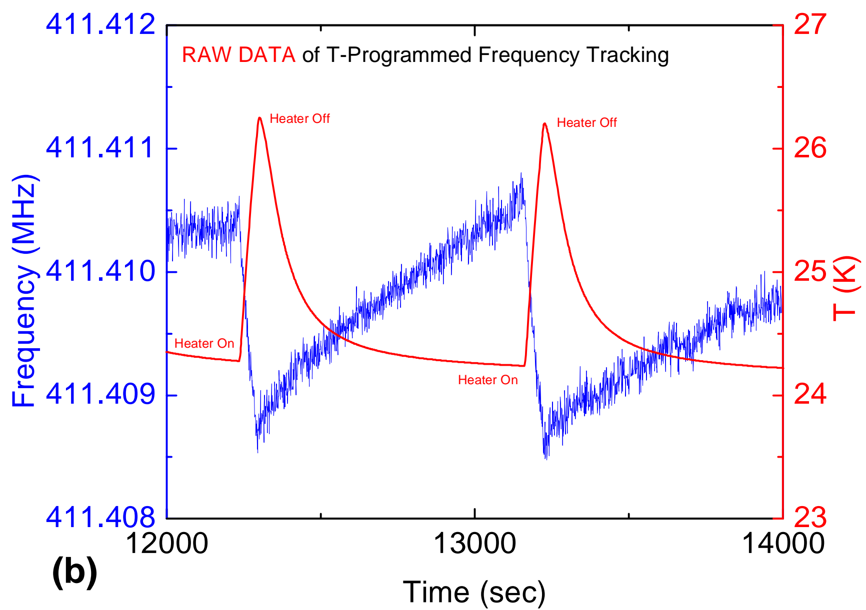

Fig. 4.5 Demonstration of temperature-programmed resonance frequency shifting and real-time frequency locking and tracking for UHF NEMS, **(a)** for the 420MHz device and **(b)** for the 411MHz device.

The plots in Fig. 4.4 demonstrate some typical resonance data detected from several selected UHF NEMS devices by using the bridge detection scheme shown in Fig. 4.3. In Fig. 4.4 (a), the resonances are from a pair of devices both very close to 420MHz and with measured Q~1200. The resonances have shown amplitude dependency on the magnetic field B when the RF driving power is fixed. The shown data have been calibrated and converted into a voltage signal that is referred to the preamplifier, indicating that the level of the signal amplitude is roughly in the 10nVolt to 1μVolt range.

In Fig. 4.4 (b), the resonances are at 428MHz and 482MHz and with $Q\approx2500$ and $Q\approx2000$ respectively. In this set of data, the magnetic field is fixed at B=6T, and the RF driving power is swept and it can be clearly seen that both resonators are approaching their nonlinear regime with increasing RF drive. It is also observed that the 482MHz device has a substantially higher onset of nonlinearity than the 428MHz device does, which confirms the scaling of the device dynamic range with its dimensions [20]. Intuitively, the 482MHz device is short than the 428MHz (with same width and thickness) and thus is stiffer, therefore implying a high onset of nonlinearity. Note in each of the plots in Fig. 4.4, after the background response is subtracted, the resonances in a pair are exactly out-of-phase, as expected according to the nature of the bridge circuit. Also note that here in this un-optimized balancing and nulling, the obtained *RSBR* (in dB) is much lower than that attainable by the high-resolution bridge in making the NEMS oscillator.

Once the UHF NEMS resonance is detected by using the network analyzer, then the detecting circuit can be incorporated in the PLL system. The network analyzer is replaced by the VCO to drive device at the device resonance frequency. As illustrated in Fig. 4.1 and Fig. 4.2, usually one can perform open-loop testing to optimize loop parameters and then move on to closed-loop mode. Once the closed-loop is locked, the

VCO starts to track the resonance frequency. An interesting, simple but convincing experiment we usually do is to have PLL track the temperature-programmed resonance frequency shifting. As we alter the device temperature, the resonance frequency shifts (for our SiC devices, the resonance frequency temperature coefficient is negative), and the PLL tracks this change and follows the temperature change very well, as shown in Fig. 4.5. This real-time tracking of frequency shifting steps, translated from heating pulses, is essentially similar to the PLL tracking the frequency shifting steps caused by added mass pulses (*e.g.*, shutter gated mass loading effect as illustrated in [10, 11]).

4.3 Frequency Stability of UHF NEMS Resonators in PLL

In the present study, we focus on examining the noise floor or the sensitivity of generations of UHF NEMS devices. We do not perform mass accretion experiments for each particular device. Instead, we embed each detected UHF NEMS resonance into the PLL to study the frequency stability at the conditions where the temperature is stabilized and there is no mass loading. So the sources for the frequency instability are either intrinsic noise processes in the UHF NEMS device itself, or thermal fluctuations of the environment and the electrical interfaces to the device.

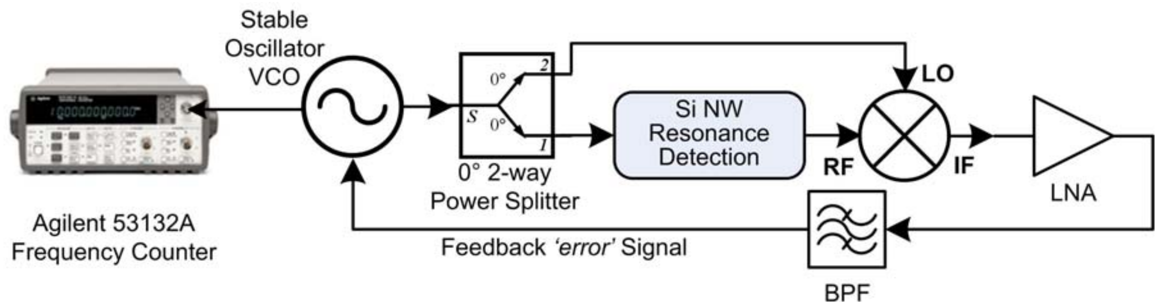

Fig. 4.6 Scheme and setup for measuring the NEMS resonator frequency stability with the NEMS-PLL system.

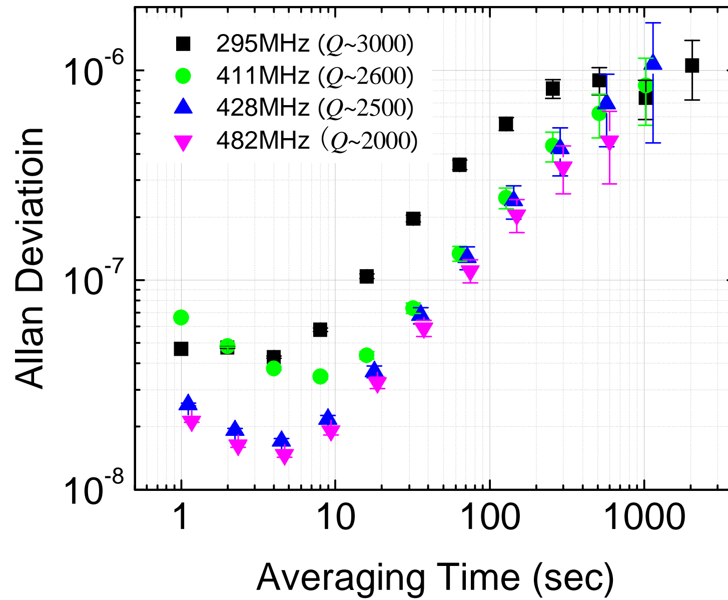

Fig. 4.7 Measured Allan deviation as a function of averaging time for a family of UHF NEMS resonators.

In the UHF NEMS-PLL system, the frequency stability is measured with the scheme shown in Fig. 4.6, by using a counter to record the instantaneous output driving frequency of the VCO. This is different from the frequency stability measurement in the self-oscillating system where one only needs to record and analyze the oscillator output frequency. As shown in Fig. 4.6, a precise universal counter (Agilent 53132A) is used to carry out this time-domain measurement, and the frequency stability is evaluated by the statistics of the measurement ensemble. As discussed in Chapter 2 and 3, with this we measure the Allan deviation [21,22], the widely used criterion for frequency stability. For a finite measurement ensemble with N samples, the Allan deviation is

$$\sigma \cong \frac{1}{\sqrt{2}}\left[\frac{1}{(N-1)}\sum_{i=1}^{N}\left(\frac{\bar{f}_{i+1}-\bar{f}_i}{f_0}\right)^2\right]^{\frac{1}{2}}, \tag{4-2}$$

where f_0 is the resonance frequency, and $\bar{f}_i$ is the measured (averaged) frequency in the ith time interval. As plotted in Fig. 4.7, the measured Allan deviation as a function of averaging time, for several UHF NEMS resonators, shows the characteristics of a typical crystal resonator, with a similar tendency as that of a quartz crystal resonator. The data show that the short-term frequency stability of the NEMS resonators is optimized to be in the 10^{-8} to 10^{-7} range, with minimum Allan deviation values at about $\tau \approx 5$sec averaging time for all these resonators.

4.4 Phase Noise of UHF NEMS Resonators in PLL

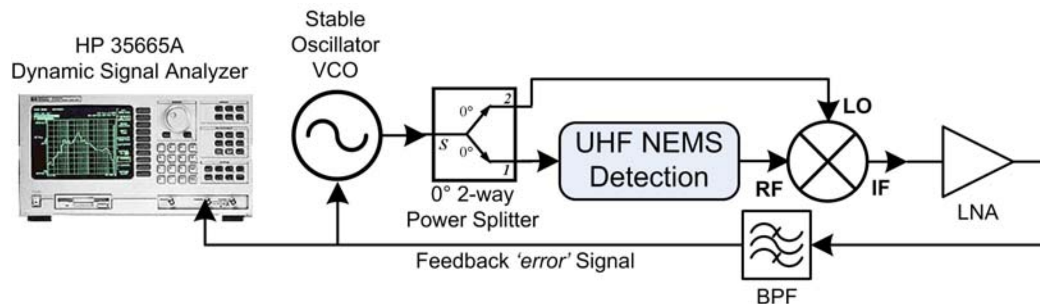

Fig. 4.8 Scheme and setup of measuring the phase noise of UHF NEMS resonators in the NEMS-PLL system.

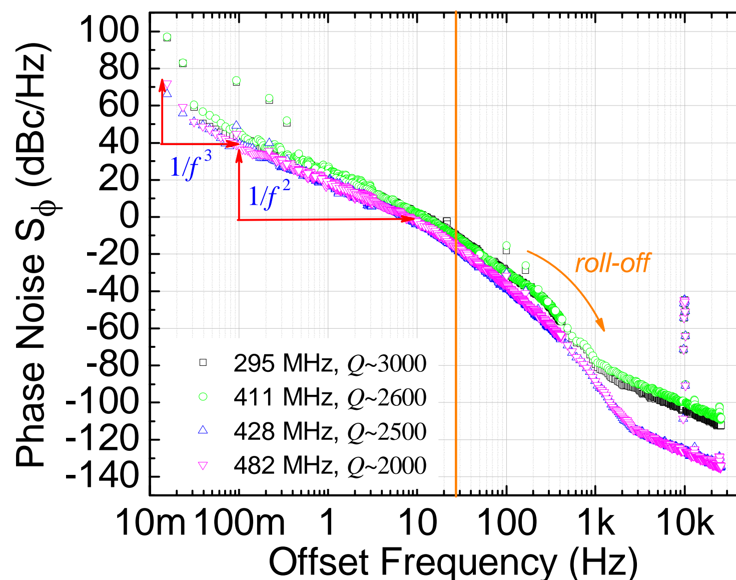

Fig. 4.9 Phase noise performance of generations of UHF NEMS resonators. Shown are the measured phase noise spectra versus offset frequency from the carrier.

In general, the phase noise performance of a resonator (crystal, MEMS or NEMS) can be characterized either in a self-oscillating mode, or by phase-locking a much more stable and lower-noise source to the resonance to perform phase detection to measure the noise spectrum. In the former oscillator mode, a special phase noise analyzer can be used to directly measure the phase noise spectrum (as the one presented in Chapter 3); in the latter PLL mode, a more commonly available (less expensive) noise spectrum analyzer can be used to measure the noise in the phase detection signal and with this the phase noise information can be retrieved.

In this study, the phase noise spectrum is measured using the scheme shown in Fig. 4.8 with the UHF NEMS-PLL system. The noise spectrum of the control voltage of the VCO, $S_V(\omega)$ is directly measured by a dynamic signal analyzer (HP 35665A), at the port where the error signal is fed back to the VCO as control voltage. Hence the frequency noise spectrum of the VCO output induced by the VCO input control voltage noise is

$$S_f(\omega) = K_V{}^2 S_{\mathrm{V}}(\omega), \tag{4-3}$$

where K_{V} [Hz/volt] is the gain of the VCO in the frequency modulation mode. Thus the equivalent phase noise spectrum is [22]

$$S_\phi(\omega) = \frac{1}{\omega^2} S_f(\omega), \tag{4-4}$$

where $\omega=2\pi f$ is the offset frequency in radius (with f in Hz). The measured phase noise as a function of offset frequency from the carrier is collected in Fig. 4.9 for several NEMS resonators. It is observed that in the range of 0.01Hz to 0.1Hz, the phase noise has $1/f^3$ behavior while in the range of 0.1Hz to 10Hz, it approximately follows $1/f^2$ for all this family of UHF NEMS resonators. The far-from-carrier roll-off (~25Hz) is

attributed to the measurement system time constant. Analyses show that the ultimate phase noise performance is limited by thermomechanical noise of the device itself; while here in the practical system, as there is a mismatch between the noise floor of the preamplifier and that of the NEMS device, the real phase noise is currently limited by the thermal noise of the preamp plus other noise processes in the measurement electronic system. If a specialized phase noise analyzer would be available to directly and carefully calibrate the phase noise performance of the NEMS-PLL system, it could be connected to the output of the VCO and this should yield the same results as obtained here.

4.5 Roadmaps of UHF NEMS Resonators and Performance

Based on the foregoing measurements and milestones achieved, we have been able to build roadmaps of the characteristics and performance of these generations of UHF NEMS devices. These roadmaps are very important and meaningful. They also have a lot of implications for the achievable scaling capabilities of UHF NEMS, and on the routes toward the ultimate goals of UHF-NEMS-based sensing and communication applications.

For the family of UHF NEMS devices operating in the range of 300~500MHz, all characterized in the PLL system with resonances read out by bridge scheme, their basic specs (device dimensions, mass, frequency, *Q*), achieved dynamic range (*DR*) and measured frequency stability performance (Allan deviation) are listed in Table 4-1.

We carefully examine the noise floor and onset of nonlinearity of each of these devices to estimate their ideal, intrinsic dynamic ranges. Since in these measurements the readout preamplifier noise is not matched to the intrinsic noise floor of the device, the practical dynamic range is compromised. Fig. 4.10 shows the scaling of both the intrinsic and achievable dynamic ranges of UHF devices we have made so far. In the analyses, some

of the UHF devices demonstrated in pushing the 1GHz operating frequency barrier are also included [23]. For these devices, the dimensions, resonance frequency and *Q*'s have been measured but their noise floor and dynamic ranges have not been examined. Table 4-2 presents the roadmaps of the noise floor and dynamic range for the UHF NEMS devices working in the range of 400MHz~1GHz.

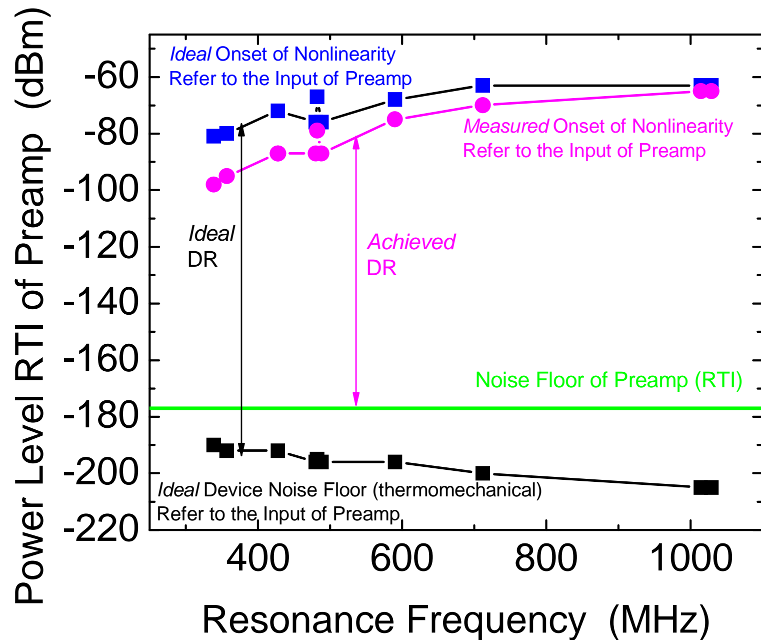

Fig. 4.10 Ideally intrinsic dynamic range and practically achievable dynamic range specifications of the UHF NEMS resonators.

As illustrated in Chapter 2, the power handling capability of a resonator device is another very important metric that is especially crucial for communication and signal processing applications. So we have also built an extended roadmap of the power handling for all the VHF/UHF/microwave NEMS resonator devices we have so far demonstrated, as shown in Table 4-3. For VHF NEMS resonators (with f_0 100MHz or so), typically we have the RF power sent to the devices in nanowatt (nW) range, about or over 90% of which is dissipated as *heat* on the DC resistance for the devices; the power goes to the mechanical resonance, thus the power handling of the NEMS resonator, is in

picowatt (pW) range (note that Q always plays a role in determining the exact numbers, as the Q trades off with power handling). As the rules of thumb, we have:

(i) For 10−100MHz VHF NEMS resonators, $P_{\text{drive,max}}$: 0.1−10nW range; and *power handling* P_C: 1−100pW range.

(ii) For 300MHz−1GHz UHF NEMS resonators, $P_{\text{drive,max}}$: 0.1−100μW range; and *power handling* P_C: 0.1−100nW range.

These typical numbers are confirmed by the typical total driving power level seen in our experiments, and the mechanical domain calculations and the estimations based on the circuit model are of the same orders of magnitudes.

Note all the calculations and analyses of the specifications and metrics of UHF NEMS are based on the theoretical foundations and formulae discussed in Chapter 2.

Table 4-1 UHF NEMS resonator devices specs and performance

Resonance Frequency (MHz)	NEMS Device Dimensions			Device Mass (fg, 10^{-15}g)	M_{eff} (fg)	Q	DR (dB)	σ_A (τ=1sec)	Mass Sensitivity (1zg=10^{-21}g)
	L (μm)	w (nm)	t (nm)						
295	2.65	180	80	160.2	118	~3000	80	4.7×10^{-8}	15 zg
420	1.8	150	100	111.1	82	~1200	90	3.1×10^{-7}	67 zg
411	1.7	120	80	72.3	53	~2600	85	6.6×10^{-8}	10 zg
428	1.65	120	80	75.5	54	~2500	90	2.5×10^{-8}	4 zg
482	1.55	120	80	70.9	52	~2000	98	2.1×10^{-8}	3 zg

Table 4-2 Dynamic range specs of UHF NEMS resonators

Resonance Frequency (MHz)	L (μm)	w (nm)	t (nm)	Device Mass (fg)	RF Q	Intrinsic Noise Floor Displacement (fm)	Intrinsic Noise Floor (Voltage, pV)	Intrinsic Noise Floor (dBm)	Intrinsic Dynamic Range (dB)	Achieved Dynamic Range in Measurements (dB)
428	1.65	120	80	75.5	2500	1.44	51.0	-192	120	90
482	1.55	120	80	70.9	2000	1.11	41.7	-197	128	98
339	1.6	140	80	71.3	3600	2.52	68.7	-190	109	N.A.
357	1.55	160	80	78.9	3000	2.02	56.2	-192	112	N.A.
480	1.32	140	80	61.3	1600	1.07	34.2	-196	120	N.A.
488	1.31	150	80	60.8	1600	1.05	33.8	-196	120	N.A.
590	1.6	140	80	71.2	1700	0.75	35.8	-196	132	N.A.
712	1.55	160	80	78.9	900	0.39	21.8	-200	137	N.A.
1014	1.11	120	80	44.2	500	0.23	13.0	-205	142	N.A.
1029	1.09	120	80	43.4	500	0.23	12.8	-205	142	N.A.

Thermal noise of preamp: -177dBm

Table 4-3 Power handling specs of 3C-SiC VHF/UHF NEMS resonators

Resonance Frequency (MHz)	L (μm)	w (nm)	t (nm)	Device Mass (fg)	Effective Mass M_{eff} (fg)	Measured Q	Critical Displacement (amplitude) a_C (nm)	Effective Stiffness k_{eff} (N/m)	Resonator Mechanical Energy at the Critical Amplitude (fJ)	Power Handling
124	2.5	200	80	177.2	130.2	1300	1.47	79.0	0.085	50.9 pW
133	2.35	150	80	124.9	91.8	5000	0.71	64.1	0.016	2.7 pW
190	2.35	150	100	145.0	106.6	5200	0.99	151.9	0.075	17.2 pW
199.6	3.1	180	100	229.5	168.7	7500	1.51	265.3	0.30	50.6 pW
240.5	1.8	150	100	111.1	81.6	1500	1.37	186.4	0.18	176.8 pW
295.4	2.66	170	80	160.2	117.8	3000	2.60	405.7	1.37	850.2 pW
420	1.8	150	100	111.1	81.6	1200	2.68	568.4	2.04	4.5 nW
395	1.75	120	80	74.4	54.7	2600	1.65	336.8	0.46	455.3 pW
411.4	1.7	120	80	72.3	53.1	2600	1.62	355.0	0.47	482.7 pW
428	1.65	120	80	75.5	55.5	2500	1.66	401.3	0.55	644.4 pW
482	1.55	120	80	70.9	52.1	2000	1.77	478.0	0.75	1.1 nW
339	1.6	140	80	71.3	52.4	3600	0.99	237.8	0.12	68.5 pW
357	1.55	160	80	78.9	58.0	3000	1.07	291.8	0.17	124.4 pW
480	1.32	140	80	61.3	45.1	1600	1.43	409.8	0.42	785.6 pW
488	1.31	150	80	60.8	44.7	1600	1.43	420.1	0.43	821.0 pW
590	1.6	140	80	71.2	52.3	1700	2.50	719.1	2.25	4.9 nW
712	1.55	160	80	78.9	58.0	900	3.89	1160.6	8.78	43.6 nW
1014	1.11	120	80	44.2	32.5	500	3.81	1318.7	9.58	122.0 nW
1029	1.09	120	80	43.4	31.9	500	3.73	1333.4	9.27	119.9 nW

Black: tested by the author (the work on the 124MHz, 133MHz, 190MHz in collaboration with Jack)

Blue: data from X.M.H. Huang's thesis work for resonance frequencies, dimensions and Q's.

The UHF NEMS resonators roadmaps are encouraging and stimulating. For example, as shown in Tables 4-1 and 4-2, for the close to 500MHz devices, we have experimentally achieved ~100dB dynamic range and the excellent frequency fluctuation noise floor (Allan deviation) leads to a mass sensitivity of 3zg. This manifests that probably the most intriguing promise of these UHF NEMS-PLL systems is that the measured frequency stability is translated into unprecedented mass sensitivity if the devices are used as inertial mass sensors, based on the analyses in [9]. For all the devices measured with the PLL scheme, the mass sensitivity values go deep into the zeptogram (10^{-21}g) scale. In fact, given 1zg≈0.6kDalton, the demonstrated mass sensitivity indicates that we have already had the capability of weighing biomolecules with mass in the 10-100kDalton ranges, and distinguishing some of them with fine enough resolution. Further, this suggests that single-molecule mass detection with single-Dalton sensitivity becomes possible and applicable with UHF NEMS.

It is also clearly verified by the roadmaps that frequency stability and thus the overall mass sensing performance relies on a combination of high frequency and high Q. Therefore, scaling up operating frequency and simultaneously retaining high Q remains a great challenge for NEMS mass sensor engineering. Besides, we note that to fully understand the origin and mechanism of the deteriorating long-term stability (long-term drifting) shown in Fig. 4.7, and to develop techniques for optimizing both short-term and long-term stability, study upon various possible drifting and aging effects in the system is needed. Realistically, long-term drifting mechanisms may be unavoidable as they persist in many other conventional time bases, but it would be still very valuable if the Allan deviation can be engineered so that the $\sigma_A \sim 1/\sqrt{\tau}$ and/or flat regions are wide enough to cover the averaging time range of interest. Or equivalently, the noise is thermal noise or $1/f$ noise limited and the knee point between $1/f$ noise and $1/f^2$ noise is really low at offset frequency, *i.e.*, really close to carrier.

4.6 From UHF NEMS to Local Oscillators for CSAC

It is interesting and enlightening to evaluate the performance of these UHF NEMS resonators in the context of frequency control, besides that of the mass sensing. In fact, considerable efforts with UHF NEMS resonators have been dedicated to strive for their best performances to meet the stringent requirements of local oscillators (LO) for microfabricated chip-scale atomic clocks (CSAC) [24], in which the physics cell can be based on, for examples, Cs (9.2GHz), Rb^{87} (6.8GHz), or Rb^{85} (3.0GHz). The LO frequency stability and phase noise performance requirements have been analyzed preliminarily by John Kitching [25]. Here we only highlight the comparisons between the performance of our UHF NEMS resonators and the CSAC LO requirements, as shown in Fig. 4.11 for frequency stability (Allan deviation) and Fig. 4.12 for phase noise, respectively. The phase noise measured from the UHF NEMS oscillator (as detailed in Chapter 3) is also included in Fig. 4.12 for comparison.

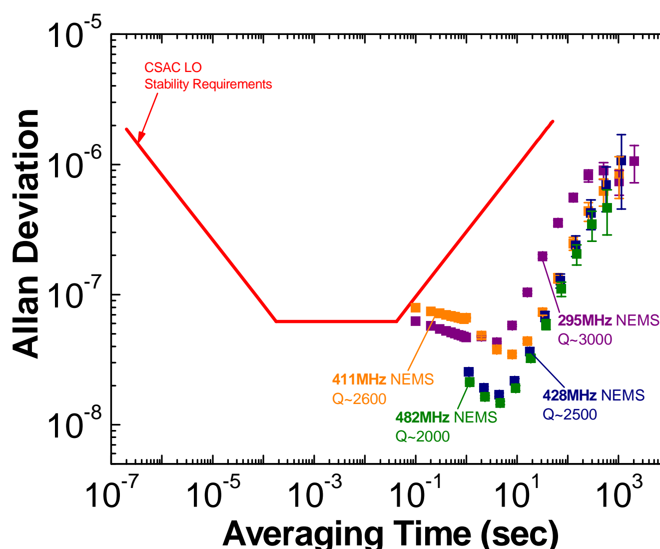

Fig. 4.11 Measured frequency stability of UHF NEMS resonators vis-à-vis LO requirements for Rb^{87} 6.8GHz CSAC.

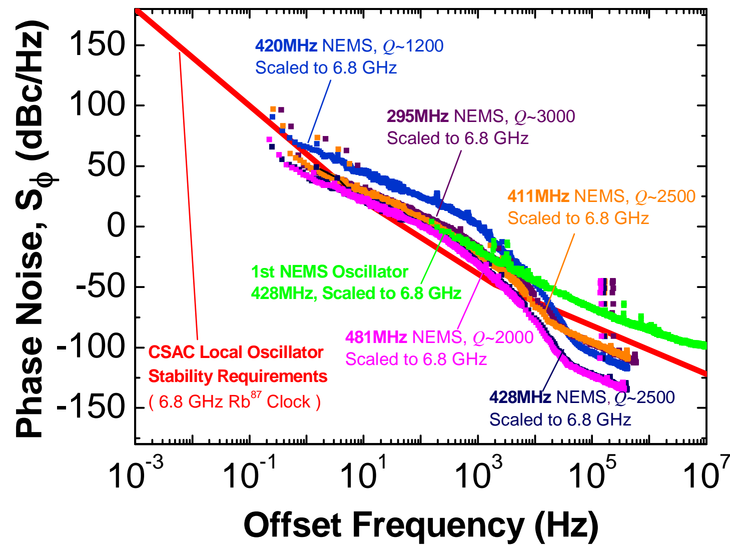

Fig. 4.12 Measured phase noise of UHF NEMS resonators and oscillator vis-à-vis LO requirements for Rb^{87} 6.8GHz CSAC.

It is shown that in the measurable regimes, the UHF NEMS resonators' performance meet or approach the CSAC LO requirements. We note that a linear scaling from ~300-500MHz to 6.8GHz is applied in the comparison. In reality, however, it is not guaranteed to achieve the same specifications as the frequency is scaled and converted by multiplication utilizing frequency synthesizers.

Moreover, by combining phase noise performance with power handling capabilities of these UHF NEMS resonators (as shown in Table 4-3), we have experienced stringent challenges in dealing with the trade-offs between power handling, *Q*, and operating frequency. In order to pursue microwatt (μW) power handling with UHF and high-*Q* resonators for high-profile low-noise LO applications, it seems better to abandon the beam-structures and explore with much stiffer geometries and modes. For ultrasensitive mass detection, beam-structured resonators are still preferred as they can achieve a better balance in providing both excellent responsivity and stability.

4.7 NEMS Resonator Arrays with Phase-Locked Loops

In practice of NEMS resonators for sensing applications, the scenario may be much more complicated than that in the lab settings for initial demonstrations. For physical and biological sensing with NEMS resonators, besides sensitivity, often selectivity and efficiency are also very important. For NEMS resonant mass sensing, the capturing efficiency can be very low due to the small areas of NEMS resonators. In general, one could alleviate this issue by pre-concentrating the species to be detected, or by focusing the incoming flux upon the responsive devices. On the other hand, implementation of arrays of NEMS devices can be a solution.

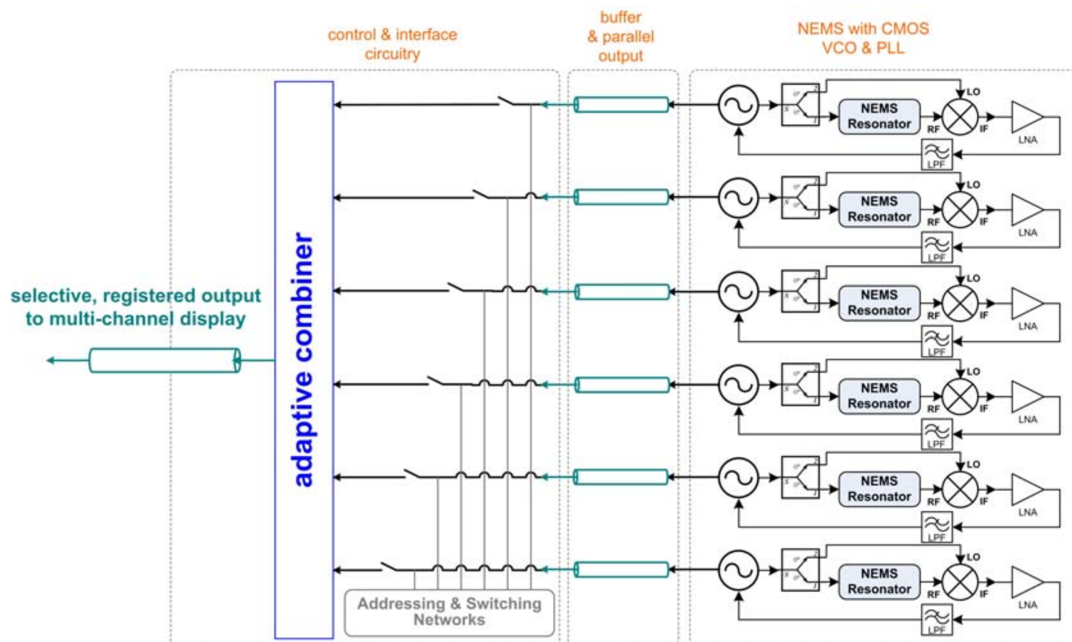

Fig. 4.13 Schematic and design of NEMS-PLL array for real-time multiplexing sensing.

Shown in Fig. 4.13 is the schematic illustration of a system of NEMS-PLL array. Here for each single device in the array of NEMS resonators, a PLL is needed to make it possible for the array to perform parallel, multiplexing sensing. Eventually this should be implemented by interfacing NEMS resonator arrays with integrated circuits on the same chip. This could be very challenging for NEMS engineering and the uniformity of

the NEMS devices and the components in the PLLs should be carefully addressed. Moreover, as compared to the NEMS oscillator arrays discussed in Chapter 3, here for each set of NEMS-PLL, a low-noise VCO, and frequency conversion element such as the mixer is required, which also draws special attention for the design of feedback and control circuitry.

4.8 Chapter Summary

In summary, in the study presented in this chapter, we have demonstrated generations of UHF SiC doubly-clamped NEMS resonators. The successful integration of a low-noise phase-locked loop with these resonators has been employed to directly characterize the frequency stability and phase noise performance of the NEMS. Roadmaps of Allan deviation and phase noise for 300~500MHz UHF NEMS are built. The measured frequency stability is translated into unprecedented mass sensitivity and the data show that ultrasensitive mass detection based on UHF NEMS resonators is intriguing and very promising for approaching single-Dalton sensitivity. The unique NEMS-PLL integration allows for real-time, low-noise detection of miniscule mass loading and fluctuation upon NEMS devices. The roadmaps imply that high-frequency and high-Q engineering is crucial for both sensitive detection and low phase noise, stable oscillator applications.

Bibliography

[1] D.A. Buttry, M.D. Ward, "Measurement of interfacial processes at electrode surfaces with the electrochemical quartz crystal microbalance", *Chem. Rev.* **92**, 1355-1379 (1992).

[2] C.K. O'Sullivan, G.G. Guilbault, "Commercial quartz crystal microbalances—theory and applications", *Biosensors & Bioelectronics* **14**, 663-670 (1999).

[3] N.V. Lavrik, P.G. Datskos, "Femtogram mass detection using photothermally actuated nanomechanical resonators", *Appl. Phys. Lett.* **82**, 2697-2699 (2003).

[4] B. Ilic, H.G. Craighead, S. Krylov, W. Senaratne, C. Ober, P. Neuzil, "Attogram detection using nanoelectromechanical oscillators", *J. Appl. Phys.* **95**, 3694-3703 (2004).

[5] B. Ilic, Y. Yang, H.G. Craighead, "Virus detection using nanoelectromechanical devices", *Appl. Phys. Lett.* **85**, 2604-2606 (2004).

[6] A. Gupta, D. Akin, R. Bashir, "Single virus particle mass detection using microresonators with nanoscale thickness", *Appl. Phys. Lett.* **84**, 1976-1978 (2004).

[7] A. Gupta, D. Akin, R. Bashir, "Detection of bacterial cells and antibodies using surface micromachined thin silicon cantilever resonators", *J. Vac. Sci. & Tech. B* **22**, 2785-2791 (2004).

[8] L. Johnson, A. Gupta, D. Akin, A. Ghafoor, R. Bashir, "Detection of vaccinia virus mass using micromechanical cantilever sensors", *Sensors & Actuators B* **115**, 189-197 (2006).

[9] K.L. Ekinci, Y.T. Yang, M.L. Roukes, "Ultimate limits to inertial mass sensing based upon nanoelectromechanical systems", *J. Appl. Phys.* **95**, 2682-2689 (2004).

[10] K.L. Ekinci, X.M.H. Huang, M.L. Roukes, "Ultrasensitive nanoelectromechanical mass detection", *Appl. Phys. Lett.* **84**, 4469-4471(2004).

[11] Y.T. Yang, C. Callegari, X.L. Feng, K.L. Ekinci, M.L. Roukes, "Zeptogram-scale nanomechanical sensing", *Nano Lett.* **6**, 583-586 (2006).

[12] F.M. Gardner, *Phaselock Techniques* (3rd ed.), Hoboken, NJ: John Wiley & Sons (2005).

[13] R.E. Best, *Phase-Locked Loops Design, Simulation and Applications* (5th ed.), New York: McGraw-Hill Co., Inc. (2003).

[14] W.C. Lindsey, M.K. Simon (eds.), *Phase-Locked Loops & Their Application*, New York: IEEE Press (1978).

[15] B. Razavi (ed.), *Monolithic Phase-Locked Loops and Clock Recovery Circuits: Theory and Design*, New York: IEEE Press (1996).

[16] C. Callegari, X.L. Feng, Y.T. Yang, M.L. Roukes, "Wide-range mass sensing with NEMS resonators: a frequency modulation locking scheme", *to be published* (2006).

[17] X.L. Feng, Y.T. Yang, C. Callegari, M.L. Roukes, "Ultra-high frequency nanomechanical resonator integrated with phase-locked loop", *Proc. ASME Nano2004-Integrated Nanosystems: Design, Synthesis & Applications*, Art. No. Nano2004-46037, Sept. 22-24, Pasadena, CA, USA (2004).

[18] K.L. Ekinci, Y.T. Yang, X.M.H. Huang, M.L. Roukes, "Balanced electronic detection of displacement in nanoelectromechanical systems", *Appl. Phys. Lett.* **81**, 2253-225 (2002).

[19] X.M.H. Huang, X.L. Feng, C.A. Zorman, M. Mehregany, M.L. Roukes, "VHF, UHF and microwave frequency nanomechanical resonators" (invited article), *New J. Phys.* **7**, Art. No. 247 (2005).

[20] H.W.C. Postma, I. Kozinsky, A. Husain, M.L. Roukes, "Dynamic range of nanotube- and nanowire-based electromechanical systems", *Appl. Phys. Lett.* **86**, Art. No. 223105 (2005).

[21] A.N. Cleland, M.L. Roukes, "Noise processes in nanomechanical resonators", *J. Appl. Phys.* **92**, 2758-2769 (2002).

[22] J.A. Barnes, A.R. Chi, L.S. Cutler, et al., "Characterization of frequency stability", *IEEE Trans. Instr. & Meas.* **IM-20**, 105-120 (1971).

[23] X.M.H. Huang, *Ultrahigh Frequency and Microwave Nanomechanical Systems*, Ph.D. Thesis (Advisor: M.L. Roukes), California Institute of Technology (2004).

[24] S. Knappe, V. Shah, P.D.D. Schwindt, L. Hollberg, J. Kitching, L.A. Liew, J. Moreland, "A microfabricated atomic clock", *Appl. Phys. Lett.* **85**, 1460-1462 (2004).

[25] J. Kitching, "Local oscillator requirements for chip-scale atomic clocks", *unpublished report for private communications*, Dated April 5 (2003).

Chapter 5

Dissipation in Ultra-High Frequency Single-Crystal SiC Nanomechanical Resonators

Dissipation is an important issue for virtually all mechanical resonant devices. Understanding and controlling dissipation in MEMS and NEMS resonators are very intriguing. It is of particular significance for high frequency NEMS resonators, and the higher the frequency the more acute the dissipation issue. This chapter is focused on experimental study of dissipation in ultra-high frequency (UHF) devices. The energy dissipation Q^{-1} (where Q is the quality factor) and resonance frequency characteristics of single-crystal 3C-SiC UHF nanomechanical resonators are measured, for a family of UHF resonators with resonance frequencies of 295MHz, 395MHz, 411MHz, 420MHz, 428MHz, and 482MHz. A temperature dependence of dissipation, $Q^{-1} \propto T^{0.3}$ has been identified in these 3C-SiC devices. Possible mechanisms that contribute to dissipation in typical doubly-clamped beam UHF resonators are analyzed. Device size and dimensional effects on the dissipation are also examined. Clamping losses are found to be particularly important in these UHF resonators. The temperature dependence of resonance frequency is also investigated, and an average frequency temperature coefficient of about −45ppm/K is found in T=20–100K range.

5.1 Energy Dissipation in Mechanical Resonators

As briefly introduced in Chapter 2, the quality factor (*Q*) of a mechanical resonator is a measure of the device's energy storage capability. Every realistic mechanical resonator dissipates energy and requires pumping in power to sustain its operation. High *Q*'s or small level of energy dissipation implies many important merits such as narrow resonance linewidth, low noise and high sensitivity (resolution). In fact, pursuing high or even ultra-high *Q*'s has a quite long history [1] and it is cliché to stress its importance.

From the application point of view, generally all high *Q* mechanical resonators can be used as sensitive probes for studying a variety of physical phenomena and systems. Representative examples of such applications include single-crystal silicon resonators with $Q \sim 10^4 – 10^8$ for measuring mechanical properties of physical systems [2], and quartz and sapphire resonators with $Q \sim 10^9$ for gravitational wave detections [1]. Both of these are truly macroscopic (typical dimension >1cm) or even bulky mechanical resonators. Besides sensing and probing, high-*Q* crystal resonators have also established their roles in the distinct application field of frequency control and standards, for their high stability and spectral purity, as addressed in Chapter 3. From the standpoint of fundamentals, understanding energy loss mechanisms on its own poses wealthy interesting problems, such as internal friction and thermoelastic effects in solids on which Zener's theory was developed as early as dated in 1930's [3].

The challenges and difficulties of pursuing ultra-high *Q*'s are due to the fact that there can be many energy loss processes that may be system dependent, and a lot of them are not well understood. This is especially true for various types of the emerging MEMS and NEMS resonators. Energy loss issues persist in such systems and sometimes the measured *Q*'s could not be quantitatively or even qualitatively explained by existing theories and models.

In principle, in experimental studies one can approach the problems by isolating *intrinsic* dissipation processes and *extrinsic* losses and damping effects and examining them separately with specific designs and controls, such as some early studies on thermoelastic internal friction [4] and gas damping [5] in micromachined Si resonators.

In theoretical aspects, however, heretofore there is not a comprehensive theory or general framework for predicting the *Q*'s and energy losses in MEMS and NEMS resonators with relatively large ranges of materials, dimensions and resonator types. Direct computer simulations of *Q*'s and dissipation processes are not routine yet, from atomistic (such as molecular dynamics and Monte Carlo methods) to continuous techniques (such as FEM); and the techniques we can employ in calculating *Q*'s are rather primitive. Fundamentally, with size scaling, MEMS and NEMS resonators become truly *mesoscopic* systems and they are excellent objects for probing the dissipation origins. In these systems, there may exist quite different energy loss mechanisms; or the same losses may become different in relative significance, as compared to the macroscopic cases. Currently, it is still far from having satisfactory knowledge and control of the dissipation processes in these systems, despite many observations and analyses reported in this field.

For *Q*'s of shrinking mechanical resonators, it is interesting to see that *Q* decreases as the device volume (V) is decreased from macroscopic to nanoscale (*e.g.*, linear dimension from about 0.1−10cm to about 100nm−1μm), with an approximate scaling relation of $Q \sim V^{1/3}$, as summarized in [6]. Since $V^{1/3}$ is of linear dimension scale, this implies an *intuition* that the *Q* is size dependent and deteriorates with increasing surface-to-volume ratio. Focusing on NEMS resonators, beyond this intuitive understanding, it is desired to gain more rational understandings—we need to understand what are the dominant and important dissipation origins and mechanisms, and among which what can be engineered and what are fundamental.

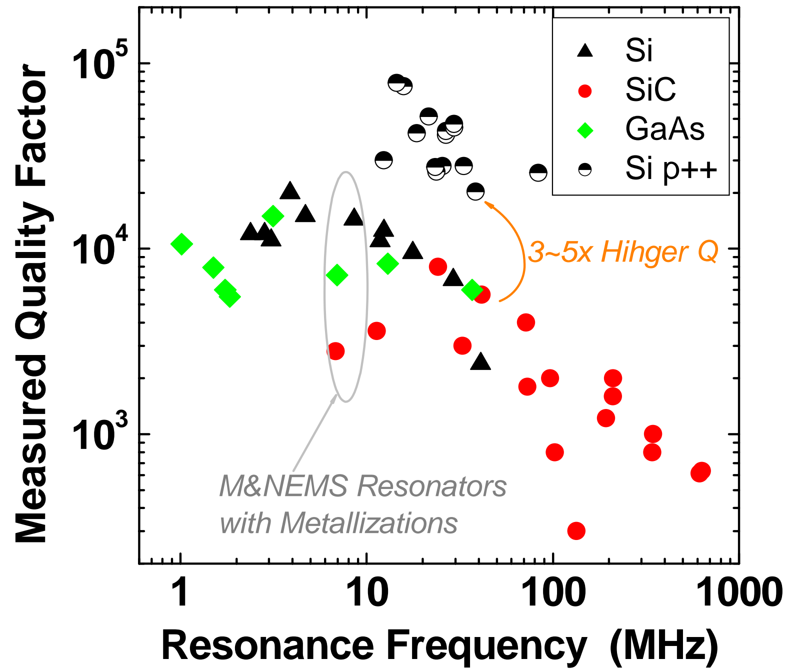

Fig. 5.1 Quality factor versus resonance frequency, the trade-off, for devices made of various materials. The materials used in making these HF/VHF/UHF devices include Si and SiC (both with metallization layers on the devices), GaAs and p++ Si [7,8].

5.2 The Issue of Dissipation in UHF NEMS

As discussed in the previous Chapters, high Q's are of central importance for high frequency NEMS resonators in their applications ranging from novel force and mass sensors [9-13], to nanomechanical signal processing [14] and fundamental quantum measurements [9,15,16]. In most of these applications, operating at high frequencies is indispensable for NEMS to win over conventional devices (*e.g.*, radio frequencies are required for signal processing, very-high or even ultra-high frequencies are required for ultra-sensitive mass detection and quantum measurements). Hence materials having large modulus-to-density ratio (E/ρ) such as SiC [8,17] and diamond [18] have been used, and smaller devices have been aggressively pursued with *top-down* lithographical nanofabrication, and *bottom-up* nanowire [19] and nanotube [20].

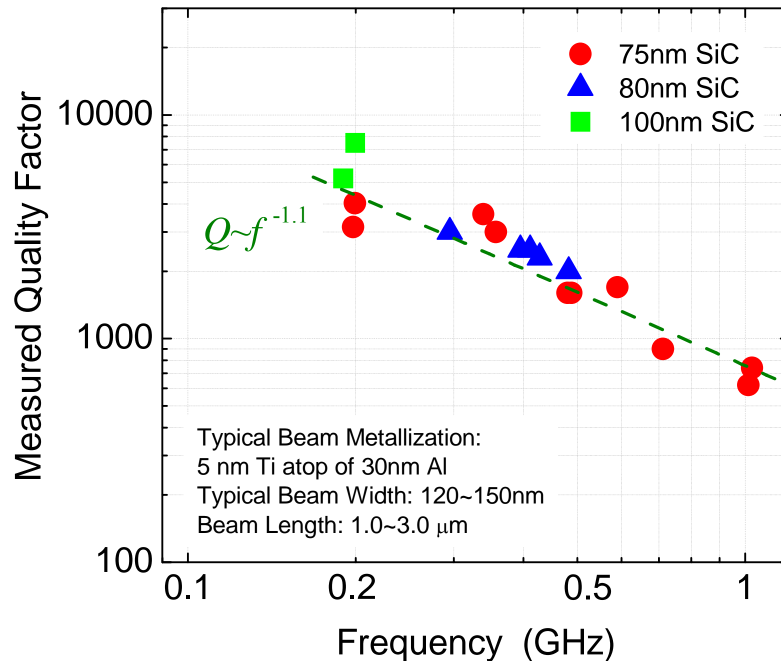

Fig. 5.2 Quality factor versus resonance frequency for VHF/UHF SiC NEMS resonators. The trade-off relationship is approximately $Q \sim f^{-1.1}$.

On the other hand, however, we have already found, one disadvantage of frequency scaling is that the device Q decreases as the resonant frequency increases (*i.e.*, as the device size has to be reduced to scale up the frequency) [7,8,21]—thus Q-engineering is crucial for retaining high Q while scaling up the frequency. As shown in Fig. 5.1 and Fig. 5.2, measured Q's from previous HF/VHF NEMS resonators, and more recent UHF ones, in various structural materials (*e.g.*, metallized Si and SiC, and heavily-doped Si and GaAs, etc.), all clearly demonstrate this trade-off of comprised Q's at higher frequencies for the same category of material and process.

For the recently most popular and attractive *bottom-up* material—nanotubes, however, rather low Q (only ~80) is attained in the only high frequency nanotube resonator realized so far (55MHz) [20]. Moreover, recent study has shown that nanotube resonators *inherently* suffer from lower Q's and multi-walled nanotube resonators have even larger dissipation because of their constitutive properties [22]—this will compromise the

potential applications of nanotube-based mechanical resonators; whereas with the latest breakthrough in growing large SiC crystals with ultra-high quality [23], SiC ascends towards probably the most promising and practical material for high-performance high-frequency NEMS thanks to its excellence in both electrical and mechanical properties. This chapter presents the investigations of dissipation in monocrystalline 3C-SiC UHF NEMS resonators.

5.3 Experimental Details

The monocrystalline 3C-SiC epitaxial layer is grown on monocrystalline silicon substrate by atmospheric pressure chemical vapor deposition (APCVD) [24], reinforced by newly developed surface roughness control and improvement techniques [25]. Doubly-clamped beam resonator devices are fabricated with a process specifically suitable for UHF SiC NEMS [8,17]. Shown in Fig. 5.3 are SEM images of a typical UHF 3C-SiC resonator. The doubly-clamped beam design simplifies understanding of device size and dimensional effects, and also minimizes the influence of complexities in, and variations from, the fabrication processes. Metallization consisting of 10nm titanium (Ti) atop a 30nm aluminum (Al) layer is deposited onto the SiC structural material. This enables patterning devices read out by magnetomotive excitation, and also detection [26] of the beam resonance from the in-plane flexural fundamental mode. The measured sheet resistance of the metallization film is 1.5Ω/□ at ~20K and 6.7Ω/□ at room temperature, with a proximately linear temperature dependency in this range. The device samples are secured in high vacuum (≤10^{-7}Torr) in a liquid He cryostat. The sample temperature is monitored by a thermometer, and controlled by a resistive heater, both mounted on the gold-plated sample stage. Feedback control of sample temperature is applied and for each measurement temperature fluctuation is limited to be within 1mK, to minimize the instantaneous resonant frequency variation due to the temperature fluctuation.

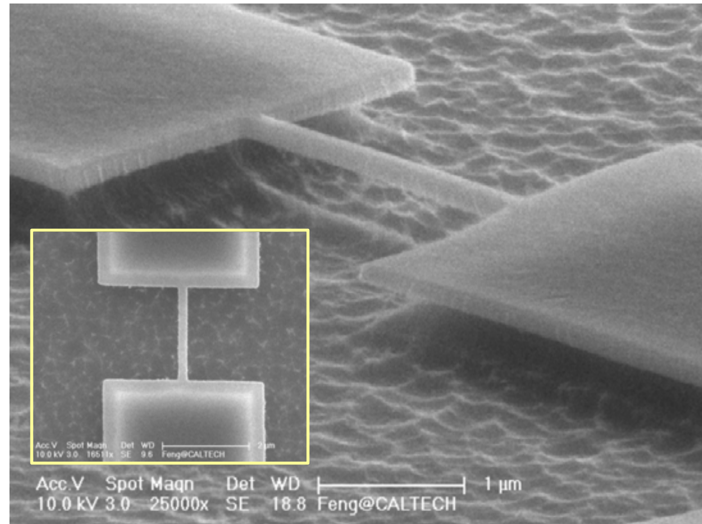

Fig. 5.3 Scanning electron micrographs of a typical single-crystal 3C-SiC UHF NEMS resonator. **Main**: Oblique view (scale bar: 1μm). **Inset**: Top view (scale bar: 2μm).

Network analysis techniques for two-port systems are used to detect the transduced magnetomotive effect from the NEMS devices and to measure the resonant frequencies and quality factors. Because the strength of the magnetomotive effect decreases as the frequency scales up and in the UHF band it is easily overwhelmed by the embedding and parasitic impedances of the system, it has been a challenge to attain large and clean resonance signals out of the electrical background. With our recently developed techniques of background suppression for UHF NEMS over wide frequency spans [27], now resonance signals with very large signal-to-background ratios (also known as "resonance on-to-off ratios", typically 5~10dB [27], as compared to previously typical values of ~0.1dB) are reliably attained and *thus quality factors can be accurately extracted from the resonance signals free from competing or even dominant response due to embedding and parasitic impedances*. Alternatively, albeit less convenient, quality factors can also be measured by a direct time-domain damped ring-down process of the resonators, which has been calibrated and verified to attain <5% discrepancy for extracted Q's as compared to those from fitting resonance curves in the network analysis

method [28]. In the present work, network analysis with elaborately minimized background response ensures better confidence for accurate extraction of Q's.

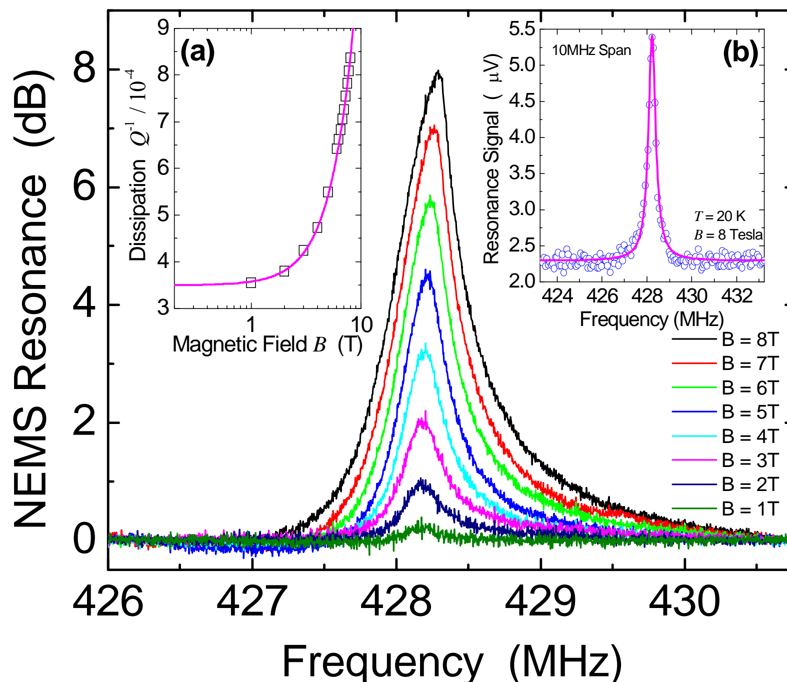

Fig. 5.4 Resonance signal of a 428MHz NEMS resonator, at various magnetic field conditions, as measured by a microwave network analyzer, utilizing detailed balancing and nulling techniques with a bridge circuitry scheme. **Inset (a)**: The magnetomotive damping effect. **Inset (b)**: A typical UHF resonance signal over a 10MHz wide frequency span.

Fig. 5.4 shows the measured resonance signal of the 428MHz device, as the magnetic field B is ramped up from 0T to 8T, with the background response signal at 0T subtracted. At B=8T, the signal-to-background ratio is 8dB at the resonance peak. The right-hand side inset of Fig. 5.4 shows the resonance signal *referred to the input of the preamplifier*, in which both the background signal and the resonance are shown in linear scale (in μVolts, 8dB at peak if converted into dB, exactly corresponding to the dB plot in Fig. 5.4; but here in the linear scale plot the absolute level of the flat background, ~2.25μV, *i.e.*, -100dBm, is clearly indicated), and a fit based on the Lorentzian approximation of the power signal perfectly matches the resonance data in a wide span of 10MHz.

Fig. 5.5 shows the measured dissipation as a function of temperature for the 3C-SiC 428MHz and 482MHz NEMS resonator devices. The radio frequency (RF) drive power, the magnetic field and the electronic detection system settings are kept the same in all these measurements, leaving temperature the only variable. Magnetic field B=6T with enough RF power (-33dBm) is calibrated and used to attain large enough resonance signals (approaching the top regime of the dynamic range) for accurate extraction of Q's in all these temperature-dependent measurements. As shown in Fig. 5.5, the measured dissipation increases with increasing temperature, with a temperature dependency of about $Q^{-1} \propto T^{0.3}$ for both devices. It should be pointed out that this dissipation temperature-dependency phenomenon is not unique for these SiC resonators. In Table 5-1 we list seemingly similar temperature dependency reported for micro- and nanomechanical resonators made of Si, GaAs, diamond and carbon nanotube, with none of their temperature dependencies clearly understood. Because dissipation in resonant devices is complicated and associated with various energy loss mechanisms, how to understand the data requires examinations of all possible dissipation processes. Assuming that the dissipation from different origins is additive and uncorrelated, the possible important mechanisms that may contribute to the measured dissipation include the 3C-SiC NEMS structure layer's intrinsic dissipation Q_0^{-1}, magnetomotive damping Q_{mag}^{-1}, thermoelastic damping Q_{ted}^{-1}, clamping losses Q_{clamp}^{-1}, metallization layer dissipation Q_{metal}^{-1}, surface loss Q_{surf}^{-1}, *etc.*,

$$\frac{1}{Q} = \frac{1}{Q_0} + \frac{1}{Q_{mag}} + \frac{1}{Q_{ted}} + \frac{1}{Q_{clamp}} + \frac{1}{Q_{metal}} + \frac{1}{Q_{surf}} \cdots \qquad (5\text{-}1)$$

We neglect the air viscous damping effect since all our measurements are performed in UHV condition. We now explore all these possible mechanisms to find out the implications of these data.

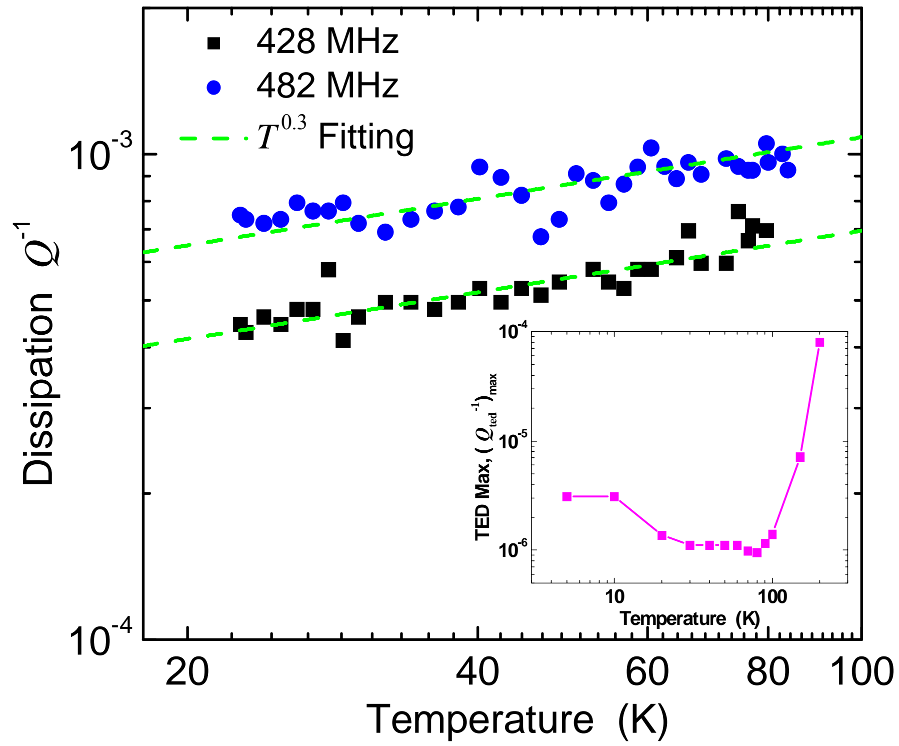

Fig. 5.5 Measured dissipation as a function of temperature for the selected 428MHz and 482MHz NEMS resonators. The dashed lines show the $Q^{-1} \propto T^{0.3}$ approximation to guide the eyes. **Inset**: Theoretical estimation of maximum possible thermoelastic dissipation as a function of temperature.

Table 5-1 Temperature dependency of Q^{-1} in various micro- & nanomechanical resonators.

Material	L (μm)	w (nm)	t (nm)	Resonant Frequency	Temperature Dependency	Method
3C-SiC (this work)	1.55, 1.65	120	80	Flexural, in-plane, 428MHz, 482MHz	Q^{-1}~$T^{0.3}$ (20~85K)	Experimental Network Analysis
Si [21]	5~25	1000	200~360	Flexural, out-of-plane, 12.4MHz, 4.7MHz	Q^{-1}~$T^{0.3}$ (4~10K)	
GaAs [21]	6~25	400~2000	~800	Torsional, 0.62, 1.02, 1.28, 2.75MHz Flexural, out-of-plane, 13MHz	Q^{-1}~$T^{0.25}$ (4~40K)	
Diamond [28]	2.5, 3, 4, and 8	80	40	Flexural, in-plane, 13.7MHz, 55.1MHz, 110.1MHz, 157.3MHz	Q^{-1}~$T^{0.2}$ (5~30K)	
Single-Walled Carbon Nanotube [22]	0.003μm (3nm)	d=0.35nm	d=0.35nm	Flexural, 300GHz	Q^{-1}~$T^{0.36}$ (50mK~293K)	Molecular dynamics simulation of ring-down process

5.4 Dissipation Mechanisms and Contributions

5.4.1 Magnetomotive Damping Effect

The family of resonance curves in Fig. 5.4 clearly shows an effective Q decrease with increasing magnetic field (as the resonance getting broadened). The measured dissipation Q^{-1} versus magnetic field is shown in the left-hand side inset of Fig. 5.4 with the quadratic fit in a dashed line (there is no data point below B=1T because for UHF SiC NEMS, the device is short and stiff and thus for B<1T the resonance is too small to be reliably extracted). This *magnetomotive damping effect* originates from the fact that the electromotive force (EMF) voltage generated by the vibrating NEMS device in the magnetic field creates a current as the device is in a closed circuit (with the resistive elements of both the device itself and the measurement system), and in the magnetic field this current induces force that intends to oppose or damp the resonating device. This effect is modeled by a loaded Q due to the impedances forming a closed circuit with the emf voltage in the detection system [26]

$$\frac{1}{Q} = \frac{1}{Q_{device}} \left(1 + R_m \frac{\mathrm{Re}(Z_{ext})}{|Z_{ext}|^2} \right), \tag{5-2}$$

where Q_{device} is the *unloaded* Q of the device itself; $R_m = Q_{device} \eta B^2 L^2 / (2\pi f_0 m)$ is the electromechanical resistance of the NEMS, with m the mass of the device and mode shape number η=0.5232 for the fundamental mode; and Z_{ext} (seen by the EMF voltage in its closed circuit) is the impedance in series to R_{m}, consisting of the DC resistance of the device, the impedance of the coaxial cable and the input impedance of the preamplifier. Shown in the left-hand side inset, the measured Q decreases by a factor of ~2.3 as from B=1T to 8T, and the fitting with eq. (5-2) leads to an estimation of the *unloaded Q* of

Q_{device}≈2860 at ~20K, which is the highest Q achieved for doubly-clamped beam resonators operating in the >400MHz range.

5.4.2 Thermoelastic Damping

The *thermoelastic damping effect* is due to the fact that when the beam is deformed and is vibrating, the strain field is coupled to local temperature field and the mechanical vibration energy is dissipated through phonon relaxation processes into thermal energy. Detailed theory and modelling regarding the thermoelastic damping, particularly in doubly-clamped beam resonators, has been developed [29]. To explore how much dissipation is contributed by thermoelastic damping in SiC NEMS, *the accurate estimation based on the theory then relies on trusty data of the thermal and mechanical properties of SiC NEMS at the temperatures of interest*, which however are, thus far very scarce, as the thermal and elastic properties of epitaxial SiC films are still awaiting systemic investigation, especially *at low dimensions* (nanoscale thin films, and nanoscale beams and wires) and at low temperatures. Empirically, here we estimate the upper limit of the thermoelastic damping in 3C-SiC based on the theory developed in [29] with the available thermal properties data at various temperatures:

$$\left(\frac{1}{Q_{ted}}\right)_{\max} = \max\left\{\frac{E\alpha^2 T}{\rho C_P}\left[\frac{6}{\xi^2} - \frac{6}{\xi^3}\frac{\sinh\xi + \sin\xi}{\cosh\xi + \cos\xi}\right]\right\} \approx 0.494\frac{E\alpha^2 T}{\rho C_P}, \qquad (5\text{-}3)$$

where E, α, ρ, C_P are the Young's modulus, thermal expansion coefficient, mass density, and heat capacity (per unit mass), respectively. Here ξ is a dimensional variable represents the relative magnitude of the characteristic size of the device (*e.g.*, device width) versus the characteristic thermal relaxation length (*e.g.*, phonon mean free path). The upper limit of thermoelastic damping, $(1/Q_{ted})_{max}$, independent of the device dimension, is assumed when the system is operating at ξ=2.225. With the parameters shown in Table 5-2, the estimated $(1/Q_{ted})_{max}$ is plotted in the inset of Fig. 5.5. This

indicates the thermoelastic damping effect in our 3C-SiC NEMS devices is not strong and could be neglected (still more than 2 orders of magnitude smaller than the measured dissipation).

Table 5-2 Properties of 3C-SiC for thermoelastic damping calculations*.

Temperature (K)	Heat Capacity (J/[g·K])	Heat Capacity (J/[m^3·K])	Thermal Expansion Coefficient (10^{-6}/K)
5	1.21×10-5	34.503	0.01
10	9.69×10-5	276.028	0.02
20	7.75×10-4	2208.222	0.0267
30	0.00262	7452.750	0.036
40	0.00620	17665.778	0.048
50	0.012	34503.472	0.060
60	0.0210	59622	0.072
70	0.0376	107160	0.084
80	0.0628	178866	0.1
90	0.0837	238488	0.12
100	0.105	298110	0.14
150	0.251	715464	0.4
200	0.418	1192440	1.5

*With density ρ = 2850kg/m^3 and Young's modulus E = 430GPa, which have achieved good agreement in reproducing the measured data (*e.g.*, device resonant frequency) of generations of 3C-SiC NEMS devices. Heat capacity (per unit volume data calculated from per unit mass data) and thermal expansion data are from [30].

This estimation is based on the conventional view that considers thermoelastic damping as a *bulk* effect and the estimation replies on the credibility of the available data on thermal and mechanical properties [30]. However, we must note that recently it has been reported that the size effect of Young's modulus has been observed in micro- and nanoscale devices [31], and the heat capacity of a NEMS device (*1D nanostructure*) might also be quite different from that of a 3D bulk sample. Hence, a clearly quantitative and conclusive understanding of the thermoelastic damping in NEMS devices would only be possible once reliable measurements are carried out to systematically characterize, and at the same time, theories are developed to explain and

reproduce, these thermal and mechanical properties. Moreover, recent studies have shown that thermal conductivity (and hence thermal diffusivity) of nanoscale beam and wire structures (with cross-section dimension in the order of 10−100nm) can be more than 2−3 orders of magnitude smaller than the bulk values [32,33]. Therefore, for the same device, calculating ξ with bulk thermal diffusivity would lead to a large error in estimated dissipation—especially when the thermoelastic damping effect is strong (*i.e.*, when the first-order estimation of $(1/Q_{\rm ted})_{\rm max}$ from eq. (5-3) is not negligible, as ξ gives the multiplying factor to $(1/Q_{\rm ted})_{\rm max}$ to determine the real amount of thermoelastic dissipation [29]).

5.4.3 Clamping Losses

Scaling 3C-SiC NEMS up to UHF range brings the doubly-clamped beam length down to only 1~2μm (*e.g.*, for given epitaxial SiC thickness 80nm and lithography process-determined width of 120nm~150nm); thus *intuitively* it could be expected that the *clamping losses* would become important. Theoretical analysis predicts that for in-plane flexural mode of beams doubly-clamped to semi-infinite supports, dissipation into the supports is $Q_{clamp}^{-1} \approx \beta(w/L)^3$, while the coefficient β is not readily modelled [34]. Our experimental data from generations of UHF NEMS achieve encouraging agreement with this prediction, as shown in Fig. 5.6 and with device characteristics listed in Table 5-3. The close fit to $Q^{-1} \sim (w/L)^3$ not only indicates that the clamping losses do play an important role and increases with shrinking devices (scaling up frequency), but also suggests that the clamping losses portion ratio (or percentage) $\eta = Q_{clamp}^{-1}/Q^{-1}$ is roughly the same in these devices.

To accurately predict clamping losses, detailed analysis and modelling of the coefficient β is desired, and we suggest not only the elastic properties of the device, but also the dimensions of the finite-size supports, as well as the fabrication details (*e.g.*,

undercut below the supports generated by the etch in order to suspend the resonator) should be considered. With Fig. 5.6 and Table 5-3, it is clearly seen that the offset between the two sets of data in Fig. 5.5 is due to the larger clamping losses in the 482MHz device than that in the 428MHz device.

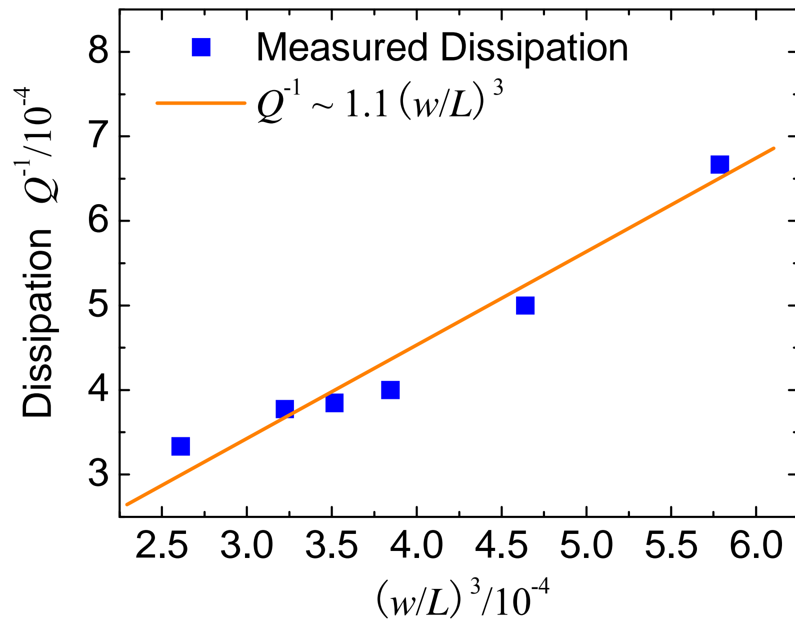

Fig. 5.6 Experimental results of dissipation in several generations of UHF NEMS resonators with dimensions and operating frequencies scaled, all measured under the same experimental conditions (the individual device characteristics are listed in **Table 5-3**). The solid line is the approximate theoretical fit based on the theory of elastic energy transmission from the vibrating NEMS device to its clamping and supporting pads.

Table 5-3 Effect of aspect ratio on the Q^{-1}.

Resonant Frequency (MHz)	Device Dimension			Aspect Ratio (L/w)	Measured Q^{-1}
	L (μm)	w (nm)	t (nm)		
295	2.65	170	80	15.65	3.33×10^{-4}
395	1.75	120	80	14.58	3.77×10^{-4}
411	1.7	120	80	14.17	3.85×10^{-4}
420	1.8	150	100	12.00	6.67×10^{-4}
428	1.65	120	80	13.75	4.00×10^{-4}
482	1.55	120	80	12.92	5.00×10^{-4}

5.4.4 Dissipation due to the Metallization Layers

The metallization layers (Ti atop Al) also contribute to the dissipation. With the general definition of dissipation $Q^{-1} = \Delta W/(2\pi W)$ (W is the energy stored in the resonator and ΔW the dissipated energy per cycle) and the assumption that the energy stored and dissipated can be split into corresponding portions in the structural layer and metallization layers [25], for our flexural mode doubly-clamped beams, we obtain

$$\frac{1}{Q} = \frac{1}{1+\frac{t_{Al}E_{Al}}{t_{SiC}E_{SiC}}+\frac{t_{Ti}E_{Ti}}{t_{SiC}E_{SiC}}}\cdot\frac{1}{Q_{SiC}} + \frac{1}{1+\frac{t_{SiC}E_{SiC}}{t_{Al}E_{Al}}+\frac{t_{Ti}E_{Ti}}{t_{Al}E_{Al}}}\cdot\frac{1}{Q_{Al}} + \frac{1}{1+\frac{t_{SiC}E_{SiC}}{t_{Ti}E_{Ti}}+\frac{t_{Al}E_{Al}}{t_{Ti}E_{Ti}}}\cdot\frac{1}{Q_{Ti}}, \quad (5\text{-}4)$$

in which t_i, E_i are thickness, Young's modulus of the layers, and Q_i^{-1} are the *phenomenological* dissipation in each layer, respectively.

The coefficients for the dissipation in metallization layers are very small, 0.0543 and 0.0293, respectively. With the measured dissipation in deposited submicron Al and Ti films from [36] (both having a plateau in the interested temperature range), the estimated dissipation in metallization layers is ~5×10^{-6} (as listed in Table 5-4), still ≤1% of the measured dissipation.

Table 5-4 Parameters for calculating the dissipation due to metallization layers.

Metallization	Thickness (nm)	Young's Modulus (GPa)	Q_{film}^{-1}	Calculated Dissipation Contribution
Al	30	68	1.0×10^{-4} [36]	5.43×10^{-6}
Ti	10	110	2.0×10^{-4} [36]	5.86×10^{-6}

5.4.5 Surface Loss

Surface loss is due to the fact that virtually all surface atoms can be treated as defect atoms that cause energy dissipation into the environment. Surface stress, adsorbates and

crystal defects on the device surface all enhance the dissipation. Exact theoretical analyses and models capturing the mesoscopic surface loss mechanisms are not yet established due the complicated and stochastic nature of the surface conditions and behavior. Nonetheless, it is still very intuitive to expect larger dissipation (lower *Q*'s) when the device surface-to-volume ratio is increased. Experiments show that for ultra-thin (t<<w) cantilevers, *Q*'s are roughly proportional to the device thickness (in the regime of surface loss dominant, when the cantilevers are long enough), which could be qualitatively explained by conventional macroscopic theory based on the concept of complex modulus ($E=E_1+iE_2$, where E_2 is the dissipative part) [37, 38].

For our UHF NEMS devices of very short beams, as shown in Table 3, the surface-to-volume ratio $2(w+t)/(wt)$ does not change much (or almost remains the same) as we keep a consistent fabrication process with relatively fixed w and t. Thus, surface loss in these devices should be approximately the same, and the measured Q differences among these devices are still dominated by clamping losses. To estimate or determine the absolute amount of surface loss, annealing and other surface treatment techniques could be applied to test how much dissipation can be reduced.

The above analysis shows that the observed dissipation temperature dependency $Q^{-1}\sim T^{0.3}$ in the temperature range of interest should be attributed to the intrinsic dissipation in the 3C-SiC material itself. Other important mechanisms superpose on this intrinsic dissipation, without changing the temperature dependency (*e.g.*, clamping losses), or without showing evidence to be able to change the temperature dependency up to the observed magnitudes (*e.g.*, thermoelastic damping). In principle, an accurate model describing this temperature dependency could possibly be developed if the mesoscopic energy dissipation nature inside monocrystalline 3C-SiC, at the atomistic level, is systematically understood. As shown in Table 5-1, the finding of the temperature dependent dissipation in 3C-SiC accumulates new evidence and data for this

intriguing fundamental open question. Also, we note that in Fig. 5.5, there is no strong evidence for the so-called Debye peaks [29] usually believed to be associated with the motions of various defects and impurities, excitation and relaxation inside the resonator material. This is probably because of the high quality of our monocrystalline 3C-SiC epilayer [25].

5.5 Resonance Frequency Temperature Coefficient

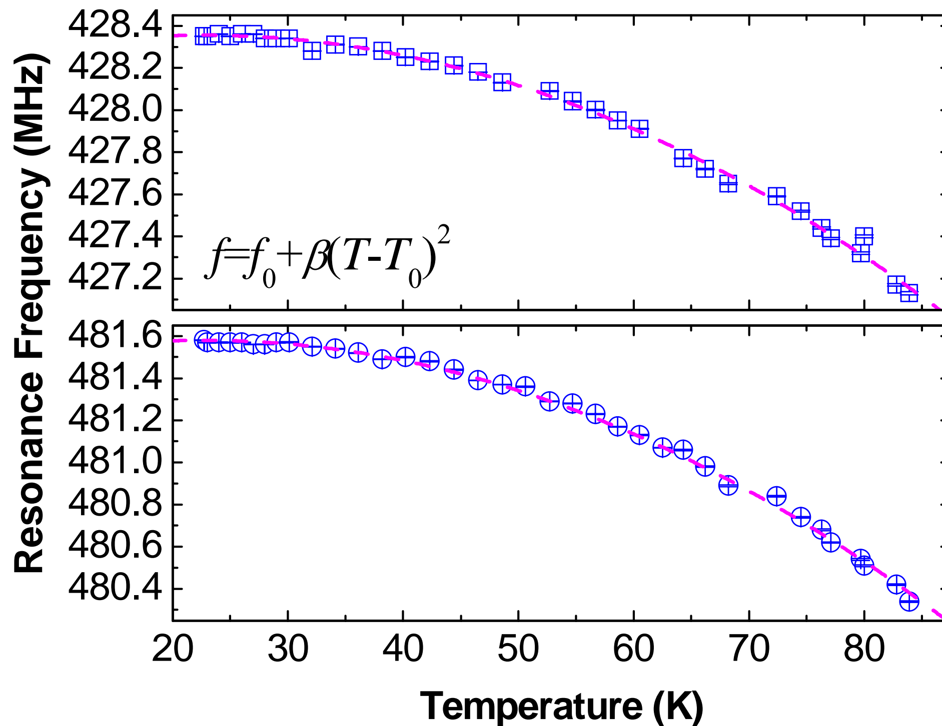

Fig. 5.7 Measured resonance frequency as a function of temperature for selected 3C-SiC UHF NEMS resonators (at carefully controlled and stabilized temperatures).

The dependence of resonance frequency upon temperature is measured and plotted in Fig. 5.7. As shown, the resonance frequency decreases as the temperature is increased. A polynomial fit to the data shows that a quadratic dependence $f=f_0+\beta(T-T_0)^2$ matches the heating-induced ($T \geq T_0$) frequency tuning data quite well, with $\beta \approx$-320Hz/K^2 for both data

traces of Fig. 5.7. We attribute this primarily to the effect of thermal expansion: The frequency changes as both the beam length and its tension are altered with temperature. The nonlinear temperature dependency results from the contributions of both the direct beam length change, $\delta f_0/f_0 \sim -2\delta L/L$ (with $\delta L/L = \alpha \cdot \delta T$ where $\alpha = \alpha(T)$ is the thermal expansion coefficient as a function of temperature); and the thermally induced tensile stress change $\delta\sigma_T$ in the beam, $\delta f_0/f_0 \sim \delta\sigma_T/2\sigma_T$ (in large tension cases with $\sigma_T >> \pi^2 E t^2/3L^2$) and $\delta f_0/f_0 \sim \delta\sigma_T$ (in small tension cases).

The results imply that the tensile stress increases monotonically when the devices are cooled down from 85K to 20K. Another observation is that the fractional frequency change does not show dependency on the device size (the two devices are different in length), and both devices have an average temperature coefficient of about -45ppm/K in the range of T=20−85K. This effect, once calibrated over a wider temperature range, can be employed to study the basic properties of SiC material, and can be further engineered for sensing applications.

5.6 Chapter Summary

In this chapter, we have investigated the dissipation in single-crystal 3C-SiC nanomechanical resonators operating at ultra-high frequencies, to gain understanding and develop engineering solutions that make optimal trade-offs between scaling up resonance frequency and attaining high Q's for UHF NEMS resonators. It is found that the temperature dependence of the dissipation in the 3C-SiC NEMS resonators studied follows $Q^{-1} \propto T^{\alpha}$, with $\alpha \approx 0.3$. It is clear that in-depth theoretical models and analyses are needed to reveal the underlying microscopic mechanisms. The magnetomotive damping effect can be appreciable, but it is relatively well understood and (to some

extent) controlled. Thermoelastic dissipation is found to be negligible for the devices of this study. The losses from metallization layers contribute ≤1% of the observed total dissipation. However, a major source of the dissipation is clamping losses through the supports for these doubly-clamped beam UHF resonators. The measured data show that the theoretical prediction $Q_{\mathrm{clamp}}^{-1} \propto (w/L)^3$ provides a rough but reasonable model for these clamping losses. Verifying and understanding the dominant clamping losses can lead to new designs and optimization guidelines for UHF NEMS enabling attainment of high *Q*'s. Moreover, because SiC can be deposited both in polycrystalline form as well as in several single-crystal polytypes with excellent properties (including 3C-SiC, 6H-SiC, 4H-SiC and 2H-SiC), it represents a particularly promising material for NEMS applications. Future collective studies of dissipation in SiC NEMS with all these SiC variations would be beneficial.

For future *Q*-engineering while scaling the frequency up, we propose and are exploring the following possibilities and promising solutions.

(i) Geometric mechanical design and optimization: By engineering and optimizing the anchoring, supports and vibrational modes (*e.g.*, free-free beams, tuning-forks, disks with wine-glass and extensional modes), the clamping losses can be reduced or minimized.

(ii) Processes engineering: By developing suitable annealing process [39], high-temperature and high-vacuum encapsulation packaging process [40,41], surface loss, interfacial loss at inhomogeneous interfaces, metallization layer dissipation and thermoelastic damping are expected to be alleviated.

(iii) Materials engineering: The development of highly-doped conducting single-crystal materials, metallic single-crystal nanowires, very-low internal loss

metallization layers, can also be anticipated to reduce the surface and interfacial losses, the internal friction in metallization and the thermoelastic damping effects.

(iv) Electrical design: In the electrical domain, engineering and development of the transduction schemes and circuit models are expected to create technologies in which the loaded-Q effects are minimized.

Bibliography

[1] V.B. Braginsky, V.P. Mitrofanov, V.I. Panov, *Systems with Small Dissipation*, Chicago: The University of Chicago Press (1985).

[2] R.N. Kleiman, G.K. Kaminsky, J.D. Reppy, R. Pindak, D.J. Bishop, "Single-crystal silicon high-*Q* torsional oscillators", *Rev. Sci. Instrum.* **56**, 2088-2091 (1985).

[3] C. Zener, "Internal friction in solids-I", *Phys. Rev.* **52**, 230-235 (1937); *and* C. Zener, "Internal friction in solids-II", *Phys. Rev.* **53**, 90-99 (1938).

[4] T.V. Roszhart, "The effect of thermoelastic internal friction on the *Q* of micromachined silicon resonators", *Tech. Digest, 1990 IEEE Solid-State Sensors and Actuators Workshop (Hilton Head 1990)*, 13-16, Hilton Head Island, SC, June 4-7 (1990).

[5] F.R. Blom, S. Bouwstra, M. Elwenspoek, J.H.J. Fluitman, "Dependence of the quality factor of micromachined silicon beam resonators on pressure and geometry", *J. Vac. Sci. Tech. B* **10**, 19-26 (1992).

[6] M.L. Roukes, "Nanoelectromechanical systems", *Tech. Digest, 2000 Solid-State Sensors and Actuator Workshop (Hilton Head 2000)*, 1-10, Hilton Head Island, SC, June 4-8 (2000).

[7] X.M.H. Huang, K.L. Ekinci, Y.T. Yang, M.L. Roukes, *et al.*, *unpublished data* (2002).

[8] X.M.H. Huang, X.L. Feng, C.A. Zorman, M. Mehregany, M.L. Roukes, "VHF, UHF and microwave frequency nanomechanical resonators" (invited article), *New J. Phys.* **7**, 247 (2005).

[9] M.L. Roukes, "Nanoelectromechanical systems face the future", *Physics World* **14**, 25-31 (2001).

[10] D. Rugar, R. Budakian, H.J. Mamin, B.W. Chui, "Single spin detection by magnetic resonance force microscopy", *Nature* **430**, 329-332 (2004).

[11] J.L. Arlett, J.R. Maloney, B. Gudlewski, M. Muluneh, M.L. Roukes, "Self-sensing micro- and nanocantilevers with attonewton-scale force resolution", *Nano Lett.* **6**, 1000-1006 (2006).

[12] K.L. Ekinci, X.M.H. Huang, M.L. Roukes, "Ultrasensitive nanoelectromechanical mass detection", *Appl. Phys. Lett.* **84**, 4469-4471 (2004).

[13] Y.T. Yang, C. Callegari, X.L. Feng, K.L. Ekinci, M.L. Roukes, "Zeptogram-scale nanomechanical mass sensing", *Nano Lett.* **6**, 583-586 (2006).

[14] C.T.C. Nguyen, "Frequency-selective MEMS for miniaturized low-power communication devices", *IEEE Trans. Microwave Theory & Techniques* **47**, 1486-1503 (1999).

[15] M.D. LaHaye, O. Buu, B. Camarota, K.C. Schwab, "Approaching the quantum limit of a nanomechanical resonator", *Science* **304**, 74-77 (2004).

[16] R.G. Knobel, A.N. Cleland, "Nanometre-scale displacement sensing using a single electron transistor", *Nature* **424**, 291-293 (2003).

[17] X.M.H. Huang, C.A. Zorman, M.Mehregany, M.L. Roukes, "Nanodevice motion at microwave frequencies", *Nature* **421**, 496 (2003).

[18] L. Sekaric, J.M. Parpia, H.G. Craighead, T. Feygelson, R.H. Houston, J.E. Bulter, "Nanomechanical resonant structures in nanocrystalline diamond", *Appl. Phys. Lett.* **81**, 4455-4457 (2002).

[19] A. Husain, J. Hone, H.W.Ch. Postma, X.M.H. Huang, T. Drake, M. Barbic, A. Scherer, & M.L. Roukes, "Nanowire-based very-high-frequency electromechanical resonator", *Appl. Phys. Lett.* **83**, 1240-1242 (2003).

[20] V. Sazonova, Y. Yaish, H. Ustunel, D. Roundy, T.A. Arias, & P.L. McEuen, "A tunable carbon nanotube electromechanical cscillator", *Nature* **431**, 284-287 (2004).

[21] P. Mohanty, D.A. Harrington, K.L. Ekinci, Y.T. Yang, M.J. Murphy, M.L. Roukes, "Intrinsic dissipation in high-frequency micromechanical resonators", *Phys. Rev. B* **66**, 085416 (2002).

[22] H. Jiang, M.F. Yu, B. Liu, Y. Huang, "Intrinsic energy loss mechanisms in a cantilevered carbon nanotube beam oscillator", *Phys. Rev. Lett.* **93**, 185501 (2004).

[23] D. Nakamura, I. Gunjishima, S. Yamaguchi, T. Ito, A. Okamoto, H. Kondo, S. Onda, K. Takatoir, "Ultrahigh-quality silicon carbide single crystal", *Nature* **430**, 1009-1012 (2004); *and* (in *news & views*), R. Madar, "Silicon carbide in contention", *Nature* **430**, 974-975 (2004).

[24] C.A. Zorman, A.J. Fleischman, A.S. Dewa, M. Mehregany, C. Jacob, S. Nishino, P. Pirouz, "Epitaxial growth of 3C-SiC films on 4 in. diam (100) silicon wafers by atmospheric pressure chemical vapor deposition", *J. Appl. Phys.* **78**, 5136-5138 (1995).

[25] X.A. Fu, C.A. Zorman, M. Mehregany, "Surface roughness control of 3C-SiC films during the epitaxial growth process", *J. Electrochem. Society* **151**, G910-G914 (2004).

[26] A.N. Cleland, M.L. Roukes, "External control of dissipation in a nanometer-scale radiofrequency mechanical resonator", *Sensors and Actuators* **72**, 256-261 (1999).

[27] X.L. Feng, C.J. White, A. Hajimiri, M.L. Roukes, "Ultra-high frequency low-noise self-sustaining oscillator with vibrating nanodevice", *to be published* (2006).

[28] A.B. Hutchinson, P.A. Truitt, K.C. Schwab, L. Sekric, J.M. Parpia, H.G. Graighead, J.E. Bulter, "Dissipation in nanocrystalline-diamond nanomechanical resonators", *Appl. Phys. Lett.* **84**, 972-974 (2004).

[29] R. Lifshitz, M.L. Roukes, "Thermoelastic damping in micro- and nanomechanical systems", *Phys. Rev. B* **61**, 5600-5609 (2000).

[30] Y.S. Touloukian, E.H. Buyco, *Thermophysical Properties of Matter* Volume **5**—*Specific Heat: Nonmetallic Solids*, IFI/Plenum, New York-Washington, 448-449 (1970); *and,* Y.S. Touloukian, R.K. Kirby, R.E. Taylor, T.Y.R. Lee, *Thermophysical Properties of Matter* Volume **13**—*Thermal Expansion: Nonmetallic Solids*, IFI/Plenum, New York-Washington, 873-878 (1977).

[31] X.X. Li, T. Ono, Y.L. Wang, M. Esashi, "Ultrathin single-crystalline cantilever resonators: fabrication technology and significant specimen size effect on Young's modulues", *Appl. Phys. Lett.* **83**, 3081-3083 (2003).

[32] W. Fon, K.C. Schwab, J.M. Worlock, M.L. Roukes, "Phonon scattering mechanisms in suspended nanostructures from 4 to 40K", *Phys. Rev. B* **66**, 045302 (2002).

[33] D.Y. Li, Y.Y. Wu, P. Kim, L. Shi, P.D. Yang, A. Majumdar, "Thermal conductivity of individual silicon nanowires", *Appl. Phys. Lett.* **83**, 2934-2926 (2003).

[34] M.C. Cross, R. Lifshitz, "Elastic wave transmission at an abrupt junction in a thin plate with application to heat transport and vibrations in mesoscopic systems", *Phys. Rev. B* **64**, 085324 (2001).

[35] B.E. White Jr., R.O. Pohl, "Elastic properties of thin films", *Mat. Res. Soc. Symp. Proc.* **356**, 567-572 (1995).

[36] X. Liu, E. Thompson, B.E. White Jr., R.O. Pohl, "Low-temperature internal friction in metal films and in plastically deformed bulk aluminum", *Phys. Rev. B* **59**, 11767-11776 (1999); *and,* P.D. Vu, X. Liu, R.O. Pohl, "Phonon scattering and internal friction in dielectric and metallic films at low temperatures", *Phys. Rev. B* **63**, 125421 (2001).

[37] K.Y. Yasumura, T.D. Stowe, E.M. Chow, T. Pfafman, T.W. Kenny, B.C. Stipe, D. Rugar, "Quality factors in micron- and submicron-thick cantilevers", *J. Microelectromech. Systems* **9**, 117-125 (2000).

[38] J. Yang, T. Ono, M. Esashi, "Energy dissipation in submicrometer thick single-crystal silicon cantilevers", *J. Microelectromech. Systems* **11**, 775-783 (2000); *and,* J. Yang, T. Ono, M. Esashi, "Surface effects and high quality factors in ultrathin single-crystal silicon cantilevers", *Appl. Phys. Lett.* **77**, 3860-3862 (2000).

[39] D.K. Armani, T.J. Kippenberg, S.M. Spillane, K.J. Vahala, "Ultra-high-*Q* toroid microcavity on a chip", *Nature* **421**, 925-928 (2003).

[40] A. Partridge, A.E. Rice, T.W. Kenny, M. Lutz, "New thin film epitaxial polysilicon encapsulation for piezoresistive accelerometers", *Tech. Digest, 14th Int. Conf. on MEMS (MEMS'01)*, 54-59 (2001).

[41] A. Partridge, "A new paradigm in time: silicon MEMS resonators vs. quartz crystals", *R&D Magazine*, April (2006).

Chapter 6

High-Performance Silicon Nanowire VHF Nanoelectromechanical Resonators

Suspended, free-standing nanoscale structures and devices provide the platforms for today's exploration with nanomechanics and NEMS. Besides the *top-down* lithographically-defined devices discussed in the previous chapters, the *bottom-up* synthesis paradigm has also been pursued in producing interesting building blocks. Bottom-up nanostructures have to face formidable challenges in assembling and integration even at the functional device level, not to mention integrated systems. Particularly for Si nanowires (NWs), which have been in the spotlight of nanoelectronics, their potential for NEMS could have been exploited as well had it been possible for direct growth of suspended Si NW devices. This chapter is focused on the demonstration of robust, versatile, VHF NEMS resonators with high performance, based on single-crystal Si NWs prepared by bottom-up chemical synthesis. The Si NWs are suspended doubly-clamped resonators as grown across lithographically-defined microtrenches by a controlled vapor-liquid-solid epitaxial growth process. We show that both metallized Si NWs and pristine semiconducting piezoresistive Si NWs are excellent resonators, thus providing great capability for versatile signal

transduction schemes. Metallized Si NW resonators operating at 200MHz with quality factor $Q\approx2000$–2500, and pristine Si NW resonators at 215MHz with $Q\approx5750$, have been demonstrated. The Si NW's piezoresistive effect has been employed for VHF resonance detection. Frequency stabilities of these Si NWs, measured by real-time frequency tracking techniques, demonstrate that they are among the most responsive and sensitive resonant mass sensors to date, with mass sensitivity well into the 20~60 zeptogram range. The ease of fabrication and high-performance characteristics of these Si NW resonators make them attractive and promising for resonant sensing, signal processing and other applications, with single devices or arrays of Si NWs.

6.1 Si NWs: Nanoelectronic *and* Nanomechanical Building Blocks

Silicon nanowires (Si NWs) have been emerging as interesting and promising building blocks for nanoscale electronics [1-4], electrically-based chemical and biological sensors [5-9], and thermoelectric devices [10], as evidenced by functional devices and rudimentary systems based upon Si NWs for such applications having been demonstrated and attracting considerable research interest. These Si NWs are usually prepared with the *bottom-up* chemical synthesis techniques involving catalyzed chemical vapor deposition (CVD) processes, characterized by a vapor-liquid-solid growth (VLS) mechanism [11,12] to allow for the promotion of anisotropic crystal growth. As one-dimensional nanostructures, they possess ever-shrinking diameters well down into the nanometer regime (typically in the 10~100nm range). Compared to their *top-down* lithographically-defined counterparts, these Si NWs have encountered great challenges in rational growth and process control, assembly, contacting and interconnection, addressing and registration, and integration, which must be addressed in order to fulfill their application potential.

Considerable efforts have been made to understand the VLS growth process in more detail, specifically the diameter, the crystalline structure and their control parameters for more predictable and reliable growth of high-quality Si NWs [11-13]. Typically, for an individual Si-NW-based device, atomic force microscope (AFM) scanning is needed to locate the Si NW and then subsequent electron-beam lithography and metallization processes are need to make the electrical contacts and interconnects [1-6,8]; or, the Si NWs dispersion is cast onto the support structure to have Si NWs bridging the contacting leads in a statistical (by luck) manner [10]. Similar to the ancient idea of "floating logs on the river", microfluidics techniques have been employed to help align and assemble Si

NWs from dispersions, to create Si NW networks and arrays of two-terminal Si NW devices [14-16], and these assembled networks and arrays have been demonstrated as functional electronic devices [14] and biological sensor arrays [7,9].

Thus far advances with Si NWs have mainly been carried out with emphasis on the aforementioned electronic devices and electrical (field-effect transistor)-based sensors. Si is a proven excellent mechanical material well-established for micro- and nano-electromechanical systems (MEMS and NEMS) [17-19], hence Si-NWs-based mechanical devices are highly expected to augment the nanomechanical devices toolbox for applications such as atomic-scale manipulation, robotics, actuation and sensing. It is also of great interest and importance to investigate the mechanical properties of Si NWs, as unexpected mechanical properties may emerge due to the variations in growth-process-dependent crystalline structures and dimensions, which may possibly result in geometric- and size-related effects. However, research in the mechanical aspects of Si NWs has been lagged largely because of the difficulties in making free-standing, suspended devices, and in devising techniques to probe their mechanical properties and further develop their mechanical functionalities. Recently, progress has been made in exploiting Si epitaxial growth in the preferred <111> directions to grow aligned, suspended Si NWs [20,21]. With careful control of their number density, length and diameter, as-grown suspended Si NW doubly-clamped beams and cantilevers have been realized [21]. This immediately makes it possible to study the mechanical properties of these Si NWs by static bending of the NWs using contact mode AFM tips [22-24]. In this chapter we present the demonstration of the Si-NWs-based NEMS resonators, operating in very-high frequency (VHF) regimes up to ~215MHz. Based on comprehensive measurements and characterizations, we show that these Si NW resonators are robust for VHF and UHF operations; they are versatile for various

transduction schemes; and they have high quality factors (Q's) and high frequency stability; and thus are excellent for ultrasensitive resonant nanosensors.

6.2 Suspended Si NWs in Microtrenches

Single-crystal Si NWs are grown to bridge across prefabricated microtrenches with (111) facing walls, by catalyzed epitaxial VLS growth in a CVD process using $SiCl_4$ as the precursor, with the complete process detailed elsewhere [21]. In order to make as-grown Si NW resonator devices, arrays of microtrenches have been designed and patterned photolithographically to serve as both supporting and conducting pads for the devices, as shown in Fig. 6.1 (a) for the arrays (with columns and rows addressed), and (b) for the close-in with the scanning electron microscope (SEM) image of a typical Si NW-in-microtrench device. The density and size of the catalyst particles dispersed onto the facing (111) surfaces between microtrenches have been carefully regulated to control the density and diameter of the resulting Si NWs. Thus the process reliably yields a single device across a microtrench for the majority of the units in the array, and with a few of microtrenches possibly bridged by two or more Si NWs, as shown in Fig. 6.1 (c), (d) and (e), respectively.

Extending to both sides of the microtrench, the Si pads are heavily doped with boron, having conductivity of ~1Ω·μm (typical sheet resistance is $R_{\square}$~1Ω/□) and providing good electrical contact and conduction. The resistances of the Si NWs have been measured by probing devices in the array. The Si NW resistivities can range from ~30Ω·μm to ~100Ω·μm, and are mainly determined by the doping and growth processes. The design of arrays of microtrenches as supporting and contacting pads for Si NWs growth allows probing and characterization of many Si NWs on the same chip, and also

makes it possible to simultaneously integrate multiple devices with signal transduction electronics.

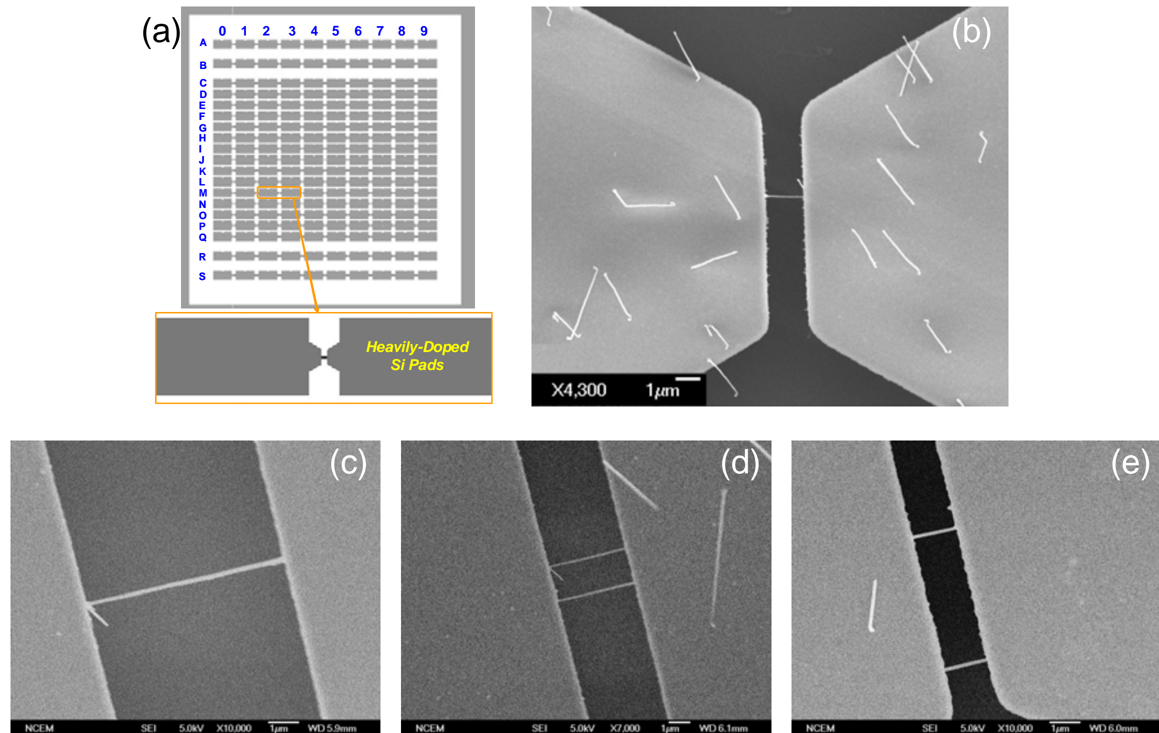

Fig. 6.1 Si NWs nanomechanical resonators prepared by VLS epitaxial growth process. **(a)** Design and pattern of arrays of microtrenches for Si NWs. **(b)** A Si NW device bridging the microtrench. Epitaxial growth only occurs between the microtrenches. On the top surface of the pads, the Si NWs grow in the conventional manner without direction control. **(c)** A Si NW resonator device with length L≈6.75μm and average diameter d≈80nm (in this case the wire is slowly tapered as it grows), and large aspect ratio of ~85. **(d)** and **(e)** Control of Si NWs density and distribution in the microtrenches can yield multiple or arrays of devices with the same length and nearly equivalent diameters.

After SEM inspection and characterization of the dimensions and surface morphology of the Si NWs-in-microtrenches and probing the device resistances, electrical connections (Al wire bonding) are made for selected devices to a high-frequency circuit board built on a sample stage. The sample is then loaded and sealed into a radio-frequency/microwave-compatible cryostat chamber, which is maintained at high vacuum and at low

temperatures for excitation of the resonators via magnetomotive transduction which is well-suited for VHF/UHF/microwave nanomechanical resonators [25]. We have controlled the microtrench width, thus the Si NW length, and the NW diameter to have control over the operating frequency of the Si NWs resonators, as the resonance frequency of a simple doubly-clamped wire resonator is proportional to diameter over length squared, d/L^2 and to Young's modulus-to-density ratio $\sqrt{E_Y/\rho}$. For pre-experiment device design, the Young's modulus of bulk material is used, and the frequency is only scaled by tailoring device dimensions.

6.3 Metallized Si NWs as VHF Resonators

VHF resonators are first realized with metallized Si NWs. Because the Si NWs typically have intrinsic resistances in the ~1−10kΩ range and even in the ~10−100kΩ range, this poses a challenge to radio-frequency (RF), especially VHF (strictly 30−300MHz) resonance detection due to the large impedance mismatch with RF electronics (with 50Ω standard), therefore we metallize these devices for better impedance matching with RF measurement components. Similar to typical VHF top-down nanomechanical resonators [25], metallization layers consisting of 5nm Ti atop 30nm Al have been deposited onto the Si NWs by either thermal or e-beam evaporation. The samples are slightly tilted during metal deposition so that the inner walls of a microtrench are not continuously coated, while allowing the Si NW to be conformally metallized (as long as it is not very deep down into the microtrench), thus the Si NW remains the only electrical path bridging the microtrench. Further probing characterizations are performed to verify that after metallization any two pads are electrically open unless bridged by one or more Si NWs. Metallized Si NWs usually have resistances of about 70−120Ω at room temperature and are very close to 50Ω at low temperatures. We employ the bridge circuit readout scheme [26] incorporating pairs of Si NWs to be able to directly start with

devices of f_0~200MHz in the more attractive VHF/UHF ranges. Although single-device based one-port reflection detection could be used for up to 100~200MHz devices [26,27], the two-port bridge detection scheme is proven to be better, especially for ≥100MHz devices [25,26].

Fig. 6.2 demonstrates the detected signals for a typical pair of metallized Si NWs. One of the device has dimensions L=2.1μm, d=118nm (aspect ratio≈18), with detected resonance frequency ~188MHz and Q≈2500; the other device has L=2.25μm, d=142nm (aspect ratio≈16), with resonance frequency ~200MHz and Q≈2000. As shown in Fig. 6.2, for the fixed magnetic field (B) bias condition, as the RF drive power is increased, the resonance response amplitude increases and the response approaches the nonlinear regime. At the fixed RF drive condition, the resonance response increases with enhanced B field, with the voltage signal amplitude having a B^2 dependency, which is a confirmed characteristic of the magnetomotive transduction [25]. In these measurements we have achieved a dramatically large signal readout with a very high signal-to-background ratio of up to 12dB as shown in Fig. 6.2 (a) and (c), by employing the high-resolution bridge-balancing and background-nulling techniques [28].

Another observation is that the Q of the 188MHz device is higher than the 200MHz device, which is consistent with the well-known f_0 versus Q trade-off [25]. Since the two devices have roughly the same aspect ratio, they may have clamping loss to roughly the same extent [29]. The lower Q of the 200MHz device may also be correlated to the influence of its backward growth (as shown in the inset of Fig. 6.2 (d)), which can be effectively viewed as a free-standing Si NW cantilever device sharing one anchoring point with the 200MHz Si NW, and thus may introduce extra mechanical dissipation.

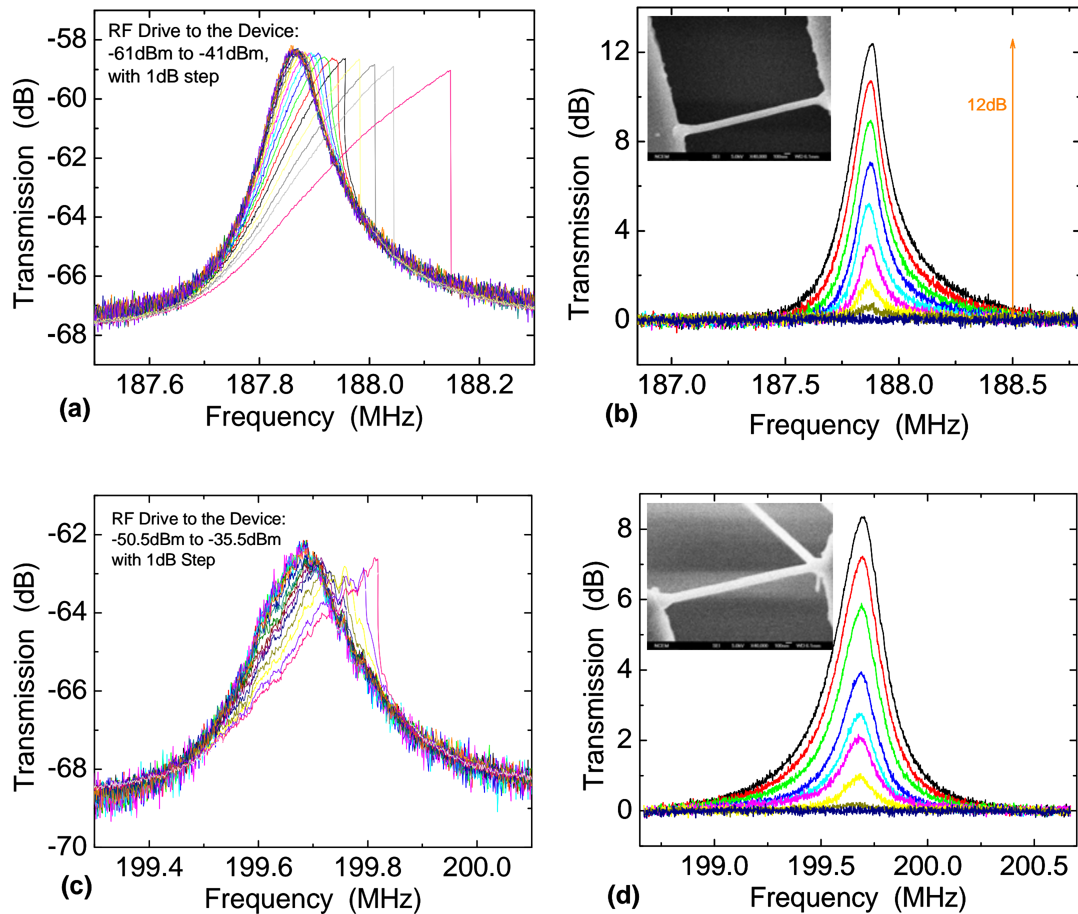

Fig. 6.2 Metallized Si NWs as VHF NEMS resonators. **(a)** and **(b)** are for the 187.8MHz device with drive RF power sweep and magnetic field sweep, respectively, with the magnetomotive transduction and a bridge detection scheme. **Inset** in **(b)** is the SEM image of the device. **(c)** and **(d)** are the drive RF power sweep and the magnetic field sweep, respectively, for the 199.7MHz device. **Inset** in **(d)** is the device SEM image where the backward Si NWs growth is noticeable for this particular device.

These initial trials with metallized up to 200MHz Si NW resonators have demonstrated that the Si NWs-in-microtrenches are robust resonators and their anchoring to both the trench walls is indeed reliably self-welded. This verifies that the self-welded anchoring at both the clamping ends does provide sound mechanical rigidity, not only for static loads as shown in the AFM bending experiments [22], but also for the dynamic resonant motions at VHF, and moreover, for operation in their deep nonlinear regimes (which implies longitudinal tension applied to the anchors). With their specifications listed in Table 6-1, the metallized Si NWs resonators have ultrasmall size and mass, excellent

operating frequencies and quite good Q's, leading to high-performance characteristics as attractive as those of their state-of-the-art top-down counterparts.

Furthermore, for fair comparisons, although the Si NWs diameters are controlled only in a statistical way as compared to top-down lithographically defined features, the main advantage of these as-grown suspended Si NWs is that the fabrication process is easier, faster and much less expensive, as no electron-beam lithography is needed. Since there is no etch process required to suspend the devices, the undercut of the anchoring pads is also avoided, which in principle makes the double clamping more close to semi-infinite and would imply less dissipation through the anchors, as compared to the case where undercut of the anchors is inevitable in the surface nanomachined beam resonators. On the other hand, the top-down method has paramount and relatively more precise control on the number and position of the devices and for multiple devices and arrays, thus realizing rational rather than random device layout.

6.4 Pristine (Non-Metallized) Si NWs as VHF Resonators

We further demonstrate VHF resonators with bare, pristine semiconducting Si NWs, *i.e.*, without the aid of the metallization layers. As these NWs have been doped during the growth process and are conducting already, albeit with high impedance (about 1~100kΩ from various growth), this challenges the effective detection at high frequencies (especially for >30MHz) due to large impedance mismatch and significant signal attenuation and reflection. We carefully choose pairs of Si NWs with fairly closely matched resistance and embed them into the high-resolution bridge detection circuitry.

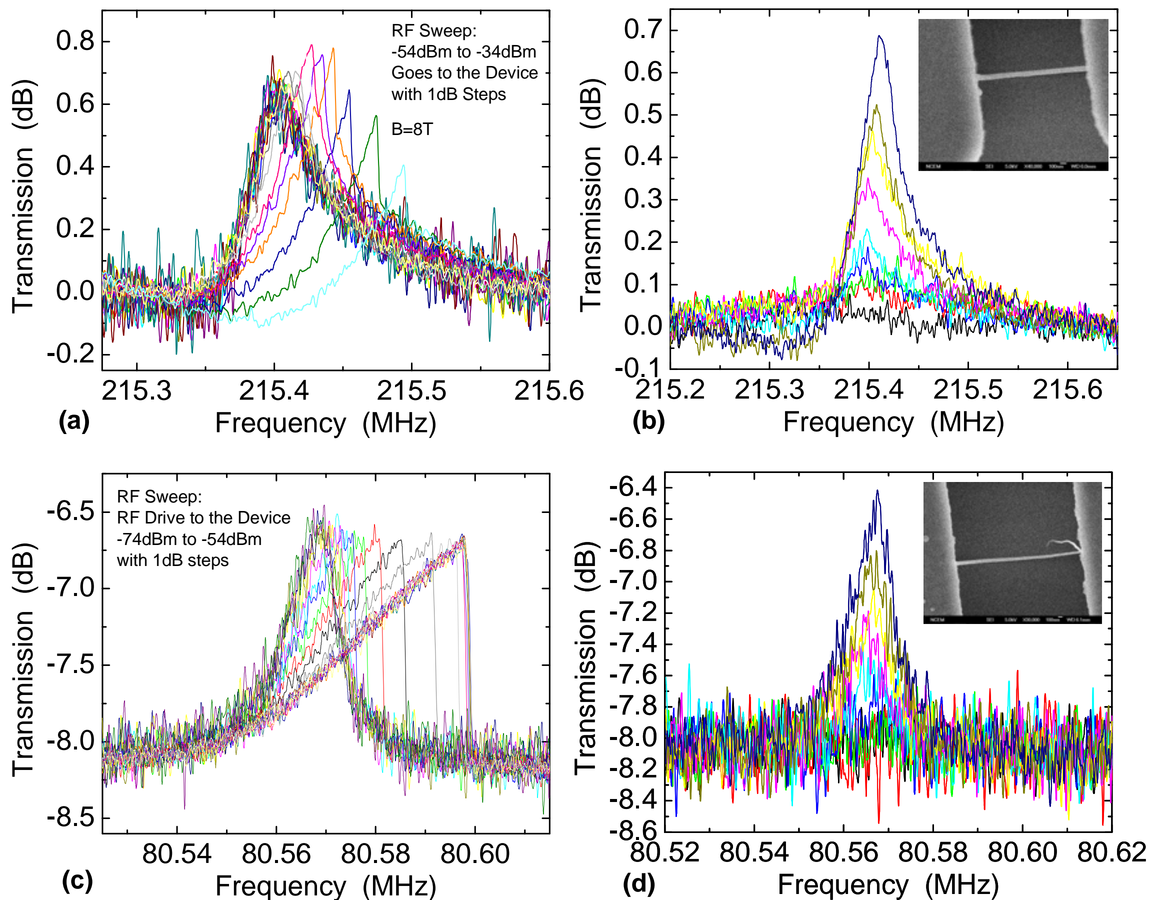

Fig. 6.3 VHF NEMS resonators based on high-impedance pristine Si NWs without metallization. **(a)** and **(b)** Measured resonance from the 215.4MHz Si NW, with RF drive power sweep and magnetic field sweep, respectively. **Inset** in **(b)** is the SEM image of the device. **(c)** and **(d)** Resonance data from the 80.57MHz Si NWs, with RF drive power sweep and magnetic field sweep. **Inset** in **(d)** is the device SEM image and again here the backward Si NWs growth is noticeable for this particular device.

Fig. 6.3 shows the measured data for a pair of such devices. One device has dimensions L=1.69μm, d=81nm (aspect ratio≈21), and measured DC resistance of 3.135kΩ, and resonance frequency of 215.415MHz with Q≈5750. The other device has dimensions L=2.77μm, d=74nm (aspect ratio≈37.4), and DC resistance of 3.616kΩ, and measured resonance frequency of 80.57MHz with Q≈13100. As shown in Fig. 6.3, both devices have demonstrated approaching-nonlinearity with an increasing RF drive power sweep, and resonance response dependence on the B field. These characteristics are similar to those of the metallized Si NWs, and typical top-down SiC NEMS resonators.

Once we obtain the onset of nonlinearity of the Si NWs, we can determine the intrinsic dynamic range for each of the devices with the ultimate noise floor limited by the thermomechanical fluctuations of the Si NWs. The ideal intrinsic dynamic ranges of the devices are also collected in Table 6-1. Typical 100–200MHz Si NW resonators have intrinsic dynamic ranges of 100–130dB, for various dimensions and *Q*'s.

In the resonance detection of these high-impedance Si NWs, the signal level is much lower than that of the metallized devices because of strong signal attenuation due to large impedance mismatch. In this case, the high-resolution bridge-balancing and background-nulling techniques have been crucial and indispensable for detecting the resonances. To the best of our knowledge, this represents the first successful ≥200MHz electromechanical resonance readout from kilo-Ohm resonators. This demonstrates that, although direct detection of resonances from kilo-Ohm devices does not scale well into the VHF/UHF regimes, carefully engineering the readout circuitry can help to push the limits for the detection of high-impedance VHF/UHF resonators. Also comparing Fig. 6.3 with Fig. 6.2, the noise level of the kilo-Ohm devices is higher than that of the metallized devices. This is because the Johnson noise from the kilo-Ohm devices is larger than that from the metallized ~50Ω devices; and the noise floor of the measurements are limited by the thermal (Johnson) noise referred to the input of the preamplifier plus the amplifier noise. In all these measurements we have calibrated the noise figure of the preamplifier to be 0.13dB (which is equivalent to a noise temperature of 9K, and a noise voltage of 0.158nVolt/√Hz). This level is higher than the typical thermomechanical noise level of the Si NW devices (~0.01nVolt/√Hz), thus for resonance detection the measurements noise floor is set by the Johnson noise. This noise floor mismatch usually induces a loss of ~25dB from the device intrinsic dynamic range, and for stable and reliable performance the device is often operating at least a few dB lower than the onset of nonlinearity, hence the practical dynamic range of the device is

typically around 70–95dB, which is already quite good and again on par with some of the best top-down SiC resonators [27]. The basic specifications of both metallized and bare Si NWs are summarized in Table 6-1. As a reference, the specifications of a representative VHF SiC resonator (190MHz) are also provided. The Si NWs have performances comparable to bottom-up SiC resonators. If further scaled up, it is expected that these Si NWs resonators can also operate routinely in the UHF and microwave ranges.

It is also observed that for similar dimensions and frequencies, pristine Si NWs have considerably higher *Q*'s than those of metallized devices. For example, both the 215MHz bare Si NW device and the 200MHz metallized device have similar aspect ratios, but the 215MHz bare Si NW device has a *Q* about 2.5 times higher than the 200MHz metallized device. This should mainly be ascribed to an effect of the metallization, which introduces an inhomogeneous interface between the structural Si NW and the conducting metal layers, and thus causes more internal friction as compared to the bare Si NW device. The same aspect ratio implies that the devices should have similar clamping loss. The higher *Q*'s of the pristine Si NWs also is a result of the fact that the devices are from epitaxially grown single-crystal Si and thus inherently have minimal internal friction, as the growth process is engineered for yielding high-quality single-crystal structures. This is consistent with the studies of quality factors from top-down NEMS devices — the heavily-doped, bare Si or GaAs beam devices have higher quality factors than their metallized counterparts [26]. This also suggests that, in devices which have to be metallized for better impedance matching and for which high *Q*'s are also desirable, it is crucial to develop engineering solutions to optimize the inhomogeneous interface between the metallization and the structural layers, and the internal friction of the metallization layers themselves.

Table 6-1 Specifications and performance of some measured VHF Si NW resonators. The Si NWs are named by their nominal resonance frequency in MHz, with "M" denotes the use of metallization layers. For comparison, we also list the specifications and performance of the 190MHz SiC resonator.

Specifications	SiNW-215	SiNW-80	SiNW-M-200	SiNW-M-188	SiC-M-190
Length L (μm)	1.69	2.77	2.25	2.1	2.3
Diameter d (nm)	81	74	142	118	w=150, t=100
Aspect Ratio	20.9	37.4	16	18	15.3
Metallization	no metallization	no metallization	30nm Al +5nm Ti	30nm Al +5nm Ti	30nm Al +5nm Ti
Device Resistance (Ω)	3.135k	3.616k	~50	~50	~50
Resonance Frequency f_0 (MHz)	215.415	80.57	199.68	187.86	190
Quality Factor (Q)	5750	13100	2000	2500	5000
Spring Constant k_{eff} (N/m)	28.4	5.45	90.3	122.5	141.1
Device Mode Mass (fg)	15.5	21.3	57.4	87.9	96
Amplitude a_C (nm)	0.8	0.6	1.6	1.8	1.0
Dynamic Range (dB)	121	105	134	135	128
Measured Frequency Stability ($\langle\delta f_0/f_0\rangle$) ($\tau$=1sec)	1.34×10^{-6}	1.45×10^{-6}	1.82×10^{-7}	1.47×10^{-7}	1.1×10^{-7}
Mass Responsivity (Hz/zg)	6.9	1.89	1.74	1.07	1.16
Mass Resolution (zg)	41	62	21	26	21

6.5 Piezoresistive Detection of Si NW Resonators

Another very attractive attribute of these Si NWs is that they are piezoresistive, with surprisingly large gauge factors approaching the order of $\sim10^3$, as was recently investigated in some initial Si NW static bending experiments combined with transport measurements by using AFM tips to bend the Si NWs or by bending a calibrated substrate upon which the Si NWs are mounted [30]. Here we explore the piezoresistive properties of these Si NWs and exploit this effect to perform piezoresistive detection of the Si NW resonators. For these VHF Si NWs, we demonstrate the combination of magnetomotive excitation and piezoresistive detection. We not only apply RF driving current through the Si NWs, as required by the magnetomotive excitation, but also apply

bias current through the NWs for piezoresistive readout. For high-impedance VHF piezoresistive Si NWs we apply an RF bias instead of a DC bias to detect the response by piezoresistive frequency down-conversion [31].

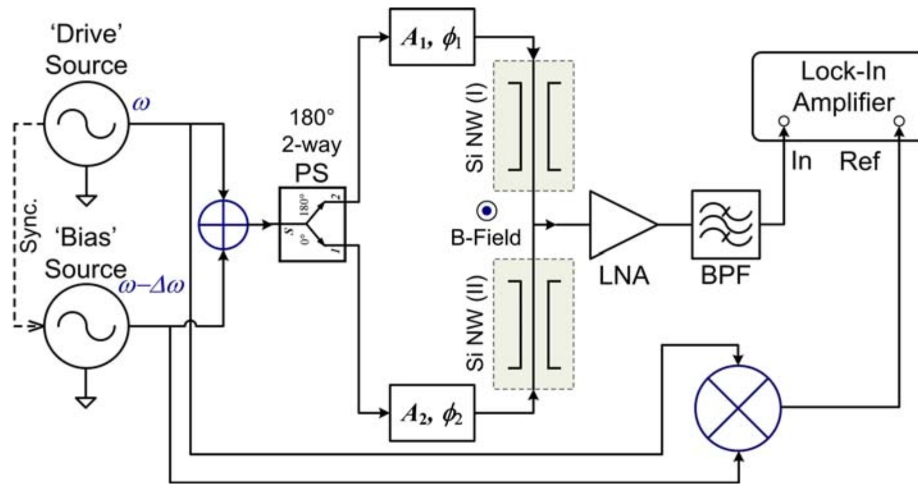

Fig. 6.4 Piezoresistive frequency down-conversion detection scheme with bridge circuit for pairs of Si NWs resonators. The 'drive' and 'bias' signals are combined (⊕) and sent to the bridge circuit consisting of the 2-way 180° power splitter (PS), the amplitude and phase adjustment (A_i, ϕ_i) and a Si NW device in either branch of the bridge. The transmission response is amplified by a low-noise amplifier (LNA) and properly filtered with a band-pass filter (BPF), and then detected by an RF lock-in amplifier with the reference signal generated by direct frequency down-conversion (⊗) from the 'drive' and 'bias' signal sources.

As shown in Fig. 6.4, in a balanced-bridge circuit scheme both of the high-impedance (kΩ) bare Si NWs server as piezoresistors for signal down-conversion. RF signals from two synchronized sources (two HP 8648B units), one the 'drive' source providing the sweeping RF current (ω) for magnetomotive excitation and the other a 'bias' source providing the RF bias (ω-$\Delta\omega$), are first combined and then sent to the bridge circuit. When the RF drive (ω) is swept in the vicinity (resonance bandwidth) of the Si NW resonance (ω_0), the magnetomotive effect excites the NW into resonant motion, which yields a device resistance change $\Delta R_i\cos(\omega t)$ for the i-th (i=1,2) device with original resistance Ri_0 in the circuit,

$$\Delta R_i = \frac{R_{i0}}{L_i} \cdot \int_0^{L_i} \left[(1+2\nu) + \frac{\Delta\gamma/\gamma}{\varepsilon} \right] \cdot \varepsilon(x) \cdot dx \equiv R_{i0} \cdot G \cdot \frac{1}{L_i} \int_0^{L_i} \varepsilon(x) \cdot dx \,, \tag{6-1}$$

where v is the Poisson ratio, γ is the resistivity, and $G \equiv (1+2\nu) + (\Delta\gamma/\gamma)/\varepsilon$ is the gauge factor. For semiconducting Si NWs, G is dominated by the $(\Delta\gamma/\gamma)/\varepsilon$ term, which is usually taken as a constant and can be of the order 10^2~10^3 [30], while the geometric term is only (1+2ν)≈1.5 given the Poisson ratio of ~0.25 for Si. The first-order net strain of the doubly-clamped Si NWs in eq. (6-1) is mainly due to the Si NW's tapered structure and the asymmetry in doping and resistivity distribution in the Si NW cross section and along the NW.

Setting RF bias far enough from the resonance will not induce appreciable Si NW movement, but the RF bias current sees and picks up the device resistance change and thus yields a piezoresistive signal (as seen by the first stage amplifier),

$$\begin{aligned} \Delta V_{PR,i} &\approx \frac{V_B}{2(R_1+R_2)} \cos[(\omega-\Delta\omega)t+\phi] \cdot \Delta R_i \cos(\omega t) \\ &= \frac{V_B \cdot \Delta R_i}{4(R_1+R_2)} \cos(\Delta\omega t - \phi) + \frac{V_B \cdot \Delta R_i}{4(R_1+R_2)} \cos[(2\omega-\Delta\omega)t+\phi] \end{aligned}, \tag{6-2}$$

where VB is the bias RF voltage (as seen by the 180° 2-way power splitter) and ϕ is the (initial) phase offset between the synchronized 'drive' and 'bias' RF signals. The up-conversion (2ω-$\Delta\omega$) component is filtered out and the down-conversion $\Delta\omega$ is picked up as the Si NW piezoresistive response, which is detected by an RF lock-in amplifier with the reference signal being provided by direct mixing of the 'drive' and 'bias' signals (Fig. 6.4).

In this scheme, the sweeping frequency 'drive' source is working as a network analyzer's source in the network analysis mode for two-port detection from which the

resonances (such as those in Fig. 6.1 and Fig. 6.2) have been obtained. While the piezoresistive signal mixing cannot be implemented in simple network analysis mode, here the synchronized 'bias' source is generating RF bias which is constantly $\Delta\omega$ away from the 'drive' frequency. One uniqueness of this scheme is that it is to date the first combination of the magnetomotive excitation, which is particularly powerful for VHF/UHF/microwave NEMS resonators [25], and the piezoresistive detection, which is very convenient and effective for high-impedance (kΩ) devices. We choose the down-conversion intermediate frequency $\Delta\omega$ to be high enough to satisfy two considerations: (i) $\Delta\omega$ is much larger than the resonance bandwidth, i.e., $\Delta\omega >> \omega_0/Q$, so that when the 'drive' source is sweeping the frequency in a wide band, only the 'drive', but not the 'bias', hit the device resonance frequency, thus only obtaining one resonance peak for each device; and (ii) $\Delta\omega$ is in the frequency range for a convenient RF lock-in detection.

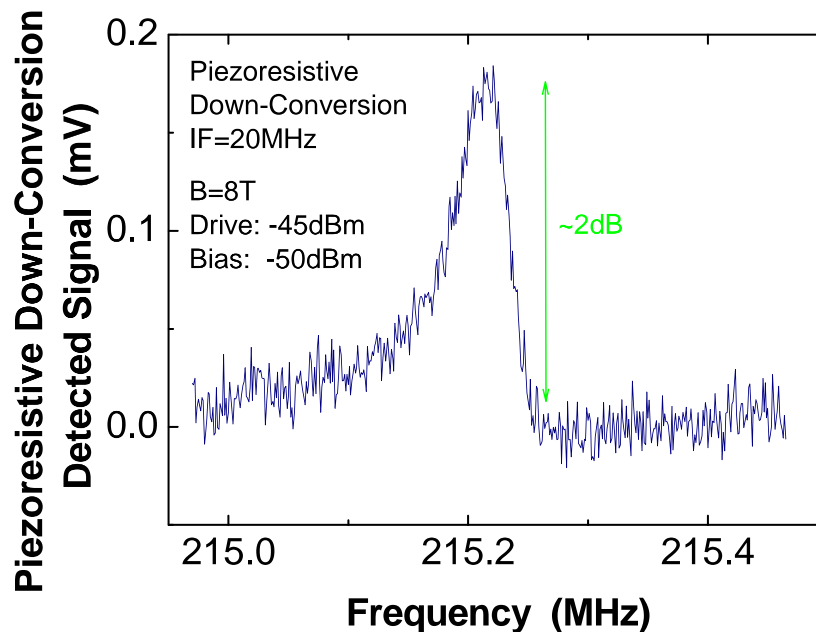

Fig. 6.5 VHF NEMS resonance transduction by the combination of magnetomotive excitation and piezoresistive detection. Resonance signal of the high-impedance 215MHz Si NW device without metallization, detected by using the piezoresistive frequency down-conversion scheme.

Fig. 6.5 shows the measured piezoresistive down-conversion signal from the 215MHz Si NW device by using an intermediate frequency $\Delta\omega$=20MHz. As shown in Fig. 6.5 inset, the piezoresistive down-conversion signal amplitude has a linear dependence on bias, confirming the piezoresistive effect as described by eq. (6-2).

6.6 Si NW Mechanical Properties Measured in Resonant Mode

Thus far, we have demonstrated that the Si NWs grown across the microtrenches are robust VHF nanomechanical resonators, and that they are also versatile devices in terms of electrical attributes and transduction schemes, either being matched to RF/microwave standard (50Ω) with metallization, or as high-impedance but heavily-doped semiconductor piezoresistors. Since the Si NWs are from single-crystal epitaxial growth, they have pretty high Q's as bare piezoresistive devices, and also decently high Q's as metallized devices. All these attributes suggest interesting applications for Si NWs.

An immediate application of the demonstrated Si NW resonators and techniques is towards the study of the basic properties of VLS epitaxial Si NWs. For instance, the measurement of the Young's modulus of these Si NWs can be made in the resonance mode, instead of using AFM to perform the tedious static bending experiments. While bending Si NWs with AFM tips appears to be straightforward for measuring the strength and elastic modulus (Young's modulus), the displacement and strain in the Si NWs are usually inferred from the AFM tip's movement and AFM cantilever's deflection, and are thus carried out with possibly large error bars. For the fundamental flexural mode of non-metallized doubly-clamped Si NW resonators, the fundamental resonance frequency is

$$f_0 = \frac{22.4}{(2\pi)L^2}\sqrt{\frac{E_Y I}{\rho A}} = 0.8913\sqrt{\frac{E_Y}{\rho}} \cdot \frac{d}{L^2}, \tag{6-3a}$$

where E_Y is the Young's modulus of Si NW, ρ is mass density (2330kg/m^3), $I=\pi d^4/64$ is the momentum of inertia and $A=\pi d^2/4$ is the cross section of the Si NW, respectively, with d the NW diameter. For metallized Si NWs, the mass loading effect of the metallization should be considered and the resonance frequency is

$$f_{0,m} = 0.8913\sqrt{\frac{E_Y}{\rho}} \cdot \frac{d}{L^2} \cdot \sqrt{\frac{m_m}{m + m_m}}, \qquad (6\text{-}3b)$$

where m is the structural Si NW mass, and m_m is the mass of the metallization layers. The resonance mode measurements have the advantage that the resonance frequency can be measured very precisely and the Young's modulus can be determined based on eq. (6-3) even without knowing the details of the displacement and strain of the device. The accuracy will partially rely on the accurate measurement of the Si NW dimensions, which is also essential for the AFM contact mode bending method. Considering that the AFM tip size is usually much larger than the diameter of a Si NW, and that AFM approaching and pushing Si NW at some sweet spot is trial-and-luck based, and difficult and time-consuming, determination of the mechanical rigidity and elastic properties by reliably measuring resonance mode frequency is a valuable technique.

Table 6-2 presents the Young's modulus extracted from the accurate measurements of the resonance frequencies of the devices, based on eq. (6-3). The Si NWs' diameters are read out from high-resolution SEM imaging with an error bar of ~2nm, and the length error is within ~2%. The mass density ρ is well-known for single-crystal Si and does not change from bulk Si to Si NWs, as the single-crystal nature of the Si NWs has been verified with STM [21]. Hence the accurate measurement of resonance frequency leads to reliable determination of Young's modulus.

As shown in Table 6-2, the Si NW Young's modulus values obtained in this study are very close to those of bulk single crystal Si (111), ~160–200GPa, as widely accepted and taken in literature; and are in very good agreement with a recent elaborate AFM bending study [22]. We note that the Si NWs in this AFM study [22] and the present resonance measurements have been produced with similar processes in the same system in the same lab, but in different batches. There is a noticeable difference in the measured Young's modulus between the above data and 93−250GPa from another recent AFM study [23]. The difference may be ascribed to such subtleties in Si NWs as defects, and detailed differences in the two kinds of AFM bending experiments and their measurements accuracy and reliabilities [22,23].

Table 6-2 Young's modulus measured by dynamic method with the resonances of the Si NW resonators, as compared to static measurements with AFM bending experiments (we note that the widely used Young's modulus of bulk Si (111) is in the range of 160–200GPa).

Experiments and Samples	Device Diameter d (nm)	Si NW Length L (μm)	Young's Modulus E_Y (GPa)
SiNW-215	81	1.69	170 ± 15
SiNW-80	74	2.77	205 ± 18
SiNW-M-200	142	2.25	187 ± 16
SiNW-M-188	118	2.1	200 ± 17
AFM Bending-Cantilever [22]	120	8	≈186
AFM Bending-Beam [22]	190	12	≈207
AFM Bending-Cantilever [23]	140	10	≈93
AFM Bending-Beam [23]	200	10	≈150
AFM Bending-Beam [23]	200	10	≈250

6.7 Frequency Stability and Mass Sensitivity of Si NW Resonators

The Si NWs' attributes also make them interesting for nanosensor applications. We perform initial experimental investigations of the frequency stability and sensitivity of these Si NWs. We embed the Si NWs resonators into low-noise phase-locked loop (PLL) circuitry for real-time resonance frequency tracking to measure the instantaneous frequency fluctuations, and thus the frequency stability characteristics as a function of averaging time [27,28]. Shown in Fig. 6.6 is the measured real-time frequency

fluctuation with 1 sec averaging time, and the instantaneous frequency fluctuation is about 0.182ppm, for the metallized 200MHz Si NW resonator. In the real-time nanomechanical mass sensing paradigm [27,32], using this device as a mass sensor with its mass responsivity of 1.74Hz/zg, its frequency stability level translates into a mass resolution of 21g (1zg=10^{-21}g). The Si NWs' frequency stability and mass sensitivity performance are again comparable to the performances of some of the best top-down mass sensors made of single-crystal high-quality SiC. In particular, the 21zg noise floor is almost exactly the same as that achieved in the 100-zeptogram real-time mass loading steps monitored by a 190MHz SiC resonator [27]. The measured results of the frequency stability data and corresponding mass sensitivity for several other Si NWs devices are also collected in Table 6-2.

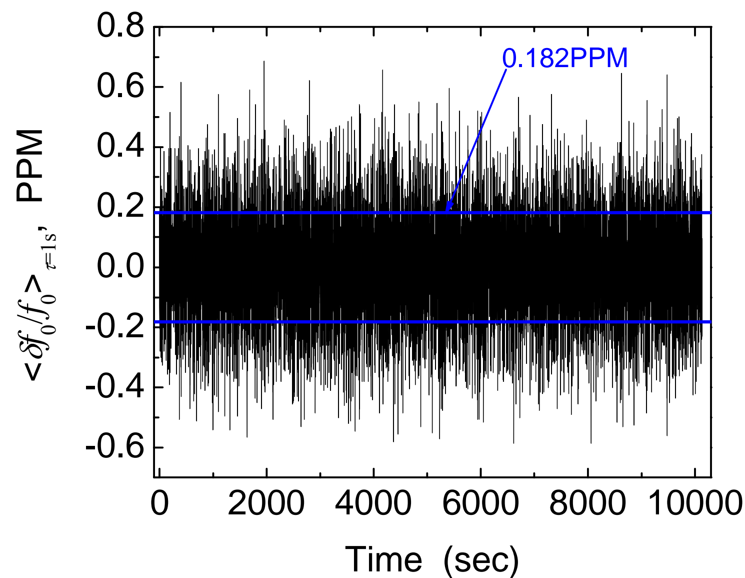

Fig. 6.6 Si NW resonator frequency stability characteristics. Fractional frequency fluctuation of the 200MHz metalized Si NW resonator, measured in real time with an averaging time of $\tau \approx 1$sec for each readout of the frequency data tracked by the phase-locked loop. The measured noise floor is 0.182PPM, which combined with the device mass responsivity, 1.74Hz/zg, leads to a resonant mass resolution of 21zg.

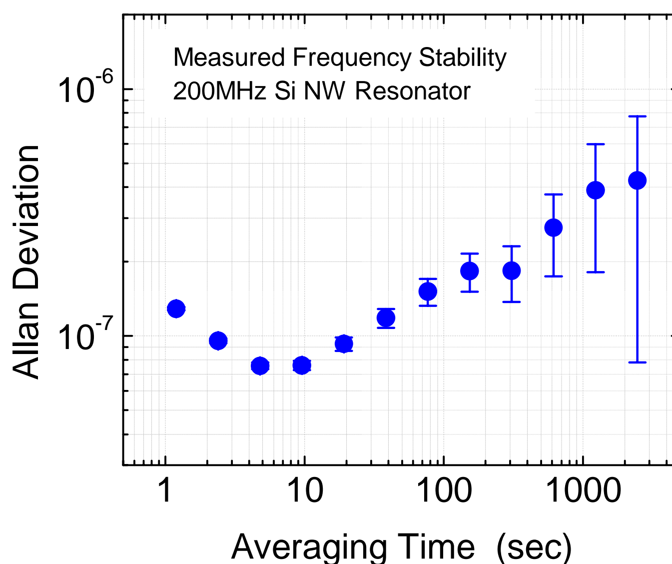

Fig. 6.7 Measured frequency stability performance, the Allan deviation as a function of averaging time, for the 200MHz Si NW resonator. The optimized Allan deviation achieved is 7.6×10^{-8} for around 5~10secs averaging time.

6.8 Quality Factor and Dissipation Issue of Si NW Resonators

Just like for the top-down SiC NEMS resonators, the quality factor and dissipation issue in the Si NW resonators are also of great interest and importance. We have conducted careful measurements of the *Q*'s and hence the dissipation in these VHF Si NWs. Our measurements and analyses follow the logic and approaches we have employed in studying the dissipation of top-down UHF SiC resonators in Chapter 5. Fig. 6.8 shows the measured dissipation as a function of device temperature for both the 188MHz and 200MHz metalized Si NW devices. The weak power law dependency of dissipation on temperature is again clearly visible. The dashed line in Fig. 6.8 shows the Q^{-1}~$T^{0.3}$ fit to guide the eyes—the Q^{-1}~$T^{0.3}$ dependency has also been identified in top-down Si MEMS and NEMS resonators (see Chapter 5). Here we see that this dependency fits the experimental data of 200MHz device very well, and fits that of the 188MHz device fairly well in the low-T range, while showing a visible deviation for T>60K.

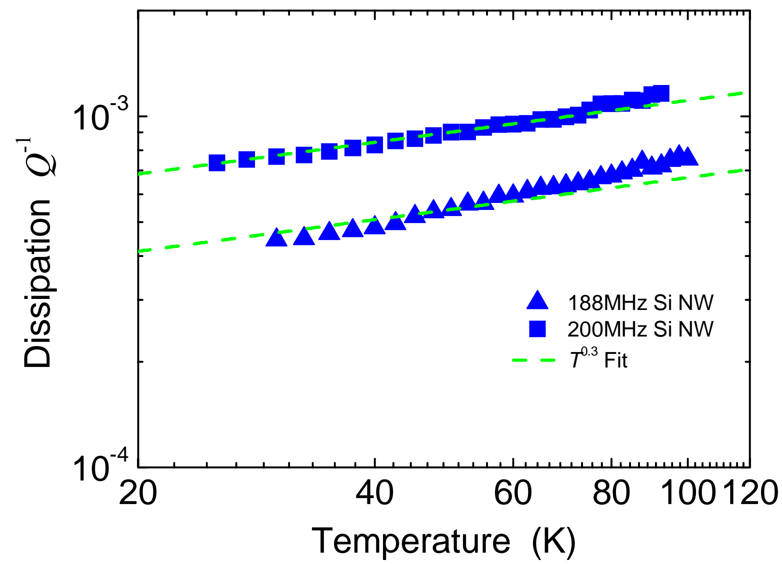

Fig. 6.8 Measured dissipation Q^{-1} as a function of temperature for two metalized Si NW resonators (200MHz and 188MHz devices). The dash line is the $Q^{-1} \propto T^{0.3}$ weak power-law dependency, as has been found in top-down Si MEMS and NEMS resonators.

The almost constant difference (offset) between the two traces in Fig. 6.8 is ascribed to the difference in clamping loss in these two devices, similar to the case of the SiC devices in Chapter 5. In these VHF Si NW resonators, the measurements also manifest that the clamping losses are the most significant and dominating dissipation mechanism. In brief, this is because of the energy radiation (loss) from the resonant mode of the vibrating Si NW to its supporting pads at the two self-welded ends. There is an interesting subtlety worth mentioning here: Although for these as-grown suspended Si NWs there is no etching undercut of the supporting pads, which is inevitable in top-down NEMS resonators, the self-welded clamping joints at the facing microtrench walls are usually fatter than the Si NW itself; this may have an effect resembling that of the etch undercut in the top-down devices and hence comprise the clamping losses.

6.9 Comparison with Other Nanowire Resonators

It would also be of interest to compare the Si NWs with other bottom-up nanowire-based rudimentary devices. The first bottom-up nanowire-based VHF NEMS resonator (105MHz) was demonstrated in a platinum (Pt) nanowire [33], where the device is assembled and connected to electrodes by painstaking processes including runs of AFM scanning and locating, coordinate mapping and e-beam lithography. The device then had to be suspended by wet etch and super critical point drying processes [33]. In comparison, the Si-NW-in-microtrench devices in the present work are fabricated in a much more systematic and controllable manner, thus having greatly enhanced yield of functional devices (over 80% of suspended doubly-clamped Si NW devices have reasonable resistances). Besides, the material itself, single-crystal Si, represents much more practical applications in nanoelectronic and electromechanical devices than Pt could promise. Furthermore, the Si NWs in this work are already operating in the ≥200MHz range and are allowing for various signal transduction schemes.

Compared to some of the smallest NWs made by the superlattice pattern transfer technique, which are especially attractive for making high-density arrays and crossbar junctions [34], the Si NWs in this work have great advantages in terms of fabrication and the development of field-effect-based electronic and electromechanical devices. In particular for as-grown free-standing Si NWs, recent progress has been made in controllable growth of vertically aligned Si NW arrays on patterned Si substrate by using Au colloid dispersion [35], selective growth of vertically and laterally aligned Si NW arrays by the use of galvanic displacement processes [36] and high-density Si NW arrays with uniform diameter and spacing by use of a porous anodic alumina mask for Si NW epitaxial growth [37]. By elaborate engineering of variants of these processes, it would be possible to make arrays of suspended cantilever and doubly-clamped Si NWs with

desired diameter, density and spacing, for large-scale integrated resonator arrays. With these arrays, interesting phenomena of Si NW resonator arrays, such as collective modes [38], coupling between individual resonators in the array, and the energy propagation in high density arrays, and their potential applications, could all be investigated in the near future.

From another point of view, to consider the ultimate limits of the Si-NW-based nanomechanical resonators, we note that the present Si-NW-in-microtrench devices and the aligned Si NW arrays typically have their diameters in the 40~150nm range where the aligned epitaxial growth can have reliable, high yield with high quality. Meanwhile, to date the smallest Si NWs reported are of molecular dimensions with as small as 3nm diameter [39], grown by using silane with very small Au particle catalysts in a process that does not directly yield suspended devices and arrays of devices. We expect to combine the molecular scale Si NW growth techniques with the suspended Si NWs and arrays technologies, so that Si NW resonators of molecule dimensions can be made. Further scaling down the Si NWs dimensions, ultimately to the molecular scale, can not only offer resonators operating well into the microwave regime, but also may provide unique probes for fundamental studies such as quantum electro mechanics [40].

6.10 Chapter Summary

In the work presented in this chapter, we have demonstrated that the single-crystal Si NWs grown in pre-patterned microtrenches by epitaxial VLS process are excellent NEMS resonators. These Si NWs are as-grown suspended and can be fabricated as either cantilevers or doubly-clamped resonators. They are robust and the self-welded junctions between the Si NWs and the microtrench walls provide rigid clamping anchors for the resonators to allow for VHF and UHF operations. The Si NWs are versatile resonators,

which can be metallized or doped to utilize as piezoresistors, thus allowing different resonance transduction schemes. Besides the mangetomotive transduction, which is suitable for VHF/UHF resonators, we have also successfully demonstrated the novel scheme of combining magnetomotive excitation and piezoresistive detection. With well-controlled piezoresistive properties of the Si NWs this can be further used as a detection scheme with other excitation techniques (*e.g.*, electrostatic). The Si NWs have proven themselves to have high performances in terms of quality factors, operating frequencies and resonance frequency stabilities, comparable to those of the best top-down NEMS resonators. The measured frequency stabilities for the Si NWs, combined with their superb mass responsivities, demonstrate that they are among the state-of-the-art nanomechanical mass sensors with sensitivities well in the zeptogram regime. Currently, ongoing research is focused on making even smaller high-quality suspended Si NWs for UHF/microwave operation and other related enabling technologies.

Bibliography

[1] Y. Cui, C.M. Lieber, "Functional nanoscale devices assembled using silicon nanowire building blocks", *Science* **291**, 851-853 (2001).

[2] Y. Huang, X.F. Duan, Y. Cui, L.J. Lauhon, K.-H. Kim, C.M. Lieber, "Logic gates and computation from assembled nanowire building blocks", *Science* **294**, 1313-1317 (2001).

[3] Y. Cui, Z.H. Zhong, D.L. Wang, W.U. Wang, C.M. Lieber, "High performance silicon nanowire field effect transistors", *Nano Lett.* **2**, 149-152 (2001).

[4] G.F. Zheng, W. Lu, S. Jin, C.M. Lieber, "Synthesis and fabrication of high-performance n-type silicon nanowire transistors", *Adv. Mater.* **16**, 1890-1893 (2004).

[5] Y. Cui, Q.Q. Wei, H.K. Park, C.M. Lieber, "Nanowire nanosensors for highly sensitive and selective detection of biological and chemical species", *Science* **293**, 1289-1292 (2001).

[6] J.I. Hahm, C.M. Lieber, "Direct ultrasensitive electrical detection of DNA and DNA sequence variations using nanowire nanosensors", *Nano Lett.* **4**, 51-54 (2004).

[7] F. Patolsky, G.F. Zheng, Q. Hayden, M. Lakadamyali, X.W. Zhuang, C.M. Lieber, "Electrical detection of single viruses", *Proc. Nat. Aca. Sci.* **101**, 14017-14022 (2004).

[8] W.U. Wang, C. Chen, K.H. Lin, Y. Fang, C.M. Lieber, "Label-free detection of small-molecule—protein interactions by using nanowire nanosensors", *Proc. Nat. Aca. Sci.* **102**, 3208-3212 (2005).

[9] G.F. Zheng, F. Patolsky, Y. Cui, W.U. Wang, C.M. Lieber, "Multiplexed electrical detection of cancer markers with nanowire sensor arrays", *Nature Biotech.* **23**, 1290-1301 (2005).

[10] (a) D.Y. Li, Y.Y. Wu, P. Kim, L. Shi, P.D. Yang, A. Majumdar, "Thermal conductivity of individual silicon nanowires", *Appl. Phys. Lett.* **83**, 2934-2936 (2003). (b) D.Y. Li, Y.Y. Wu, R. Fan, P.D. Yang, A. Majumdar, "Thermal conductivity of Si/SiGe superlattice nanowires", *Appl. Phys. Lett.* **83**, 3186-3188 (2003).

[11] Y.Y. Wu, P.D. Yang, "Direct observation of vapor-liquid-solid nanowire growth", *J. Am. Chem. Soc.* **123**, 3165-3166 (2001).

[12] Y. Cui, L.J. Lauhon, M.S. Gudiksen, J.F. Wang, C.M. Lieber, “Diameter-controlled synthesis of single-crystal silicon nanowires”, *Appl. Phys. Lett.* **78**, 2214-2216 (2001).

[13] J.B. Hannon, S. Kodambaka, F.M. Ross, R.M. Tromp, “The influence of the surface migration of gold on the growth of silicon nanowires”, *Nature* **440**, 69-71 (2006).

[14] Y. Huang, X.F. Duan, Q.Q. Wei, C.M. Lieber, “Direct assembly of one-dimensional nanostructures into functional networks”, *Science* **291**, 630-633 (2001).

[15] D.M. Whang, S. Jin, Y. Wu, C.M. Lieber, “Large-scale hierarchical organization of nanowire arrays for integrated nanosystems”, *Nano Lett.* **3**, 1255-1259 (2003).

[16] S. Jin, D.M. Whang, M.C. McAlpine, R.S. Friedman, Y. Wu, C.M. Lieber, “Scalable interconnection and integration of nanowire devices without registration”, *Nano Lett.* **4**, 915-919 (2004).

[17] K.E. Petersen, “Silicon as a mechanical material”, *Proc. IEEE* **70**, 420-457 (1982).

[18] A.N. Cleland, M.L. Roukes, “Fabrication of high frequency nanometer scale mechanical resonators from bulk Si substrates”, *Appl. Phys. Lett.* **69**, 2653-2655 (1996).

[19] M.L. Roukes, “Nanoelectromechanical systems face the future”, *Physics World* **14**, 25-31 (2001).

[20] M.S. Islam, S. Sharma, T.I. Kamins, R.S. Williams, “Ultrahigh-density silicon nanobridges formed between two vertical silicon surfaces”, *Nanotechnology* **15**, L5-L8 (2004).

[21] R.R. He, D. Gao, R. Fan, A.I. Hochbaum, C. Carraro, R. Maboudian, P.D. Yang, “Si nanowire bridges in microtrenches: integration of growth into device fabrication”, *Adv. Mater.* **17**, 2098-2102 (2005).

[22] A. San Paulo, J. Bokor, R.T. Howe, R.R. He, P.D. Yang, D. Gao, C. Carraro, R. Maboudian, “Mechanical elasticity of single and double clamped silicon nanobeams fabricated by the vapor-liquid-solid method”, *Appl. Phys. Lett.* **87**, 053111 (2005).

[23] M. Tabib-Azar, M. Nassirou, R. Wang, S. Sharma, T.I. Kamins, M.S. Islam, R.S. Williams, “Mechanical properties of self-welded silicon nanobridges”, *Appl. Phys. Lett.* **87**, 113102 (2005).

[24] S. Hoffmann, I. Utke, B. Moser, J. Michler, S.H. Christiansen, V. Schmidt, S. Senz, P. Werner, U. Gösele, C. Ballif, "Measurement of the bending strength of vapor-liquid-solid grown silicon nanowires", *Nano Lett.* **6**, 622-625 (2006).

[25] X.M.H. Huang, X.L. Feng, C.A. Zorman, M. Mehregany, M.L. Roukes, "VHF, UHF and microwave nanomechanical resonators", *New J. Phys.* **7**, 247 (2005).

[26] K.L. Ekinci, Y.T. Yang, X.M.H. Huang, M.L. Roukes, "Balanced electronic detection of displacement in nanoelectromechanical systems", *Appl. Phys. Lett.* **81**, 2253-2255 (2002).

[27] Y.T. Yang, C. Callegari, X.L. Feng, K.L. Ekinci, M.L. Roukes, "Zeptogram-scale nanomechanical mass sensing", *Nano Lett.* **6**, 583-586 (2006).

[28] X.L. Feng, C.J. White, A. Hajimiri, M.L. Roukes, "Ultra-high frequency low-noise self-sustaining oscillator with vibrating nanodevice", *to be published* (2006).

[29] X.L. Feng, C.A. Zorman, M. Mehregany, M.L. Roukes, "Dissipation in single-crystal SiC UHF nanomechanical resonators", *Tech. Digest of the 2006 Solid-State Sensors, Actuators & Microsystems Workshop (Hilton Head 2006)*, 86-89, Hilton Head Island, SC, June 4-8 (2006).

[30] R.R. He, P.D. Yang, "Giant piezoresistance effect in silicon nanowires", *to be published* (2006).

[31] I. Bargatin, E.B. Myers, J. Arlett, B. Gudlewski, M.L. Roukes, "Sensitive detection of nanomechanical motion using piezoresistive signal down-mixing", *Appl. Phys. Lett.* **86**, 133109 (2005).

[32] K.L. Ekinci, Y.T. Yang, M.L. Roukes, "Ultimate limits to inertial mass sensing based upon nanoelectromechanical systems", *J. Appl. Phys.* **95**, 2682-2689 (2004).

[33] A. Husain, J. Hone, H.W.C. Postma, X.M.H. Huang, T. Drake, M. Barbic, A. Scherer, M.L. Roukes, "Nanowire-based very-high-frequency electromechanical resonator" *Appl. Phys. Lett.* **83**, 1240-1242 (2003).

[34] N.A. Melosh, A. Boukai, F. Diana, B. Gerardot, B. Badolato, P.M. Petroff, J.R. Heath, "Ultrahigh-density nanowire lattices and circuits", *Science* **300**, 112-115 (2003).

[35] A.I. Hochbaum, R. Fan, R.R. He, P.D. Yang, "Controlled growth of Si nanowire arrays for device integration", *Nano Lett.* **5**, 457-460 (2005).

[36] D. Gao, R.R. He, C. Carraro, R.T. Howe, P.D. Yang, R. Maboudian, "Selective growth of Si nanowire arrays via galvanic displacement processes in water-in-oil microemulsions", *J. Am. Chem. Soc.* **127**, 4574-4575 (2005).

[37] I. Lombardi, A.I. Hochbaum, P.D. Yang, C. Carraro, R. Maboudian, *Chem. Mater.* "Synthesis of high density, size-controlled Si nanowire arrays via porous anodic alumina mask", **18**, 988-991 (2006).

[38] E. Buks, M.L. Roukes, "Electrically tunable collective response in a coupled micromechanical array", *J. Microelectromechanical Syst.* **11**, 802-807 (2002).

[39] Y. Wu, Y. Cui, L. Huynh, C.J. Barrelet, D.C. Bell, C.M. Lieber, "Controlled growth and structures of molecular-scale silicon nanowires", *Nano Lett.* **4**, 433-436 (2004).

[40] K.C. Schwab, M.L. Roukes, "Putting mechanics into quantum mechanics", *Phys. Today* July Issue, 36-42 (2005).

Chapter 7

Conclusions and Perspectives

This chapter concludes the thesis by delineating a realistic path to single-Dalton mass sensitivity with UHF NEMS resonators. A futuristic outlook of the technologies developed in the thesis is described. Some interesting and important research topics are envisioned, and the enabling UHF NEMS technologies for these topics are discussed.

7.1 Concluding Remarks

Low-noise self-oscillation and phase-locking with UHF NEMS resonators have been developed as the two key technologies that are indispensable for implementing the generic protocol of real-time NEMS mass sensing, and for developing the sensor system at the back end of a NEMS-based mass spectrometer. With typical ~500MHz devices, we have achieved mass sensitivity approaching the level of ~1zg (~0.6kDalton). This

level of sensitivity is readily useful for mass sensing of many typical biomolecules (with their masses in the 1−100zg range).

In pushing for the ultimate mass resolution required for mass spectrometry, our analyses have shown that the single-Dalton (1amu) mass sensitivity is realistically within reach if we continue to extend our roadmap beyond the demonstrated 200~500MHz range (see Preface). As listed in Table 7.1, with next generations of UHF/microwave NEMS resonators (from 500MHz to 1GHz), sensitivity can be further improved from hundreds of yoctograms to the single-Dalton (1 Dalton=1.66yg) level. The prediction of this extended roadmap is realistic: All the device dimensions proposed here are practically achievable with today's nanofabrication technologies; their Q's are moderate by taking account what we have observed compromise in Q's of UHF devices. The major challenges will be efficient signal detection from these even smaller devices, and noise matching issues, which might prevent us from smoothly approaching the 10^{-9}~10^{-10} frequency stability. According to our recent related efforts and successful experience, we think these challenges will be overcome by further elaborately engineering low-noise oscillator and phase-locking technologies for these devices.

Table 7-1 *Realistic* roadmap and path toward single-Dalton mass sensitivity with NEMS.

Resonance Frequency (Device)	Device Dimensions L(μm)×w(nm)×t(nm)	Quality Factor Q	Active Device Mass M_{eff} (fg)	Dynamic Range (dB)	Frequency Stability σ_A (1sec)	Mass Sensitivity δM (yg)
650 MHz (SiC Beam)	1.38×120×80	2000	40	104	1.2×10^{-9}	137
1 .03GHz (SiC Beam)	1.1×120×80	1000	32	113	6.8×10^{-10}	62
1.03 GHz (Smaller SiC Beam)	0.7×50×50	1500	5.6	110	4.0×10^{-10}	6.4
1.0 GHz (Si NW, Bottom-Up)	L=0.625μm, d=50nm	2000	2.1	100	3.2×10^{-10}	1.9

Still more, besides NEMS mass sensing, we note that both technologies are of at least equal importance for engineering high-performance UHF NEMS resonators for applications in nanomechanical signal processing, communication and computation.

Our investigation on the dissipation mechanisms in UHF NEMS resonators leads to useful guidelines for future device Q-engineering. The work on high-performance Si NW resonators suggests a promising alternative for approaching some of the above applications, particularly when molecular-scale devices will play a key role.

7.2 Perspectives and Future Topics

We propose and discuss the following interesting research topics and directions extending beyond the work in this thesis.

Immediately a prototype of single-biomolecule (mass) counting with NEMS can be developed based on the sensitivity already demonstrated in this thesis. Currently we have an in-progress project in which we aim to weigh individual, big biomolecules one by one. The next steps along this direction include weighing and distinguishing binary mixtures of biomolecules with large enough mass difference, demonstrating yoctogram sensitivity and approaching single-Dalton sensitivity. All these are important milestones toward NEMS-based mass spectrometry.

In parallel, transforming present UHF NEMS technologies into integrated, on-chip NEMS technologies is another inviting but challenging topic. This would be the prerequisite for applications of NEMS in signal processing and communication. On this path, the major challenges would be integrated transduction of UHF NEMS resonators,

and integration with IC and packaging, which would require pushing the limits for both device nanofabrication and the scaling laws. In fact, the recent successful commercialization of Si MEMS resonators technologies by Discera (www.discera.com) and SiTime (www.sitime.com) has conveyed encouraging messages, because these MEMS resonators faced similar practical challenges as NEMS today do. Along this direction, but thinking of scaling down the best of MEMS resonators, it is interesting to envision nanofabricated bulk acoustic resonators (nanoBARs) and nanodisk resonators that would promise the highest frequency-quality factor-product ($f \times Q$), and thus being the best candidate for ultralow power nanomechanical signal processing. This exploration would help open up new possibilities of further miniaturizing the state-of-the-art BAR and disk resonators. For beam-structured NEMS resonators, coupled resonators and arrays of resonators are expected to boost up power handling capability and are worth studying for potential applications in tunable oscillators and filters.

For some moderate mass sensing applications where the sensitivity down to the single-molecule level is not very crucial and our UHF NEMS technologies are already more than enough sensitive, it is desirable to engineer the technologies into portable or handset systems. In this regard, both the PLL and oscillator modes can be used, but the oscillator mode has a special advantage of being an active system and not requiring external stable (or moderately stable) VCOs. In particular, the oscillator mode provides a generic solution for the signal output of arrays of NEMS resonators. Moreover, the oscillator mode also suggests a possible solution for wideband measurements of NEMS resonators in fluids.

The low-noise UHF NEMS technologies have significant implications for fundamental physics research from which many of today's NEMS structures have originated. In a generalized sense, the technologies we have developed are sensing and detection technologies involving low-loss nanomechanical devices, which are essentially very

interesting mesoscopic systems under certain physical conditions. For instance, for quantum electromechanics (QEM) measurements (such as quantum limited displacement sensing and Fock state detection), in principle all the NEMS oscillator, phase-locking, NW and high-Q technologies are relevant and can be possibly useful. These technologies can also be used in probing mesoscopic phenomena inside some specifically designed NEMS devices, and the wealthy phenomena and processes on the surface of a NEMS device. Furthermore, these technologies can also be employed to study a wide spectrum of coupling effects when the UHF NEMS device is involved as a sensor or probe in the coupling. For example, it would be very interesting to study the coupling between a NEMS resonator and a nearby cofabricated photonic device (*e.g.*, a nanofabricated laser). This kind of exploration may lead to novel transductions that are particularly useful for mesoscopic nanodevices but not available if simply scaling down from the macro world and MEMS. However, most of these fundamental studies would probably have to be performed in ultra-high vacuum at cryogenic temperatures.

Facing the future, although today's NEMS technologies are still in their sprouting stage, roughly like transistors in the 1950's and MEMS in the 1990's, we have good reasons to believe that exploring NEMS and engineering NEMS is a great enterprise. In particular, high-performance UHF NEMS resonators offer immense potential applications that critically rely on NEMS engineering—for which there is plenty of room, indeed.

Appendix A

List of Major Instruments and Apparatus

A.1 Vacuum Systems

1. Large Ultra-High Vacuum (UHV) System

Large UHV Chamber:	Home Built
Pumps Installed: Turbo-V 250	Varian
Backing/Rough Pump: Diaphragm Vacuum Pump	Varian

2. Small High Vacuum Cryostat Systems (Two Cryostat Dippers)

Small Cryostat Chambers (Dippers):	Home Built
Movable Pump Station: Turbo-V 300	Varian

A.2 Cryogenic Apparatus

Large Helium Dewar:	Precision Cryogenic Systems, Inc.
Superconducting Magnet Power Supply IPS120-10:	Oxford Instruments
LakeShore 331 Temperature Controller:	LakeShore

A.3 Instruments for Electronic Measurements

Instrument	Manufacturer
Agilent 34401A Digit Multimeter	Agilent
Agilent 4395A Network/Spectrum/Impedance Analyzer	Agilent
Agilent 53132A Universal Counter	Agilent
Agilent E3611A DC Power Supply	Agilent
Agilent Infinium 8000 Series Oscilloscope	Agilent
HP 35665A Dynamic Signal Analyzer	Hewlett Packard
HP 3577A (5Hz-200MHz) Network Analyzer	Hewlett Packard
HP 8563E (9kHz-26.5GHz) Spectrum Analyzer	Hewlett Packard
HP 8648B (100kHz-2GHz) Signal Generator	Hewlett Packard
HP 8720C (50MHz-20GHz) Network Analyzer:	Hewlett Packard
RDL NTS-1000B Phase Noise Analyzer[①]	RDL Inc.
SR560 Low-Noise Preamplifier:	Stanford Research Systems
SR830 DSP Lock-In Amplifier:	Stanford Research Systems
SR844 RF Lock-In Amplifier:	Stanford Research Systems

All the small components and subassemblies involved in the systems and measurements are not listed.

[①]Courtesy of Prof. Ali Hajimiri and his group.

A.4 Nanofabrication and Characterization Instruments

Instrument	Manufacturer
Karl Suss MJB3 Mask Aligner	Karl Suss
Nikon Optiphot (Japan 281438) Optical Microscope	Nikon
Samco UV&Ozone Dry Stripper, Model UV-1	Samco
Headway Spinner, Model PWM32	Headway Research Inc.
04644 Series Digital Hot Plate/Stirrer	Cole-Parmer
Ultrasonic Bath and Cleaner	Cole-Parmer
JEOL JSM-6400 Scanning Microscope	JEOL
Sirion High Resolution SEM	FEI Company
Quanta (Environmental) SEM	FEI Company
NanoScope Dimension 3000/3100 AFM and Scanning Probe Microscope	Digital Instruments
Edwards Auto 306 Thermal Evaporator	Edwards
Temescal BJD-1800 Electron-Beam Evaporator	Temescal
ECR Plasma Etch System	Home Built
XeF_2 Etch System[②]	Home Built
MEI Wire Bonder, Model 1204W, Serial 6318	Marpet Enterprises Inc.
Alessi REL-3200 Probe Station with Optical Microscope	Alessi

[②] Courtesy of Prof. Axel Scherer and his group.

Appendix B

NEMS Resonator with the Damped Harmonic Oscillator Model

The simple harmonic oscillator (SHO)[①] has far more wealthy and profound implications and applications beyond its seemingly simplicity as covered in elementary physics. "It is the key tool that permits experimenters to detect extremely weak mechanical forces and electromagnetic signals and to produce highly stable standards of time and frequency. The oscillator, for example, underlies radio and microwave receivers, gravitational-wave detectors, clocks, searches for quarks, tests of the equivalent principle, and tests of theories of superfluidity and superconductivity. ..." [1]. It is of the same fundamental significance in the research of NEMS.

Inevitably any of the NEMS resonators we build would be dissipative, again of the similar issue addressed in [1]. Here we briefly document the mathematical description of the *damped* SHO (DSHO) and its frequency response, which has been widely used, *e.g.*, in the analyses of device transduction schemes and in the modeling of the feedback controls of NEMS resonators.

[①]Note here the word *oscillator* is simply adopted from convention in widely used textbooks and literatures. More precisely it should be *resonator*, as addressed in Chapter 3.

The frequency-domain response of the DSHO can be written as the relation between the displacement and driving force as follows (and as addressed in Chapter 2),

$$\boldsymbol{a}(\omega)=\frac{\boldsymbol{F}(\omega)}{\left(k_{eff}-M_{eff}\,\omega^2\right)+j\dfrac{M_{eff}\,\omega_0\omega}{Q}}=\frac{\boldsymbol{F}(\omega)}{k_{eff}}\cdot\frac{1}{\left(1-\dfrac{\omega^2}{\omega_0^2}\right)+j\dfrac{\omega}{Q\omega_0}}. \tag{B-1}$$

Here $k_{eff}=M_{eff}\,\omega_0^2$ is the effective stiffness, with M_{eff} the effective mass and ω_0 the angular frequency at the fundamental resonance. Both displacement and force here are complex variables. Normalized to the *static* displacement $a(\omega=0)\equiv F(\omega=0)/k_{eff}$, we have the *normalized* force−displacement transduction relation

$$\boldsymbol{H}(x)=\frac{1}{\left(1-x^2\right)+j\,x/Q}, \tag{B-2}$$

where $x\equiv\omega/\omega_0$. The amplitude response is then

$$H(x)\equiv\left|\boldsymbol{H}(x)\right|=\frac{1}{\sqrt{\left(1-x^2\right)^2+x^2/Q^2}}, \tag{B-3}$$

and the phase response is

$$\phi\equiv\angle\boldsymbol{H}(x)=\arctan\left(\frac{-x/Q}{1-x^2}\right). \tag{B-4}$$

The frequency-domain response functions for both amplitude and phase, as described by eqs. (B-3) and (B-4), with various given device Q’s, are plotted in Fig. B.1. Likewise, Fig. B.2 shows the first derivatives of the amplitude and phase response functions, and Fig. B.3 demonstrates the second derivatives. These characteristics are important for the analyses and designs of device transfer functions and feedback controls.

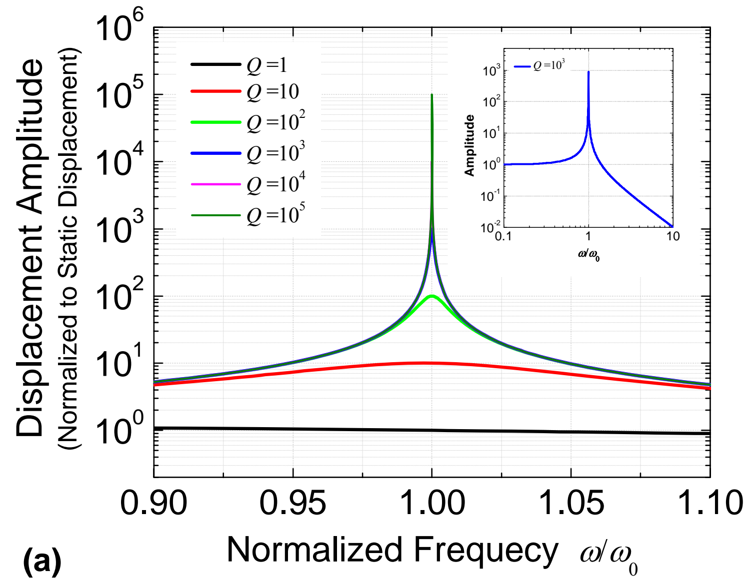

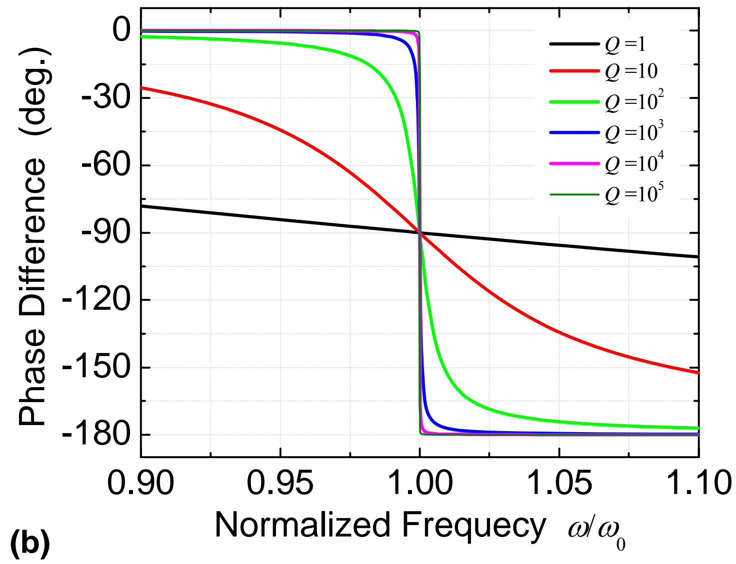

Fig. B.1 Frequency-domain response of the damped harmonic resonator. **(a)** Amplitude and **(b)** phase, as functions of frequency of the driving force.

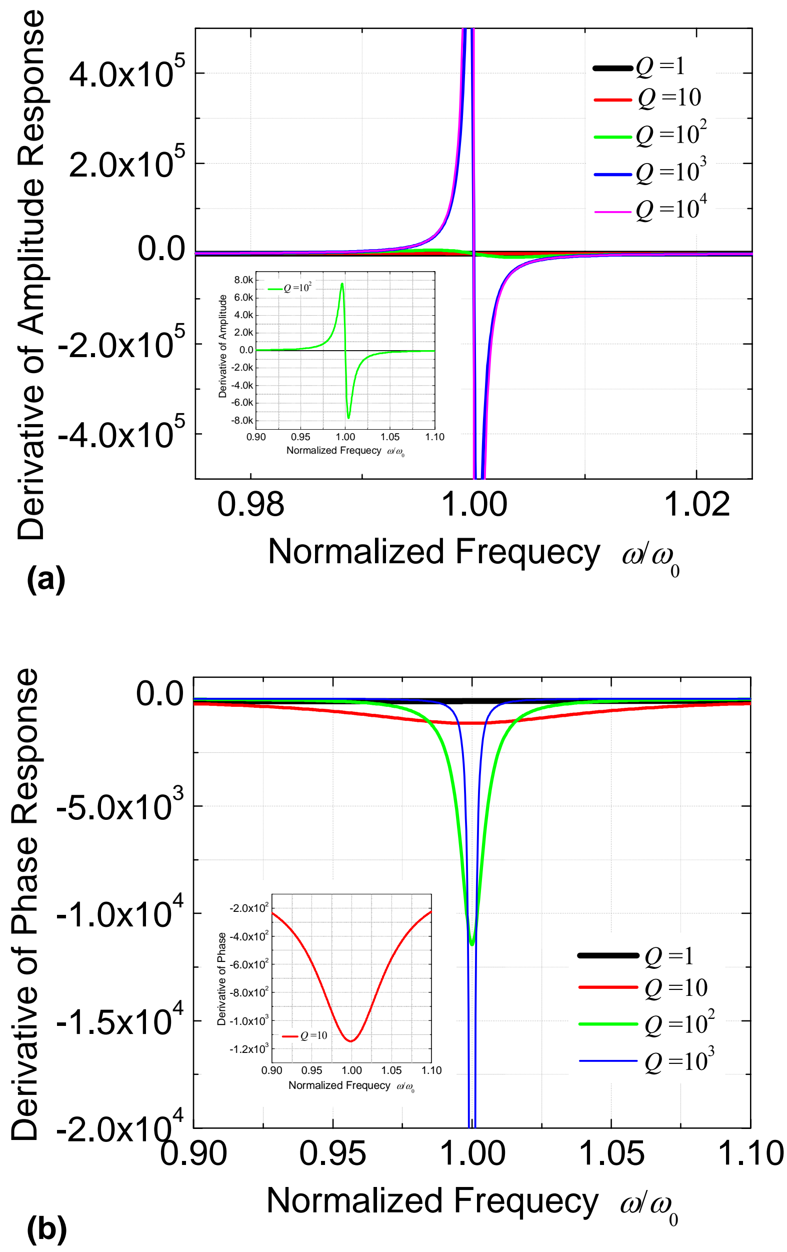

Fig. B.2 Frequency-domain response of the damped harmonic resonator. The *first derivatives* of **(a)** amplitude and **(b)** phase, respectively, as functions of frequency of the driving force.

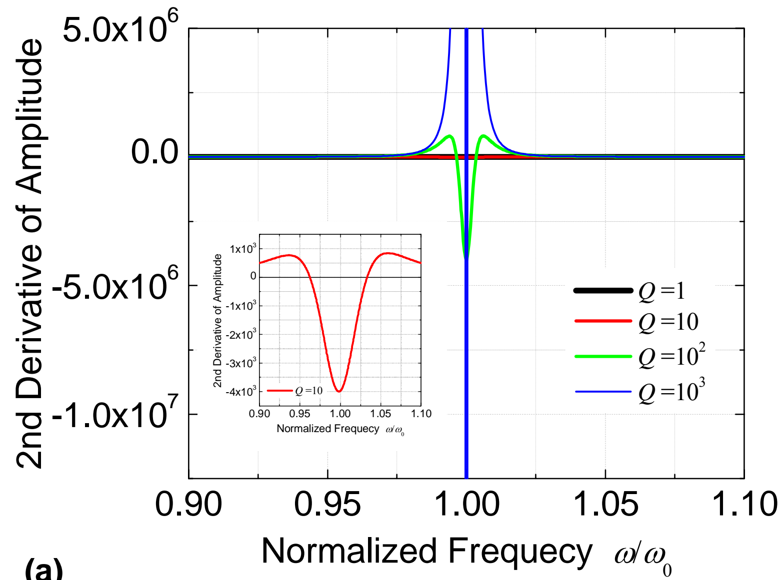

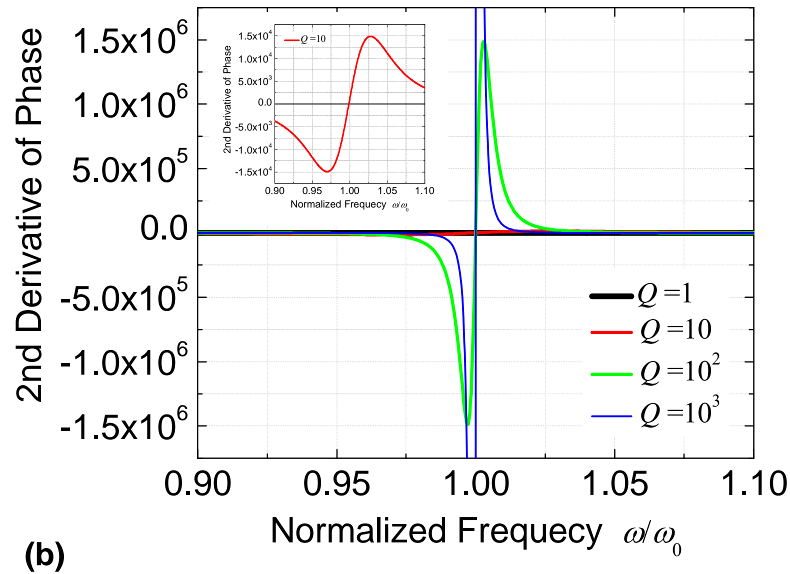

Fig. B.3 Frequency-domain response of the damped harmonic resonator. The *second derivatives* of **(a)** amplitude and **(b)** phase, respectively, as functions of frequency of the driving force.

Bibliography

[1] V.B. Braginsky, V.P. Mitrofanov, V.I. Panov, *Systems with Small Dissipation*, Chicago: The University of Chicago Press (1985).

Appendix C

A Note on the Quality Factor (*Q*)

C.1 The Lorentzian Function

The general form of the Lorentzian function is

$$y(x) = y_0 + \frac{A}{\pi} \cdot \frac{\left(\frac{1}{2}\Gamma\right)}{(x - x_0)^2 + \left(\frac{1}{2}\Gamma\right)^2}, \tag{C-1}$$

where y_0 is offset, A is a scale factor; Γ is an important parameter called "Full Width at Half Maximum (FWHM)"— its meaning is exactly what it says.

Sometimes, the *normalized* Lorentzian function is also very useful, *i.e.*,

$$L(x) = \frac{1}{\pi} \cdot \frac{\frac{1}{2}\Gamma}{(x - x_0)^2 + \left(\frac{1}{2}\Gamma\right)^2}, \tag{C-2a}$$

with

$$\int_{-\infty}^{\infty} L(x) = 1. \tag{C-2b}$$

C.2 Resonance, *Q*, and Their Connections to Lorentzian

The *original definition* of the quality factor (Q) of a resonator is regarding the energy dissipation — "the quality factor is the ratio of energy stored in the resonator, to the energy lost (dissipated) per radian of periodic motion of the system",

$$Q = 2\pi \frac{E}{\Delta E}, \tag{C-3a}$$

where E is the stored energy and ΔE is the energy lost (dissipated) per cycle (for convenience). Often it is also written as

$$Q = \omega_C \frac{E}{P_C}, \tag{C-3b}$$

where ω_C and P_C are the carrier frequency and carrier power, respectively.

Based on this original definition, many formulas can be developed (*e.g.*, the Zener's model, etc.). Considering the frequency response, the important thing is, for a resonator, it can be derived that the *power spectrum* of the resonant system has the following form (an excellent example to verify this is probably just to look at a beam resonator modeled as a simple harmonic oscillator driven by thermomechanical fluctuation)

$$P(\omega) = P_0 + C \cdot \frac{\frac{1}{2}\Gamma}{(\omega - \omega_0)^2 + \left(\frac{1}{2}\Gamma\right)^2}, \tag{C-4a}$$

which is exactly the same form of a standard Lorentzian, as presented in eqs. (C-1) and (C-2). Within this context, the quality factor of the resonance determined by the resonance power spectrum is

$$Q = \frac{\omega_0}{\Gamma}, \tag{C-4b}$$

which can be proved to be in consistence with the original definition in eqs. (C-3a) and (C-3b).

This provides a much easier way to determine the Q, which otherwise would be more difficult, as according to eqs. (C-3a) and (C-3b), one has to do time-domain measurement to determine the Q (eqs. (C-3a) and (C-3b) imply that the Q can be determined by time-domain ring-down counts of cycles). So now, Q can be identified by measuring frequency-domain response, or more accurately, the power spectrum of the resonance in the frequency domain.

C.3 The Specific Case of Magnetomotive NEMS Resonator

In the case of magnetomotive transduction of NEMS resonator, one has the EMF voltage signal response as the detected resonance signal

$$\boldsymbol{V}_{EMF}(\omega) = C\frac{j\omega}{\omega_0^{\ 2} - \omega^2 + \frac{j\omega\omega_0}{Q}}, \tag{C-5}$$

where C is a constant determined by some detailed parameters in the magnetomotive transduction. Thus, the power spectrum of the resonance is (note the voltage is complex)

$$P(\omega) \sim \left|\boldsymbol{V}_{EMF}(\omega)\right|^2 = \boldsymbol{V}_{EMF}(\omega)\cdot\tilde{\boldsymbol{V}}_{EMF}(\omega) \sim \frac{C_1\omega^2}{\left(\omega^2 - \omega_0^{\ 2}\right)^2 + \left(\frac{\omega\omega_0}{Q}\right)^2}. \tag{C-6}$$

We see that this power signal of the resonance is Lorentzian, in the condition of high Q approximation. In fact, in the vicinity of resonance frequency ω_0, $\omega=\omega_0+\delta\omega$, and in the limit of high Q, eq. (C-6) transforms into (high Q assures that some high order terms can be thrown away)

$$P(\omega) \sim D \cdot \frac{1}{(\omega-\omega_0)^2 + \left(\frac{1}{2}\frac{\omega_0}{Q}\right)^2}, \tag{C-7a}$$

or,

$$P(\omega) \sim D_1 \cdot \frac{\frac{1}{2}\frac{\omega_0}{Q}}{(\omega-\omega_0)^2 + \left(\frac{1}{2}\frac{\omega_0}{Q}\right)^2}. \tag{C-7b}$$

So compare to eqs. (C-4a) and (C-4b), we see that the power signal of the resonance is Lorentzian in the limit of high Q's; and the Q can be extracted from the power signal curve of the resonance with the same and correct convention, as defined in eq. (C-4b) and consistent with eqs. (C-3a) and (C-3b).

In real implementation, fitting to Lorentzian is just to fit the power signal resonance curve to eqs. (C-7a) or (C-7b). For example, the Lorentzian function embedded in the software Origin fits to eq. (C-7b), or more accurately, the general form eq. (C-1), with an offset. If we program with Matlab or others to do the fitting, both (C-7a) and (C-7b) and other equivalent forms can be used, see whichever is convenient.

Then, take a look at the amplitude of the voltage signal of a magnetomotively-transduced resonance, from eqs. (C-5) and (C-6), we see that the amplitude of the voltage signal is

$$\left|\boldsymbol{V}_{EMF}(\omega)\right| = C\frac{|j\omega|}{\left|\omega_0{}^2 - \omega^2 + \dfrac{j\omega\omega_0}{Q}\right|}. \tag{C-8}$$

We note that it is NOT Lorentzian. All we can do with this is, according to eqs. (C-6) to (C-7a) & (C-7b), the amplitude of the voltage signal can be approximated to the square root of a Lorentzian, in the high Q limit.

$$\left|\boldsymbol{V}_{EMF}(\omega)\right| \sim \sqrt{\frac{C_1\omega^2}{\left(\omega^2 - \omega_0{}^2\right)^2 + \left(\dfrac{\omega\omega_0}{Q}\right)^2}} \sim D_2 \cdot \sqrt{\frac{\dfrac{1}{2}\dfrac{\omega_0}{Q}}{(\omega - \omega_0)^2 + \left(\dfrac{1}{2}\dfrac{\omega_0}{Q}\right)^2}}. \tag{C-9}$$

With this, to extract Q from a voltage signal resonance curve, it can be readily done by adding this function to Origin's user-defined fitting function, or simply convert voltage signal (amplitude) data into voltage-squared ($|V|^2$, which is then power signal) and fit this data directly with Lorentzian. Or, implement eq. (C-9) with Matlab or other software.

Summary: The power signal of a magnetomotively-transduced NEMS resonance is Lorentzian with the high Q approximation. If we have voltage signal (amplitude) data, note that it is not Lorentzian, but the square-root of Lorentzian, with the same high Q approximation. So, it is conceptually not correct to directly fit a voltage signal to Lorentzian, even though one can force a fitting program to fit the data to Lorentzian and get Q number might be very close to the one obtained by correctly fitting to the voltage data to the square-root of Lorentzian, *i.e.*, eq. (C-9).

C.4 The Mysterious $\sqrt{3}$

What if we do a brute fitting — we just force a program to fit the voltage data trace (not power data trace) to Lorentzian? Although such things have been done in some literatures in this community, as said, this is not correct thing to do because the voltage data is not Lorentzian. Now let us see what will happen anyway.

The brute-force fit can still give us the resonance frequency ω_0, and the FWHM as it sees (even though with inappropriate data, the brute fit can still try to get the FWHM as what it does is just a routine). We can calculate the FWHM by knowing that the voltage data is actually the square-root of Lorentzian. From eq. (C-9) or simply following eq. (C-1), we have

$$|\boldsymbol{V}| \sim \sqrt{A_0 \cdot \frac{\frac{1}{2}\Gamma}{(\omega-\omega_0)^2 + \left(\frac{1}{2}\Gamma\right)^2}}, \tag{C-10}$$

Where A_0 is a scale factor, and $\Gamma$is the FWHM of the Lorentzian power signal, as in eq. (C-4b). The "Half Maximum" seen by the brute fit is then

$$\frac{1}{2} \cdot \sqrt{A_0 \frac{2}{\Gamma}} = \sqrt{A_0 \frac{1}{2\Gamma}}. \tag{C-11}$$

The "Full Width at Half Maximum (FWHM)" seen by the brute fit is then the distance between the solutions of the equation (let it assume "Half Maximum")

$$\sqrt{A_0 \cdot \frac{\frac{1}{2}\Gamma}{(\omega-\omega_0)^2 + \left(\frac{1}{2}\Gamma\right)^2}} = \sqrt{A_0 \frac{1}{2\Gamma}}. \tag{C-12}$$

Solving eq. (C-12) yields

$$(\omega - \omega_0)^2 = \frac{3}{4}\Gamma^2, \tag{C-13}$$

And the two roots assuming the "Half Maximum" are

$$\omega_+ = \omega_0 + \frac{\sqrt{3}}{2}\Gamma \quad \text{and} \quad \omega_- = \omega_0 - \frac{\sqrt{3}}{2}\Gamma. \tag{C-14}$$

Therefore, the "Full Width at Half Maximum" seen by the brute fit is

$$FWHM = \omega_+ - \omega_- = \sqrt{3}\Gamma; \tag{C-15}$$

and thus,

$$Q_{BruteFit} \equiv \frac{\omega_0}{FWHM} = \frac{\omega_0}{\sqrt{3}\Gamma} = \frac{Q}{\sqrt{3}}. \tag{C-16}$$

This means that the Q from the brute fit of the voltage signal is $\sqrt{3}$ times smaller than the real Q of the resonance defined in eq. (C-4b) because the FWHM the brute fit can obtain from the voltage signal curve is $\sqrt{3}$ times larger than the original FWHM defined in the Lorentzian power signal.

Summary: As shown above, by doing not quite correct thing—fitting voltage signal to a Lorentzian, one may still approach the real Q by simply multiplying the result by $\sqrt{3}$, assuming that the brute fit can still identify ω_0 and FWHM with decent confidence while taking a non-Lorentzian data trace as a Lorentzian one. In the existing literatures from this community, we find sometimes this $\sqrt{3}$ correcting factor

is applied when brute-force fitting of amplitude signal is implemented; while in the rest cases, it is then incorrect to fit amplitude signal to Lorentzian without any corrections.

Appendix D

A Note on NEMS Oscillator Phase Noise, and Phase Noise Comparison

This note clarifies the principles and procedures for fair comparisons of NEMS oscillator phase noise performance and that of other oscillators (MEMS oscillators, crystal oscillators, *etc.*). Based on this, it is probably the time for us to consider defining a specific figure of merit (FOM) for NEMS oscillators for this kind of comparisons.

D.1 NEMS Oscillator Phase Noise Data

Fig. D.1 shows the original raw data of the 428MHz NEMS oscillator phase noise, as directly measured by the RDL NTS-1000B phase noise analyzer at the output of the NEMS oscillator.

Suppose we compare and evaluate the phase noise performance of two oscillators operating at carrier frequencies f_{c1} and f_{c2}, respectively. Fig. D.2 schematically displays the spectra of these two oscillators.

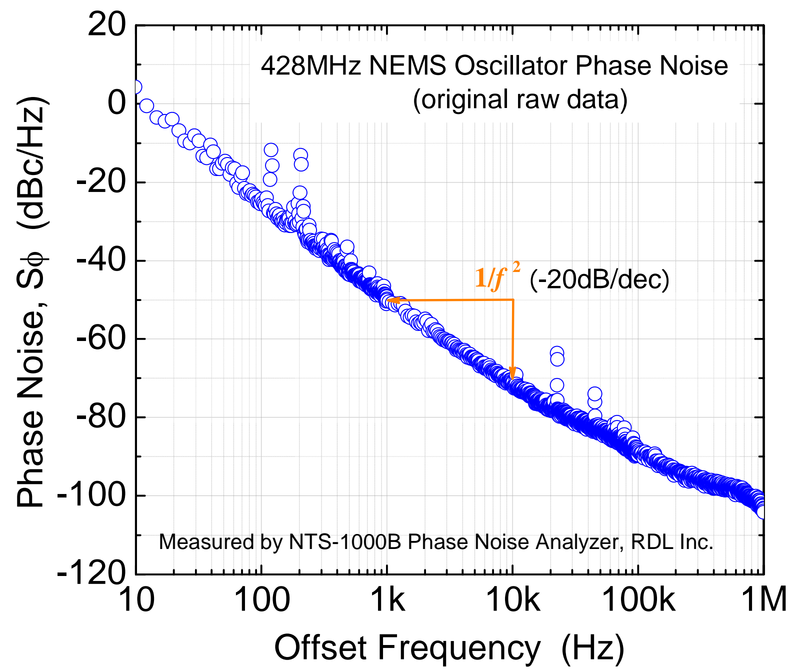

Fig. D.1 Phase noise data of the 428MHz NEMS oscillator, as directly measured by the RDL NTS-1000B phase noise analyzer (raw data, no frequency dividing or rescaling).

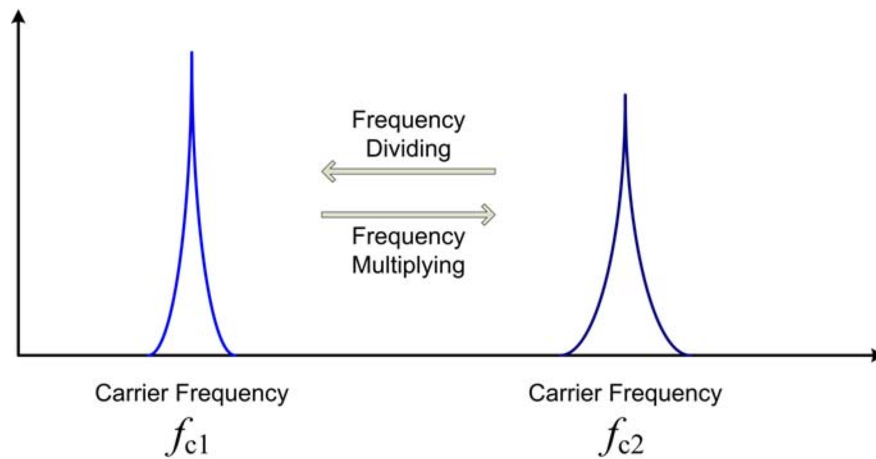

Fig. D.2 Schematic for comparison between two MEMS/NEMS oscillators operating at different (carrier) frequencies.

D.2 Method 1 ("Normalizing Offset Frequency to Carrier")

Note the fact that the offset frequency referred to its carrier is different from one oscillator to the other, or in other words, the "skirt" should rescale as the carrier frequency is rescaled. So when we rescale the performance at f_{c1} to that of f_{c2}, we need to rescale the offset frequency proportionally,

$$\Delta f_2 = \frac{f_{c2}}{f_{c1}} \cdot \Delta f_1 . \tag{D-1}$$

Here for a fair comparison *the offset frequencies are normalized to their own carrier frequencies*. This leads to a *horizontal shift* (displacement) from the old to the new offset frequency, which on the usually used log plot is

$$\log(\Delta f_2) - \log(\Delta f_1) = \log\left(\frac{f_{c2}}{f_{c1}}\right). \tag{D-2}$$

Consequently the phase noise shift (vertical) caused by this offset frequency shift is

$$\Delta S_\phi[\text{dBc/Hz}] = |\text{Slope}| \cdot [\log(\Delta f_2) - \log(\Delta f_1)] = |\text{Slope}| \cdot \log\left(\frac{f_{c2}}{f_{c1}}\right). \tag{D-3}$$

Note we usually have the following slopes and power-laws in a measured phase noise spectrum:

Slope[S_ϕ vs log(Δf)] = −10 to 0dB/dec (flat) for the far-from-carrier 'tail'

Slope[S_ϕ vs log(Δf)] = −20dB/dec for $1/f^2$ phase noise (thermal noise)

Slope[S_ϕ vs log(Δf)] = −30dB/dec for $1/f^3$ phase noise ($1/f$ noise) and steeper for higher powers of f.

We illustrate the phase noise offset by this method in Fig. D.3 (horizontal shift from **blue** trace to **black** trace).

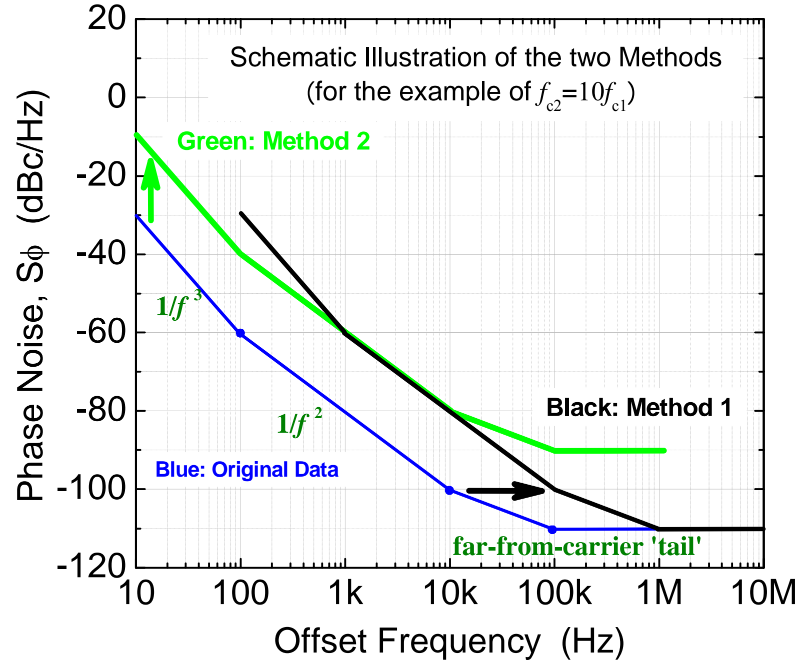

Fig. D.3 Phase noise spectrum shift by offset frequency rescaling and carrier frequency dividing (example: f_{c2}=10f_{c1}).

D.3 Method 2 ("Carrier Frequency Dividing")

We can compare S_ϕ / f_c^2 rather than directly compare phase noise S_ϕ. This is based on the consideration of the S_ϕ —f_c trade-off and it is *roughly*[①] consistent with some of the figures of merit (FOMs) used in the RF IC community in comparing and evaluating CMOS LC VCOs, such as in [1,2]. Hence, if we use S_ϕ / f_c^2 as the criteria for

---

[①] As we haven't considered other specs such as power consumption yet, See Section D.5. Also when we compare S_ϕ/f_c^2, it is the lower the value, the better, while it is usually the higher the value the better for other FOMs.

comparing (on the same plot) the phase noise of two oscillators working f_{c1} and f_{c2}, the phase noise spectrum offset due to this carrier frequency dividing is

$$\Delta S_\phi[\text{dBc/Hz}] = 10\log\left(\frac{S_\phi}{f_{c1}^{\ 2}}\cdot f_{c2}^{\ 2}\right) - 10\log(S_\phi) = 20\log\left(\frac{f_{c2}}{f_{c1}}\right). \quad \text{(D-4)}$$

This is also illustrated in Fig. D.3 as the *vertical shift* from **blue** to **green** (also with the example of f_{c2}=10f_{c1}).

D. 4 Comparison between Method 1 and Method 2

Fig. D.3 clearly demonstrates the effects of applying both Method 1 and Method 2 (with the case of multiplying to a higher carrier frequency of a 10×; for down dividing just plug f_{c2}/f_{c1} into eqs. (D-3) and (D-4) to compute the offset in phase noise in dBc/Hz).

Interestingly, for $1/f^2$ phase noise (thermal noise), both methods yield the same results. For other than $1/f^2$ phase noise behavior, the two methods lead to different results, with Method 1 leading to favorable far-from-carrier phase noise but a bit unfavorable close-to-carrier phase noise, and Method 2 leading to opposite results. These effects are reversed in cases of carrier frequency scaling down, as log(f_{c2}/f_{c1}) becomes negative for $f_{c2}<f_{c1}$.

The difference is because, in Method 1 the phase noise offset is determined by the original slope times the horizontal offset frequency scaling; while in Method 2, everything is simply shifted vertically by 20dB times the carrier frequency scaling, regardless of the original slope. This universal 20dB factor is due to the brute-force definition of $S_\phi / f_c^{\ 2}$, based on the rough assumption that phase noise measured at offset

frequency Δf from carrier f_c is proportional to $(f_c/\Delta f)^2$,② as dictated by the classical Leeson's model [3].

So my comments are: Method 1 is intuitive in the physics picture and captures the scaling proportionality; Method 2 is simpler and even coarse, but it is convenient as an FOM for engineering applications.

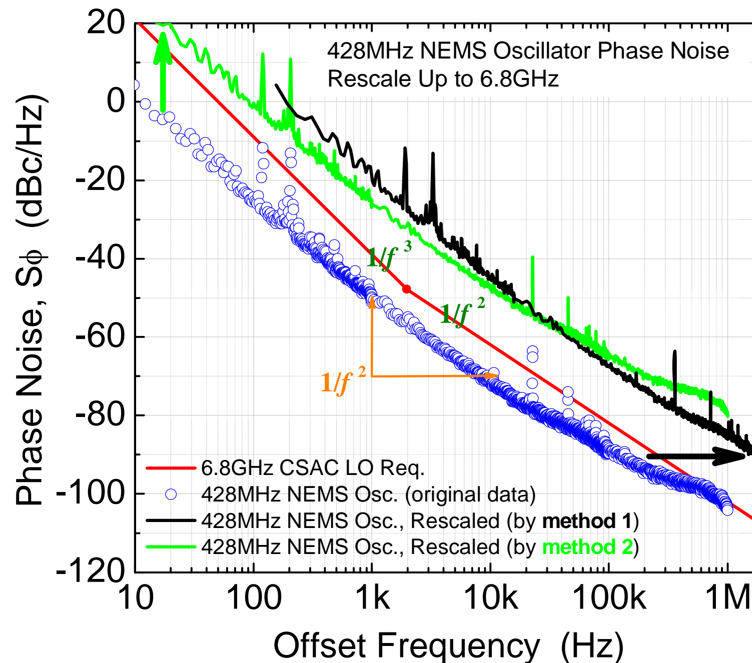

Fig. D.4 428MHz NEMS oscillator phase noise rescaled up to 6.8GHz CSAC LO carrier, using both Methods 1 & 2, in comparison with the CSAC LO phase noise requirements.③

In particular, for our NEMS oscillators and resonators to compare with 6.8GHz CSAC LO requirements, applying the above two Methods introduces minor difference, because our NEMS phase noise is pretty close to $1/f^2$ behavior (thermal noise) throughout the

---

②This is not always true though; only exactly true for thermal noise limited case. And this actually explains why Method 1 and Method 2 yield completely the same result for $1/f^2$ phase noise (thermal noise).

③The CSAC LO requirements are from [4]. Some newly update on the requirements can be found in [5]. The LO requirements described in [5] are more stringent than in [4] (actually there are some issues in the requirements from [4]).

offset frequency range where we have valid measured data. As shown in Fig. D.4, by using Method 1 and Method 2, we only have slight difference in the NEMS phase noise rescaled to 6.8GHz. Method 1 gives better far-from-carrier phase noise and Method 2 gives better close-to-carrier noise. As shown in Fig. D.5 is the example of rescaling the NEMS oscillator phase noise down to 10MHz carrier, the effects are reversed.

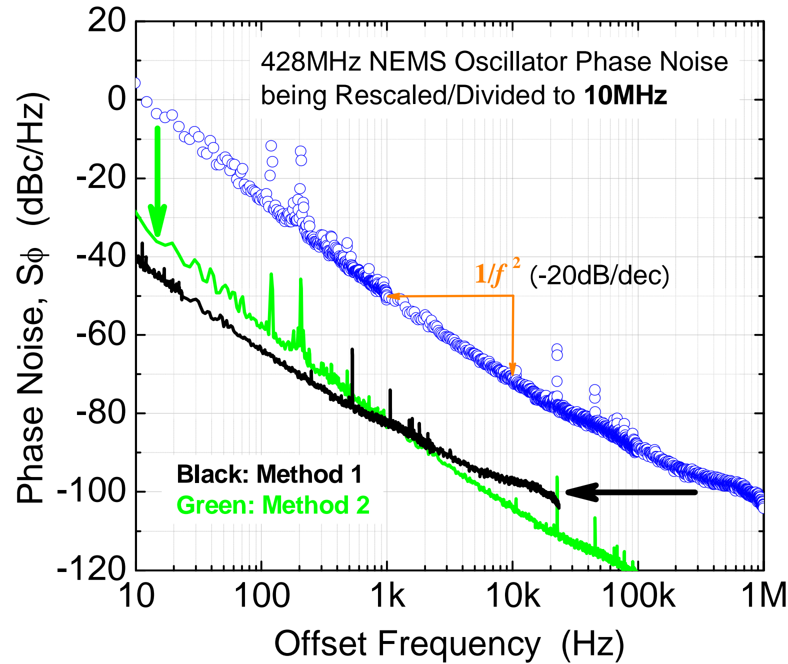

Fig. D.5 428MHz NEMS oscillator phase noise rescaled down to 10MHz carrier (for fair comparison with crystal oscillator), using both Methods 1 & 2.

D.5 Extended Discussion on FOM

Like the figure of merit (FOM) for RF amplifiers can be defined as "Gain×Bandwidth/Power Consumption", which reflects the trade-offs in the design and implementation, we also need to think of defining a meaningful and comprehensive FOM for NEMS/MEMS oscillator/resonator phase noise.

As mentioned above, in the RF CMOS LC VCOs, considering the trade-offs of phase noise, power consumption, oscillator frequency, and tuning range, several kinds of FOMs have been defined [1,2,6-9] and most of them are quite intuitive and easy to calculate.

So we could learn from these FOMs defined for these LC VCOs and define a FOM for NEMS/MEMS oscillators, incorporating not only the phase noise and carrier frequency considered in the aforementioned Method 1 and Method 2, but also the power consumption. So we can compare $\frac{S_\phi}{f_c^2} \cdot P_{con}$ for different oscillators, the smaller the better. With this comparison, we can define a FOM in decibel, dBF (dB for FOM),

$$\text{FOM [dBF]} = 10\log(S_\phi)\ \text{[dBc/Hz]} - 20\log(f_c)\ \text{[dB]} + P_{con}\ \text{[dBm]}. \qquad \text{(D-5)}$$

Note here dBm is power refer to 1mWatt, or, P_{con} [dBm]=log(P_{con}/1mWatt). Here in calculating FOM [dBF], all the dB-related units (dBc/Hz, dBm) are simply taken as dB in getting their decibel values regardless their reference. Again, in using this FOM [dBF] for comparison, the lower the value, the better.

For some of presently available MEMS oscillators and NEMS oscillators, now the power consumption can be quite high and especially when the MEMS/NEMS devices are off-chips, and when some discrete elements are used. In this case, it would be hard to do a fair comparison with the power consumption, so eq. (D-5) will simplify to comparing S_ϕ / f_c^2 as in Method 2. But eq. (D-5) can ultimately be the FOM for comparisons of all future on-chip MEMS/NEMS oscillators.

D.6 Selected Comparisons

Besides the aforementioned local oscillators for CSAC, we have also compared the phase noise performance of the newly-demonstrated 428MHz NEMS oscillator (as detailed in Chapter 3) to that of various other crystal oscillators, including both some of the state-of-the-art micron-scale ones based upon vibrating MEMS resonators and the conventional high-performance quartz crystal oscillators that are dominating today's practical applications. In all these comparisons, we use Method 1 for rescaling.

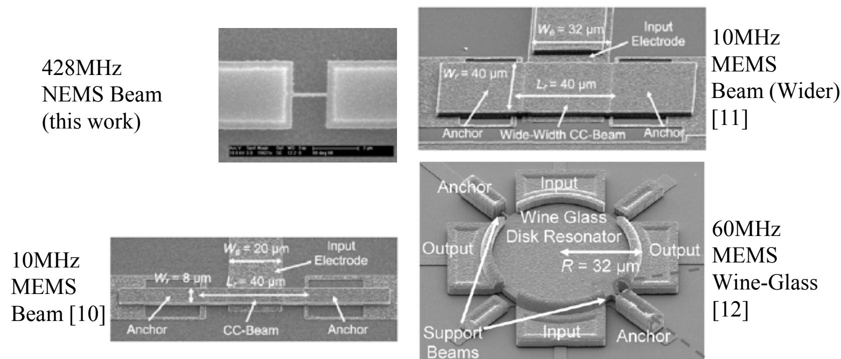

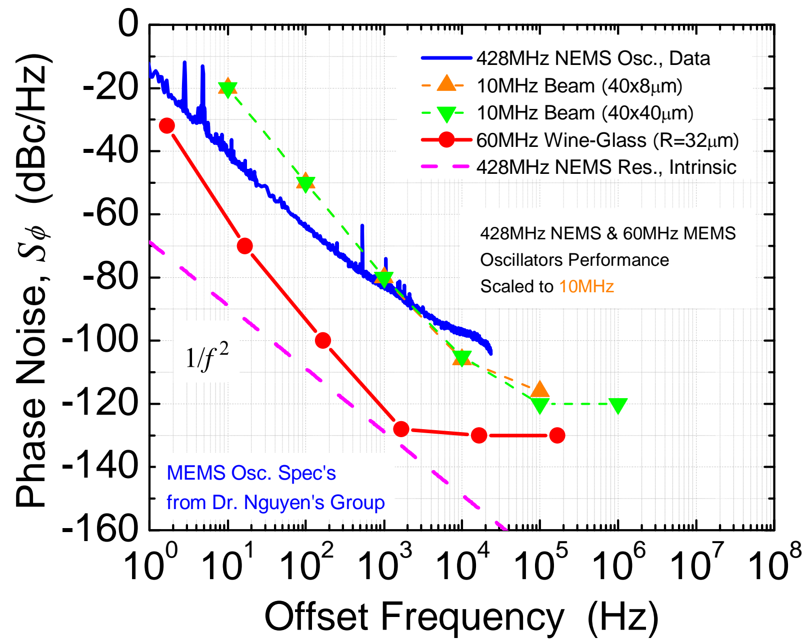

Fig. D.6 UHF NEMS oscillator phase noise performance in comparison with that of the recently developed *state-of-the-art* HF/VHF vibrating MEMS oscillators (data from [10-12]).

Fig. D.6 shows the comparison with some of the best MEMS oscillators based on vibrating MEMS resonators recently reported [10-12]. Compared to the NEMS resonator, these MEMS devices are micromechanical resonators that have much larger volume and operate at much lower frequencies, namely, a 10MHz doubly-clamped beam [10], another 10MHz but wider doubly-clamped beam [11] for enhanced power handling, and a 60MHz wine-glass disk [12] for both enhanced frequency and power handling. In comparison, all phase noise is scaled to 10MHz carrier using Method 1. It is seen that the wider beam 10MHz MEMS oscillator does not perform noticeably better than the thin beam one does. The 60MHz wine-glass MEMS oscillator has considerably better phase noise. The phase noise of the first realized 428MHz NEMS oscillator, yet unoptimized, is comparable to that of the MEMS beams with much larger device sizes and much lower frequencies. The ultimate phase noise limit is set by the 428MHz NEMS resonator. If realistically approached, this can outperform the wine-glass MEMS oscillator.

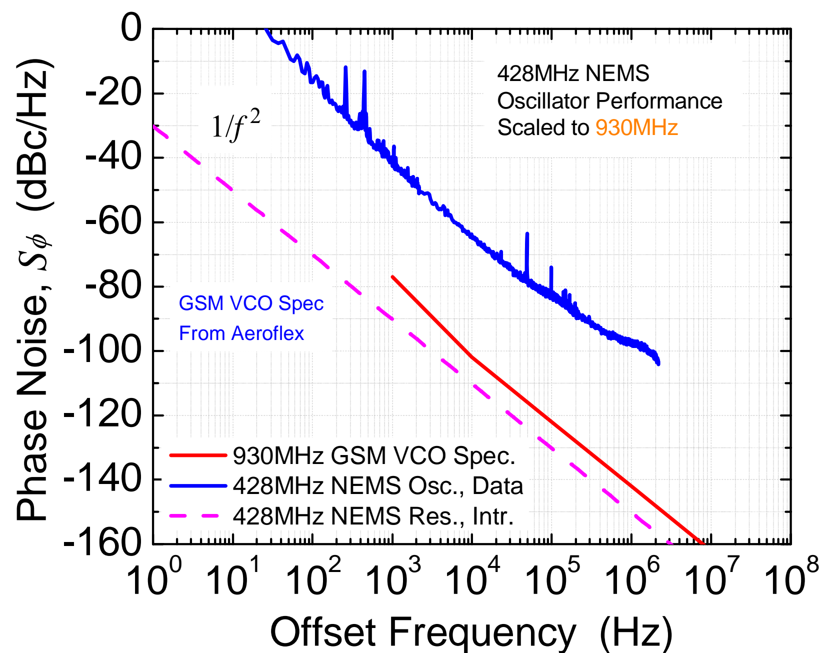

Fig. D.7 UHF NEMS oscillator phase noise performance compared with that of a high-performance 930MHz GSM VCO in actual applications (data from Aeroflex).

Fig. D.7 demonstrates a comparison with the 930MHz GSM VCO, data rescaled to 930MHz carrier using Method 1. Comparison with some more advanced quartz crystal oscillators are collected in Fig. D.8, all data rescaled to 13MHz carrier using Method 1. Both figures show that the phase noise performance of the first UHF NEMS oscillator is not as good as that of the advanced quartz crystal oscillators. On the other hand, engineering of detection and control circuits for NEMS oscillator would reduce its phase noise to match the intrinsic noise performance of the NEMS resonator. Moreover, engineering of NEMS resonator devices could further scale down the intrinsic noise limit. One probable approach is to develop NEMS oscillators based on arrays of mechanically-coupled NEMS resonators. As discussed in Chapter 3, this would enable better power handling capability while still taking advantage of the high-frequency characteristics of NEMS devices.

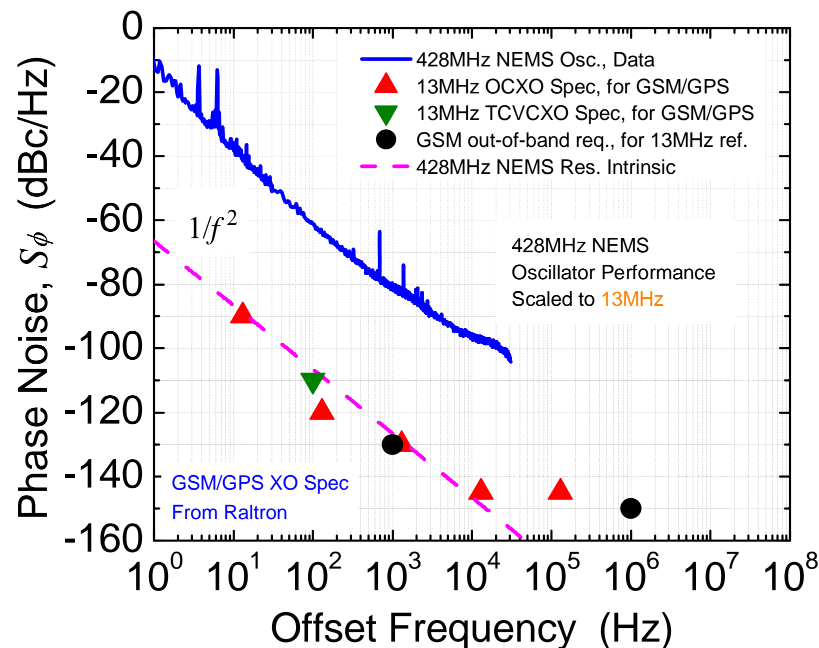

Fig. D.8 UHF NEMS oscillator phase noise performance compared with that of *state-of-the-art* Quartz XOs used as references in GSM VCOs (data from Analog Devices, Raltron, *etc.*).

Bibliography

[1] T.I. Ahrens, T.H. Lee, "A 1.4GHz 3mW CMOS LC low phase noise VCO using tapped bond wire inductance", *Proc. 1998 Int. Symp. Low Power Electronics & Design (ISLPED'98)*, 16-19, Monterey, CA, Aug. 10-12 (1998).

[2] D. Ham, A. Hajimiri, "Concepts and methods in optimization of integrated LC VCOs", *IEEE JSSC* **36**, 896-909 (2001).

[3] D.B. Leeson, "A simple model of feedback oscillator noise spectrum", *Proc. IEEE* **54**, 329-330 (1966).

[4] J. Kitching, "Local oscillator requirements for CSAC", *Private Communications* (2003). Now available online: http://tf.nist.gov/ofm/smallclock/LO%20Requirements.pdf

[5] A. Brannon, J. Breitbarth, Z. Popovic, "A low-power, low phase noise local oscillator for chip-scale atomic clocks", *2005 IEEE MTT-S Int. Microwave Symposium Digest*, 1535-1538, Long Beach, CA, June 12-17 (2005).

[6] A. Wagemans, P. Baltus, R. Dekker, A. Hoogstraate, H. Maas, A. Tombeur, J. van Sinderen, "A 3.5 mW 2.5 GHz diversity receiver and a 1.2 mW 3.6 GHz VCO in silicon-on-anything", *Digest of Tech. Papers, ISSCC'98*, 250-251, San Francisco, CA, Feb. 5-7 (1998).

[7] J.O. Plouchart, B.U. Klepser, H. Ainspan, M. Soyuer, "Fully-monolithic 3V SiGe differential voltage-controlled oscillators for 5GHz and 17GHz wireless applications", *Proc. ESSCIRC'98*, 332-335, Haag, Netherlands, Sept. 22-24 (1998).

[8] P.G.M. Baltus, A.G. Wagemans, R. Dekker, A. Hoogstraate, H. Maas, A. Tombeur, J. van Sinderen, "A 3.5-mW, 2.5-GHz diversity receiver and a 1.2-mW, 3.6-GHz VCO in silicon on anything", *IEEE JSSC* **33**, 2074-2079 (1998).

[9] E. Hegazi, H. Sjoland, A.A. Abidi, "A filtering technique to lower LC oscillator phase noise", *IEEE JSSC* **36**, 1921-1930 (2001).

[10] S. Lee, M.U. Demirci, C.T.C. Nguyen, "A 10-MHz micromechanical resonator Pierce reference oscillator for communications", *Digest of Tech. Papers, Transducers'01*, 1094-1097, Munich, Germany, June 10-14 (2001).

[11] Y.M. Lin, S. Lee, Z. Ren, C.T.C. Nguyen, "Series-resonant micromechanical resonator oscillator", *Tech. Digest IEDM 2003*, 961-964, Washington DC, Dec. 8-10 (2003).

[12] Y.M. Lin, S. Lee, S.S. Li, Y. Xie, Z. Ren, C.T.C. Nguyen, "60-MHz wine-glass micromechanical-disk reference oscillator", *Digest of Tech. Papers, ISSCC 2004*, 322-323, San Francisco, CA, Feb. 15-19 (2004).

Appendix E

A Note on the Measures of Frequency Stability

This note deals with the concepts and measures of frequency stability (or frequency *instability*) of resonators and oscillators. In particular, given the context of resonant mass sensing of this thesis work, this note addresses the relationship between the often used *RMS fractional frequency shift* and the more professional *Allan deviation* widely used in the frequency control community.

In the context of analyzing the mass sensitivity of NEMS resonators, based on the assumption that the accreted mass to the resonator, δM, is a small fraction of the effective vibratory resonator mass M_{eff}, one can have [1]

$$\delta M \cong \frac{\partial M_{eff}}{\partial \omega_0}\delta\omega_0 = \Re^{-1}\delta\omega_0, \tag{E-1a}$$

or,

$$\delta M \cong \frac{\omega_0}{\Re}\cdot\frac{\delta\omega_0}{\omega_0}, \tag{E-1b}$$

where ω_0 is the resonance frequency, $\delta\omega_0 = \omega - \omega_0$ is the resonance frequency shift due to the accreted mass, and $\Re = \partial\omega_0 / \partial M_{eff}$ is the *mass responsivity* (characterizing how *responsive* the resonator is with respect to the added mass).

Eqs (E-1a) and (E-1b) are general as long as $\delta M << M_{\text{eff}}$ is assumed. In this sense, if one can monitor $\frac{\delta\omega_0}{\omega_0}$ as the *instantaneous fractional frequency shift*, then δM is the *instantaneous loaded mass*. In real measurements, however, the more useful are the RMS values as some certain averaging process is always involved in a real measurement and the RMS values are more meaningful in characterizing the mass loading physical process. Below, except specific explanation, $\frac{\delta\omega_0}{\omega_0}$ (or more strictly should be $\left\langle \frac{\delta\omega_0}{\omega_0} \right\rangle$), is simply used as the *RMS fractional frequency shift*, and δM (more strictly, should be $\langle \delta M \rangle$) is the *RMS loaded mass*.

The easiest way to see the relationship between the RMS fractional frequency shift and the Allan deviation is to carefully examine their definition and compare them in the *time domain*.

First, define the *instantaneous fractional frequency shift* (from the nominal value ω_0) as

$$y(t) = \frac{\delta\omega_0(t)}{\omega_0} = \frac{\omega(t) - \omega_0}{\omega_0}. \tag{E-2}$$

In real measurement with averaging time τ, one has the measured value of fractional frequency shift for the arbitrary ith time interval

$$\bar{y}_i = \frac{1}{\tau}\int_{t_i}^{t_i+\tau} y(t)dt \ . \qquad \text{(E-3)}$$

By definition, the RMS fractional frequency shift (variation) is

$$\frac{\delta\omega_0}{\omega_0} = \left\langle \left(\frac{\omega-\omega_0}{\omega_0}\right)^2 \right\rangle^{\frac{1}{2}} = \frac{1}{\omega_0}\left\langle (\omega-\omega_0)^2 \right\rangle^{\frac{1}{2}}, \qquad \text{(E-4a)}$$

or equivalently can be measured via the *RMS frequency shift*

$$\delta\omega_0 = \left\langle (\omega-\omega_0)^2 \right\rangle^{\frac{1}{2}}, \qquad \text{(E-4b)}$$

where $\langle \ \rangle$ denotes infinite time average, or ideal ensemble average. In real measurements, the *RMS fractional frequency shift (variation)* is based on a finite ensemble average

$$\frac{\delta\omega_0}{\omega_0} \cong \left[\frac{1}{N-1}\sum_{i=1}^{N}\left(\frac{\overline{\omega}_i-\omega_0}{\omega_0}\right)^2\right]^{\frac{1}{2}}, \qquad \text{(E-5)}$$

where $\overline{\omega}_i$ is the measured (averaged) frequency in the *i*th interval. Note here for the finite ensemble, the RMS value is based on sample standard deviation.

The *Allan Variance* is defined as the sample variance of two adjacent averages of the instantaneous fractional frequency shift

$$\sigma^2(\tau) = \left\langle \frac{(\bar{y}_{i+1}-\bar{y}_i)^2}{2} \right\rangle. \qquad \text{(E-6)}$$

Note that this definition keeps the same as those in [2] (and ref. 20, 21 therein) and [3].

Thus one has the *Allan variance* formula from a finite data ensemble in a real measurement

$$\sigma^2(\tau) \cong \frac{1}{2} \cdot \frac{1}{N-1} \sum_{i=1}^{N} \left(\frac{\overline{\omega}_{i+1} - \overline{\omega}_i}{\omega_0} \right)^2 . \tag{E-7}$$

Note that this definition is similar to the MRS definition, except for the factor 1/2. Then, by definition, *Allan deviation* is the square root of Allan variance,

$$\sigma(\tau) \cong \left[\frac{1}{2} \cdot \frac{1}{N-1} \sum_{i=1}^{N} \left(\frac{\overline{\omega}_{i+1} - \overline{\omega}_i}{\omega_0} \right)^2 \right]^{\frac{1}{2}} = \frac{1}{\sqrt{2}} \left[\frac{1}{N-1} \sum_{i=1}^{N} \left(\frac{\overline{\omega}_{i+1} - \overline{\omega}_i}{\omega_0} \right)^2 \right]^{\frac{1}{2}} . \tag{E-8}$$

Now we compare eq. (E-5) and eq. (E-8). For a not-so-bad measurement, if the system still has decent relatively-long-term stability, usually the averagely measured data $\overline{\omega}_{i+1}$ and $\overline{\omega}_i$ won't be deviated from the nominal value ω_0 too much, then comparing eqs. (E-5) and (E-8) shows that one should expect

$$\sigma \approx \frac{1}{\sqrt{2}} \cdot \frac{\delta\omega_0}{\omega_0} . \tag{E-9}$$

Note that the averaging time should be the same in calculating both the *Allan deviation* and the *RMS fractional frequency shift.* For systems with not-so-good stability for longer-term than the minimum averaging time in the measurement, *e.g.*, in case $(\overline{\omega}_{i+1} - \omega_0) \approx (\overline{\omega}_i - \omega_0) > (\overline{\omega}_{i+1} - \overline{\omega}_i)$, then one should expect

$$\frac{\delta\omega_0}{\omega_0} \approx \sqrt{2} \cdot \sigma + \Delta_{offset} , \tag{E-10}$$

where the offset value should be determined by the longer-term (drifting) frequency deviation from the nominal value ω_0. In the end, for a specific case, which is more

suitable would heavily depends on the time scale of the offset term, *i.e.*, at what time scale it is considered to be relatively long-term and over which there may be considerable deviation from the nominal resonance frequency ω_0.

Shown in Table 1 below are some real data from several generations of the NEMS resonators, in fairly good agreement with eqs. (E-9) and (E-10).

Table E-1 Comparison and summary of measured data from generations of NEMS resonators.

	$\delta\omega_0/\omega_0$ (1sec RMS)	σ (τ=1sec)	Ratio $\frac{\delta\omega_0/\omega_0}{\sigma}$
124MHz (Q~1300)	4.83×10^{-7}	3.82×10^{-7}	1.26
133MHz (Q~5000)	1.49×10^{-7}	9.76×10^{-8}	1.53
190MHz (Q~5200)	6.31×10^{-7}	4.39×10^{-7}	1.44
295MHz (Q~3000)	6.77×10^{-8}	4.69×10^{-8}	1.44
420MHz (Q~1200)	4.76×10^{-7}	3.12×10^{-7}	1.52
411MHz (Q~2600)	1.21×10^{-7}	6.63×10^{-8}	1.82

References

[1] K.L. Ekinci, Y.T. Yang, M.L. Roukes, "Ultimate limits to inertial mass sensing based upon nanoelectromechanical systems", *J. Appl. Phys.* **95**, 2682-2689 (2004).

[2] A.N. Cleland, M.L. Roukes, "Noise processes in nanomechanical resoantors", *J. Appl. Phys.* **92**, 2758-2769 (2002).

[3] J.A. Barnes, A.R. Chi, L.S. Cutler, *et al.*, "Characterization of frequency stability", *IEEE Trans. Instr. & Meas.*, **IM-20**, 105-120 (1971).